

Electrocaloric materials and devices



Samuel Crossley

King's College

University of Cambridge

This dissertation is submitted for the degree of

Doctor of Philosophy

July 25, 2013

Electrocaloric materials and devices

Samuel Crossley

The temperature and/or entropy of electrically polarisable materials can be altered by changing electric field E . Research into this electrocaloric (EC) effect has focussed on increasing the size of the EC effects, with the long-term aim of building a cooler with an EC material at its heart.

Materials and experimental methods are briefly reviewed. A ‘resetting’ indirect route to isothermal entropy change ΔS for hysteretic first-order transitions is described. An indirect route to adiabatic temperature change ΔT , without the need for field-resolved heat capacity data, is also described.

Three temperature controllers were built: a cryogenic probe for 77-420 K with ~ 5 mK resolution, a high-temperature stage with vacuum enclosure for 295-700 K with ~ 15 mK resolution, and a low-temperature stage for 120-400 K with electrical access via micropositioners. Automation enables dense datasets to be compiled.

Single crystals of inorganic salts $(\text{NH}_4)_2\text{SO}_4$, KNO_3 and NaNO_2 were obtained. Applying 380 kV cm^{-1} across $(\text{NH}_4)_2\text{SO}_4$, it was found that $|\Delta S| \sim 20 \text{ J K}^{-1} \text{ kg}^{-1}$ and $|\Delta T| \sim 4 \text{ K}$, using the indirect method near the Curie temperature $T_C = 223 \text{ K}$. Without the ‘resetting’ indirect method, $|\Delta S| \sim 45 \text{ J K}^{-1} \text{ kg}^{-1}$ would have been spuriously found. Preliminary indirect measurements on KNO_3 and NaNO_2 give $|\Delta S| \sim 75 \text{ J K}^{-1} \text{ kg}^{-1}$ for $\Delta E \sim 31 \text{ kV cm}^{-1}$ near $T_C = 400 \text{ K}$ and $|\Delta S| \sim 14 \text{ J K}^{-1} \text{ kg}^{-1}$ for $\Delta E \sim 15 \text{ kV cm}^{-1}$ near $T_C = 435 \text{ K}$, respectively.

A cation-ordered $\text{PbSc}_{0.5}\text{Ta}_{0.5}\text{O}_3$ ceramic showing a nominally first-order transition at 295 K was obtained. The Clausius-Clapeyron phase diagram is revealed via indirect measurements where $|\Delta S| \sim 3.25 \text{ J K}^{-1} \text{ kg}^{-1}$ and $|\Delta T| \sim 2 \text{ K}$, and direct measurements where $|\Delta T| \sim 2 \text{ K}$. Clamped samples show broadening of the field-induced transition.

Epitaxial, $\sim 64 \text{ nm}$ -thick SrTiO_3 films were grown by pulsed laser deposition on NdGaO_3 (001) substrates with a $\text{La}_{0.67}\text{Sr}_{0.33}\text{MnO}_3$ bottom electrode. The indirect method gives $|\Delta S| \sim 8 \text{ J K}^{-1} \text{ kg}^{-1}$ and $|\Delta T| \sim 3.5 \text{ K}$ near 180 K with $|\Delta E| = 780 \text{ kV cm}^{-1}$.

Finite element modelling (FEM) was used to optimise the geometry of multilayered capacitors (MLCs) for EC cooling. Intrinsic cooling powers of 25.9 kW kg^{-1} are predicted for an optimised MLC based on PVDF-TrFE with Ag electrodes.

Declaration

This dissertation is submitted for the degree of Doctor of Philosophy in Materials Science & Metallurgy. Work took place between 05-Jan-2010 and 30-June-2012 under the supervision of Dr Neil D. Mathur. Except where specific reference is made to the work of others, this is the result of my own work. No part of this work has been submitted for any other qualification at this or any other institution. This dissertation does not exceed the limit of length.

Acknowledgements

First and foremost, I am indebted to Neil Mathur for conceiving and expertly supervising this work. Even at busy times, Neil always found time to help out and advise me at every stage. This dissertation has been enormously enhanced by his extremely thorough proof-reading.

I thank Sohini Kar-Narayan for help and advice throughout the project, especially with respect to the design and construction of equipment, without which no data could have been taken. Sohini's hands-on approach in the laboratory is one I feel I have inherited, and I am certain I could have had no better role model. Sohini also led the Scanning Thermal Microscopy measurements. I thank Xavier Moya for sharing his knowledge of thermodynamics and calorics, and for help with pulsed laser deposition. I thank Lee Phillips and Wenjing Yan also for help with pulsed laser deposition. I thank Emmanuel Defay for expert advice and support, particularly with impedance spectroscopy.

I thank my collaborators in Materials Science, Thirumurugan Alagarsamy, Wei Li and Anthony Cheetham, for providing crystals of $(\text{NH}_4)_2\text{SO}_4$, KNO_3 and NaNO_2 . I thank Roger Whatmore (Tyndall National Institute, RoI) for providing high quality ceramic $\text{PbSc}_{0.5}\text{Ta}_{0.5}\text{O}_3$. I thank Olatz Idigoras for helping prepare ceramic samples for measurement.

I thank Josée Kleibeuker for suggestions which proved key to the success of the pulsed laser deposition of SrTiO_3 on NdGaO_3 (001) substrates. I thank James McGinnigle for developing a prototype of the finite element model of a multilayered capacitor.

I thank Nadia Stelmashenko, Ahmed Kursumovic and John Durrell for support and advice on technical matters throughout the project. I thank Mary Vickers for training and support with X-ray equipment, and for measuring reciprocal space maps. I thank Robert Cornell for performing the differential scanning calorimetry. I thank the staff of the departmental metal workshop, Olatz Idigoras and Abhijeet Sangle for help with machining of apparatus.

I thank everyone in the Device Materials group, especially office 225, for miscellaneous training and advice in the lab, and for being supportive colleagues and friends.

I thank my family and former tutors for getting me here and supporting me.

I dedicate this work to my lovely fiancée Madzia, who supported me, kept me going, and put up with a lot of late-night working and anxiety.

Contents

1	Background	1
1.1	Ferroelectrics	1
1.1.1	Definitions	1
1.1.2	Phase diagrams	4
1.1.3	Hysteresis	7
1.1.4	Order-disorder and displacive transitions	11
1.1.5	Landau phenomenological theory	13
1.1.6	Landau theory and the soft mode	16
1.1.7	Critical behaviour	17
1.1.8	Relaxor ferroelectrics	19
1.2	Electrocaloric effects	20
1.2.1	Phenomenology	20
1.2.2	Timeline	24
1.2.3	Survey of candidate materials	35
1.2.3.1	Perovskites	36
1.2.3.2	Lithium niobate and lithium tantalate	37
1.2.3.3	Hexagonal manganites	37
1.2.3.4	Tungsten bronzes	38
1.2.3.5	Pyrochlores	38

1.2.3.6	Layered oxides	38
1.2.3.7	Barium flourides	38
1.2.3.8	Molybdates	39
1.2.3.9	Boracites	39
1.2.3.10	Colemanite	39
1.2.3.11	‘Other oxides’	39
1.2.3.12	Halides	39
1.2.3.13	Antimony sulphide iodides	40
1.2.3.14	Nitrites	40
1.2.3.15	Nitrates	40
1.2.3.16	Potassium dihydrogen phosphate family	40
1.2.3.17	Sulphates	40
1.2.3.18	Alums	41
1.2.3.19	Guanidiniums	41
1.2.3.20	Selenites	41
1.2.3.21	Cyanides	42
1.2.3.22	Triglycine sulphate family	42
1.2.3.23	Rochelle salt family	42
1.2.3.24	‘Complex organic compounds’	42
1.2.3.25	Liquid crystals	43
1.2.3.26	Polymers	43
1.2.3.27	Summary of candidate materials	44
1.2.4	Efficiency of electrocaloric effects	46
1.3	Summary	47

2 Instrumentation and theory of measurement 49

2.1	Adiabatic temperature change $\Delta T(\Delta E)$	50
2.2	Dielectric $\varepsilon(f)$ spectra	53
2.3	Ferroelectric $P(E)$ loops	56
2.4	Isothermal ΔS via the ‘indirect’ method	58
2.4.1	Major and minor loops	61
2.4.2	‘Standard’ and ‘resetting’ versions	64
2.5	Calorimetry, interconversion of adiabatic ΔT and isothermal ΔS	67
3	Apparatus for measurements in 77-700 K	69
3.1	Cryogenic probe	71
3.1.1	Probe head 1	71
3.1.2	Probe head 2	71
3.1.3	Wiring	75
3.1.4	Vacuum	76
3.1.5	Temperature control	76
3.1.6	Collaborative experiments on Lawsonite	77
3.2	High-temperature stage	78
3.2.1	Wiring	81
3.2.2	Vacuum	81
3.2.3	Temperature control	82
3.2.4	Previous configuration	84
3.3	Cryogenic stage	87
3.3.1	Temperature control	91
3.4	Software	92
3.4.1	Measurement control	92
3.4.2	Data processing	96

4	Electrocaloric effects in inorganic salts	97
4.1	$(\text{NH}_4)_2\text{SO}_4$	100
4.1.1	Crystal growth	105
4.1.2	Device preparation	105
4.1.3	Dielectric constant	110
4.1.4	Zero-field ΔS	112
4.1.5	$P(E)$ loops	114
4.1.6	Isothermal $ \Delta S $	120
4.1.7	Adiabatic $ \Delta T $	130
4.1.8	Conclusions	135
4.2	KNO_3	136
4.2.1	Crystal growth	139
4.2.2	Device preparation	139
4.2.3	Dielectric constant	139
4.2.4	Zero-field ΔS	143
4.2.5	$P(E)$ loops	145
4.2.6	Isothermal $ \Delta S $	147
4.2.7	Conclusions	153
4.3	NaNO_2	154
4.3.1	Crystal growth	156
4.3.2	Device preparation	156
4.3.3	Dielectric constant	156
4.3.4	$P(E)$ loops	159
4.3.5	Isothermal $ \Delta S $	161
4.3.6	Conclusions	164

5	Electrocaloric effects in $\text{PbSc}_{0.5}\text{Ta}_{0.5}\text{O}_3$ ceramics	165
5.1	Lead scandium tantalate	167
5.2	Samples	169
5.3	Measurement strategy	170
5.4	Dielectric constant	171
5.5	Zero-field ΔS	173
5.6	$P(E)$ loops	175
5.7	Isothermal $ \Delta S $	177
5.8	Adiabatic $ \Delta T $ (via indirect method)	181
5.9	Adiabatic $ \Delta T $ (via direct method)	184
5.10	Thinned $\text{PbSc}_{0.5}\text{Ta}_{0.5}\text{O}_3$	192
5.10.1	$P(E)$ loops	192
5.10.2	Isothermal $ \Delta S $	195
5.11	Conclusions	198
6	Electrocaloric effects in strained epitaxial films of SrTiO_3	199
6.1	Electrocaloric effects in thin films	199
6.2	Epitaxial films	199
6.3	Materials	201
6.3.1	SrTiO_3	201
6.3.2	NdGaO_3	204
6.3.3	Electrodes: $\text{La}_{0.67}\text{Sr}_{0.33}\text{MnO}_3$ and Pt	205
6.4	Pulsed laser deposition	206
6.5	Atomic force microscopy and X-ray diffraction	211
6.6	Film growth and characterisation	213
6.6.1	$\text{SrTiO}_3 \text{NdGaO}_3$ monolayer	213

6.6.2	LSMO NdGaO ₃ monolayer	216
6.6.3	SrTiO ₃ LSMO NdGaO ₃ bilayer	218
6.7	Measurement strategy	223
6.8	Dielectric constant	223
6.9	$P(E)$ loops	225
6.10	Isothermal $ \Delta S $	227
6.11	Conclusions	229
7	Modelling of multilayered capacitors for cooling	231
7.1	Lumped thermal circuit model	232
7.2	Finite element model	236
7.2.1	Generation of mesh	240
7.2.2	Interpretation of simulated data	242
7.2.3	Testing of mesh	243
7.3	Geometric optimisation of MLCs for cooling	243
7.3.1	Optimisation of d_e and d_{EC}	243
7.3.2	Effect of electrode material on optimal d_e and d_{EC}	245
7.3.3	Optimisation of L	247
7.4	Optimisation of realistic coolers	249
7.5	Predicted cooling powers for MLCs	250
7.5.1	Accuracy of predictions	253
7.6	New lumped thermal circuit models	254
7.6.1	Recreation of previous lumped model	254
7.6.2	Requiring heat to flow to the nearest terminal	256
7.6.3	Short thermal homogenisation step	259
7.6.4	Geometric optimisation via lumped model	263

7.6.5	Analytical expression for the ‘magic ratio’	266
7.7	Conclusions	268
8	Conclusions and Outlook	270
	Bibliography	276

List of Figures

1.1	Ising ferromagnet	4
1.2	Phase diagrams.	6
1.3	Ferroelectric domains	8
1.4	Hysteretic 1st-order transition	10
1.5	Displacive transition in BaTiO ₃	12
1.6	Landau free energies	15
1.7	Curie-Weiss behaviour	17
1.8	Electrocaloric phase diagrams	22
1.9	Electrocaloric cycle	23
1.10	Electrocaloric publications	25
2.1	Electrocaloric cycles: isothermal to adiabatic	51
2.2	Thermometry	52
2.3	Dielectric characterisation	55
2.4	Illustrations of experimental $P(E)$ data	57
2.5	Illustrations of experimental $P(E)$ data	60
2.6	Driving fields for $P(E)$	63
2.7	‘Resetting’ indirect procedure	66
3.1	Cryogenic probe — schematic (head 1)	73
3.2	Cryogenic probe — schematic (head 2)	74

3.3	Cryogenic probe — photograph	74
3.4	Paschen curve	76
3.5	Performance of cryogenic probe	77
3.6	High-temperature stage — schematic	79
3.7	High-temperature stage — photograph	80
3.8	Temperature control of high-temperature stage	83
3.9	Previous version of high-temperature stage	86
3.10	Cryogenic stage - schematic	89
3.11	Cryogenic stage - photograph	90
3.12	Measurement software — schematic	94
3.13	Measurement software — screenshot	95
4.1	Crystal structure of paraelectric $(\text{NH}_4)_2\text{SO}_4$	102
4.2	Thinning of $(\text{NH}_4)_2\text{SO}_4$ crystals	108
4.3	Measuring thickness and area of $(\text{NH}_4)_2\text{SO}_4$ crystals	109
4.4	Dielectric data for $(\text{NH}_4)_2\text{SO}_4$	111
4.5	Calorimetry results for $(\text{NH}_4)_2\text{SO}_4$	113
4.6	$P(E)$ loops of $(\text{NH}_4)_2\text{SO}_4$ Crystal B	116
4.7	$P(E)$ loops of $(\text{NH}_4)_2\text{SO}_4$ Crystal B	117
4.8	$P(E)$ loops of $(\text{NH}_4)_2\text{SO}_4$ Crystal C	119
4.9	Selected $P(T)$ for $(\text{NH}_4)_2\text{SO}_4$ (‘standard’ method)	122
4.10	Isothermal $ \Delta S $ for $(\text{NH}_4)_2\text{SO}_4$ (‘standard’ method)	123
4.11	Isothermal $ \Delta S $ for $(\text{NH}_4)_2\text{SO}_4$ (‘standard’ method)	125
4.12	Isothermal $ \Delta S $ for $(\text{NH}_4)_2\text{SO}_4$ (‘resetting’ method)	127
4.13	Isothermal $ \Delta S $ for $(\text{NH}_4)_2\text{SO}_4$ — comparison	129
4.14	Adiabats for $(\text{NH}_4)_2\text{SO}_4$ Crystal B	131

4.15	Adiabats for $(\text{NH}_4)_2\text{SO}_4$ Crystal C	132
4.16	Adiabatic $ \Delta T $ for $(\text{NH}_4)_2\text{SO}_4$	134
4.17	Crystal structure of KNO_3	138
4.18	Dielectric data for KNO_3	141
4.19	Dielectric data for KNO_3 — reproducibility	142
4.20	Calorimetry results for KNO_3	144
4.21	$P(E)$ loops for KNO_3	146
4.22	Selected $P(T)$ for KNO_3 (‘standard’ method)	148
4.23	Spurious isothermal $ \Delta S $ for KNO_3 (‘standard’ method)	149
4.24	Isothermal $ \Delta S $ for KNO_3 (‘resetting’ method)	151
4.25	Isothermal $ \Delta S $ for KNO_3 (‘resetting’ method)	152
4.26	Crystal structure of NaNO_2	155
4.27	Dielectric data for NaNO_2	158
4.28	$P(E)$ loops of NaNO_2	160
4.29	Selected $P(T)$ for NaNO_2	162
4.30	Isothermal $ \Delta S $ for NaNO_2	163
5.1	Perovskite structure	166
5.2	Dielectric data for PST	172
5.3	Calorimetry results for PST	174
5.4	$P(E)$ loops of 420 μm -thick PST	176
5.5	Selected $P(T)$ for PST	178
5.6	Isothermal $ \Delta S $ for PST	179
5.7	Isothermal $ \Delta S $ for PST	180
5.8	$E - T$ adiabats for PST (indirect)	182
5.9	Adiabatic $ \Delta T $ for PST (indirect)	183

5.10	Nominally adiabatic ΔT for PST (direct, qualitative)	186
5.11	Nominally adiabatic ΔT for PST (direct, qualitative)	187
5.12	Nominally adiabatic ΔT for PST (direct, qualitative)	189
5.13	Nominally adiabatic ΔT for PST (direct, quantitative)	191
5.14	$P(E)$ loops for thinned PST	194
5.15	Mechanical clamping of PST samples	195
5.16	Selected $P(T)$ for thinned PST	196
5.17	Isothermal $ \Delta S $ for thinned PST	197
6.1	Pseudo-cubic cell of DyScO_3	201
6.2	Phase diagram of epitaxial films of SrTiO_3	203
6.3	Pseudo-cubic cell of NdGaO_3	204
6.4	‘Mark X’ PLD system	208
6.5	‘Mark X’ PLD system vacuum diagram	210
6.6	X-ray diffraction	212
6.7	SrTiO_3 monolayer on NdGaO_3 (001) substrate	215
6.8	LSMO film on NdGaO_3 (001) substrate	217
6.9	SrTiO_3 LSMO bilayer on NdGaO_3 (001) substrate	219
6.10	XRD for SrTiO_3 LSMO bilayer	221
6.11	Reciprocal space map for SrTiO_3 LSMO bilayer	222
6.12	Dielectric data for epitaxial SrTiO_3 film	224
6.13	$P(E)$ loops for epitaxial SrTiO_3 film	226
6.14	Isothermal $ \Delta S $ for epitaxial SrTiO_3 film	228
7.1	Multilayered capacitor	232
7.2	Lumped thermal circuit model of MLC	234
7.3	FEM model of MLC	238

7.4	PHP interface to FEM program	239
7.5	20-node brick-shaped FEM element	240
7.6	Optimisation of d_e and d_{EC}	244
7.7	Effect of varying κ_e	246
7.8	Effect of varying L	248
7.9	Heat pathways in lumped thermal circuit models	256
7.10	Lumped thermal circuit model Q	257
7.11	Lumped thermal circuit model H	261
7.12	Optimisation of d_e and d_{EC} with lumped model H	264
7.13	Effect of varying L on lumped model H	265
8.1	Adiabats for $\text{PbSc}_{0.5}\text{Ta}_{0.5}\text{O}_3$	273

List of Tables

1.1	Critical exponents	18
1.2	Summary of promising materials	45
3.1	Comparison of bespoke cryostats	70
4.1	Zero-field thermal changes at ferroelectric transitions	99
4.2	Phases of KNO_3	136
4.3	Transitions of KNO_3	136
7.1	Lumped model parameters and results	235
7.2	FEM simulation parameters and results	252
7.3	Lumped model results (C and CE)	255
7.4	Lumped model results (C, CE and Q)	258
7.5	Lumped model results (C, CE, Q and H)	262

Notation

Electromagnetism textbooks write electric field \mathbf{E} and polarisation \mathbf{P} in a bold and non-italicised type face to indicate that they are vector fields. Ferroelectrics are normally studied in a plate-like geometry with flat electrodes on either surface such that $\mathbf{E} = (0, 0, E_z)$ and $\mathbf{P} = (0, 0, P_z)$. As a result, it is usual to represent them simply as scalar fields E and P , where $E = |\mathbf{E}| = E_z$ and $P = |\mathbf{P}| = P_z$. Other electromagnetic vector fields are treated in an analogous way.

Chapter 1

Background

The focus of this dissertation is electrocaloric effects: electrically-driven thermal changes often related to ferroelectric phase transitions. A material with a large reversible electrocaloric effect near room temperature could form the basis of a new kind of heat pump. Because no known material has been demonstrated to show the right set of properties to be exploited for practical cooling, academic focus remains set on measuring new materials, or finding ways to improve the properties of measured ones.

This introductory Chapter provides a general discussion of ferroelectrics and electrocalorics, briefly outlining the most useful physical theories and models. Electrocalorics literature is reviewed via two complementary sections, the first of which is organised as a timeline and the second in terms of materials. Familiarity with thermodynamic laws and potentials, phase transitions and electromagnetism is assumed.

1.1 Ferroelectrics

Some electrostatics and thermodynamics of ferroelectrics and analogous ferromagnetic systems are briefly reviewed, with a focus on phenomenology.

1.1.1 Definitions

Two electrical charges q and $-q$ separated by a distance d constitute an electric dipole \mathbf{p} which is specified by a vector of magnitude qd and direction along the line joining $-q$ to q . An electrical dipole acts as a source of an electric field, with an electrostatic

potential in circular polars of $V = (|p| \cos \vartheta) / (4\pi\epsilon_0 r^2)$ for $r \gg d$ (where ϵ_0 is the permittivity of free space) [1].

Due to charge cancellation, an array of small aligned dipoles behaves as a single large dipole with the end charges alone as its component charges. Thus, aligned angstrom-scale dipoles from charge displacement in a unit cell or molecule, together constitute a macroscopic electric dipole moment. Polarisation P is given by this macroscopic dipole moment, normalised by volume [1].

By definition, ferroelectric materials show a *spontaneous* polarisation P_S whose direction is *switchable* with an applied electric field E . The switching process is discontinuous in P and is sometimes regarded as a first-order phase transition with a latent heat of zero [2]. Like any first-order phase transition, $P(E)$ for a ferroelectric is in practice always somewhat hysteretic in E . At the Curie temperature T_C , ferroelectrics transform to a non-polar paraelectric¹ phase. This transition may be first or second order [3].

Ferroelectrics are a subset of pyroelectrics, which are themselves a subset of paraelectrics. Pyroelectrics show a spontaneous polarisation, but its polarity need not be switchable by an applied field. Dielectrics have a non-zero susceptibility $\chi = \frac{1}{\epsilon_0} \partial P / \partial E$, i.e. they are polarisable in an applied field. The capacitance C of an electrode-dielectric-electrode layered structure is enhanced by a factor of $\epsilon = \chi + 1$ over that of the same capacitor with free space substituted for the dielectric, where ϵ is the ‘dielectric constant’² [1, 3].

Polarisation has dimensions of charge per unit area, reflecting the fact that a uniformly polarised solid has charge on its polar surfaces. This surface charge may be termed ‘trapped charge’ to distinguish it from ‘free charge’ in the conduction band [1]. Free charge can carry direct or alternating current. Trapped charge has no such long-range mobility, but it is able to oscillate when an alternating current flows.

Poled single crystals of ferroelectric materials show spontaneous electrical dipoles, so at first glance they might be expected to exert strong attractive and repulsive forces on each other in an analogous way to ferromagnets. In fact, the external fields are usually completely screened by free charge at the surface of the material, although they can persist for a short amount of time and may be used to generate enormous voltages³.

¹Or ‘dielectric’. Unlike their magnetic analogues, there is no universally accepted distinction.

²Ignoring dielectric losses, see discussion in Chapter 2.

³For example, this was exploited by Naranjo *et al.* (2005) to generate measurable amounts of nuclear fusion [4].

The absence of attraction and repulsion forces between poled ferroelectrics meant that ferroelectricity was far less obvious to early researchers than ferromagnetism [3]. Ferroelectricity was discovered in 1920 when dielectric hysteresis was noticed in Rochelle salt by Valasek [5].

1.1.2 Phase diagrams

Ferromagnetic and liquid-vapour systems will be briefly discussed to enhance understanding of ferroelectric systems.

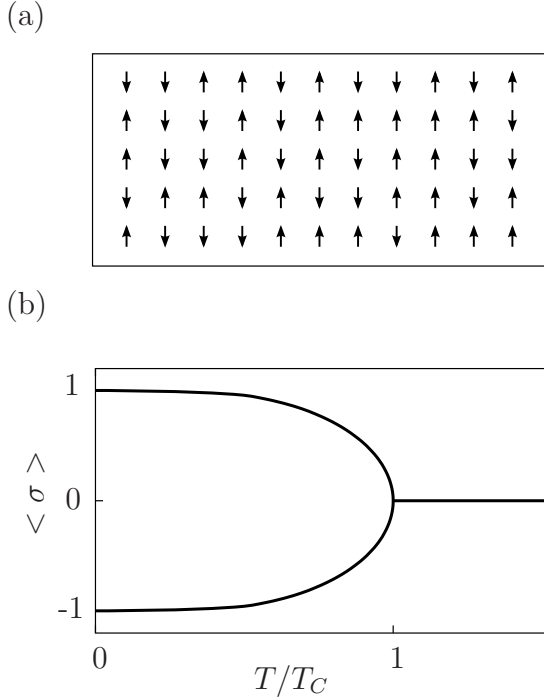


Figure 1.1: **(a)** Ising model of ferromagnet. **(b)** $\langle \sigma \rangle = \alpha M_S$ as a function of T/T_C for mean-field Ising.

mean value of σ for all the spins in the magnet. It is then possible to solve for $\langle \sigma \rangle$ as a function of temperature, giving $\langle \sigma \rangle = \tanh(\frac{T_C}{T} \langle \sigma \rangle)$ for the case of zero applied field (Figure 1.1b) [6]. As $\langle \sigma \rangle$ drops continuously to zero at T_C , the mean-field Ising transition from the ferromagnetic to the paramagnetic phase is second-order, which is also experimentally observed in many ferromagnetic materials [6].

Many textbooks on critical phenomena point out the similarities between Ising ferromagnets and liquid-vapour systems [2, 7]. Both may be depicted as a first-order phase coexistence line (ignoring hysteresis effects) in $B - T$ or $p - T$ space (where p is pressure) terminated by a critical point⁴ at $(B_{\text{crit}}, T_{\text{crit}})$ or $(p_{\text{crit}}, T_{\text{crit}})$ [Figure 1.2a-b]. The gradients of the first-order lines are given by a Clausius-Clapeyron

Ferromagnets show a spontaneous magnetisation M_S which is switchable by an applied magnetic field H . Macroscopic magnetic moments are the result of aligned spins or orbital moments in a solid, so although ferromagnetism is phenomenologically analogous to ferroelectricity, their microscopic origins are quite different. The Ising model for magnets assumes that spins are arranged in a lattice (Figure 1.1a) and that they interact only with nearest-neighbour spins via a coupling energy of form $J\sigma_i\sigma_j$ (where J is a material-dependent coupling constant and σ is a property of a spin equal to 1 if the spin is ‘up’ and -1 if the spin is ‘down’) [6]. The Ising model can be solved via a mean-field assumption which replaces σ_j in the previous expression with $\langle \sigma \rangle$, i.e. the

⁴I.e. a second-order phase transition.

equation: $dp/dT = |\Delta S|/|\Delta V|$ for the liquid-vapour system (where ΔS and ΔV are the entropy change and volume change at the transition, respectively) and analogously $dB/dT = |\Delta S|/|\Delta M|$ for the magnetic system (i.e. zero, as the entropies of the spin-up and spin-down states are identical) [6]. In the liquid-vapour case, the critical point corresponds to a fluctuation-dominated state of matter related to *critical opalescence*.

Many ferroelectric-paraelectric transitions are second-order and thus phenomenologically similar to the Ising ferromagnet. Theoretical treatments working in close analogy to the magnetic case sometimes use a ‘pseudospin’ nomenclature to represent the electric dipoles. However, a large number of ferroelectrics show first-order phase transitions and cannot be described with Ising-like models [3, 8]. Idealised phase diagrams for first-order and second-order ferroelectrics are illustrated in Figure 1.2c-d. The Clausius-Clapeyron equation for first-order lines is $dE/dT = |\Delta S|/|\Delta P|$, where ΔP is the polarisation change at the transition⁵. For simplicity, Figure 1.2 ignores hysteresis, which may occur along both the E and T axes. This deficiency will be corrected in the next Section.

Overall, Figure 1.2 illustrates that the four systems of Ising ferromagnetism, liquid-vapour and two flavours of ferroelectricity have more in common than intuition might suggest. All four can be the bases of a thermodynamic refrigeration cycle, because the entropy fields in all four cases are non-uniform, particularly in the vicinity of the critical points. Liquid-vapour systems are the basis of almost all commercial cooling technology near room temperature, and magnetic refrigeration is used in commercial cryogenic systems to achieve temperatures well below the lambda point of He³. Only ferroelectric refrigeration — electrocaloric refrigeration — remains to be commercialised in any form.

It should be noted that critical fluctuations in ferroelectric order parameters are rarely reported, as the critical region is generally very narrow or blurred by impurities or lattice defects [3, 9].

⁵This assumes that P is the order parameter for these phase transitions. Materials in which this is not true are termed ‘improper’ ferroelectrics [3].

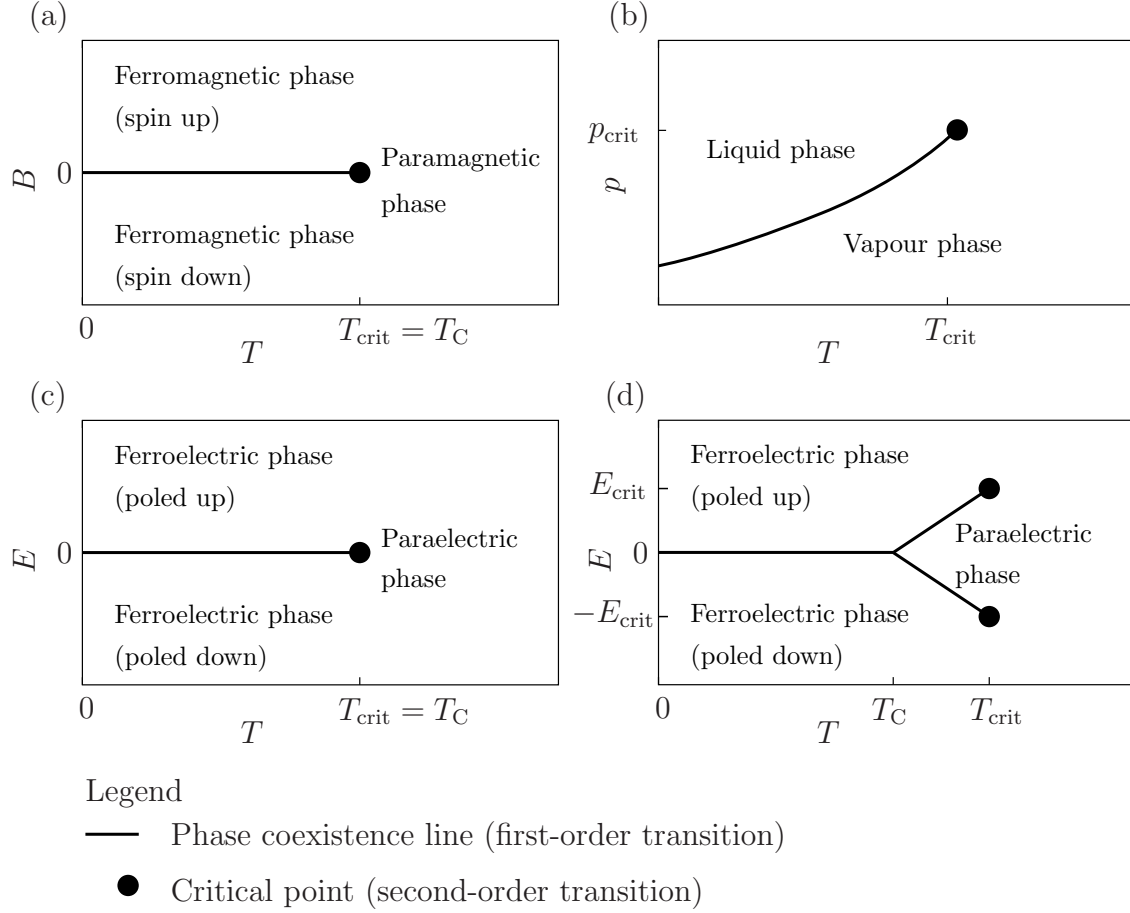


Figure 1.2: Phase diagrams of **(a)** an Ising ferromagnet, **(b)** a liquid-vapour system, **(c)** an Ising-like ferroelectric system and **(d)** a ferroelectric system with a first-order transition to the paraelectric phase (at zero field). See, for example, [2]. Hysteresis at first-order transitions has been ignored. The gradients of all the first-order lines are described by the Clausius-Clapeyron equations: $dB/dT = |\Delta S|/|\Delta M|$ for the magnetic system, $dp/dT = |\Delta S|/|\Delta V|$ for the liquid-vapour system and $dE/dT = |\Delta S|/|\Delta P|$ for the two ferroelectric systems.

1.1.3 Hysteresis

Hysteresis is often observed at first-order phase transitions, including hysteresis due to ferroic switching and hysteresis of T_C between heating and cooling. Ferroic switching hysteresis is the result of a process known as domain-wall pinning or nucleation [3].

A ferroelectric domain is a part of the material in which the dipoles are all aligned. Domains form because there is an electrostatic energy cost at external surfaces proportional to $\mathbf{P} \cdot \hat{\mathbf{n}}$ (where \mathbf{P} is vector polarisation and $\hat{\mathbf{n}}$ is the normal vector to the surface) which is minimised by having \mathbf{P} point within the plane of the surface. A simple example of an arrangement of domains that achieves this is shown in Figure 1.3a.

Domain structure is affected by factors such as grain size, material defects, lattice strain and sample geometry. Materials cooled from above T_C with no applied field often tend to adopt a domain configuration such that the average polarisation of the crystal is zero. Once a field is applied, the domains align and the material is said to be ‘poled’. During poling, domain walls move and nucleate. Ferroic switching hysteresis is the result of domain walls becoming ‘pinned’ against defects, impurities or grain boundaries in the material [3].

Figure 1.3b illustrates the $P(E)$ behaviour predicted by models such as Ising, which ignore domains. Figure 1.3c illustrates the hysteretic $P(E)$ behaviour expected for real systems (this too, however, is idealised — a full discussion of the form of measured ferroelectric $P(E)$ loops will be given in Chapter 2). The value of E coinciding with polarisation reversal is termed the ‘coercive field’, E_C . As domain wall motion is a dynamic process, E_C is a function of the frequency of the driving field [3].

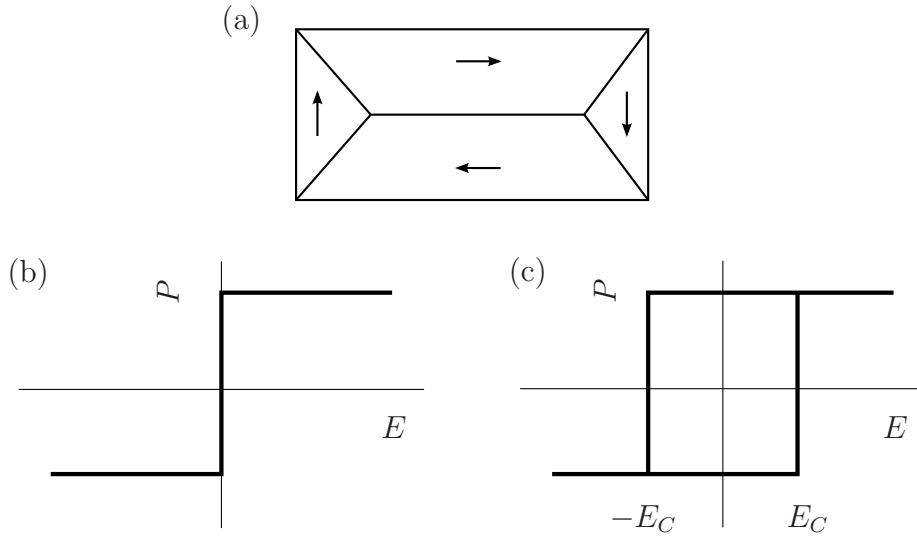


Figure 1.3: **(a)** Illustration of a possible arrangement of ferroelectric domains which minimises $\mathbf{P} \cdot \hat{\mathbf{n}}$. Direction of polarisation is denoted by arrows. **(b)** Illustration of $P(E)$ behaviour in an idealised Ising-like ferroelectric, which ignores hysteresis. **(c)** *Simplified* illustration of ferroelectric hysteresis. A discussion of the form of observed $P(E)$ behaviour will be given in Chapter 2.

Hysteresis of T_C between heating and cooling (‘thermal hysteresis’) is often observed in first-order ferroelectric-paraelectric transitions [3]. Furthermore, nominally ‘first-order’ phase transitions in ferroelectric materials may not be perfectly discontinuous in T due to factors such as impurities. A total of four temperatures, T_{h1} , T_{h2} , T_{c1} and T_{c2} , are thus required to fully describe such a transition, where the subscripts ‘h’ and ‘c’ denote heating and cooling respectively, and the subscripts ‘1’ and ‘2’ refer to the start and finish temperatures of the transition (Figure 1.4) [10]. The transition regions on heating and cooling may overlap, although in the Figure they do not for purposes of clarity. A field dependence is expected for T_{h1} , T_{h2} , T_{c1} and T_{c2} from the Clausius-Clapeyron equation $dT/dE = |\Delta P|/|\Delta S|$ (the marked values in the Figure correspond to zero applied field) [6].

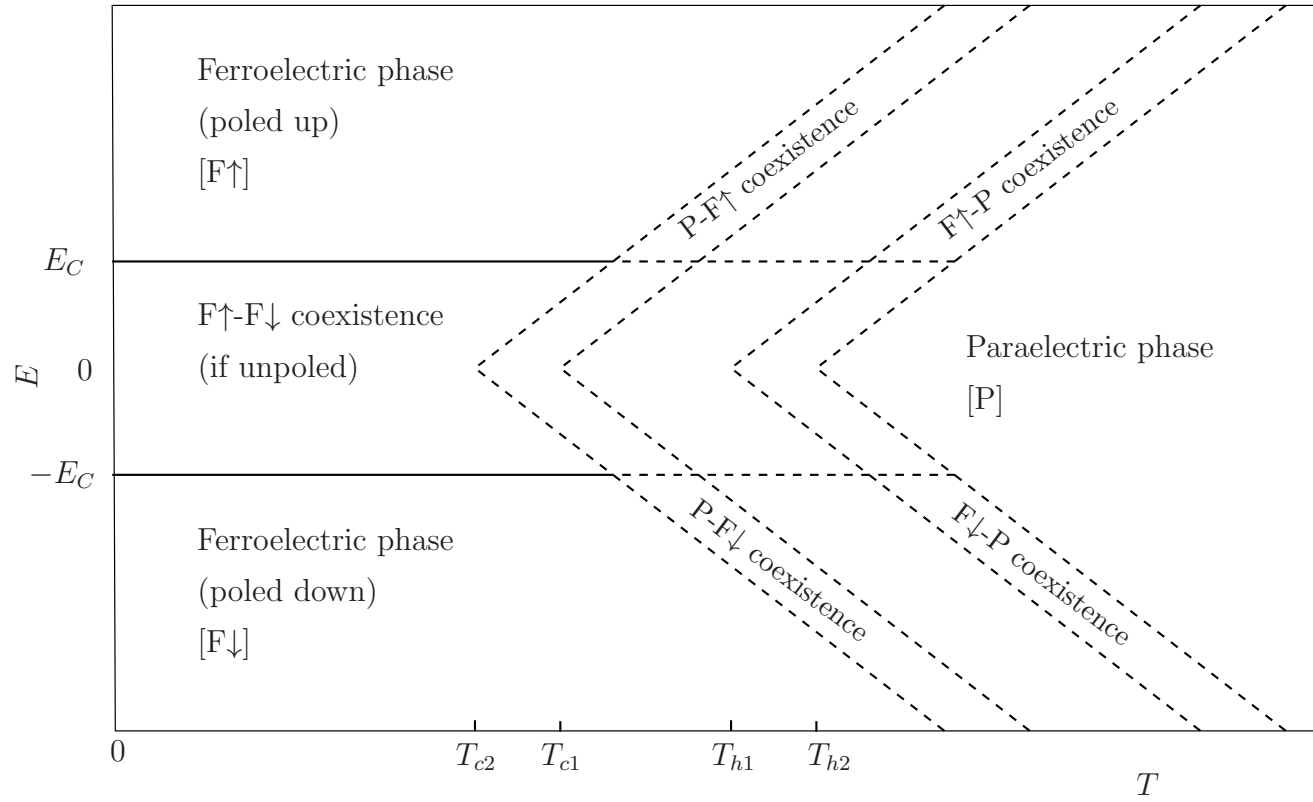


Figure 1.4: Illustration of an imperfect, thermally and electrically hysteretic first-order phase transition in a ferroelectric.

1.1.4 Order-disorder and displacive transitions

In a poled ferroelectric, there exists an activation energy barrier E_{act} that any particular microscopic dipole must overcome to reverse its polarity with respect to the polar axis of the crystal. The switching probability is small if this energy barrier is large compared to $k_B T$ (where k_B is the Boltzmann constant). Thus a class of ferroelectrics with a phase transition to a paraelectric state at $T_C = E_{\text{act}}/k_B$ might be expected. Such transitions are termed ‘order-disorder’, with potassium dihydrogen phosphate (KH_2PO_4) often cited as a prototypical example [3].

By contrast, in a ‘displacive’ transition to a ferroelectric phase, an ion or group of ions in a centrosymmetric (e.g. cubic) unit cell become displaced below T_C , breaking symmetry and generating a spontaneous microscopic dipole where previously there was none. Barium titanate (BaTiO_3) is often cited as a prototypical example of a displacive ferroelectric transition (Figure 1.5) [3, 7].

While it is often useful to classify ferroelectric phase transitions as either ‘order disorder’ or ‘displacive’, there are grey areas between these two extremes. Progress was achieved via a key insight by W. Cochran in 1960 [11]. In his own words: ‘A ferroelectric or an anti-ferroelectric transition in certain crystals is the result of an instability of the crystal for a certain mode of vibration, and can be treated as a problem in lattice dynamics’. Ferroelectric phase transitions coincide with ‘softening’ (lowering of frequency) of an optical phonon (the ‘soft mode’) located at the Brillouin zone centre⁶. Soft modes may be observed via a range of spectroscopic tools such as infra-red or Raman. Soft mode analysis has been used to [3]:

- Identify the driving instability of the phase transition and thus supercede the simplistic ‘order-disorder’ and ‘displacive’ classification system, although that system remains very useful in practice.
- Define the fundamental primary order parameter Ψ of a phase transition. The relationship between Ψ and P is not necessarily one of direct proportionality. Materials for which Ψ and P are not strongly coupled are termed ‘improper ferroelectrics’.

⁶i.e. a standing wave. This is an *optical* phonon which can be illustrated with an infinite diatomic chain of atoms of types A and B. A vibrational mode exists where each pair of A and B oscillate in phase with respect to each other. The wavevector of such a mode with respect to the overall crystal lattice is zero.

- Understand antiferroelectricity - it too can be associated with a soft optical mode, but displaced from the zone centre.
- Investigate the parallelism between ferroelectricity and its stress-strain analogue, ferroelasticity [12].

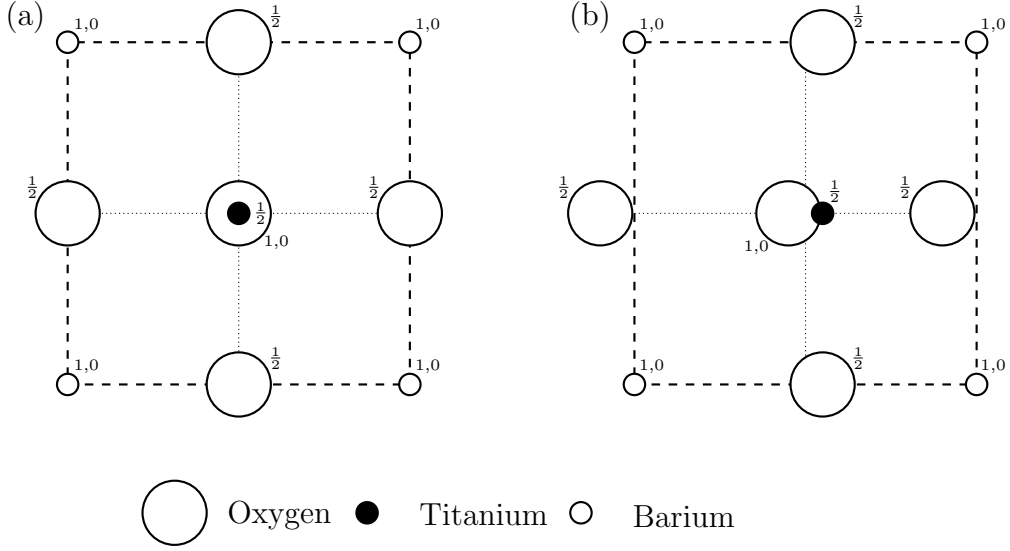


Figure 1.5: Illustration of the 393 K displacive phase transition in prototypical perovskite BaTiO₃ [3]. **(a)** Unit cell of the cubic paraelectric phase (dashed line: cell boundary). Numeric labels indicate displacement out of the plane of the paper. The lattice parameter is 404 pm. **(b)** Unit cell of the pseudo-cubic (i.e. tetragonal) ferroelectric phase. The O and Ti ions displace by 5 pm with respect to the origin of the cubic parent (or prototype) lattice. Atomic displacements exaggerated for illustrative purposes, and the small distortion of the lattice parameter is not shown.

1.1.5 Landau phenomenological theory

The Landau theory of ferroelectric phase transitions is simple, general and powerful [13]. Assuming that P is proportional to the order parameter for the transition, the Gibbs free energy $G(P, T)$ with respect to the paraelectric phase is approximated as a 6th-order polynomial of form:

$$G = \frac{1}{2}aP^2 + \frac{1}{4}bP^4 + \frac{1}{6}cP^6 - EP \quad (1.1)$$

Where terms in odd powers of P are prohibited for symmetry reasons. That G is minimised at equilibrium follows directly from the first two laws of thermodynamics [6]. As this is a phenomenological theory, suitable forms for the Landau coefficients $a - c$ are found by inspection, such that the solution of $\partial G/\partial P = 0$ at zero applied field traces out the observed form of $P_S(T)$ (Figure 1.6a-b).

The forms of $G(P, T)$ consistent with $P_S(T)$ are illustrated in Figure 1.6c-h for first-order and second-order transitions [8]. Parameter a is temperature dependent with $\partial a/\partial T > 0$. Materials which have $a(T) = a'(T - T_0)$, where T_0 is a temperature near or equal to T_C , are said to satisfy the Curie-Weiss law. Parameter c is always positive to ensure divergence of G towards $+\infty$ at large $|P|$. Negative values of b correspond to first-order transitions, and positive values of b correspond to second-order transitions. The special case of $b = 0$ corresponds to a ‘tricritical transition’ [9].

Differentiating Equation 1.1 and ignoring high-order terms in P gives $\chi = \partial P/\partial E \sim 1/a(T)$. Plots of $1/\chi$ against T are commonly seen in literature, partly because they give information about $a(T)$, via this expression.

The Gibbs free energy due to strain in pseudo-cubic displacive ferroelectrics such as BaTiO₃ can be approximated as [8]:

$$G_{\text{strain}} \sim \frac{1}{2}K\eta^2 + Q\eta P^2 - \eta\sigma \quad (1.2)$$

Where η is the tetragonal strain (strain of the tetragonal unit cell with respect to the cubic parent cell), K is Young’s modulus, Q is the coefficient of strain-polarisation coupling (whose lowest term is in P^2 because strain is invariant upon reversal of P), and σ is an external stress. Minimising G with respect to η gives $K\eta + QP^2 - \sigma = 0$ and thus $\eta = \sigma - QP^2/K$. Substituting this into Equation 1.2 and adding Equation 1.1 gives:

$$G = -\frac{1}{2} \frac{(\sigma - QP^2)^2}{K} + \frac{1}{2}aP^2 + \frac{1}{4}bP^4 + \frac{1}{6}cP^6 - EP \quad (1.3)$$

The strain term expands to include terms in both P^2 and P^4 . Strain is thus capable of modifying the a and b coefficients of the Landau free energy, affecting both T_C and the order of the transition, respectively [8]. For example, certain materials such as SrTiO_3 are not ordinarily ferroelectric, but can become ferroelectric under strain (these are termed ‘incipient’ ferroelectrics). Strain cannot generally be ignored in treatments of ferroelectric phase transitions.

For an unclamped sample ($\sigma = 0$) Equation 1.3 becomes:

$$G = \frac{1}{2}aP^2 + \frac{1}{4}(b - \frac{2Q^2}{K})P^4 + \frac{1}{6}cP^6 - EP \quad (1.4)$$

Spontaneous strain reduces the quartic term in the Landau free energy, and is thus potentially capable of driving a second-order transition to first-order.

Overall Landau theory has proven extremely useful to scientists, for reasons such as the following [8]:

- For first-order transitions, even though the order parameter P is discontinuous, $G(P, T)$ is a continuous analytical function throughout the temperature range. This allows metastable states to be modelled, which can help explain thermal hysteresis of T_C .
- Although Landau theory fails very close to critical points because it ignores thermodynamic fluctuations, for ferroelectrics the critical region is generally small or blurred by imperfections.
- Modelling the coupling of ferroelectricity to strain is straightforward in Landau theory.
- Landau theory sets qualitative statements such as ‘the sample shows a weak first-order transition’ on a sounder quantitative footing. In this example, it is implied that b is negative, but small.

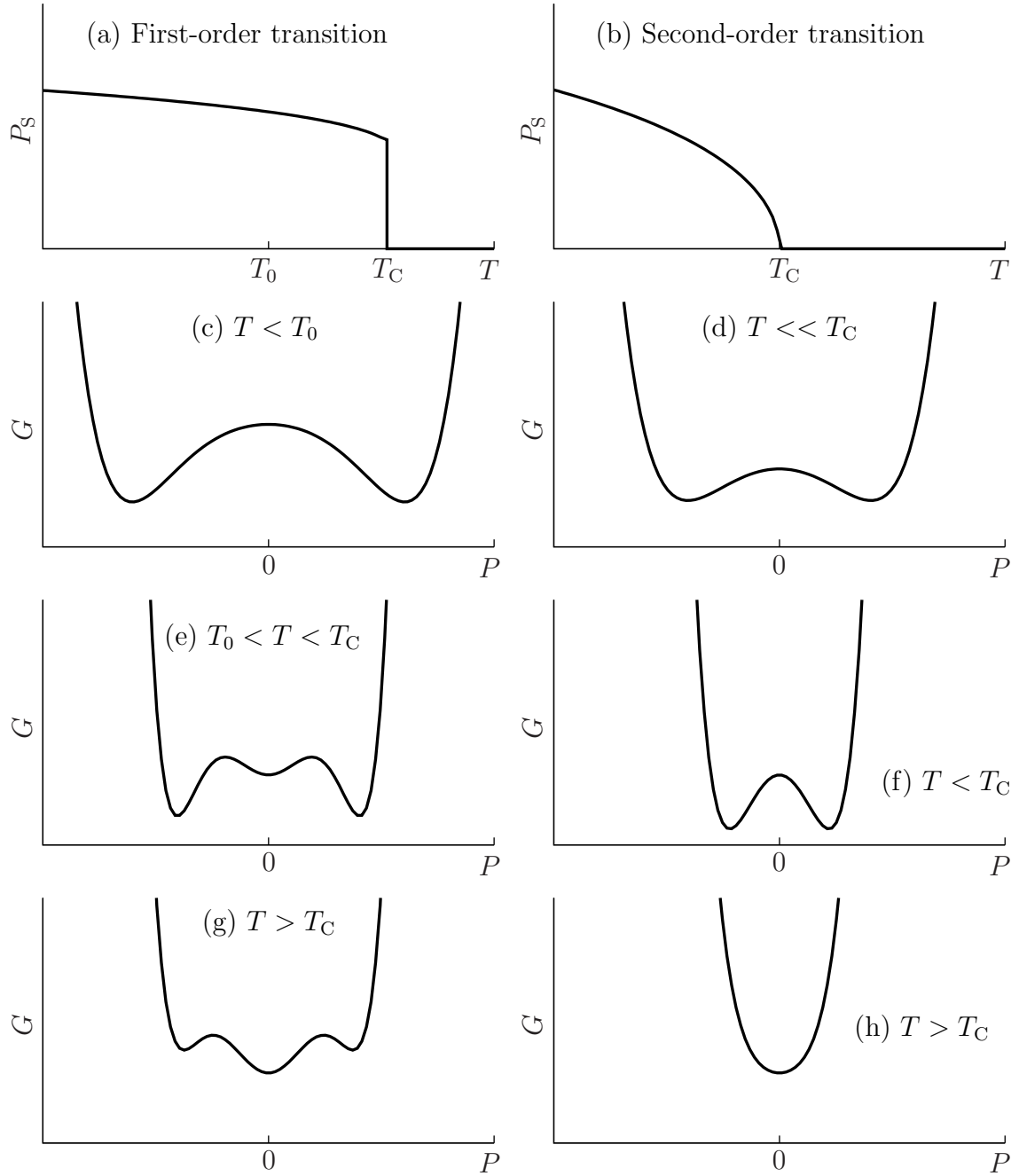


Figure 1.6: **(a)** Illustration of $P_s(T)$ for a first-order ferroelectric phase transition. **(b)** Illustration of $P_s(T)$ for a second-order ferroelectric transition. **(c)(e)(g)** Illustration of $G(P, T)$ consistent with a first-order ferroelectric phase transition. **(d)(f)(h)** Illustration of $G(P, T)$ consistent with a second-order ferroelectric phase transition [8].

1.1.6 Landau theory and the soft mode

A simple ferroelectric unit cell could show a single dipole obeying Hook's law for a mass on a spring [14]:

$$m \frac{\partial^2 u_{\text{opt}}}{\partial t^2} = -K u_{\text{opt}} \quad (1.5)$$

$$U(u_{\text{opt}}) = \frac{1}{2} K u_{\text{opt}}^2 \quad (1.6)$$

Where m is an appropriate reduced mass, K is a spring constant, u_{opt} is the dipole displacement (the subscript 'opt' reminds us that this is an optical phonon mode at the Brillouin zone centre) t is time and U is internal energy. Polarisation P is related to u_{opt} via [14]:

$$P = \frac{1}{V_{\text{cell}}} e^* u_{\text{opt}} \quad (1.7)$$

Where V_{cell} is the real-space unit-cell volume and e^* is an appropriate reduced charge. From Landau theory at zero applied field:

$$G = \frac{1}{2} a(T) P^2 + \frac{1}{4} b P^4 + \frac{1}{6} c P^6 \quad (1.8)$$

Thus $K \propto a(T)$ to a first harmonic approximation. The solution to Equation 1.5 is a vibrational mode of frequency $\omega^2 \propto K$ [14]. For Curie-Weiss materials:

$$\omega_{\text{soft}}^2 \propto a(T) \quad (1.9)$$

Thus Landau theory is consistent with the observed softening (i.e. reduction in ω) of an optical phonon at the Brillouin zone centre near ferroelectric phase transitions. A useful result whose generality transcends these crude approximations is that from $\chi = 1/a(T)$, $\omega^2 \propto 1/\chi$ [14].

1.1.7 Critical behaviour

Critical fluctuations analogous to critical opalescence in liquid-vapour systems are rarely observed in ferroelectrics, because the critical regions are small and often blurred by factors such as impurities, defects and strain [3]. By contrast, near-critical behaviour is well studied and often well understood in terms of Landau and mean-field theories [8]. In near-critical regions the temperature dependence of various thermodynamic quantities is described by critical exponents in the same way as for ferromagnetic and liquid-vapour systems, and all critical systems in nature. Table 1.1 summarises the main critical exponents in ferroelectrics (e.g. [9]). Although only second-order phase transitions pass directly through critical points, the behaviour of observables near first-order ferroelectric transitions can also follow critical exponent laws (though the form of the observed ‘pole’ at T_C is different). Typical Curie-Weiss ($\gamma = 1$) behaviour of low-field susceptibility near first and second-order transitions is illustrated in Figure 1.7. Heat capacity at a first-order transition normally shows a strong peak due to latent heat.

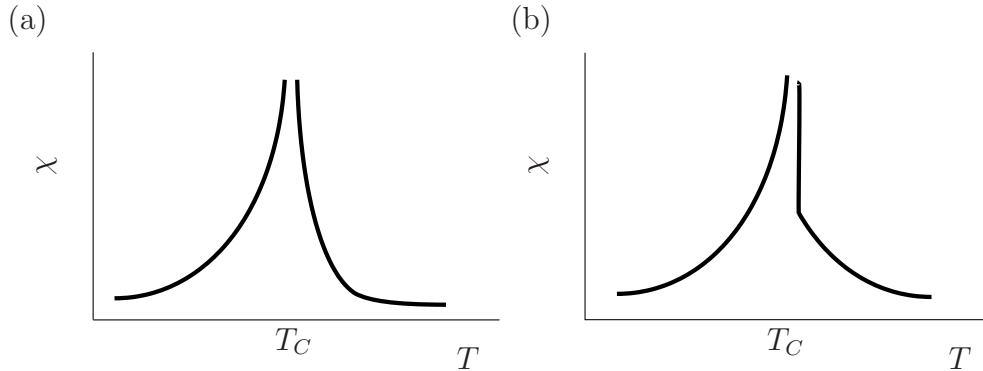


Figure 1.7: Illustration of Curie-Weiss behaviour, $\chi = \frac{1}{\epsilon_0} \frac{\partial P}{\partial E} = |t|^{-\gamma}$ where $\gamma = 1$ in the near-critical region and t is reduced temperature (Table 1.1) around **(a)** a critical point and **(b)** a first-order transition. After Chandra and Littlewood [8].

<i>Variable</i>	<i>Description</i>	<i>Ideal 2nd order behaviour</i>	<i>Ising result</i>
t	Reduced temperature $\frac{T-T_{\text{crit}}}{T_{\text{crit}}}$		
J	Reduced field $\frac{E-E_{\text{crit}}}{E_{\text{crit}}}$	$J = \Psi^\delta \ (t = 0)$	$\delta = 3$
Ψ	Order parameter P	$\Psi = t ^\beta \ (t < 0, J = 0)$	$\beta = 0.5$
C	Heat capacity at constant J	$C = t ^{-\alpha} \ (J = 0)$	$\alpha = 0$
χ	Susceptibility $\frac{1}{\varepsilon_0} \frac{\partial P}{\partial E}$	$\chi = t ^{-\gamma} \ (J = 0)$	$\gamma = 1$
ξ	Correlation length (length scale of thermodynamic fluctuations).	$\xi = t ^{-\nu} \ (J = 0)$	$\nu = 0.5$

Table 1.1: Behaviour of various observable quantities in near-critical regions in ferroelectrics (e.g. [9]). The subscript ‘crit’ denotes ‘value at the critical point’. Different exponents for positive or negative t are common.

1.1.8 Relaxor ferroelectrics

Materials such as lead magnesium niobate $\text{PbMg}_{1/3}\text{Nb}_{2/3}\text{O}_3$ (PMN) can show a disordered spatial distribution of Mg and Nb ions. This leads to a slow decay of spontaneous polarisation P_S , and a broad non-Curie-Weiss peak in χ whose maximum occurs at a different temperature depending on frequency. This is the characteristic behaviour of relaxor ferroelectrics (or simply ‘relaxors’). Because of the frequency dependence, the observed dielectric anomalies cannot formally be associated with a conventional ‘phase transition’ [15].

The idea of ‘polar nano-regions’ (PNRs) — nanoscale regions with a particular local composition — has been attributed [16] to Bokov and Mylnikova, who were influenced by experimental work of Smolensky and Agronovskaya. The situation is more complex than a mixture of slightly different materials with slightly different Curie temperatures, leading to a range of Curie temperatures for the material as a whole, and a broad transition. According to Cowley [16] and Bokov [17], there is no well-defined global symmetry breaking at the ‘transition’ of a relaxor, i.e. these systems show glass-like properties. In glasses, the ‘transition’ is not between different phases of matter, but between ergodic⁷ and non-ergodic regimes of the same phase.

Two imprecisely-defined temperatures, are used to describe relaxor materials. Polar nano-regions nucleate at the Burns temperature T_B , and they subsequently become ‘frozen’, i.e. non-ergodic at the glass transition temperature T^* [16]. Theories of equilibrium thermodynamics cannot apply to relaxors in the non-ergodic regime because ergodicity is the central axiom of statistical physics. However, many non-ergodic relaxors undergo an irreversible field-driven phase transition to a conventional ferroelectric phase (i.e. a state in which the average crystal symmetry is ferroelectric). This field-induced transition can occur at relatively low fields (1.7 kV cm^{-1} for PMN), and indeed some relaxors do not enter the non-ergodic regime as they transform directly to the ferroelectric phase near T^* [16].

Relaxors remain a particularly active area of theoretical and experimental research. Their high and broad dielectric peaks have led to their widespread industrial use as capacitor dielectrics, and they have been suggested for large electrocaloric effects due to their disordered structure [18].

⁷‘Ergodic: relating to or denoting systems or processes with the property that, given sufficient time, they include or impinge on all points in a given space and can be represented statistically by a reasonably large selection of points.’ From the Oxford English Dictionary.

1.2 Electrocaloric effects

1.2.1 Phenomenology

‘The electrocaloric effect is the temperature change of a crystal which results from an adiabatic application of an electric field’ wrote Lines and Glass in their textbook of 1977 [3]. This adiabatic temperature change ΔT represents an upper bound on the decrease of temperature that an electrocaloric material could generate in an attached load in a single thermodynamic cycle. Much progress has occurred in electrocalorics since 1977, and a modern definition would surely mention isothermal heat $Q = T\Delta S$, where ΔS is the isothermal entropy change induced by the electric field. Isothermal heat sets an upper bound on the cooling power per thermodynamic cycle. The expression $T|\Delta S| \sim c_E|\Delta T|$ is often used to interconvert between ΔT and ΔS , i.e. by assuming that specific heat capacity at constant field c_E is constant over the section of $T - E$ space traversed. This assumption is particularly dubious for first-order systems where c_E is affected by latent heat. Proper interconversion between ΔS and ΔT requires mapping of entropy in $E - T$ space; this is non-trivial and will be discussed in Section 2.5. In summary, because of the role of c_E , a large value of $T\Delta S$ is no guarantee of a large value of ΔT , and both ΔT and $T\Delta S$ should ideally be measured directly, the former by thermometry and the latter by calorimetry.

The phase diagram of an ideal $b \ll 0$ (i.e. strongly first-order) ferroelectric is illustrated in Figure 1.8a (adapted from Figure 1.2). Far below T_C , even though the entropies of the up-poled and down-poled phases are identical, some thermal disorder might be overcome under field. An isothermal path through $E - T$ space from below T_C , beginning at strong negative field and ending at strong positive field, would be expected to show small variations in entropy as a result (illustrated in Figure 1.8a-b, path 1). Slightly above T_C , a strong field applied isothermally would induce the first-order phase transition and reduce the entropy of the material by the latent entropy of the transition (path 2). In this case isothermal $\Delta S(E)$ would show a step function at a value of $|E|$ determined by the Clausius-Clapeyron relation. Increasing T to just below the critical point T_{crit} , a degree of continuous (i.e. second-order) character might permeate the isotherm (path 3). Exactly at T_{crit} , the field-induced transition would be entirely second order (path 4). Above T_{crit} no transition would take place, but significant continuous field-driven entropy changes might nonetheless occur in the supercritical regime (path 5).

An idealised phase diagram for a $b < 0$ (second-order) ferroelectric is illustrated in Figure 1.8c. Far below T_C , small variations in entropy would be expected due to the overcoming of thermal disorder under high field, even though there is no nominal entropy change between the up-poled and down-poled phases (path 6). Continuous transitions with varying entropy profiles would be expected around the critical point, with the peak entropy change occurring at the critical point itself (paths 7-9).

Figure 1.8 is meant only as an illustrative, qualitative prediction of the isothermal entropy changes that might be seen experimentally in an electrocaloric material. Surprisingly, there are very few experimental datasets in literature which systematically explore the $E - T$ phase diagram to provide empirical insight.

Electrocaloric effects in a given material are limited by the practical difficulties of applying large voltages, avoiding dielectric breakdown, and avoiding leakage current. Thus, materials with large values of zero-field ΔS do not necessarily show large values of isothermal ΔS , as the necessary electric fields may not be attainable.

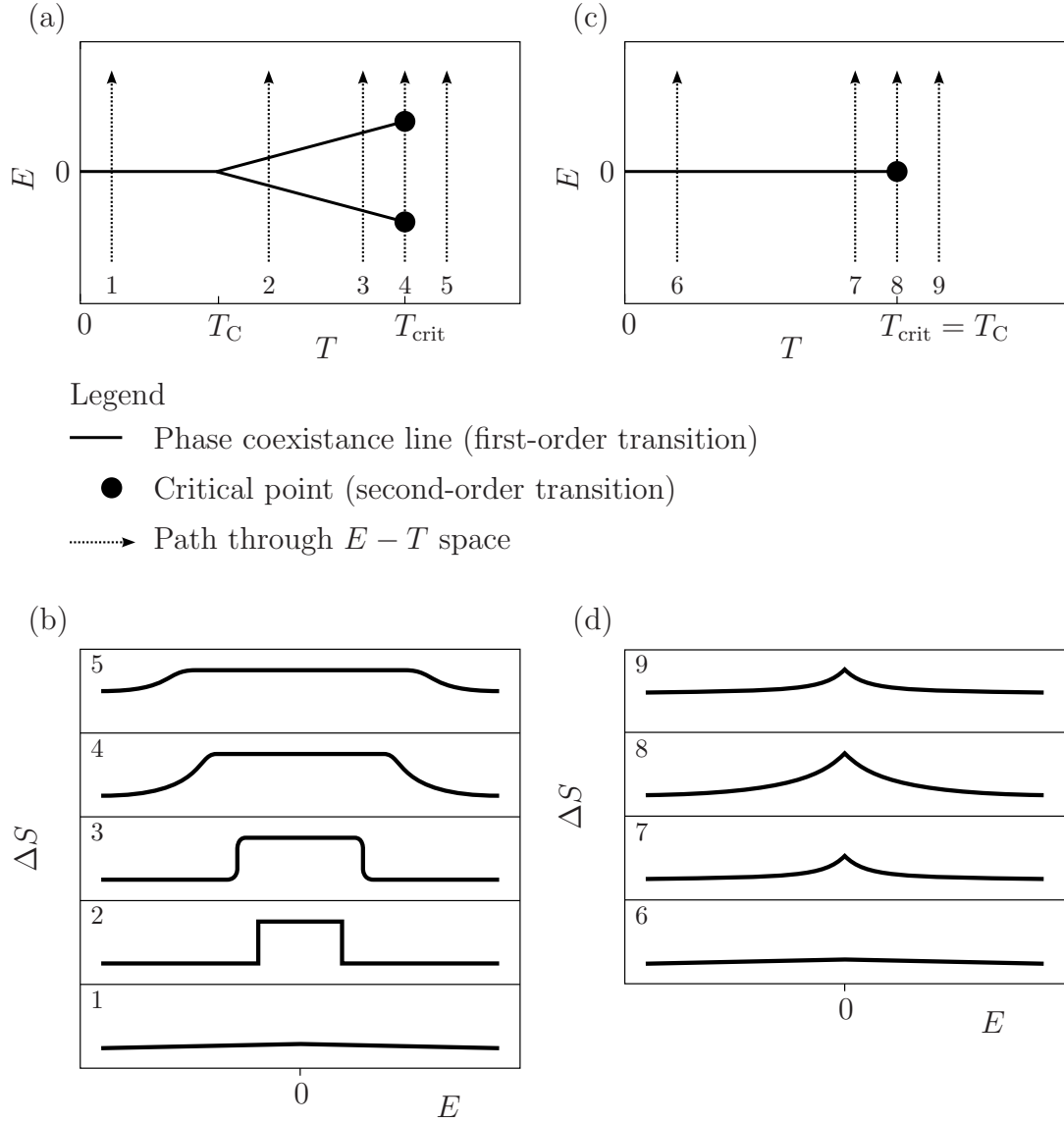


Figure 1.8: Adapted from Figure 1.2. **(a)** Illustration of $E - T$ phase diagram for an ideal first-order ferroelectric. Hysteresis is ignored. **(b)** Qualitative illustration of entropy changes that might be expected on taking various isothermal paths through the phase diagram of (a). **(c)** Illustration of $E - T$ phase diagram for an ideal second-order ferroelectric. Hysteresis is ignored. **(d)** Qualitative illustration of entropy changes that might be expected on taking various isothermal paths through the phase diagram of (c).

Practical electrocaloric devices may use a four-stage cycle to cool a load. The four stages are [19]:

- Application of a field across the electrocaloric material, causing its temperature to increase by $|\Delta T|$.
- Dumping of electrocaloric heat to a reservoir. The electrocaloric material returns to ambient temperature, with the field still on (assuming Joule heating due to leakage current is small).
- Removal of the field, causing the electrocaloric material to cool down by $|\Delta T|$.
- Withdrawal of heat from the load.

These stages are illustrated in Figure 1.9, and are discussed in greater detail in Chapter 2.

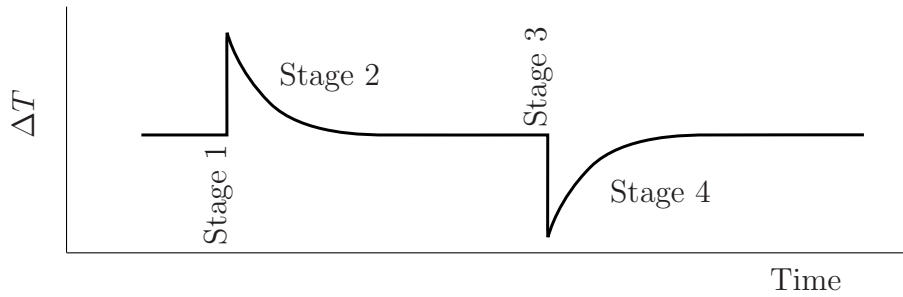


Figure 1.9: Illustrative example of a four-stage electrocaloric cycle.

Experimentally, the Maxwell relation $(\partial P / \partial T)_E = (\partial S / \partial E)_T$ may be used to access isothermal $\Delta S(\Delta E)$ from a suitably dense dataset of $P(E, T)$. This has proven particularly useful for the study of thin films, where adiabatic ΔT or isothermal Q are especially difficult to access due to small thermal masses. For a full discussion of the use of the Maxwell relation, see Chapter 2.

1.2.2 Timeline

Research in the 20th century focussed on finding electrocaloric effects in bulk materials, but the largest effects found were ~ 2.5 K. Thin films proved the key to unlocking ‘giant’ effects of 12 K or higher, as their characteristic high breakdown fields gave access to new high-field regimes of the phase diagram. Seminal papers by Mischenko *et al.* in 350 nm $\text{Pb}(\text{Zr}_{0.95}\text{Ti}_{0.05})\text{O}_3$ [20] (2006) and Neese *et al.* in 1 μm -thick poly(vinylidene fluoride-trifluoroethylene) (55/45 mol %) [PVDF-TrFE] [21] (2008) have catalysed a new interest in the electrocaloric effect as a candidate cooling technology (Figure 1.10). Multilayered capacitors have been proposed to harness the thin-film technology for rapid cooling of macroscopic loads [19].

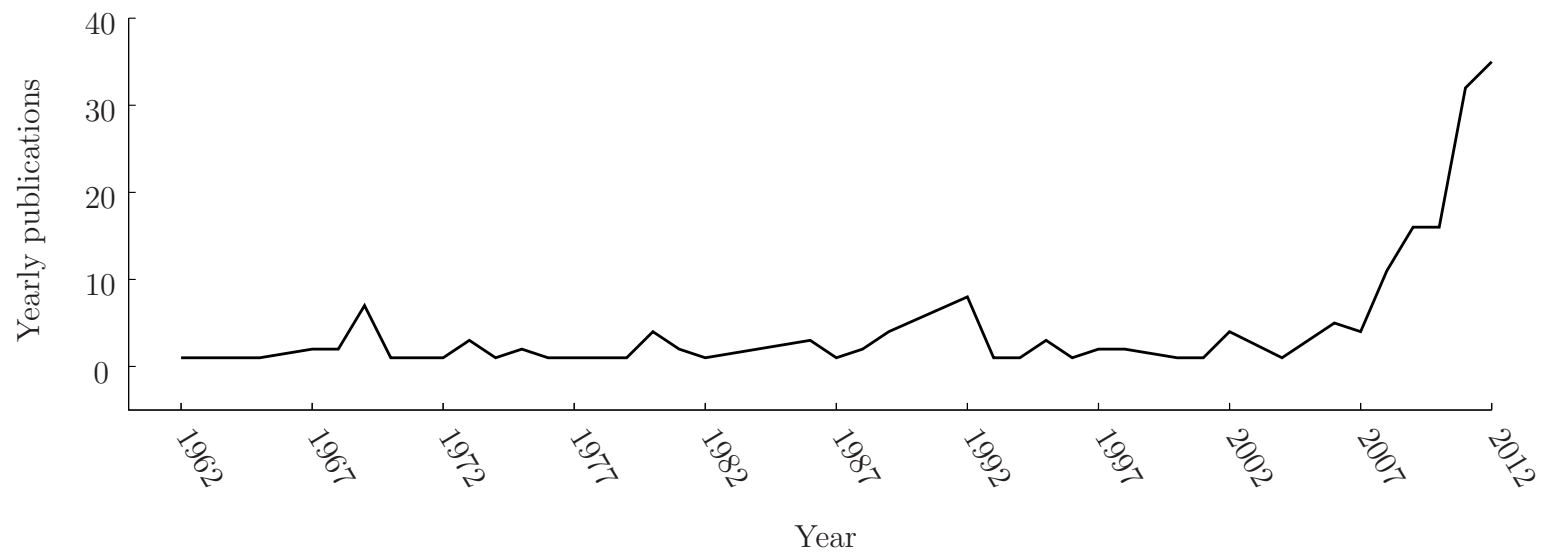


Figure 1.10: Publications in electrocalorics for the period 1962-2012. Data are the number of hits of a search for publication titles containing the word ‘electrocaloric’, using Thomson Reuters Web of Science.

The important historical papers as far as early 2013 are presented below in the form of a timeline.

1824

■ Carnot develops his eponymous theorem, theoretical concepts of reversible and irreversible work, theoretical heat engines, and theoretical refrigerators.

1845

■ Joule demonstrates that heat and work are two forms of the same thing — a flow of energy.

1861

■ Maxwell's equations for electromagnetism are published.

1865

■ Clausius defines new functions of state, entropy S and internal energy U , completing the process of identifying the first two laws of thermodynamics. William Thompson (Lord Kelvin) also played a major role in the development of the second law.

1873

■ Gibbs proposes a 'free energy' $G = U - TS + pV$ whose *minimisation* for a gas under isothermal and isobaric conditions reflects global entropic *maximisation* and energy conservation. Free energy soon proved to be an indispensable tool for applying the laws of thermodynamics to realistic systems.

1881

■ Emil Warburg describes heating during a magnetic $M(H)$ loop measurement in iron well below T_C . Although he cited other authors who had previously measured similar phenomena, his work is often incorrectly reported as the first observation of a magnetocaloric effect.

1921

■ Valasek discovers dielectric hysteresis in Rochelle Salt, the first observation of ferroelectricity [5].

1930

■ The first electrocaloric study is conducted, on Rochelle Salt, by Kobeko and Kurtschatov [22].

■ Sawyer Tower circuit is developed for measuring $P(E)$ loops [23].

1935

■ Ferroelectricity is found in KH_2PO_4 (KDP) and related compounds [24].

1937

■ Landau theory of phase transitions is published [13].

1942

Leon J. Sivian files a patent for pyroelectric energy recovery [25]. Pyroelectricity would soon find widespread application in passive infra-red sensors.

1946

Ferroelectricity is found in BaTiO_3 , the first ceramic ferroelectric to be discovered [26].

1949-50

Ferroelectricity is found in KNbO_3 [27], LiNbO_3 [28], LiTaO_3 [28] and PbTiO_3 [29], and incipient ferroelectricity is found in KTaO_3 [27]. Over the subsequent three decades most of the families of ferroelectrics known today were identified, with the notable exception of ferroelectric polymers.

1960

Cochran identifies ferroelectricity with the condensation of a ‘soft’ phonon mode, profoundly influencing experimental and theoretical work on ferroelectrics [11].

1964

Kikuchi and Sawaguchi observe a $|\Delta T| = 0.3$ K electrocaloric effect in free-standing SrTiO_3 single crystals at 11 K with a driving field of 7 kV cm^{-1} [30]. Early interest in the electrocaloric effect focussed on cryogenic cooling, perhaps inspired by the success of magnetocalorics in that application.

1966

Strukov reports a $|\Delta T| = 0.1$ K electrocaloric effect in triglycine sulfate $(\text{NH}_2\text{CH}_2\text{COOH})_3 \cdot \text{H}_2\text{SO}_4$ (TGS) (this paper from the former USSR could not be tracked down, but the Figures are reproduced in Lines and Glass [3]).

1968

Thacher reports electrocaloric effects in various $\text{PbZr}_x\text{Ti}_{1-x}\text{O}_3$ (PZT) materials, and Sn-doped PZT [31]. Effects of $|\Delta T| = 1.6$ K were reported. Thacher found the directly measured results to be in good agreement with those obtained via the Maxwell relation $(\partial P / \partial T)_E = (\partial S / \partial E)_T$.

1969

Kawai reports piezoelectricity in poly (vinylidene fluoride) (PVDF) [32]. The exceptional properties of this new family of ferroelectrics would become apparent in the next decade.

1977

Hailing a ‘coming of age of the ferroelectric phenomenon’, Lines and Glass publish what would become a classic textbook on ferroelectrics [3]. The electrocaloric effect is briefly mentioned.

Electrocaloric effects of $|\Delta T| \sim 0.2$ K are found at low temperatures in the incipient ferroelectric KTaO_3 by Lawless [33].

1981

Tuttle and Payne report $|\Delta T| = 2.5$ K electrocaloric effects in $\text{Pb}_{0.99}\text{Nb}_{0.02}(\text{Zr}_{0.75}\text{Sn}_{0.20}\text{Ti}_{0.05})_{0.98}\text{O}_3$ using applied fields of 30 kV cm^{-1} [34].

1989

Shebavovs *et al.* publish the first in a series of papers on electrocaloric effects in ceramic $\text{PbSc}_{0.5}\text{Ta}_{0.5}\text{O}_3$ (PST) [35–38]. Effects of $|\Delta T| = 2.4$ K are reported near room temperature. A variety of levels of cation ordering are tested, yielding first-order ferroelectric behaviour and relaxor behaviour. Multilayers are considered and measured, but the opportunity to use the metallic electrodes for heat extraction is not identified.

Scott tabulates zero-field entropy change, and various other parameters, for a number of ferroelectric materials [39].

A widely-cited article, ‘Ferroelectric Memories’ by Scott and Paz de Araujo is published [40]. The authors explain how recent advances in thin-film technology have enabled direct commercial exploitation of ferroelectricity in computer memory, 66 years after the phenomenon was discovered by Valasek. Lead-based ferroelectrics are inferior to $\text{SrBi}_2\text{Ta}_2\text{O}_9$ for many memory applications, as the volatility of lead is linked to rapid ageing.

1992

Sinyavsky and Brodyansky describe the construction of an electrocaloric fridge using PST blocks as the working body and various liquids as coolants [41]. The direction of flow of coolant is used to alternately direct electrocaloric heat to a reservoir and withdraw it from a load.

2006

Mischenko *et al.* at Cambridge and Cranfield (UK) report ‘giant’ $|\Delta T| = 12$ K electrocaloric effects observed indirectly via the Maxwell relation in 350 nm-thick sol-gel films of $\text{Pb}(\text{Zr}_{0.95}\text{Ti}_{0.05})\text{O}_3$ (PZT) near the T_C of 493 K [20]. The thin-film geometry enables large field changes of 480 kV cm^{-1} to be applied across the film, as breakdown fields are high in films. This high-field regime appears to hold the key to large effects.

2008

Neese *et al.* at Penn State (USA) report ‘giant’ $|\Delta T| = 12$ K electrocaloric effects in $1 \mu\text{m}$ -thick poly(vinylidene fluoride-trifluoroethylene) (55/45 mol %) [PVDF-TrFE] near the T_C of 350 K [21]. The polymer outperforms the PZT films of Mischenko *et al.* in terms of mass-normalised isothermal entropy change: $55 \text{ J K}^{-1} \text{ kg}^{-1}$ for the polymer against $8 \text{ J K}^{-1} \text{ kg}^{-1}$ in the ceramic. However the applied fields are larger for the polymer, at 2000 kV cm^{-1} . In the same work, effects of $|\Delta T| = 12$ K are measured in a relaxor copolymer poly(vinylidene fluoride-trifluoroethylene-chlorofluoroethylene) (59.2/33.6/7.2 mol %) [PVDF-TrFE-CFE] near 320 K. Again, these measurements all rely on the Maxwell relation.

Akçay *et al.* publish theoretical study into effect of lateral clamping and epitaxial strain on electrocaloric properties of BaTiO_3 thin films [42]. Lateral clamping was predicted to modify the order of the 400 K phase transition of BaTiO_3 from first to second order, with a corresponding reduction and broadening of electrocaloric effects. Compressive strain was predicted to raise the temperature in which maximum electrocaloric effects occur and lower their temperature dependence, whereas tensile strain was predicted to have the opposite effect.

2009

‘Giant’ electrocaloric effect of $|\Delta T| = 5$ K measured in lead-free ceramic films of $\text{SrBi}_2\text{Ta}_2\text{O}_9$ (SBT) via the Maxwell relation [43].

‘Giant’ electrocaloric effect of $|\Delta T| = 9$ K measured in ceramic films of relaxor $\text{PbMg}_{1/3}\text{Nb}_{2/3}\text{O}_3\text{--PbTiO}_3$ (PMN-PT) via the Maxwell relation [44].

Kar-Narayan and Mathur demonstrate serendipitous electrocaloric effects of $|\Delta T| = 0.5$ K in multilayered capacitors (MLCs) with a Y5V dielectric based on BaTiO_3 . Furthermore, the results provide grounding for a lumped circuit model of hypothetical MLCs based on PZT or PVDF-TrFE, suggesting such an MLC could deliver 2.9 kW kg^{-1} of cooling power, a value which seems promising when set in the context of conventional commercial coolers ($\sim 20 \text{ kW}$) [19, 45].

2010

A team from Penn State (USA) and the Jozef Stefan Institute (Slovenia) reports electrocaloric effects of 20 K in irradiated PVDF-TrFE and 45 K in $\text{Pb}_{0.92}\text{La}_{0.08}\text{Zr}_{0.65}\text{Ti}_{0.35}\text{O}_3$ thin films (both relaxor ferroelectrics) [46]. However, the method is to use a thermal model to extrapolate millikelvin temperature changes measured in the thin film, with larger thermal masses still attached, and as such is not a true direct measurement.

The same team report the first direct measurement of a ‘giant’ electrocaloric effect, in free-standing polymer films based on PVDF-TrFE-CFE [47] and PVDF-TrFE [48]. Effects of ~ 12 K are reported in both cases, observed directly via a small bead thermistor.

2011

- Scott publishes a review article on the electrocaloric effect [49].
- ‘Giant’ electrocaloric effect of $|\Delta T| = 6.9$ K measured in ceramic films of relaxor PST via the Maxwell relation [50].
- The International Symposium on Integrated Functionalities (ISIF) hosts a session dedicated to electrocalorics, the first such session at a conference.
- Rožič and coworkers study electrocaloric effects in bulk relaxor PMN-PT using direct and indirect methods [18]. The results suggest that the Maxwell relation is unsafe to apply to relaxor ferroelectrics in the non-ergodic regime.

2012

- Jia and Sungtaek demonstrate continuous cooling using Y5V MLCs [51].

2013

- Kar-Narayan *et al.* explore the possibility of directly measuring electrocaloric heat in thin films using Scanning Thermal Microscopy (SThM) and infra-red imaging. The results confirm that electrocaloric heat could be observed via SThM in films of micron thickness or greater. [52].
- Moya *et al.* report giant electrocaloric strength ($|\Delta T|$ or Q , normalised by electric field) of $220 \text{ mK} [\text{kV cm}^{-1}]^{-1}$ in single crystals of BaTiO_3 [10].

- Defay *et al.* analyse the electrocaloric efficiency of thin films for coolers. The authors find that polymer films (η for PVDF-TrFE is 7.3) are more efficient than ceramic (η for Zr-rich PZT is 3.0). This work is described in detail in Section 1.2.4.
- Effects of $|\Delta T| = 45$ K predicted in thin films of relaxor $\text{Pb}_{0.8}\text{Ba}_{0.2}\text{ZrO}_3$ near room temperature [53].

1.2.3 Survey of candidate materials

Scientific papers directly concerned with electrocalorics are relatively few in number (Figure 1.10). Only a tiny fraction of known ferroelectrics have been considered for electrocaloric effects, and furthermore ferroelectric properties can be hugely modified by factors such as strain, microstructure and stoichiometry. Various commonly-reported measurements can sometimes be used to predict the electrocaloric performance of a material which has not been directly characterised for electrocaloric effects:

- **Zero-field entropy change ΔS** at or near the phase transition (measured via calorimetry) should, for ‘proper’ ferroelectrics at least, be driveable electrically, in the absence of parasitic effects such as leakage current and dielectric breakdown. The largest reported mass-normalised *isothermal* ΔS are of order $55 \text{ J K}^{-1} \text{ kg}^{-1}$ in low-density polymers [21]. However, ‘giant’ adiabatic temperature changes have also been seen in dense materials with values of $\Delta S \sim 8 \text{ J K}^{-1} \text{ kg}^{-1}$ [20]. For this reason, and also when considering practical cooling, there is a strong case for normalising ΔS by volume [54]. Despite this, normalisation by mass remains the norm in literature.
- **Pyroelectric coefficient $|\partial P/\partial T|$** , i.e. the charge given up per unit area of the material, per unit temperature increase. The most notable pyroelectrics such as $\text{Sr}_x\text{Ba}_{1-x}\text{Nb}_2\text{O}_6$ (SBN) show coefficients of just under $1 \text{ } \mu\text{C cm}^{-2} \text{ K}^{-1}$ near T_C [55]. An important caveat is that pyroelectric coefficients are normally quoted for zero-field, whereas the electrocaloric effect depends on the *field integrated* pyroelectric coefficient. For example, ferroelectric polymers have small zero-field pyroelectric coefficients, but still display a large electrocaloric effect because they are able to withstand enormous electric fields E of up to 4000 kV cm^{-1} with minimal decay of $|\partial P/\partial T|$ at large E [21].
- **Dielectric constant** shows a peak near second-order phase transitions. A sharp peak in $\varepsilon(T)$ for a second-order transition can indicate a sharp transition and a large pyroelectric coefficient. Large loss tangents can indicate parasitic leakage which degrades electrocaloric performance.
- **Ferroelectric $P(E)$ loops** reported in literature are occasionally dense enough in T to be used to estimate electrocaloric isothermal ΔS by the Maxwell relation. Just above first-order phase transitions, double $P(E)$ loops are sometimes

reported, where the double loop corresponds to the *field induced* ferroelectric phase, with isothermal $|\Delta S|$ approximately the same as zero-field $|\Delta S|$.

In 1973 E. C. Subbarao compiled a then comprehensive list⁸ of ferroelectric and antiferroelectric materials, divided into 25 classes [56]. This list, plus ferroelectric polymers, but ignoring metals with ferroelectric crystal symmetry, has been used as a starting point for the following concise systematic discussion of *materials classes* from an electrocalorics perspective. In the majority of cases this has involved picking the best-known members of a materials class and searching literature for the electrocalorics ‘indicators’ of zero-field ΔS , $|\partial P/\partial T|$, $\varepsilon(T)$, and field-induced transitions reflected in double $P(E)$ loops.

In what follows, values of P_S and T_C , if not otherwise specified, are taken from Subbarao [56].

1.2.3.1 Perovskites

Prior to the ‘thin-film era’ (2006 onwards), values of electrocaloric adiabatic $|\Delta T|$ greater than one K had only been reported in lead-based perovskites such as $\text{PbZr}_x\text{Ti}_{1-x}\text{O}_3$ (PZT) (sometimes doped with Sn) [31, 34] and $\text{PbSc}_{0.5}\text{Ta}_{0.5}\text{O}_3$ [35]. Furthermore, Zr-rich PZT, in thin-film form, was the first ‘giant’ electrocaloric material to be reported [20]. The $|\Delta T| \sim 45$ K effects claimed recently were in films of relaxor perovskite $\text{Pb}_{0.8}\text{Ba}_{0.2}\text{ZrO}_3$ [53]. Thus, lead-based perovskites are among the most studied, and most promising⁹ electrocaloric materials. However the PZT, PLZT, PMN-PT and PST systems barely scratch the surface of this family, with various niobates, tantalates and tungstates¹⁰, all of which are ferroelectric with Curie temperatures ranging from 83 K ($\text{PbCo}_{0.5}\text{W}_{0.5}\text{O}_3$) to 763 K (PT). $\text{PbSc}_{0.5}\text{Ta}_{0.5}\text{O}_3$ will be discussed in detail in Chapter 5.

BaTiO_3 (BTO) shows small electrocaloric effects of about 1 K above its first-order transition temperature of ~ 396 K, however single crystals of BTO were recently shown by Moya *et al.* [10] to exhibit a giant electrocaloric strength of $|\Delta T|/|\Delta E| = 220 \text{ mK} [\text{kV cm}^{-1}]^{-1}$. This work also demonstrated good agreement

⁸A version of this list may be found in Appendix F of Lines and Glass [3].

⁹At least if the toxicity of lead is to be ignored.

¹⁰Epitaxial films containing lead tungstates have recently attracted interest in the field of multiferroics [57].

between direct electrocaloric measurements (from both thermometry and calorimetry), and indirect measurements via the Maxwell relation, and the Clausius-Clapeyron equation. BTO-based multilayered capacitors (MLCs) show serendipitous electrocaloric effects and play an important role in research into practical electrocaloric coolers (see Chapter 7 for a full discussion) [19, 45].

The $\text{Ba}_x\text{Sr}_{1-x}\text{TiO}_3$ (BST) system shows values for T_C that range from 396 K for pure BTO through to 0 K in the limit of x tending to zero. The Sr doping also broadens the transition and provides a pyroelectric coefficient of $\sim 0.75 \mu\text{C cm}^{-2} \text{ K}^{-1}$ at room temperature for $x = 0.65$ [58]. Haini *et al.* recently demonstrated that highly strained epitaxial films of the incipient ferroelectric SrTiO_3 on DyScO_3 substrates can exhibit T_C values above room temperature [59], however no experimental electrocaloric studies on such samples hitherto exist in literature (see Chapter 6 for a full discussion).

Many more ferroelectric perovskites are known, such as BiFeO_3 , NaNbO_3 , WO_3 and KIO_3 . An important feature of nearly all ferroelectric perovskites is that due to the cubic prototype structure of the paraelectric phase, they may be poled along any high-symmetry axis, reducing the penalty to P_S normally associated with polycrystalline ferroelectric ceramics.

1.2.3.2 Lithium niobate and lithium tantalate

These materials are notable for large pyroelectric effects over a wide temperature range and exceptionally low leakage currents, properties which were recently put to imaginative use by Naranjo *et al.* in a bench-top nuclear fusion reactor [4]. At $71 \mu\text{C cm}^{-2}$, LiTaO_3 has the largest spontaneous polarisations of any known bulk ferroelectric. These properties are promising, but testing these materials for electrocaloric effects presents challenges: T_C is 1483 K in LiTaO_3 and 938 K in LiNbO_3 . The high values of T_C could potentially be reduced via strain engineering or doping.

1.2.3.3 Hexagonal manganites

Rare-earth manganites such as hexagonal YMnO_3 have attracted attention as potential multiferroic¹¹ materials. Values of T_C are generally above 600 K. The small number of studies of ferroelectric $P(E)$ behaviour in these materials report interesting

¹¹Simultaneous ferroelectricity and ferromagnetism.

ferrielectric¹² properties [60–62]. No information could be found from which to predict electrocaloric properties.

1.2.3.4 Tungsten bronzes

Tungsten bronze ferroelectrics constitute a large family of uniaxial ferroelectrics. The relaxor $\text{Sr}_x\text{Ba}_{1-x}\text{Nb}_2\text{O}_6$ (SBN) is a noteworthy pyroelectric showing peak coefficients of up to $0.9 \mu\text{C cm}^{-2} \text{ K}^{-1}$ near $T_C \sim 370 \text{ K}$ [55]. Furthermore, it is lead free and can be grown epitaxially on SrTiO_3 or MgO substrates by pulsed laser deposition [63, 64].

1.2.3.5 Pyrochlores

The best known is $\text{Cd}_2\text{Nb}_2\text{O}_7$, which shows a complex and diffuse multi-stage transition near 180 K. The 1989 study of Swartz gives a small peak pyroelectric coefficient of around $0.08 \mu\text{C cm}^{-2} \text{ K}^{-1}$ [65], and the zero-field entropy change of the transition is $0.8 \text{ J K}^{-1} \text{ kg}^{-1}$ [39].

1.2.3.6 Layered oxides

These include the Aurivillius phases, a series of compounds with large and complex layered unit cells containing perovskite-like units responsible for ferroelectricity (which is uniaxial). $\text{SrBi}_2\text{Ta}_2\text{O}_9$ (SBT) became famous for its application in ferroelectric memories [40], and perhaps for this reason it is one of the small number of materials whose electrocaloric properties have been measured, in polycrystalline films grown by sol-gel [43]. Large $|\Delta T| \sim 5 \text{ K}$ effects were measured via the Maxwell relation. An oriented film could show larger effects as the electric field could be applied exclusively down the polar axis. The layered oxides tend to have high values of T_C (the value for SBT is 608 K).

1.2.3.7 Barium fluorides

Various compounds of formula BaMF_4 , where M is a divalent cation, are known to be ferroelectric, and have attracted interest as potential multiferroics [66]. However, their

¹²Showing simultaneous ferroelectric-like and antiferroelectric-like properties.

ferroelectric phase transitions cannot be accessed, as in all cases the T_C is greater than the melting temperature.

1.2.3.8 Molybdates

Rare earth molybdates analogous to $\text{Gd}_2(\text{MO}_4)_3$ were studied in the 1960s and 70s, perhaps because of ready availability of single crystals and the coexistence of ferroelasticity. $\text{Gd}_2(\text{MO}_4)_3$ shows a very sharp first-order transition at 432 K. Fouskova estimated a zero field entropy change of an unremarkable $1.16 \pm 0.42 \text{ J K}^{-1} \text{ kg}^{-1}$ [67].

1.2.3.9 Boracites

$\text{Ni}_3\text{B}_7\text{O}_{13}\text{I}$ attracted early interest as a multiferroic at low temperatures [68]. A small $P_S = 0.08 \text{ } \mu\text{C cm}^{-2}$ and a diffuse transition around 64 K suggest that any electrocaloric effects would be small.

1.2.3.10 Colemanite

The naturally occurring mineral $\text{Ca}_2\text{B}_6\text{O}_{11} \cdot 5\text{H}_2\text{O}$ shows a second-order transition to a ferroelectric phase at 267 K, with a small peak pyroelectric coefficient of around $0.05 \text{ } \mu\text{C cm}^{-2} \text{ K}^{-1}$ [69].

1.2.3.11 ‘Other oxides’

$\text{Pb}_5\text{Ge}_3\text{O}_{11}$ (PGO) is one of several oxides in this miscellaneous category. $\text{Pb}_5\text{Ge}_3\text{O}_{11}$ shows a promising peak pyroelectric coefficient of around $0.5 \text{ } \mu\text{C cm}^{-2} \text{ K}^{-1}$ [70] near $T_C \sim 450 \text{ K}$.

1.2.3.12 Halides

HCl is not best known for its ferroelectric properties, but it is indeed ferroelectric below 98.4 K. The other hydrogen halides also show ferroelectric phases at cryogenic temperatures. The HCl transition is first-order with a very large entropy change of $367 \text{ J K}^{-1} \text{ kg}^{-1}$ [71]. The $P(E)$ data reported by Hoshino *et al.* showed no signs of parasitic leakage [72]. An electrocaloric study of HCl could be rewarding, if the

practical difficulties of working with this material (a corrosive gas at room temperature) could be overcome.

1.2.3.13 Antimony sulphide iodides

The transition in SbSI occurs at 293 K and is first-order, with an entropy change of $2.7 \text{ J K}^{-1} \text{ kg}^{-1}$ [73]. Ferroelectric properties of the common ore FeS ($T_C = 286$) are reported to be similar to SbSI [74], but have not been widely studied.

1.2.3.14 Nitrites

NaNO_2 is often cited in textbooks because order-disorder ferroelectricity is easy to rationalise from the spontaneous dipole moment of the NO_2 molecule. NaNO_2 shows a very large zero-field entropy change of $76.8 \text{ J K}^{-1} \text{ kg}^{-1}$ at $T_C = 437 \text{ K}$ [75]. For further details, see Chapter 4.

1.2.3.15 Nitrates

Bulk KNO_3 is ferroelectric only on cooling in a narrow temperature interval of 398 K to approximately 388 K (thin films show a wider range). KNO_3 has a large zero-field entropy change of $53.4 \text{ J K}^{-1} \text{ kg}^{-1}$ [39]. Thick-film fabrication is straightforward from melt [76]. For further details, see Chapter 4.

1.2.3.16 Potassium dihydrogen phosphate family

KH_2PO_4 (KHP) shows a large zero-field entropy change of $29.4 \text{ J K}^{-1} \text{ kg}^{-1}$ at $T_C = 123 \text{ K}$ [39]. KD_2PO_4 (KDP) shows a slightly smaller entropy change of $20.9 \text{ J K}^{-1} \text{ kg}^{-1}$ at its 213 K transition [39]. These were among the first ferroelectrics to be discovered. It is possible to produce enormous single crystals of these compounds, such as the 380 kg specimen on display at Lawrence Livermore National Laboratory.

1.2.3.17 Sulphates

Two ferroelectric sulphates, $(\text{NH}_4)_2\text{SO}_4$ and NH_4HSO_4 are known to show very large zero-field entropy changes at their respective phase transitions at 223 K and 270 K [39].

Only the latter with a zero-field entropy change of $67.8 \text{ J K}^{-1} \text{ kg}^{-1}$, has been considered for electrocaloric effects, but the conclusion reached was that ionic conductivity was too high in the crystals measured [77]. The former, ammonium sulfate, shows a zero-field entropy change of $133 \text{ J K}^{-1} \text{ kg}^{-1}$ and its electrocaloric properties have not hitherto been measured. For further details, see Chapter 4.

1.2.3.18 Alums

Compounds similar to $\text{NH}_4\text{Fe}(\text{SO}_4)_2 \cdot 12\text{H}_2\text{O}$ show mostly cryogenic values of T_C . Information in the literature is very limited, but a short abstract attributed to Jona *et al.* [78] reports double hysteresis loops in $\text{NH}_4\text{Fe}(\text{SO}_4)_2 \cdot 12\text{H}_2\text{O}$ up to 2 K above $T_C = 88 \text{ K}$ with a driving field of 20 kV cm^{-1} , indicating a field-driven first-order phase transition. Given values for P_S of $0.4 \text{ } \mu\text{C cm}^{-2}$ and ρ of 1.71 g cm^{-3} [79], the mass-normalised entropy change may be estimated via Clausius-Clapeyron as $|\Delta S| = (P_S/\rho)(dE/dT) = 2.4 \text{ J K}^{-1} \text{ kg}^{-1}$. Powder is readily available commercially, and the melting point of 310 K could enable straightforward fabrication of thick films from melt [79].

1.2.3.19 Guanidiniums

These materials have chemical formulae similar to $\text{GAl}(\text{SO}_4)_2 \cdot 6\text{H}_2\text{O}$ (where G is the Guanidinium ion $\text{C}(\text{NH}_2)_3^+$), and inaccessible ferroelectric transitions due to melting or decomposition. A recent paper by Szafranski found that this was not the case for GhClO_4 , which shows a series of very large zero-field entropy changes of total magnitude $162 \text{ J K}^{-1} \text{ kg}^{-1}$, at high temperatures [80]. Electrical losses prevented characterisation in the transition region, and would prohibit the harnessing of these entropy changes for an electrocaloric effect.

1.2.3.20 Selenites

The little-studied $\text{LiH}_3(\text{SeO}_3)_2$ melts at 383 K, before reaching T_C , however the T_C can be lowered below the melting point via hydrostatic pressure [81], revealing the transition to be sharp and second order. Other selenites have mostly cryogenic values of T_C , and are not well studied. Makita and Miki experimented on $\text{NaH}_3(\text{SeO}_3)_2$, reporting a large zero-field entropy change of $24 \text{ J K}^{-1} \text{ kg}^{-1}$ at the 194 K first-order

phase transition [82].

1.2.3.21 Cyanides

Various hydrated potassium cyanide complexes with chemical formulae similar to $\text{K}_4\text{Mn}(\text{CN})_6 \cdot 3\text{H}_2\text{O}$ are reported to show ferroelectricity with T_C values just below room temperature. They are unlikely to be measured for electrocaloric effects as, like all cyanides, they are acutely toxic.

1.2.3.22 Triglycine sulphate family

$(\text{NH}_2\text{CH}_2\text{COOH})_3 \cdot \text{H}_2\text{SO}_4$ (TGS) is often cited as the prototypical order-disorder type ferroelectric. Strukov reported electrocaloric effects of 0.1 K under fields of 2 kV cm^{-1} , (his plots are shown in Lines and Glass [3]) but the zero-field entropy change at the 322 K transition is a reasonable $6.5 \text{ J K}^{-1} \text{ kg}^{-1}$ [39] suggesting that this material could show larger effects, perhaps under higher fields. TGS also shows a high peak pyroelectric coefficient of $0.3 \text{ } \mu\text{C cm}^{-2} \text{ K}^{-1}$ [83].

1.2.3.23 Rochelle salt family

As well as being the first ferroelectric material to be identified, $\text{NaKC}_4\text{H}_4\text{O}_6 \cdot 4\text{H}_2\text{O}$ was the first to be measured for electrocaloric effects, in the experiments of Kobeko and Kurchatov in 1930 [22]. Later work has revealed that the zero-field entropy change is an uncompetitive $0.12 \text{ J K}^{-1} \text{ kg}^{-1}$ [39].

1.2.3.24 ‘Complex organic compounds’

$\text{SC}(\text{NH}_2)$ is a molecular ferroelectric. A 1959 study reported ferroelectric $P(E)$ loops below 169 K, ‘antiferroelectric’ loops between 169 K and 176 K, a second ferroelectric phase from 176 K to 180 K and ‘antiferroelectric’ loops again above 180 K [84]. Later work confirmed that the ‘antiferroelectric’ double loops are in fact field-driven phase transitions to ferroelectric phases [85], confirming that this is an electrocaloric material. The transition at 169 K has an unremarkable entropy change of $2.0 \text{ J K}^{-1} \text{ kg}^{-1}$ [86].

A few organomercurials are ferroelectric but also acutely toxic, and furthermore usually melt or decompose before their T_C can be accessed [56].

1.2.3.25 Liquid crystals

A number of liquid crystals are ferroelectric but the values of P_s are generally small, making measurements challenging. A 1986 review by Glass *et al.* examined the suitability of liquid crystals for pyroelectric infra-red detectors [83]. A range of biphenyl esters were considered, the best of which showed a peak pyroelectric coefficient of $0.035 \mu\text{C cm}^{-2} \text{ K}^{-1}$ at T_C of 323 K. The authors singled out mechanical flexibility, low thermal conductivity and ease of fabrication of thin films as distinguishing features of liquid crystals over conventional pyroelectric materials.

Liquid crystals can show anisotropic thermal conductivity, with thermal conductivity in directions parallel and perpendicular to the molecular director differing by up to a factor of 3. This allows them to be used as ‘thermal transistors’. Epstein and Malloy noted that this could permit non-mechanical control of thermal circuits in a practical electrocaloric cooler [87]. A patent application based on this idea was recently received [88].

1.2.3.26 Polymers

Ferroelectric polymers are among the most promising materials for electrocaloric effects [21]. Effects of $|\Delta T| = 12 \text{ K}$ in polymers were first measured (via the Maxwell relation) by a team led by Qiming Zhang at Penn State, in $1 \mu\text{m}$ -thick films of poly(vinylidene fluoride-trifluoroethylene) (55/45 mol %) [PVDF-TrFE] and the relaxor poly(vinylidene fluoride-trifluoroethylene-chlorofluoroethylene) (59.2/33.6/7.2 mol %) [PVDF-TrFE-CFE] [21] near their respective Curie temperatures of 350 K and 330 K. Effects of $|\Delta T| = 21 \text{ K}$ were reported later in superior-quality specimens of these materials [89]. Effects of $\sim 12 \text{ K}$ were measured directly in PVDF-TrFE and PVDF-TrFE-CFE by Lu *et al.*, [47, 48] the first and so far only credible reports of ‘giant’ electrocaloric effects measured directly.

Some of the distinguishing features of ferroelectric polymers are that they are mechanically flexible, can withstand extremely large electric fields of 4000 kV cm^{-1} or more (this is the main reason they can show large electrocaloric effects despite small values of polarisation $\sim 6 \mu\text{C cm}^{-2}$), and are only available as stretch-cooled thin films, ferroelectricity arising from the resulting strain. Polymers encompass a full range of ferroelectric phenomenology, with some such as PVDF-TrFE-CFE behaving as relaxors and others such as pure PVDF showing first-order transitions.

1.2.3.27 Summary of candidate materials

Table 1.2 summarises the materials from the previous discussion that could show promise for electrocaloric effects.

Material	T_C (K)	Why promising	Refs
Perovskites	83-763	Several are known to show large effects.	[20, 34, 35]
LiTaO ₃ & LiNbO ₃	1483 & 938	Noteable pyroelectrics, v. high P_S	[4]
Sr _x Ba _{1-x} Nb ₂ O ₆	370	Large pyroelectric coefficient $\sim 0.9 \mu\text{C cm}^{-2} \text{ K}^{-1}$	[55]
SrBi ₂ Ta ₂ O ₉	608	Lead free, polycrystalline films show $ \Delta T = 5 \text{ K}$	[43]
Pb ₅ Ge ₃ O ₁₁	450	Large pyroelectric coefficient $\sim 0.5 \mu\text{C cm}^{-2} \text{ K}^{-1}$	[70]
HCl	98.4	Large zero-field $ \Delta S = 367 \text{ J K}^{-1} \text{ kg}^{-1}$	[71, 72]
SbSI	293	Room temperature transition, zero-field $ \Delta S = 2.7 \text{ J K}^{-1} \text{ kg}^{-1}$	[73]
NaNO ₂ *	436	Large zero-field $ \Delta S = 76.8 \text{ J K}^{-1} \text{ kg}^{-1}$	[75]
KNO ₃ *	397	Large zero-field $ \Delta S = 53.4 \text{ J K}^{-1} \text{ kg}^{-1}$	[39]
KH ₂ PO ₄	123	Large zero-field $ \Delta S = 29.4 \text{ J K}^{-1} \text{ kg}^{-1}$, large single crystals easy to grow	[39]
(NH ₄) ₂ SO ₄ *	223	Large zero-field $ \Delta S = 133 \text{ J K}^{-1} \text{ kg}^{-1}$	[39]
NH ₄ HSO ₄	270	Large zero-field $ \Delta S = 67.8 \text{ J K}^{-1} \text{ kg}^{-1}$	[39]
NH ₄ Fe(SO ₄) ₂ ·12H ₂ O	88	Melting point of 310 K, zero-field $ \Delta S = 2.4 \text{ J K}^{-1} \text{ kg}^{-1}$	[78]
NaH ₃ (SeO ₃) ₂	194	Large zero-field $ \Delta S = 24 \text{ J K}^{-1} \text{ kg}^{-1}$	[82]
(NH ₂ CH ₂ COOH) ₃ ·H ₂ SO ₄	322	Zero-field $ \Delta S = 6.5 \text{ J K}^{-1} \text{ kg}^{-1}$ near room temperature	[39]
Ferroelectric polymers	~ 350	Several are known to show large effects.	[21, 89]

Table 1.2: Summary of the materials considered in the present Section that could show promise as electrocaloric materials. For all materials, P_S and T_C have been tabulated by Subbarao [56]. Materials marked with a ‘*’ have been studied for the present work (Chapter 4).

1.2.4 Efficiency of electrocaloric effects

The content of this Section is taken from published work led by Emmanuel Defay [54], which demonstrated the use of Landau theory to show that non-electrocaloric edge layers in thin films have a significant impact on electrocaloric efficiency. The author of the present work was a co-author on the aforementioned published work.

In the following algebra, a subscript of ‘e’ denotes ‘corresponding to non-electrocaloric edge layer of film’, a subscript of ‘i’ denotes ‘corresponding to electrocaloric interior of film’ and no subscript denotes ‘corresponding to entire film’. The starting point is the standard Landau expansion for free energy:

$$G = \frac{1}{2}a(T - T_C)P_i^2 + \frac{1}{4}bP_i^4 + \frac{1}{6}cP_i^6 - E_iP_i + s^2\tilde{C} \quad (1.10)$$

where s is in-plane strain and $s^2\tilde{C}$ is elastic energy. Minimising with respect to P_i :

$$E_i = a(T - T_C)P_i + bP_i^3 + cP_i^5 \quad (1.11)$$

The non-electrocaloric edge layers are incorporated via $tE = t_iE_i + 2t_eE_e$ (where t is thickness), $D_i \sim P_i$ (where D is electric displacement), $D = D_i = D_e$ (series capacitors) and $D_e = \varepsilon_eE_e$, giving $E \sim E_i + 2t_eD/t\varepsilon_e$. This gives:

$$E \sim \left(a(T - T_C) + \frac{2t_e}{t\varepsilon_e} \right) D + bD^3 + cD^5 \quad (1.12)$$

Leading directly to an expression for electrocaloric work W (i.e. the electrical work required to drive the electrocaloric effect) via $|W| = |\int_{D_1}^{D_2} EdD|$. Electrocaloric heat Q follows from Equation 1.10 via $\Delta S_i = -(\partial G/\partial T)_{P_i}$, $\Delta S = \Delta S_i t_i/t$ and $|Q| = T|\Delta S|$. Electrocaloric efficiency η may then be evaluated as $|Q|/|W|$. The materials PVDF-TrFE and Zr-rich PZT (characterised for electrocaloric effects in [21] and [20]) were considered in [54]. To obtain t_e and any Landau coefficients that could not be deduced from alternative sources of information, Equation 1.12 was fitted against experimental $D(E)$ data. The inclusion of the non-electrocaloric edge layers was essential for both materials in order to achieve a reasonable match to $D(E)$ data. Furthermore it was shown that the edge layers reduce η by a factor of almost 2 for Zr-rich PZT, from 7.8 to 3.4. The PVDF-TrFE showed a value of η of 7.3 (calculated

from experimental data via an integration method — refer to [54] for full details) and thus outperformed the Zr-rich PZT in terms of efficiency.

1.3 Summary

Electrocaloric effects in first-order and second-order ferroelectric materials may be rationalised in terms of an $E - T$ phase diagram, but relaxors are more complicated, and not well understood. A huge number of ferroelectric and related materials remain uncharacterised. A thin-film geometry is associated with large breakdown fields, and is currently the only known way to achieve electrocaloric effects with $|\Delta T|$ in the range of 10s of K. These ‘giant’ electrocaloric effects were revealed by seminal papers by Mischenko *et al.* in 350 nm-thick $\text{Pb}(\text{Zr}_{0.95}\text{Ti}_{0.05})\text{O}_3$ [20] (2006) and Neese *et al.* in 1 μm -thick poly(vinylidene fluoride-trifluoroethylene) (55/45 mol %) [PVDF-TrFE] [21] (2008). Since 2006 there have been many further papers reporting ‘giant’ effects of up to $|\Delta T| = 45$ K [53] in various ferroelectric oxide films and polymer films. Apart from the work of Lu *et al.* on polymers [47, 48], all such results on films have so been indirect, via the Maxwell relation. Thus there is considerable interest in confirming the large number of indirect results via direct measurements.

Engineering research on practical electrocaloric cooling has also gained momentum since the beginning of the ‘thin film era’ in 2006. Multilayered capacitors have recently been proposed [19, 45] and demonstrated [51], for continuous cooling using the electrocaloric effect.

In summary, opportunities to contribute to the field of electrocalorics are multifold:

- The vast majority of ferroelectric materials remain untested, despite many showing large zero-field entropy changes and pyroelectric coefficients (Table 1.2).
- Liquid crystals and halides could show exceptional electrocaloric properties, but a creative approach would be required to characterise them.
- It is important to perform direct electrocaloric measurements on a greater number of thin films to confirm the ‘giant’ effects measured indirectly, and gain empirical understanding of the underlying mechanism of ‘giant’ effects.
- Ferroelectric coupling to strain should not be ignored. Strain could hold the key to larger or more accessible effects.

- Systematic exploration of $E - T$ phase diagrams is surprisingly rare. As a result, the fundamental mechanisms of electrocaloric effects associated with ferroelectric phase transitions are surprisingly poorly understood.
- Prototype electrocaloric fridges have only just begun to appear (continuous cooling was recently demonstrated with a commercial multilayered capacitor showing $|\Delta T| \sim 0.5$ K using a liquid meniscus to control the thermal circuit) and there is much scope for further creative engineering.

Electrocalorics in 2013 is thus an exciting field, as it unites diverse scientific disciplines, theories and experimental methods. The remainder of this dissertation is structured as follows.

- Chapter 2 outlines the theory of measurement of electrocaloric effects and related phenomena.
- Chapter 3 describes bespoke cryostats and associated software, for measuring electrical and electrocaloric properties of samples in 77-700 K.
- Chapter 4 describes investigations of electrocaloric effects in the inorganic salts $(\text{NH}_4)_2\text{SO}_4$, KNO_3 and NaNO_2 .
- Chapter 5 describes investigations of electrocaloric effects in $\text{PbSc}_{0.5}\text{Ta}_{0.5}\text{O}_3$ ceramic.
- Chapter 6 describes investigations of electrocaloric effects in epitaxial films of SrTiO_3 on NdGaO_3 (001) substrates.
- Chapter 7 describes geometric optimisation of multilayered capacitors via thermal modelling, for practical exploitation of electrocaloric materials as coolers.
- Chapter 8 summarises key results and conclusions.

Chapter 2

Instrumentation and theory of measurement

For the present work, four principle types of measurement were performed on electrocaloric materials:

- Adiabatic temperature change $\Delta T(\Delta E)$ as a function of temperature.
- Dielectric constant ε from 100 Hz to 1 MHz, as a function of temperature.
- Ferroelectric $P(E)$ loops out to < 1 V to 2.5 kV, as a function of temperature.
This gave indirect access to isothermal ΔS via the Maxwell relation
 $(\partial P / \partial T)_E = (\partial S / \partial E)_T$.
- Specific heat capacity c_E as a function of temperature. This gave indirect access to zero-field ΔS .

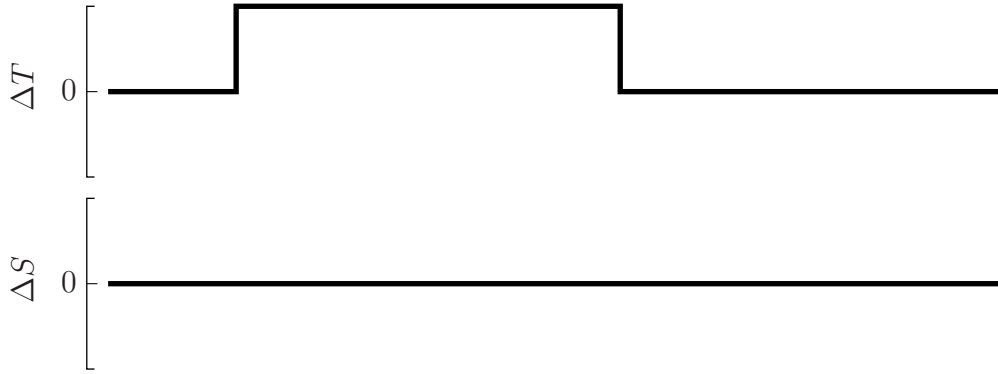
These measurements were complementary in that they each explored $E - T$ phase diagrams and electrocaloric properties in different ways. These measurements will now be described consecutively.

2.1 Adiabatic temperature change $\Delta T(\Delta E)$

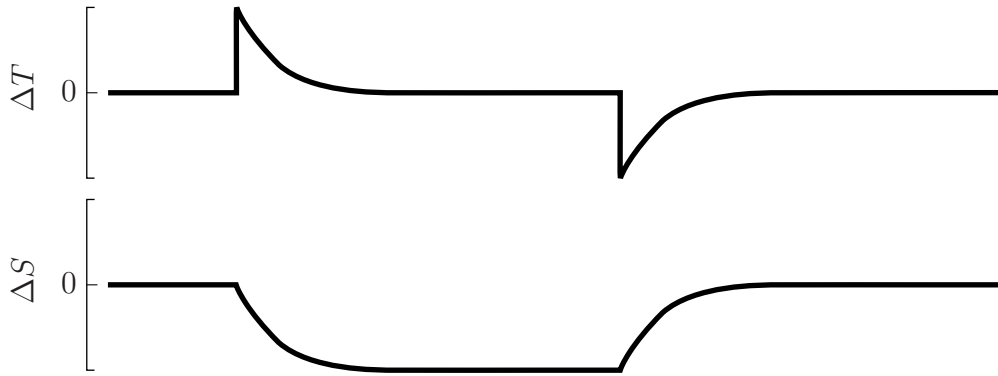
To measure $\Delta T(\Delta E)$, adiabatic or otherwise, the temperature of a sample must be monitored as an electric field E is applied and then removed. Ignoring heat due to electrical losses, the results depends on two factors, i) the electrocaloric properties of the sample and ii) the thermal environment of the sample. For an adiabatic environment, the temperature change upon application of ΔE is only lost upon subsequent removal of ΔE (Figure 2.1a). For the converse case of an isothermal environment, entropy drops when the field is applied (Figure 2.1c). Thus, in order to demonstrate electrocaloric cooling, one should work under near-adiabatic conditions (Figure 2.1b), whereupon heat is permitted to flow outwards over a timescale significantly longer than the rise-time of ΔE , such that the measured ΔT is almost as large as adiabatic ΔT .

For measurement of ΔT , chromel-alumel (‘K’ type) thermocouples with a thermoelectric constant of $25.1889 \text{ K mV}^{-1}$ [90] were fabricated by spot-welding (welder type 905 mk 2, SLEE). The weld point (or ‘hot junction’) was attached to the grounded upper electrode of the device under test (DUT) using silver paint. The free ends of the wires (or ‘cold junction’) were referenced to the surface the DUT was mounted upon by attaching a layer of electrically insulating, thermally-conductive kapton tape to the surface, and using silver paint to attach the wires on top of that (Figure 2.2). The thermoelectric voltage was measured using a digital multimeter (type 196, Keithley Instruments).

(a) Adiabatic conditions



(b) Near-adiabatic conditions



(c) Isothermal conditions

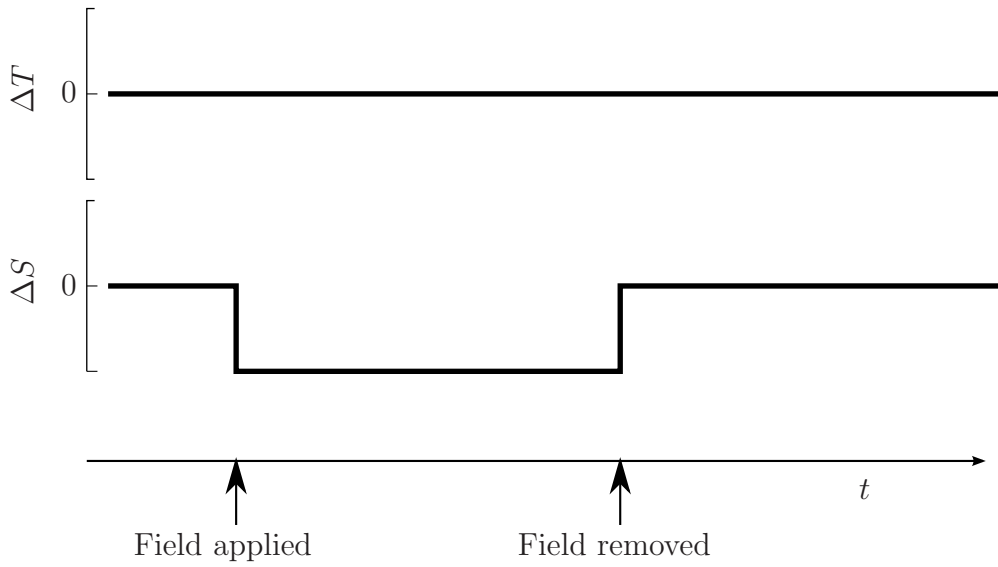


Figure 2.1: **(a)-(c)** Illustration of form of $\Delta T(t)$ and $\Delta S(t)$ (where t is time) for an electrocaloric cycle in environments ranging from adiabatic to isothermal. **(Bottom)** The common x -axis of (a)-(c), showing where the field change ΔE is applied, and subsequently removed.

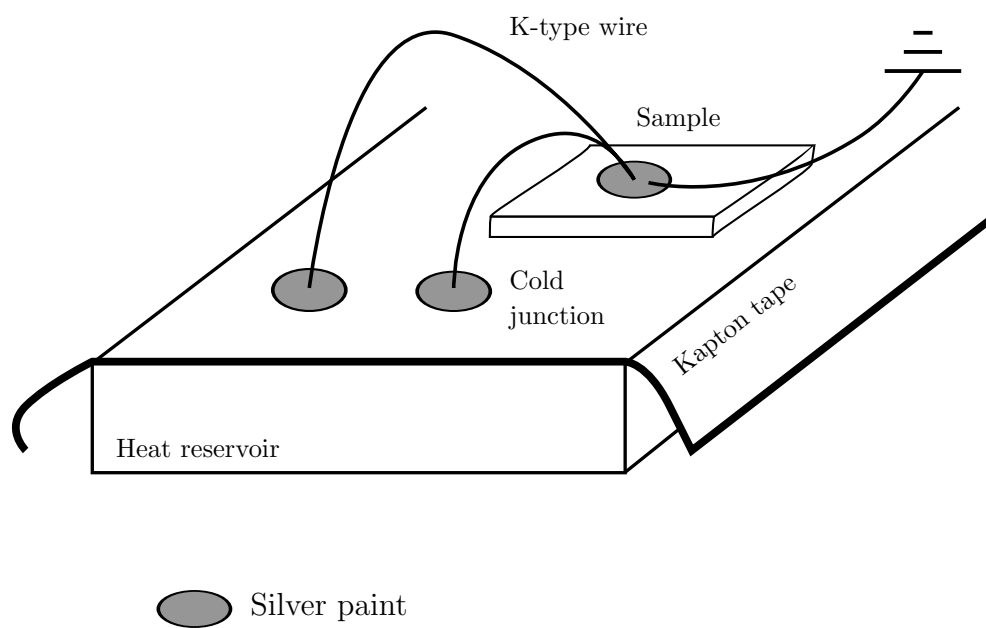


Figure 2.2: Thermometry with a K-type thermocouple referenced to the Cu heat reservoir of the temperature controller.

2.2 Dielectric $\varepsilon(f)$ spectra

Dielectric constant ε is a frequency-dependent parameter with real component ε' and imaginary component ε'' , representing the lossless and lossy components of a DUT's response to an electrical stimulus, respectively. The value of ε' is equal to $Cd/[\varepsilon_0 A]$ for a plate capacitor of electrode area A , thickness d and capacitance C , and ε'' is determined by absorption of electrical energy. The ratio $\varepsilon''/\varepsilon'$ is known as $\tan(\delta)$, and is also equal to the ratio of the imaginary and real parts of complex impedance Z . Thus, a measurement of complex Z can give both ε' and ε'' via $C = 1/[2\pi i \Im(Z)]$ (where f is frequency and an assumption of zero inductance has been made) and $\varepsilon'' = \varepsilon' \Im(Z)/\Re(Z)$. For the present work, $Z(f)$ was measured using an impedance analyser (model 4294A, Agilent Technologies) with a nominal frequency range of 40 Hz to 110 MHz.

According to Agilent literature [91], an equivalent circuit for a non-ideal capacitor is an ideal capacitor C in series with an inductor L_S and a resistor R_S , and in parallel with a second resistor R_P (Figure 2.3a). Capacitance C provides a reactance $X_C = -1/\omega C$ (where $\omega = 2\pi f$) and series inductance L_S provides a reactance $X_L = \omega L_S$, which exactly cancels out X_C at the 'self resonant frequency' $\omega_{\text{SRF}} = \sqrt{1/LC}$. At ω_{SRF} the circuit becomes purely resistive, giving a characteristic peak in $\tan(\delta)$ (Figure 2.3b). A capacitor behaves as such only at frequencies significantly below ω_{SRF} ; above ω_{SRF} it behaves primarily as an inductor. The dielectric constant cannot be easily determined near or above ω_{SRF} .

If a sample is measured at frequencies significantly below ω_{SRF} , series inductance may be neglected and the equivalent circuit reduces to just C , R_S and R_P (Figure 2.3c). Solving the circuit yields two equations (for the two components of Z) with three unknowns (C , R_P and R_S), as shown in Figure 2.3c. One can either:

- Measure a spectrum of $Z(f)$ and numerically fit the data to the equations in Figure 2.3c to recover C , R_P and R_S . This is the most accurate and time-consuming method.
- Neglect either R_P or R_S to make the equations in Figure 2.3c analytically soluble. The results will be accurate only in certain parts of the frequency range, which must be identified.

For the latter approach, it is generally safe to assume that $R_P \gg R_S$ as R_P represents the resistance of the capacitor dielectric, a nominal insulator, and R_S represents the

resistance of the capacitor electrodes, nominal conductors. The impedance of the capacitor determines which of R_P or R_S can be neglected. At low frequencies the impedance of C is large, so the series contribution of the small R_S may be neglected. This situation is shown in Figure 2.3d, and the value of C obtained is termed C_P , equivalent parallel capacitance. At high frequencies (but necessarily much less than ω_{SRF}), the impedance of C is small, so the parallel contribution of the large R_P may be neglected. This situation is shown in Figure 2.3e, and the measured value of C is termed C_S , equivalent series capacitance. At intermediate frequencies both C_S and C_P can be poor approximations to the true value of C .

Spurious capacitance and resistance in wiring can be compensated by performing a calibration measurement of the wiring system with no sample present, under open-circuit and/or closed-circuit conditions. However, if the magnitude of the parasitic impedance is much larger than that of the DUT, the resolution of the measurement is obviously greatly compromised. Small bulk ceramic DUTs typically show a capacitance of several pF away from T_C , so this was the benchmark for parasitics when constructing apparatus (this will be discussed in Chapter 3).

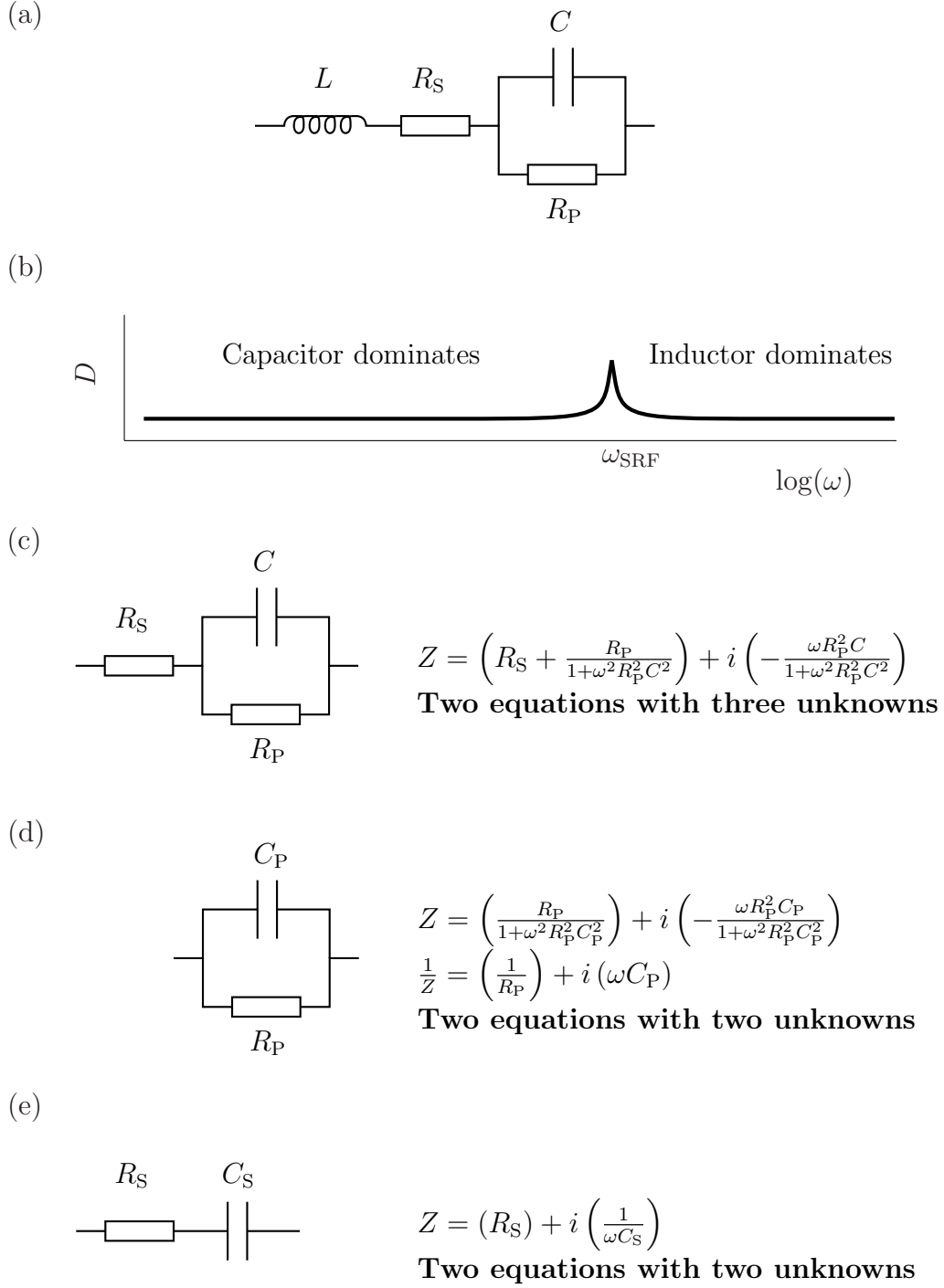


Figure 2.3: After Agilent literature [91]. **(a)** Equivalent circuit model of a real capacitor. **(b)** For the model of (a), C dominates at low frequencies, and L at high frequencies. **(c)** At low frequencies, L may be neglected. However it is still not possible to solve for C , R_P and R_S from a single measurement of the two components of Z . **(d)** Equivalent parallel capacitance $C_P \sim C$ at low frequencies. **(e)** Equivalent series capacitance $C_S \sim C$ at high frequencies provided there is no inductance-related resonance.

2.3 Ferroelectric $P(E)$ loops

Polarisation P is not readily measurable directly. For a uniformly polarised material, there is a trapped surface charge of density σ on the polar surfaces, which is dimensionally and numerically equivalent to P . A change in P of magnitude ΔP (induced, for example, by a change in E or T) is then equivalent to a change in σ of $\Delta\sigma = \Delta P$. The total charge that has moved from one polar surface to another is $\Delta Q = A\Delta\sigma$, where A is the area of the polar surface. As this process occurs over a finite time period Δt , $\Delta P = [1/A] \int_{t=0}^{t=\Delta t} I_P dt$ where $I_P = dQ/dt$ is the current associated with ΔP . In other words, *changes* in P are readily measurable, as they involve rearrangement of charge and thus *electrical current*. The integration of current to charge can be performed numerically, or with a dedicated analogue circuit, whereupon charge is directed onto the electrodes of a linear reference capacitor (the classic Sawyer-Tower circuit [23]). The initial value of P remains unmeasured and must be guessed, for example by requiring hysteretic $P(E)$ loops to be centered about the origin, or zero-field pyroelectric $P(T)$ to be zero above T_C . The source and measurement unit used for the present work was a Precision Premier II (Radiant Technologies) with an optional external amplifier (type 609E-6, Trek), to extend the source voltage range to ± 4 kV from the original range of ± 200 V.

The current I_P is just one component of the measured current I drawn/generated by the DUT and the external wiring. Ferroelectric DUTs include a passive free-space capacitance $C_f = \epsilon_0 A/d$ (where d is the distance between the electrodes), but because this is simply a function of geometry it is readily removed from the signal. Leakage pathways in the DUT, or stray capacitance in the wiring, result in a spurious non-linear contribution to $P(E)$ (Figure 2.4b-c). If the spurious components can themselves be measured, their contribution to the measured data may be removed, yielding more accurate values of $P(E)$.

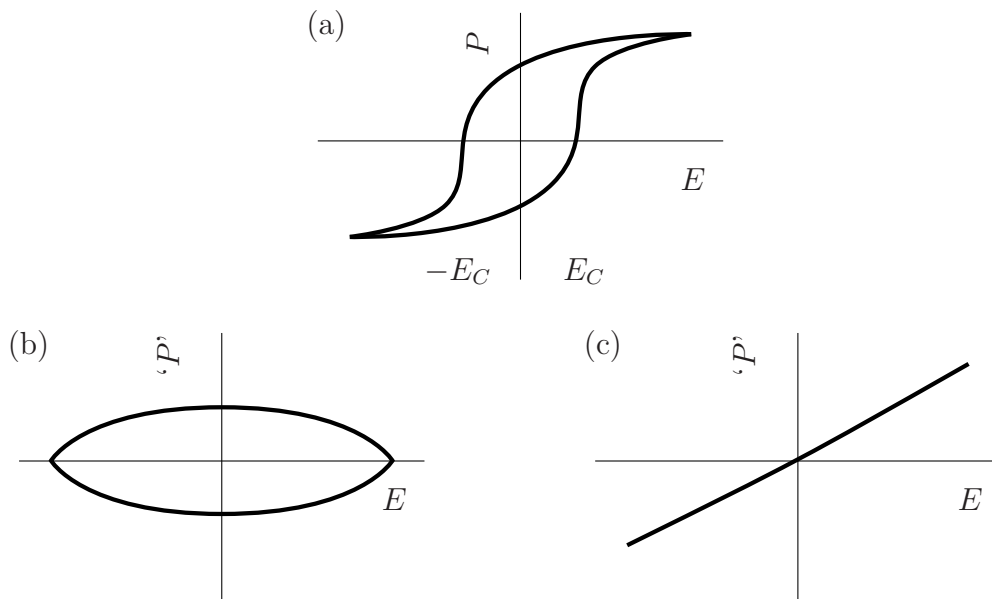


Figure 2.4: Illustrations of **(a)** non-spurious and **(b)-(c)** spurious contributions to an observed $P(E)$ loop. Experimental $P(E)$ data will in general include contributions from all of these components. **(a)** Response of a ferroelectric material. **(b)** Spurious ' $P(E)$ ' response of a parasitic resistance. **(c)** Spurious ' $P(E)$ ' response of a parasitic linear capacitance.

2.4 Isothermal ΔS via the ‘indirect’ method

The isothermal electrocaloric entropy change ΔS induced by changing the applied field from E_1 to E_2 may be evaluated via:

$$\Delta S = \int_{E_1}^{E_2} \left(\frac{\partial P}{\partial T} \right)_E dE \quad (2.1)$$

where the Maxwell relation $(\partial P / \partial T)_E = (\partial S / \partial E)_T$ has been used in the integrand.

The three measurables required are P , E and T , so Equation 2.1 is normally evaluated from a dataset of $P(E)$ loops at various T . This ‘indirect’ method assumes that:

- Equilibrium thermodynamics is applicable.
- Polarisation is a single valued function of E and T .

For $P(E)$ loops in a ferroelectric material, P is not single valued as the values measured on increasing E are different to those measured when reducing E , due to hysteresis (Figure 2.5a). The correct approach is to reject the lower positive branch of the $P(E)$ loop because it contains *ferroelectric switching*, which has no role in electrocaloric cycles, as only fields of a single polarity are applied [10].

Performing the Maxwell analysis on the upper positive branches of the $P(E)$ loops ignores the possibility of electrical hysteresis of isothermal ΔS between application and removal of a field. Such phenomena may be crudely classified as repeatable hysteresis or irrepeatable hysteresis.

An example of *repeatable* hysteresis of isothermal ΔS is a field-driven first-order phase transition, as illustrated in Figure 2.5b. Here, the DUT is in a paraelectric phase at $E = 0$, but at a critical field $E_{\text{crit}}^{\text{up}}$ a transformation takes place to a ferroelectric phase. On *reduction* of the applied field, the paraelectric phase is re-established, but at a *smaller field* $E_{\text{crit}}^{\text{down}} < E_{\text{crit}}^{\text{up}}$, due to hysteresis of the field-driven transition.

An example of *irrepeatable* hysteresis of isothermal ΔS occurs at a *thermally hysteretic* first-order phase transition (Figure 2.5c). In this case, very close to T_C , the field-driven transition to the ferroelectric phase does not reverse upon removal of the field, i.e. the initial paraelectric phase is not fully recovered.

The best way to apply the indirect method to systems that display *repeatable hysteresis* of isothermal ΔS is to measure *minor loops*, i.e. biased $P(E)$ loops in which E is

positive throughout, such that no ferroelectric switching occurs. For systems that display *irrepeatable hysteresis* of isothermal ΔS , the indirect method can still be applied provided temperature is reset to a value known to lie far from the thermally hysteretic phase transition in between each individual $P(E)$ measurement [92]. Each of these methods will now be described in detail.

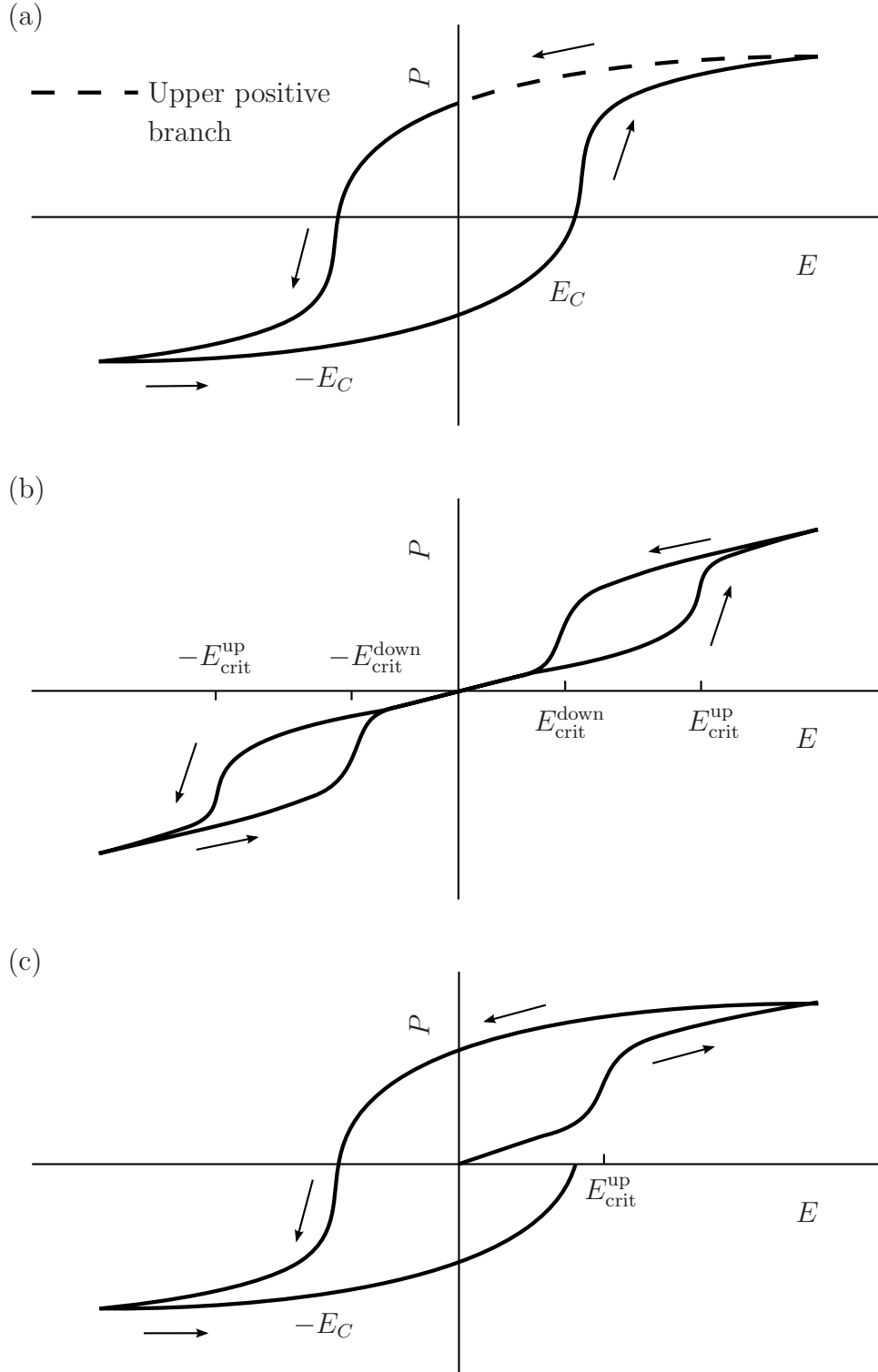


Figure 2.5: **(a)** Illustration of $P(E)$ data with the upper positive branch of the loop highlighted. **(b)** Illustration of a repeatable hysteretic field-driven first-order ferroelectric phase transition. This is *not* antiferroelectricity, despite the similar form of the loop. **(c)** Illustration of an irrepeatable hysteretic field-driven first-order ferroelectric phase transition that might occur near a thermally hysteretic transition.

2.4.1 Major and minor loops

The most common driving-field profile to measure $P(E)$ loops is a triangular wave¹ of amplitude E_{\max} (Figure 2.6a). This yields a so-called ‘major loop’ which will measure ferroelectric switching if performed on a ferroelectric material with $E_C < E_{\max}$.

However, electrocaloric cycles apply fields of a single polarity, without ferroelectric switching. Switching is absent from the *upper positive* branch of a major loop (Figures 2.5a and 2.6a), so ΔS corresponding to *removal* of the field E_{\max} may be evaluated by performing the Maxwell analysis on these branches of a dataset of major loops.

However the *lower positive* branches of major loops cannot be used to evaluate ΔS corresponding to *application* of a field E_{\max} because they are ‘contaminated’ with contributions from switching. To evaluate ΔS corresponding to *application* of a field, it is necessary to measure ‘minor loops’, that is, biased loops in which fields of only a single polarity are applied, such that no ferroelectric switching occurs.

A modified driving profile was devised (Figure 2.6b) which is initiated by a standard triangular ‘major’ loop, leaving the DUT poled in the negative direction. This is followed by a *double wave* containing a branch in which E_{\max} is applied without any ferroelectric switching, i.e. the positive half of a ‘minor’ loop. A negative double-wave at the end of the waveform provides the negative half of the minor loop. In total the modified driving profile allowed two major loops and one minor loop to be constructed, enabling electrocaloric ΔS to be predicted for both application and removal of an electric field.

The modified waveform had an added advantage in that it provided information about parasitic losses in the measurement circuit or DUT. Other than fatigue, irrepeatable hysteresis and significant deviation from isothermal conditions, there is no polarisation process which could cause the value of P at the points A and B in Figure 2.6b to be different. Excluding the aforementioned, any measured difference ‘ δP ’ must relate to electrical losses. Modelling the lossy part of the DUT as an equivalent parallel resistance R_P (Figure 2.3), the net parasitic charge that flows between points A and B is given by $Q = A\delta P$, and thus $R_P = [1/Q] \int_A^B V dt$. The time-resolved spurious contribution of R_P to the measured polarisation for the *entire waveform* may then be evaluated as ‘ $P(t)$ ’ = $[1/AR_P] \int_0^t V dt$, and removed from the measured data.

To test the performance of the modified driving profile in measuring parasitic losses in a

¹Ferroelectric properties are known to be a function of dE/dt in certain materials. For this reason triangular waveforms which have constant $|dE/dt|$ are considered preferable to sinusoidal waveforms.

DUT, a 45 μF commercial multilayer capacitor (MLC) [type C3225Y5V1A476Z, TDK Corp.] with a ferroelectric Y5V dielectric with $d \sim 5.4 \mu\text{m}$ and total $A \sim 10.4 \text{ cm}^2$ was connected in parallel with a 33.0 $\text{k}\Omega$ resistor. Figure 2.6c shows the measured polarisation as a function of time. Figures 2.6d-e show respectively the major and minor $P(E)$ loops for the DUT. The value of δP (Figure 2.6c) was $17.45 \mu\text{C cm}^{-2}$, which led to the correct value for R (33.06 $\text{k}\Omega$). Figures 2.6f-g show the compensated $P(E)$ loops, i.e. with the spurious resistive contribution subtracted. The minor loop was anhysteretic, as expected for a loop in which no ferroelectric switching had occurred. Figure 2.6h shows the spurious ' $P(E)$ ' curve for the resistor alone. It is emphasised that all the plots in Figures 2.6d-h were derived from the *single measurement* presented in Figure 2.6c.

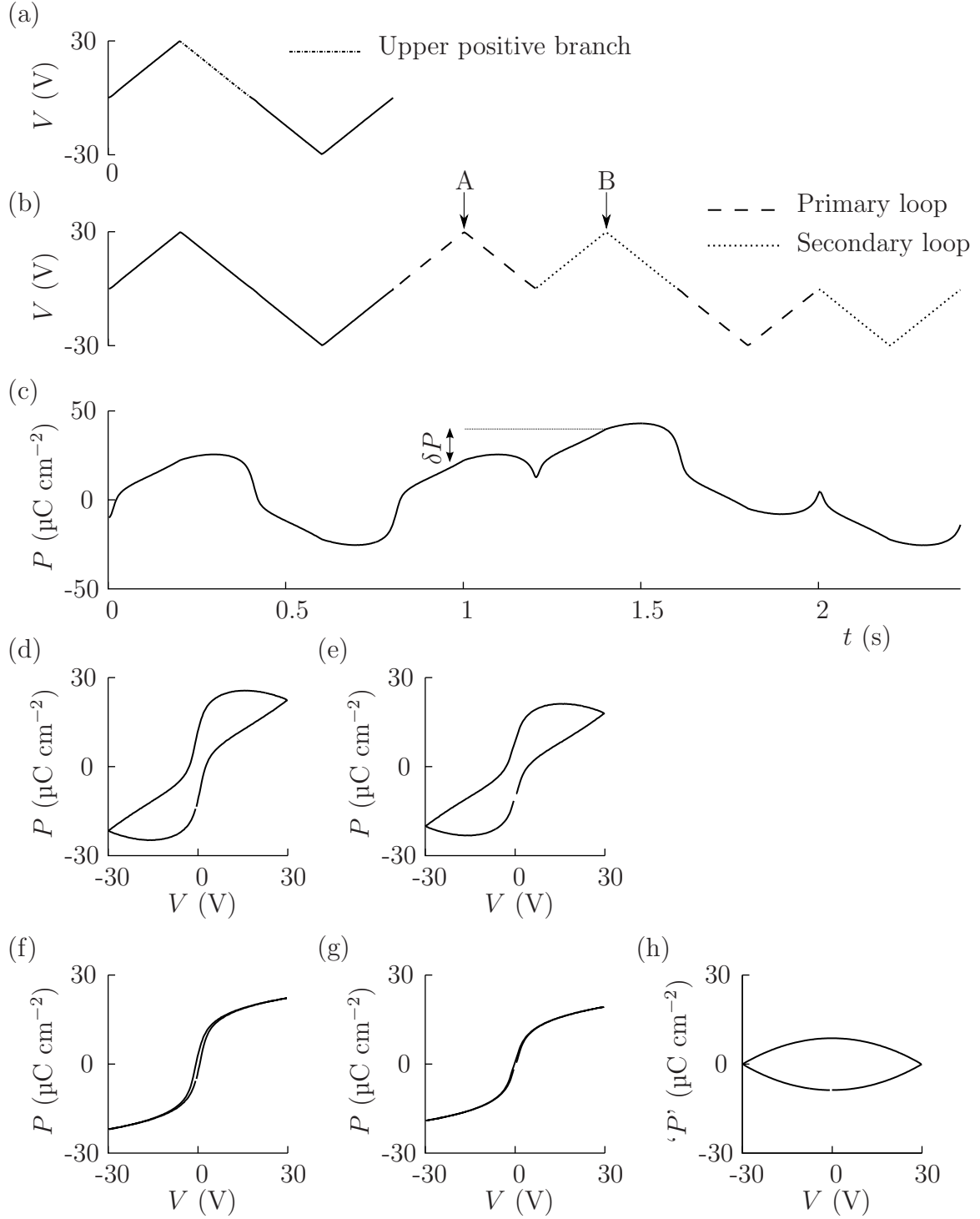


Figure 2.6: Driving field profiles for $P(E)$ measurements. Subfigures (a)-(c) share a common x -axis. **(a)** Standard triangular driving profile. **(b)** Modified driving profile to measure both major and minor loops. **(c)** $P(t)$ with the modified driving profile for a test 47 μF multilayer capacitor in parallel with a 33.0 $\text{k}\Omega$ resistor. **(d-e)** Major and minor $P(E)$ loops respectively, for the test sample. **(f-g)** Compensated major and minor $P(E)$ loops respectively, for the test sample. **(h)** Spurious ' $P(E)$ ' loop for the resistor alone.

2.4.2 ‘Standard’ and ‘resetting’ versions

Historically, a ‘standard’ method has generally been used to obtain $P(E)$ vs T datasets for subsequent processing into estimates for electrocaloric isothermal ΔS via the Maxwell relation $(\partial P/\partial T)_E = (\partial S/\partial E)_T$. In the ‘standard’ method the temperature of the sample is first set to a value T_1 and a $P(E)$ loop is taken. Following this, the sample is heated or cooled slightly to the next temperature T_2 and a second loop taken, and the process repeated until n $P(E)$ loops have been taken at a series of temperatures T_n such that $P(T)$ may be evaluated via a numerical transposition. Alternatively, $P(E)$ loops may be recorded continuously while temperature is ramped very slowly in comparison to the $P(E)$ measurement period (this latter version is preferable because it leads to better resolution in temperature, but the former method is prevalent, possibly due to shortcomings of industry-standard Radiant software²).

Magnetocaloric literature contains reports that the analogous ‘standard’ method for magnetocalorics³ fails for first-order transitions with thermal hysteresis of T_C , and thus irrepeatable hysteresis of isothermal ΔS near T_C [92–94]. For such systems, the ‘standard’ method can lead to a spurious ‘spike’ in isothermal ΔS , localised about T_C , and often in excess of the zero-field ΔS . The origin of this ‘spike’ relates to the fact that if there is irrepeatable hysteresis in $M(H)$, each $M(H)$ loop is affected by the previous $M(H)$ loop, and no longer approximates a true isotherm.

For magnetic systems, a ‘resetting’ procedure has been proposed and demonstrated as a remedy to the problems with the ‘standard’ indirect method for systems showing irrepeatable hysteresis of isothermal ΔS [92]. In between each successive $M(H)$ or analogous $P(E)$ loop, the sample is ‘reset’ via a thermal excursion away from the phase transition.

To evaluate isothermal ΔS for a ferroelectric on application of a field, it is necessary to ‘reset’ the sample to the paraelectric phase by heating above T_C , in between each successive measurement. The Maxwell analysis is performed on initial or ‘virgin’ branches of the resulting $P(E)$ loops (Figure 2.7). One could also devise a procedure for evaluating isothermal ΔS on *removal* of a field: between each successive loop the sample could be reset to a *poled* state in the ferroelectric phase (below T_C) and then heated *at field* to the measurement temperature.

²These have been overcome in the present work. See full discussion in Chapter 3.

³For ferromagnets, $(\partial M/\partial T)_H = (\partial S/\partial H)_T$.

The ‘resetting’ procedure has been demonstrated for magnetic systems, but has not hitherto been applied to electrocaloric materials.

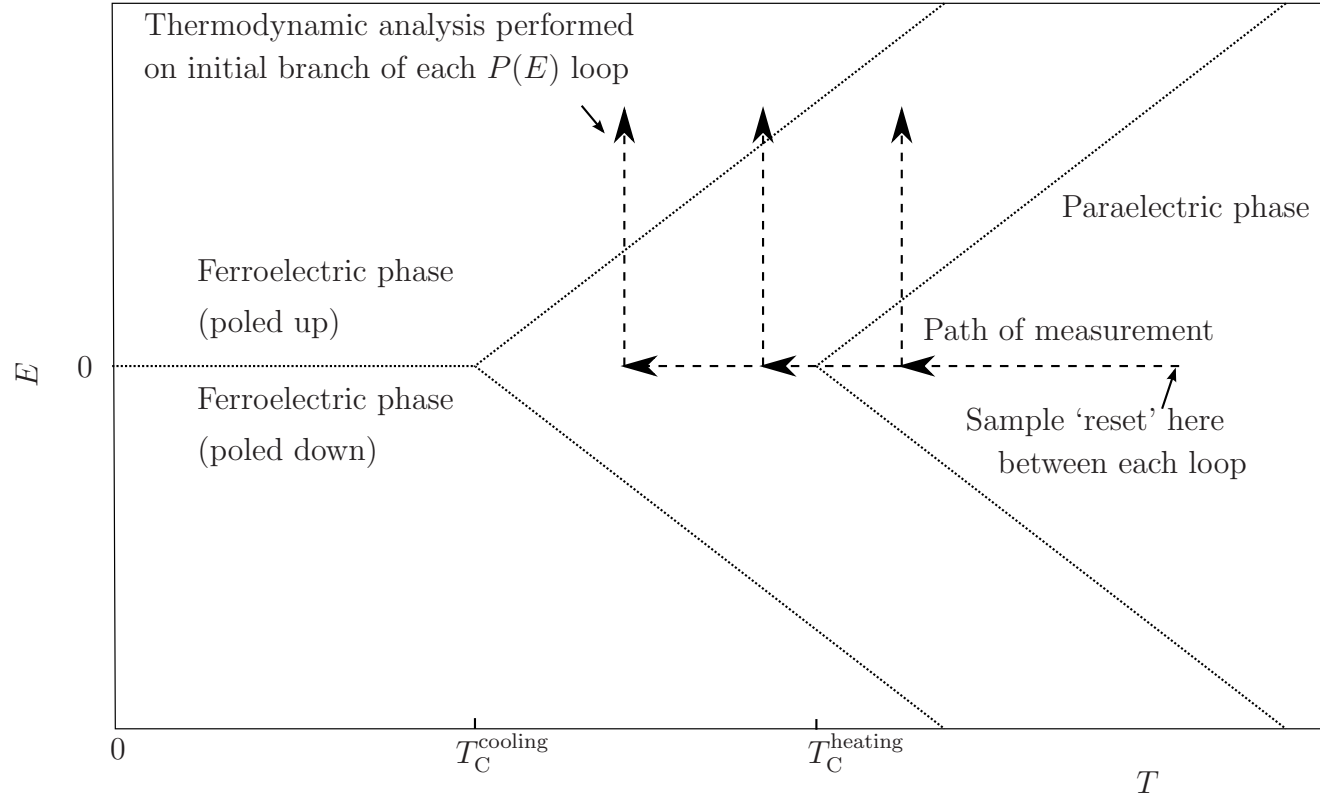


Figure 2.7: Illustration of the ‘resetting’ method for collecting $P(E)$ loops as a function of temperature, suitable for evaluating isothermal ΔS near a thermally hysteretic first-order phase transition. The arrows show the path taken in $E - T$ space for each successive loop. For illustration purposes, the phase coexistence interval on heating or cooling is not shown.

2.5 Calorimetry, interconversion of adiabatic ΔT and isothermal ΔS

Ideally, the adiabatic temperature change ΔT would be measured directly, but in practice this is often not possible, so conversion routes between ΔT and isothermal ΔS are of interest. The ‘indirect method’ gives isothermal $\Delta S(E)$ for various T . However it is not possible to directly draw adiabats from such a dataset, as the curves for isothermal $\Delta S(E)$ are all ‘floating’, i.e. they all correspond to different *starting values* of entropy because entropy is a function of temperature at zero field.

To provide all of the isothermal $\Delta S(E)$ curves with a common reference, it is necessary to measure *isofield entropy change* as a function of *temperature*, i.e. $\Delta S(T)$. This is normally done indirectly via a heat-capacity measurement in a calorimeter. Once isothermal $\Delta S(E)$ for various T are known via the Maxwell relation, and zero-field $\Delta S(T)$ via calorimetry, a two-dimensional ‘entropy map’ may be evaluated in $E - T$ space, in which adiabats are readily found by tracing lines of constant S . Such a map could alternatively be compiled via a *single* curve for isothermal $\Delta S(E)$ for any convenient T , and a *series* of curves for isofield $\Delta S(T)$ for various E , but in practice the former method is usually more convenient, as few calorimeters have the facility to apply voltages over samples (a notable exception is the one used by Moya *et al.* to measure electrocaloric effects in BaTiO₃ single crystals [10]).

For the present work a commercial differential scanning calorimeter (type DSC Q2000, TA Instruments) was used to resolve mass-normalised heat flow ϕ in samples as a function of time t , during a linear ramp of temperature. Specific heat capacity at constant field follows $c_E = \phi dt/dT$, and zero-field entropy change may then be evaluated as $\Delta S = \int_{T_0}^T [c_E/T'] dT'$. Samples were measured in an N₂-filled aluminium pan (type TZeroPan, TA Instruments) of mass ~ 50 mg. The mass of the pan and the sample were measured to within a few μg , using a precision balance (type Ultramicro, Sartorius). The measured values of ϕ were subject to a calibration offset which was removed by forcing curves taken on heating and on cooling to coincide at a temperature away from T_C (the temperature used will be specified when results are presented). These measurements were performed by Robert Cornell.

For cases where a calorimetry dataset is not available, it is sometimes possible to make use of the expression $dT = [T dS/c_E]$, where dT and dS are infinitesimal changes in adiabatic temperature change and isothermal entropy respectively, and c_E is specific

heat capacity at constant field. In these circumstances the adiabatic path for integration and the form of $c_E(E)$ are generally unknown. However, by assuming that $c_E(E) = c_{E=0}$ for the relevant range of E and T , and integrating along an isothermal path in lieu of the unknown adiabatic path, reasonably accurate results can be obtained for systems with diffuse phase transitions. This method fails close to first-order phase transitions as latent heat causes c_E to diverge at T_C .

Chapter 3

Apparatus for measurements in 77-700 K

Three bespoke cryostats were assembled to cater for different kinds of samples and temperature ranges (Table 3.1). These systems — a cryogenic probe, a high-temperature stage and a benchtop cryogenic stage — will be discussed consecutively. Bespoke measurement software will also be discussed.

System	Cryogenic probe	High-temperature stage	Cryogenic stage
Lowest temperature (K)	77 (in liq. N ₂) 5 (in liq. He)	298	110
Highest temperature (K)	420	700	400
Temperature stability (mK)	5	15	~1000 (5 min hold time)
Min stable temp. ramp (K min⁻¹)	0.1	0.1	5
Max stable temp. ramp (K min⁻¹)	5-10	1	10
Area for sample (cm x cm)	1.6 x 6 (head 1) 1.5 x 1.5 (head 2)	3.6 x 2	3 x 3
Max sample height (cm)	0.5 (head 1) 3 (head 2)	20	3
Max voltage (kV)	2.5	2.5	0.2
Min parasitic capacitance (pF)	1.8	0.8	0.4
Sample contact	Silver paint/ pogo pin (head 2)	Silver paint/ pogo pin	Micropositioner
Sample environment	Vacuum/ 1 atm dry N ₂	Vacuum/ 1 atm air	1 atm dry N ₂

Table 3.1: Comparison between the three bespoke cryostats that were assembled. The maximum voltage and the minimum parasitic capacitance are mutually exclusive for the cryogenic probe and the high-temperature stage, as each requires a different type of wire. Furthermore, for these two systems the temperature stability and ramp statistics pertain to operation in vacuum.

3.1 Cryogenic probe

This apparatus has a pole-like geometry for insertion into a cryogenic dewar of liquid nitrogen or liquid helium. Figures 3.1-3.3 show the design of the probe. Custom metalworking was mostly outsourced to the departmental metal workshop. The hollow stainless-steel inner pole (length 71 cm and diameter 1.3 cm), stainless-steel vacuum jacket (length 85 cm and diameter 2.3 cm) and vacuum fittings were taken from a pre-existing probe in the laboratory. Two probe heads were fabricated to cater for different kinds of samples.

3.1.1 Probe head 1

Probe head 1 (Figures 3.1 and 3.3b) was fashioned from a solid copper cylinder of length 8 cm and diameter 1.8 cm, which acted as the heat reservoir. Two parallel flat surfaces of dimensions 6 cm x 1.6 cm were cut into the cylinder surface to act as the sample space, leaving a short cylindrical section of length 2 cm for the tape heater. There was a vertical clearance of ~ 0.5 cm above the sample space. The tape heater was a $100\ \Omega$ wire of 15 μm -thick constantan (Scientific Wire Company) wrapped between two strips of adhesive, insulating kapton tape (3M). A hole was drilled to closely accommodate a cylindrical Pt-100 RTD (type KN 0815, Heraeus), which had been dipped in thermally conductive grease (type ‘N’, Apiezon). Grooves were made along the sides of the cylinder to accommodate wiring and electrical contact pads. A copper cuboid of dimensions 6.5 cm x 1.3 cm x 1.3 cm was adapted to serve as the mechanical attachment of the probe head to bottom of the inner pole. This block was attached to the probe head via a solid stainless-steel pole of length 6 cm and diameter 0.6 cm. A silver-solder process was used to braze the metal components together.

3.1.2 Probe head 2

Probe head 2 (Figure 3.2 and 3.3c) was adapted from an existing probe head in the laboratory. The design was similar to that of probe head 1, with the following principle differences:

- The plane of the sample space was perpendicular to the long-axis of the probe head, leading to a more limited area for samples of approximately 1.5 cm x 1.5 cm,

but removing the 0.5 cm height limit for samples mounted in probe head 1.

- As a result of the extra sample height, improvised sample holders (with electrical access) could be attached via a screw thread near the sample space. These fixtures could include pogo pin contacts, useful for making contact to small electrode pads on a thin-film sample.
- Electrical access to the sample space was via grooves cut in the copper cylinder, underneath the tape heater. Ceramic tubes were used for electrical insulation where necessary.
- The geometry and dimensions differed as shown in Figures 3.2 and 3.3c.

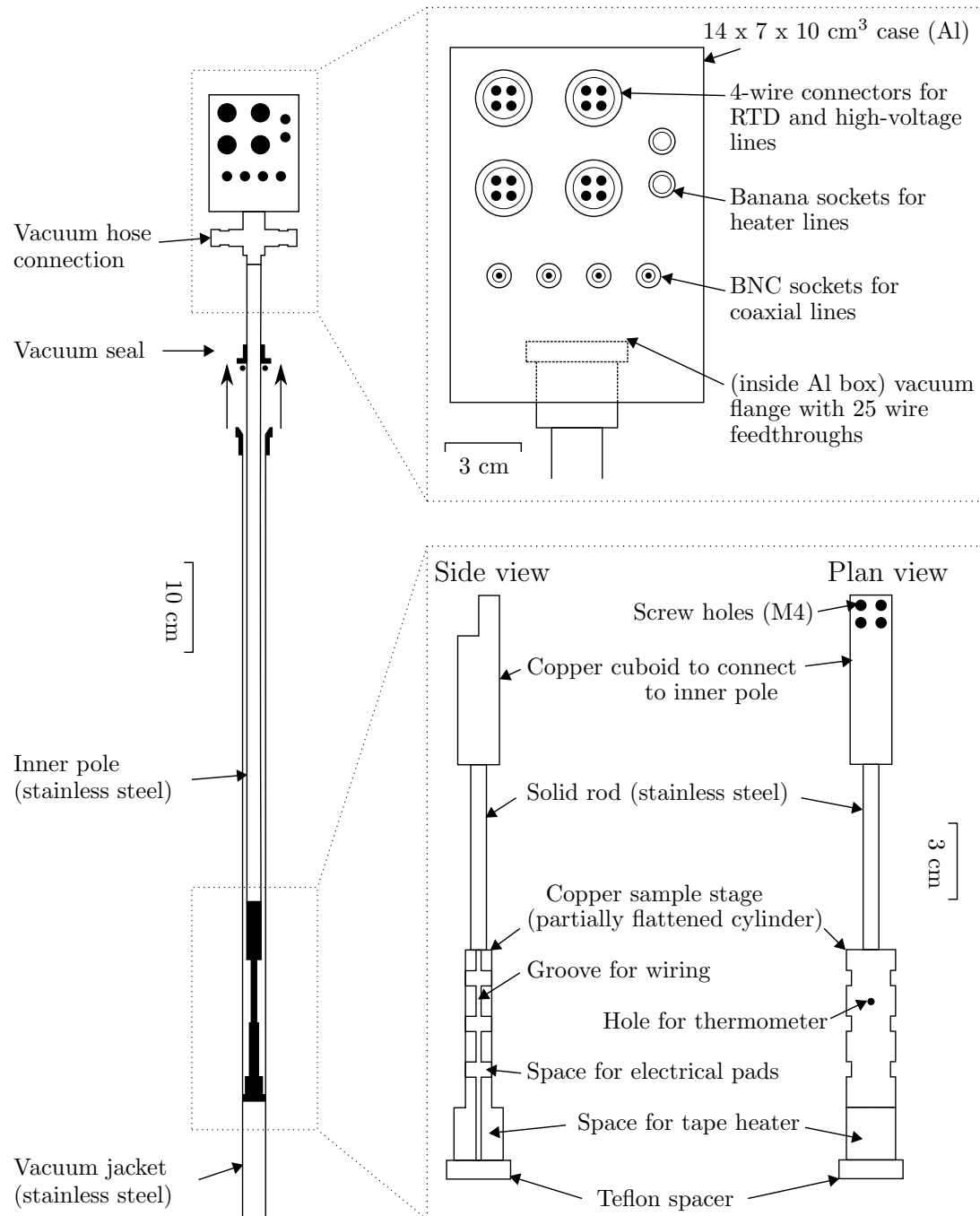


Figure 3.1: Design of cryogenic probe showing probe head 1. Scale bars are accurate to within 10 %.

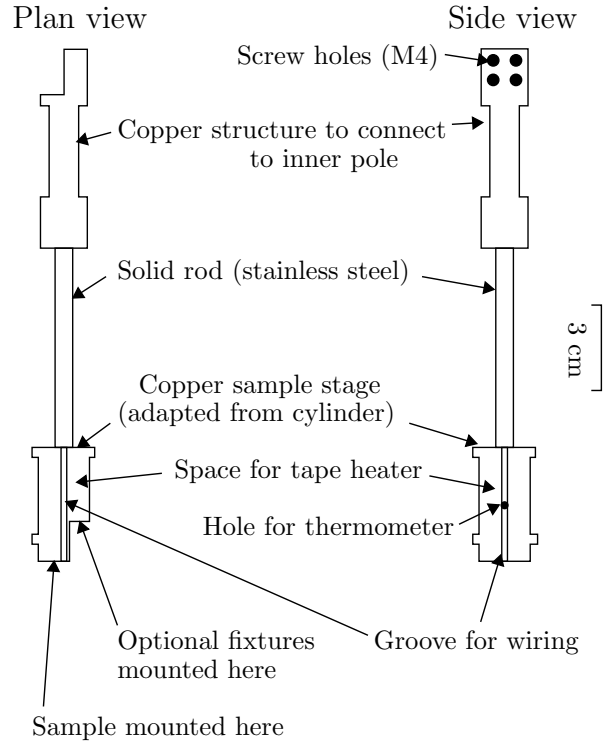


Figure 3.2: Probe head 2. Scale bars are accurate to within 10 %.

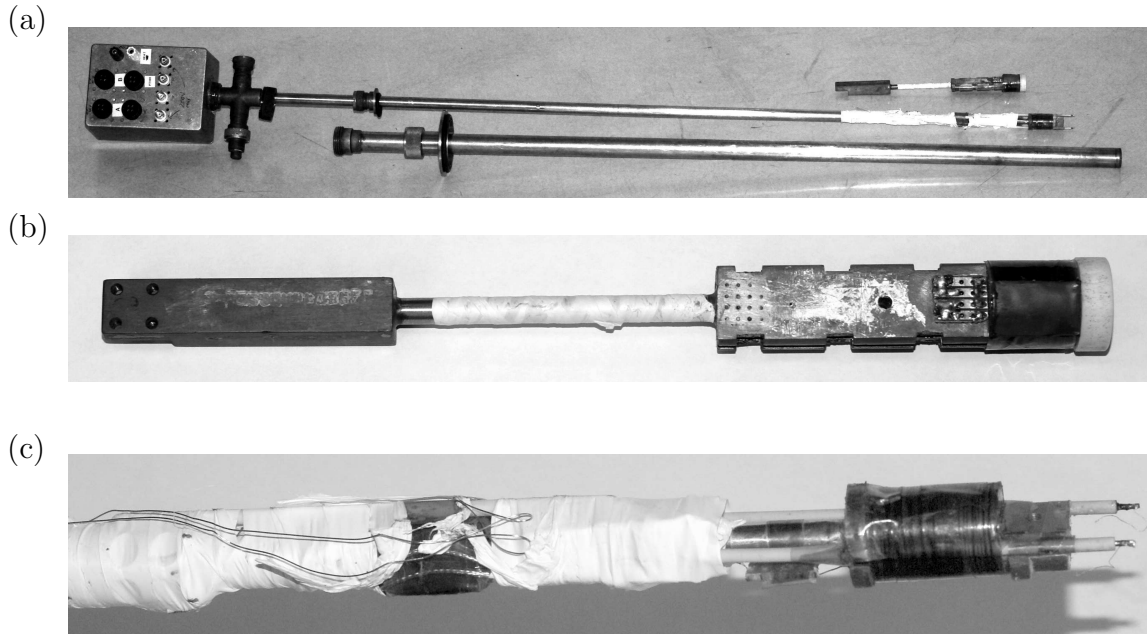


Figure 3.3: Photographs of probe. **(a)** Top: probe head 1. Middle: main part of probe with probe head 2 mounted. Bottom: outer vacuum jacket. **(b)** Close-up of probe head 1 (not wired up). **(c)** Close-up of probe head 2 (wired up).

3.1.3 Wiring

Various wires were threaded down the inner pole to the probe head. At the top of the probe, the wires were soldered to a vacuum-tight 25-wire glass-metal feedthrough flange, which was wired to electrical sockets set in an aluminium box of dimensions 10 cm x 14 cm x 7.5 cm (Onecall Farnell) as shown in Figure 3.1. At the probe head, the wires were soldered (here and elsewhere, using $\text{Pb}_{0.4}\text{Sn}_{0.6}$) to contact pads (cut from copper printed circuit board) glued to the sides of the sample space. Wires and contact pads were secured to the probe head using adhesive (GE varnish, Oxford Instruments), kapton tape and teflon tape. The following wires were used:

- 2 x 10 μm -thick copper enamelled wires for heater connection.
- 4 x 10 μm -thick copper enamelled wires for thermometer connection.
- 2 x 35 μm -thick copper enamelled wires, threaded for the entire length through highly insulating alumina tubes (type ALM308, outside diameter 3 mm, inside diameter 2x0.8 mm, Almath Crucibles). These wires were for applying high voltages across samples.
- 4 x 10 μm -thick copper enamelled wires for use with an optional extra thermometer or thermocouple mounted on the sample.
- 2 x 1 mm-thick miniature coaxial wires (type SC, teflon insulation, copper inner and outer conductors, Lakeshore Cryotronics). These shielded wires were for low-level dielectric measurements.

The shields of the coaxial wires were isolated from chassis ground so that they could be connected to the guard terminal of the Agilent 4294A impedance analyser, resulting in an effective parasitic capacitance of ~ 1.8 pF.

3.1.4 Vacuum

The probe was evacuated through a thick-walled rubber hose using a rotary vacuum pump (type E2M8, 8 l capacity, Edwards). The vacuum attained was approximately 0.04 mbar (measured near the mouth of the pump with a type PR10-K Pirani, Edwards), which dropped to 0.02 mbar when the probe was inserted into an LN₂ dewar, due to cryopumping. To achieve thermal equilibrium, an exchange gas of N₂ or He could be admitted via a

rubber bladder. However, high voltages were more likely to arc when exchange gas was used. This was consistent with Paschen's law¹ for breakdown voltage V_b as a function of pressure p (Figure 3.4), as point A in the Figure corresponded to 1 atm of air, point B to exchange gas, and point C to vacuum. To alleviate these problems, thin and flexible copper strips were attached to the probe head to form a weak thermal connection to the vacuum jacket, thus avoiding the need for exchange gas and the associated arcing.

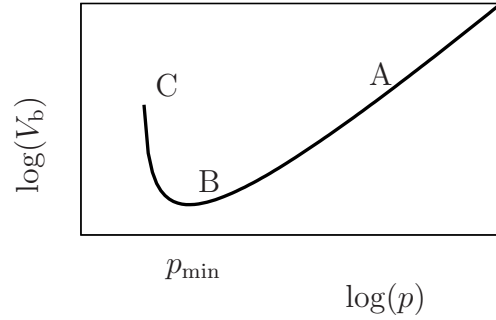


Figure 3.4: Illustration of Paschen curve.

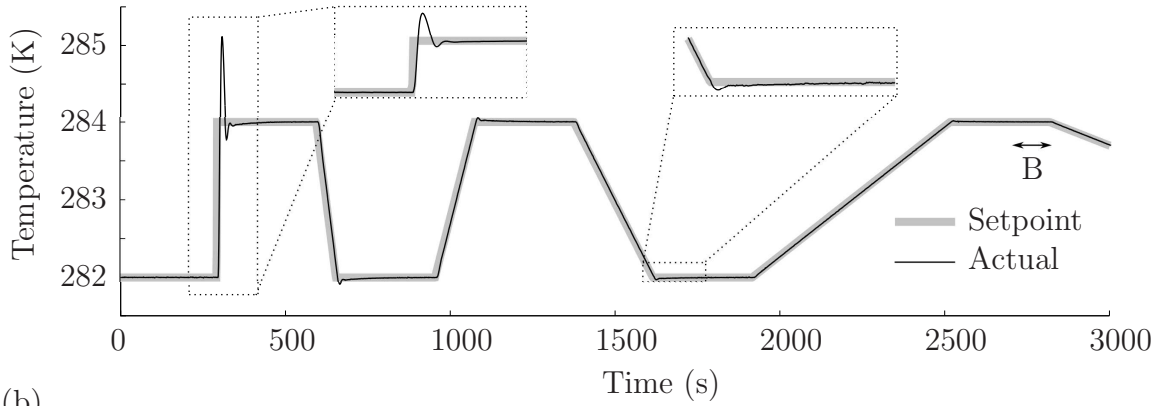
3.1.5 Temperature control

A standard calibration curve for the Pt-100 RTDs was used (Lakeshore Cryotronics). Temperature control could be automatic or manual. Manual control was via a current source (type ITC4, Oxford Instruments) for the heater and a digital multimeter (type 196, Keithley Instruments) for monitoring of temperature. Automatic control was via a proportional integral derivative (PID) controller (type 336, Lakeshore Cryotronics). Appropriate values for the P, I and D control parameters were obtained by trial and error (the final values were $P = 100$, $I = 15$ and $D = 0$ in the standard units). Using the PID controller it was possible to stabilise temperature within a few millikelvin about a setpoint, or maintain a steady temperature ramp at a rate between

¹Paschen's law states that breakdown voltage V_b across a distance d in a gas at pressure p follows $V_b = apd/[\ln(pd) + b]$, where a and b are constants that are extremely sensitive to small defects of the electrodes and impurities of the gas [95]. In practice Paschen's law is not reproducible from one system to another, even if the gases used and the values of d and p are the same, unless the systems are very precisely constructed.

$0.1 \pm 0.01 \text{ K min}^{-1}$ and $3 \pm 0.2 \text{ K min}^{-1}$ (Figure 3.5).

(a)



(b)

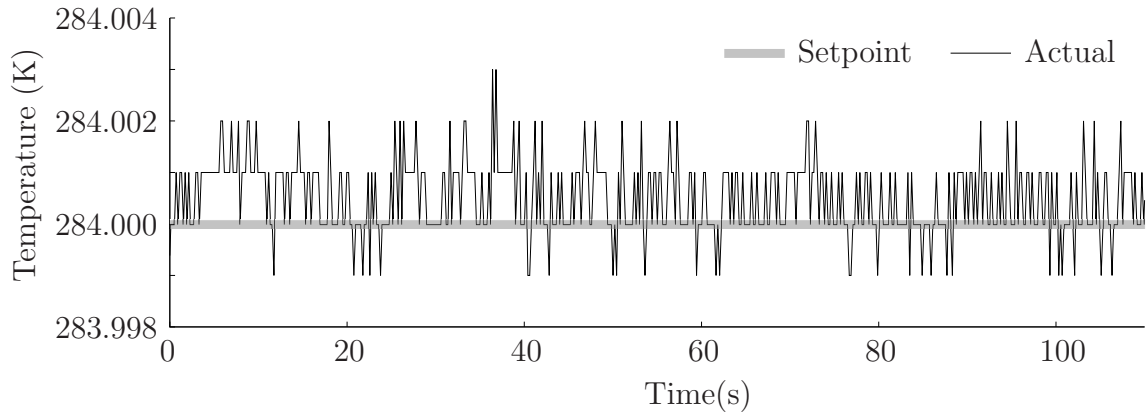


Figure 3.5: Performance of cryogenic probe. **(a)** For the case of automatic PID control, the temperature response to a series of setpoint ramps up and down, and of varying speeds, is plotted. Two sections of the plot are magnified. **(b)** The temperature versus time curve corresponding to the time range ‘B’ from (a) is plotted, with binning apparent. In 110 s, the maximum deviation from the setpoint was 3 mK.

3.1.6 Collaborative experiments on Lawsonite

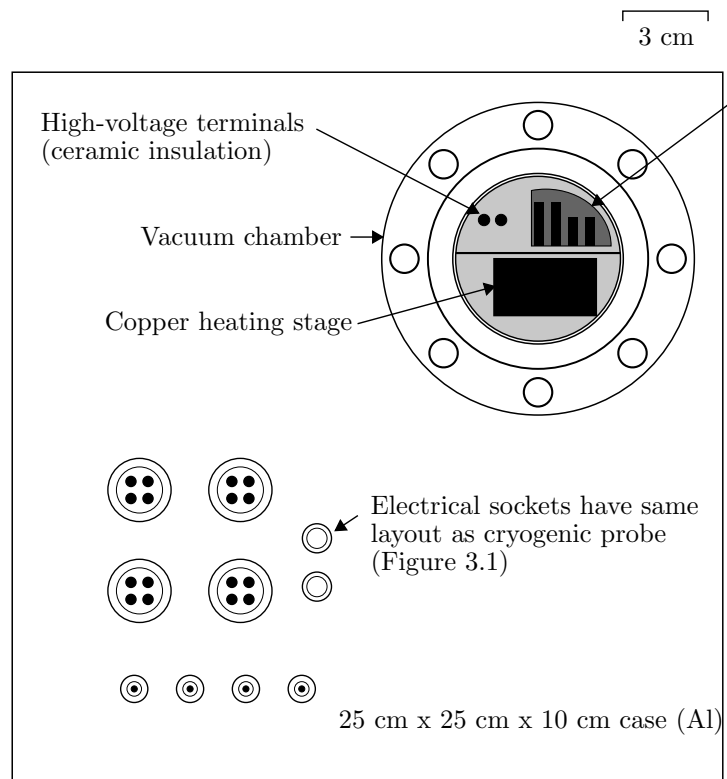
The first experiments using the probe measured improper ferroelectricity in a polycrystalline sample of the mineral Lawsonite. This collaborative work was led by Ekhard K. H. Salje (Earth Sciences, University of Cambridge) and was published in the *Journal of Physics: Condensed Matter* [96].

3.2 High-temperature stage

This stage featured a solderless copper heater in a vacuum chamber for experiments in 298-700 K.

The lower part of the apparatus (Figures 3.6 and 3.7) was a stainless-steel vacuum fitting (upper connector: conflat DN63 [outside diameter 114 mm], lower connector: conflat DN40 [outside diameter 70 mm], height 50 mm, VG Scienta), set into an aluminum box of dimensions 25 cm x 25 cm x 10 cm (Onecall Farnell). Three stainless-steel legs (M3 shafts) supported a stainless-steel circular table, of diameter 5.8 cm and thickness 0.5 cm, that sat 7 cm above the base of the vacuum fitting. The table was divided into two parts by a thin vertical sheet of stainless steel (2.5 cm high), with one side dedicated to the heater stage and the other to electrical contacts, and the dividing sheet acting as a reflective heat shield to protect the electrical contacts from thermal damage. The heater stage was made from a copper block of dimensions 3.6 cm x 2.0 cm x 0.8 cm, and mounted on 1.6 cm-high ceramic standoffs (military specification NL523W01-005) for thermal isolation from the table. The heater stage was powered by two cartridge heaters, each of length 2.5 cm and diameter 0.63 cm (E1A53-L12 firerods, Watlow), inserted in close-fitting holes drilled along the length of the stage. A flat Pt-100 RTD (type M213, area 1.7 mm x 1.25 mm, height 1 mm, Heraeus) was clamped to the bottom of the heater stage with a screw.

View from top



View from front

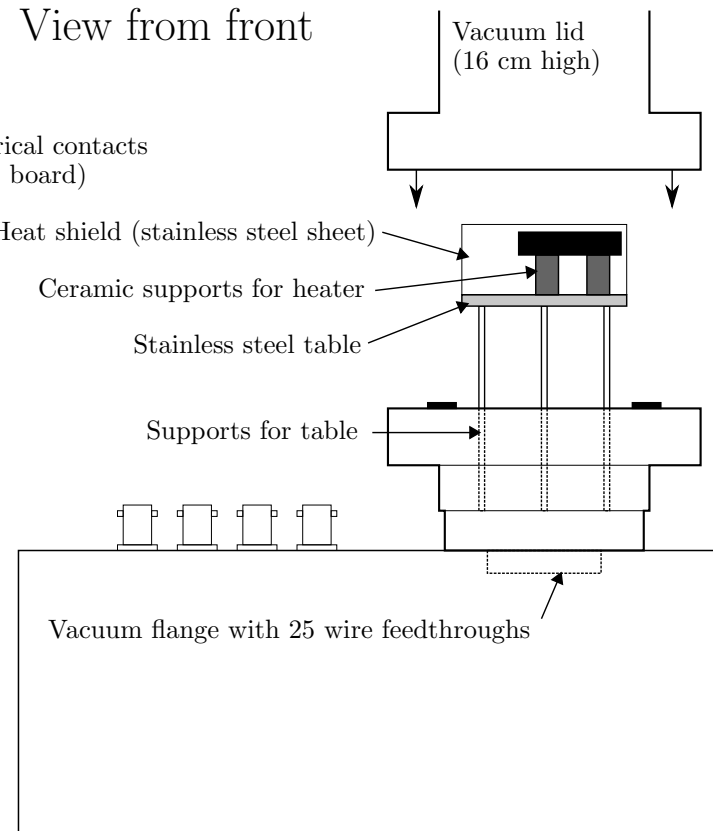


Figure 3.6: Schematic of high-temperature stage. Scale bar accurate to within 10 %.

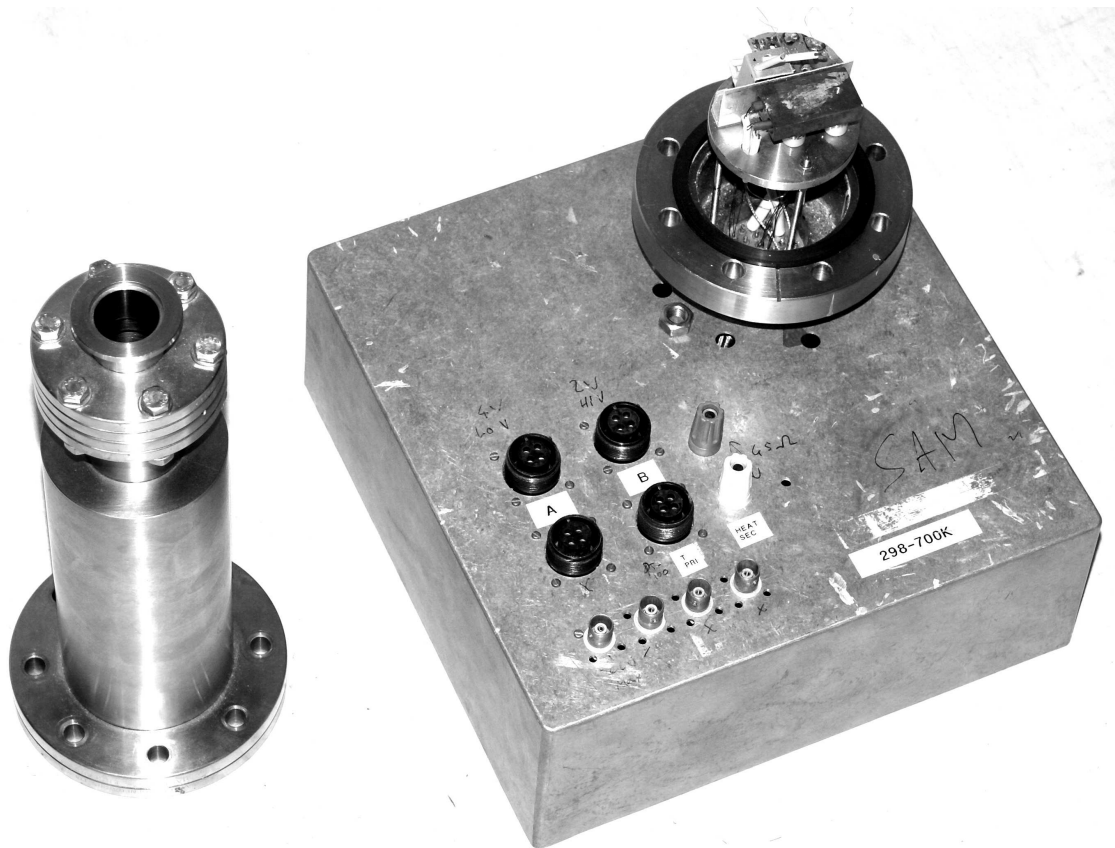


Figure 3.7: Photograph of high-temperature stage. Left: upper vacuum fitting. Right: main part of high-temperature stage.

3.2.1 Wiring

At the base of the lower vacuum fitting was a vacuum-tight 25-wire glass-metal feedthrough flange which, on the room-pressure side, was wired to electrical sockets set in the top of the aluminium box as shown in Figure 3.1, and on the vacuum side, was wired via holes in the stainless-steel table to the heater stage and electrical contacts. Electrical contacts (other than the high-voltage lines) were made from standard printed circuit boards (PCBs) mounted above the table on ceramic standoffs. The following wires were used:

- 2 x 10 μm -thick copper enamelled wires for heater connection (spot welded at the heater end to enable operation at high temperatures).
- 4 x 10 μm -thick copper enamelled wires for thermometer connection (also spot welded).
- 2 x 35 μm -thick copper enamelled wires, threaded for the entire length through highly insulating alumina tubes (type ALM308, Almath Crucibles LTD). These wires were for applying high voltages across samples. Rather than terminating at a PCB, the wire ends were left protruding slightly through the ends of the alumina tubes, to reduce the possibility of electrical arcing.
- 4 x 10 μm -thick copper enamelled wires for use with an optional extra thermometer or thermocouple mounted on the sample. These were terminated at the PCBs.
- 2 x 1 mm-thick miniature coaxial wires (type SC, Lakeshore Cryotronics) for precise low-level electrical measurements. These were terminated at the PCBs.

3.2.2 Vacuum

The upper part of the vacuum chamber was a 16 cm-high fitting (upper connector: conflat DN40 [outside diameter 70 mm], lower connector: conflat DN63 [outside diameter 114 mm], VG Scienta) which mated with the conflat DN63 fitting at the top of the lower part of the chamber. A viton rubber gasket was used (VG Scienta). The system was evacuated from the top of the upper vacuum fitting via a stainless steel flexible vacuum hose (3.5 cm outside diameter). Evacuation via a thick-walled rubber

hose was found to cause arcing during high voltage experiments, due to the poorer vacuum (see discussion of Paschen's law in Section 3.1.4).

3.2.3 Temperature control

The same instruments were used for temperature control as for the cryogenic probe (Section 3.1.5). Although it was possible to stabilise temperature within around 15 mK about a setpoint throughout the temperature range 298-700 K, below ~ 400 K in vacuum the stabilisation process could take a long time (30-60 minutes)². This was not a problem in practice because the cryogenic probe could be used at temperatures up to 420 K. Above 400 K in vacuum, appropriate values for the P, I and D control parameters were obtained by trial and error (the final values were $P = 15$, $I = 5$ and $D = 100$ in standard units). Thermal performance near 500 K is shown in Figure 3.8. Stabilisation times were significantly longer than for the cryogenic probe due to the low cooling rate of this system.

²It was possible to operate the heater stage in 1 atm of air below 400 K, and thermal stabilisation within 30 mK of a setpoint could be attained within 10-15 minutes.

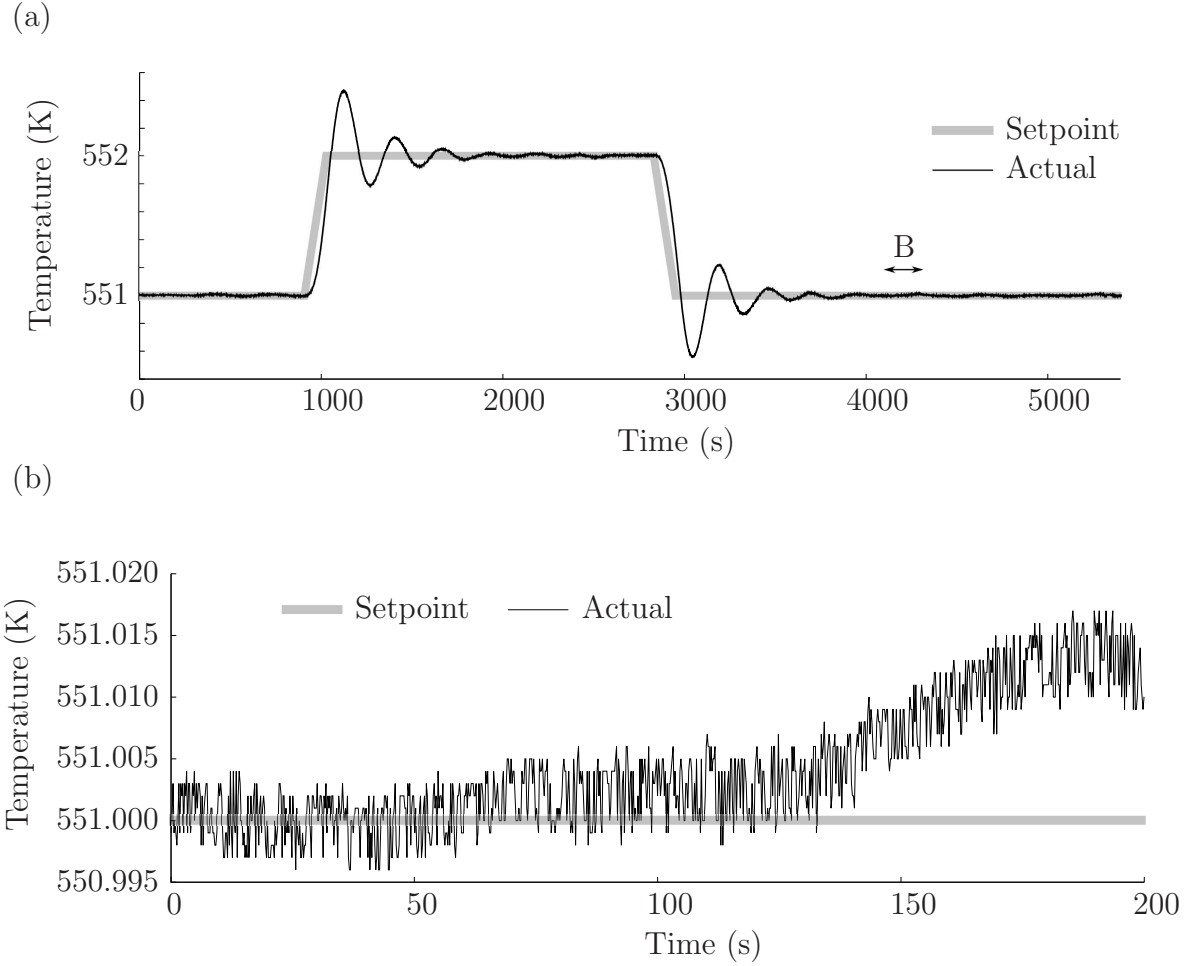


Figure 3.8: **(a)** For automatic PID control, the temperature response to a two setpoint ramps is plotted. **(b)** Temperature versus time, for the time range ‘B’ from (a), is plotted, with binning apparent. In 200 s, the maximum deviation from the setpoint was 15 mK.

3.2.4 Previous configuration

The high-temperature stage in its present form superceded an earlier version which will now also be described, partly to highlight the problems that led to its eventual rejection, and partly because it was used in collaborative experiments to measure electrocaloric effects in a single-crystal sample of BaTiO_3 (work led by Xavier Moya and published in *Advanced Materials* [10], which cited this dissertation).

The earlier version of the apparatus (Figure 3.9a) differed from the present version in the following principle ways:

- Instead of the stainless-steel table, a large ceramic hollow pillar (height 8 cm, outside diameter 5 cm, ‘pyrophyllite’ ceramic [aluminium silicate sintered at 1100 °C for two hours] was mounted on the stainless-steel legs. Machineable pyrophyllite Ceramic supplied by Ceramic Substrates and Components Ltd.
- The hollow pillar contained the heater stage, which was an adapted copper cylinder (height 4.5 cm, outside diameter 4 cm). The heater stage was powered by four cartridge heaters, each of length 2.5 cm and diameter 0.63 cm (E1A53-L12 firerods, Watlow), inserted vertically upwards in close-fitting holes.
- The thermometer was a cylindrical Pt-100 RTD (type KN 0815, length 8 mm, diameter 1.5 mm, Heraeus) inserted in a hole in the side of the heater stage.
- Electrical contacts comprised copper foils, which were stuck around the sides of the ceramic pillar with cement (type OB-500, Omega Engineering).

The apparatus suffered from various problems:

- Temperature stability within 15 mK could be attained, but because of the large thermal mass of the heater and lack of significant outward conduction pathways for heat, the stabilisation time was unacceptably long, at several hours near 400 K, and around one hour at 500 K.
- Because of the large thermal mass of the heater, the entire vacuum chamber became hot when operating at temperatures above 450 K for longer than a few hours. This resulted in thermal stress to parts of the apparatus which were not supposed to become hot (such as the glass-metal wiring feedthrough at the bottom of the vacuum chamber).

- Due to the differing thermal expansivities of the electrical contacts and the ceramic pillar to which they were stuck, the contacts tended to become unstuck after several thermal cycles.

The apparatus was accordingly modified (Figure 3.9b):

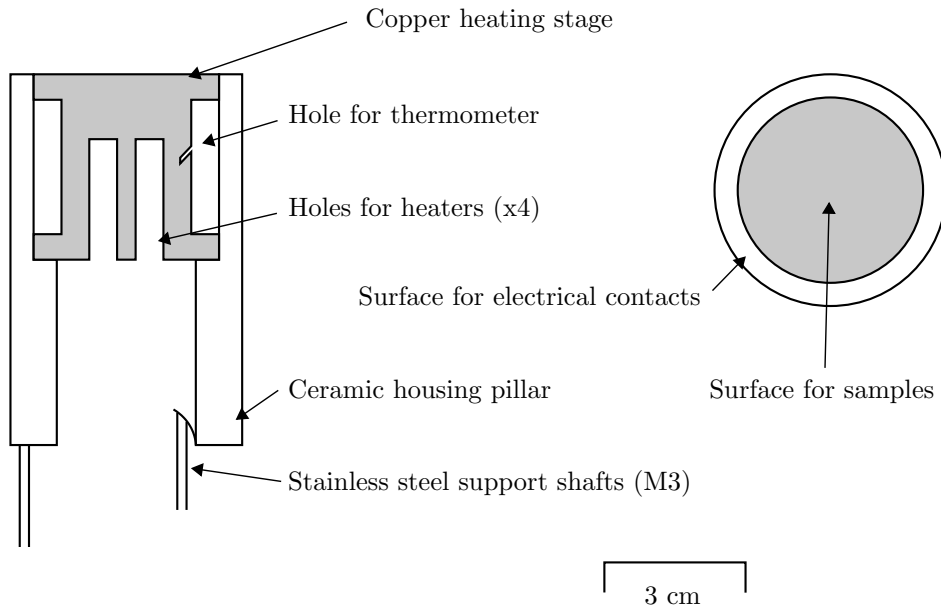
- A secondary heating stage was added at the top of the main heating stage. This secondary heating stage was a ‘T’ shaped copper block with a hole for a single cartridge heater, and an M4 screw shaft to raise it above the main heating stage. Thus the main heating stage could be used for ‘coarse’ temperature control, and the secondary heating stage for ‘fine’ control. The secondary heating stage used a type KN 0815 Pt-100 RTD, inserted in a purpose-drilled hole.
- Contacts for wiring were relocated to PCB boards hung on wires attached to the stainless steel legs below the ceramic pillar.
- 3 mm-thick solid copper pipes were attached to the main heating stage and positioned to make direct contact with the wall of the upper vacuum chamber, increasing outward heat flow and reducing the thermal time constant.

In this modified configuration the apparatus functioned and was actively used for experiments such as the published work of Moya *et al.* [10]. However it proved to be ‘high maintenance’ and a decision was reluctantly taken to rebuild it in its present configuration (Section 3.2), with a single medium-sized heater stage to replace the unnecessarily complex two-stage design.

(a)

View from front

View from top



(b)

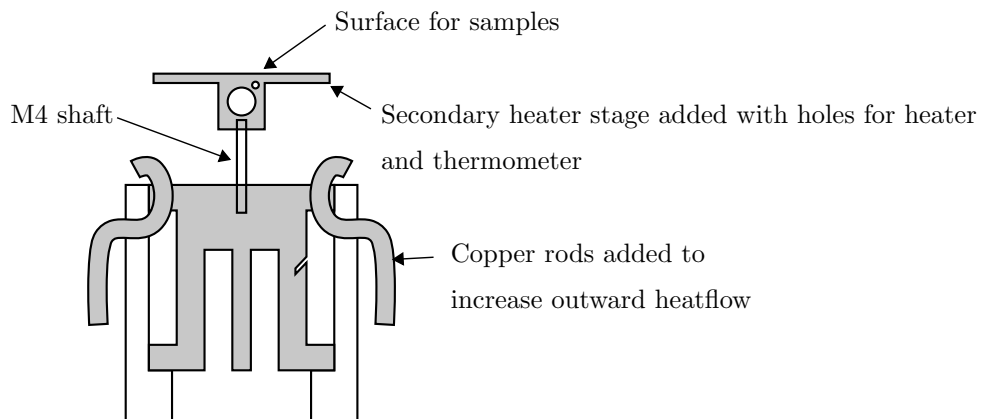


Figure 3.9: (a) Schematic of the initial design of the high-temperature stage. Scale bar accurate to within 10 %. (b) Improved design showing modifications.

3.3 Cryogenic stage

The cryogenic probe provided precise temperature control in the 77-420 K range, but it had a weakness relating to the mounting of thin films with contact pads of diameter ~ 200 μm or less. Use of small electrical pads is often essential to obtain high-quality ferroelectric data on thin films. For closed systems such as the cryogenic probe, methods such as wire bonding and spring-loaded pogo pin contacts are often employed to make contact with electrical pads, in research fields such as superconductivity. Unfortunately, wire bonding is not ideal for ferroelectric thin films employing top-bottom electroding, as the bonding process can create localised weaknesses in the film, destroying performance. For small electrical pads, pogo pins are not ideal either, as the slightest mechanical disturbance can break contact.

Micropositioners with thin tungsten tips may be used to make light contact with small electrodes on a thin film, at temperatures accessible via a benchtop heater.

Temperature control is inevitably worse than in a vacuum system, but this may be an acceptable compromise for ferroelectric films showing diffuse phase transitions. The objective of the present work was to build a benchtop apparatus to enable cryogenic temperatures to be accessed via existing micropositioners in the laboratory (type S-725-PLM, Signatone). The main challenge was the tendency of water from the air to condense in the sample space, as a result of the low temperatures. The solution was to construct an enclosure for the sample that was sufficiently open to allow the tungsten tips of the micropositioner free movement around the sample, whilst being sufficiently enclosed to sustain a slight positive pressure of dry N_2 , which was supplied as a continuous flow of gas from the laboratory N_2 line. A slight positive pressure of dry N_2 was, over time, sufficient to displace the air from the sample space, enabling the sample stage to be cooled with liquid nitrogen with no condensation issues.

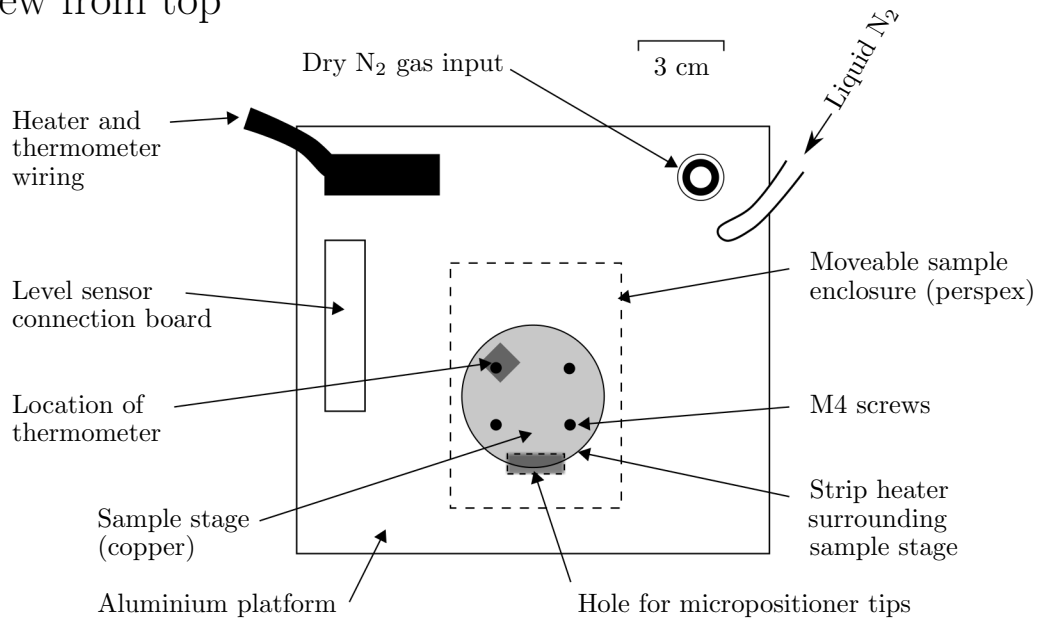
The cryogenic stage was assembled from disused components in the laboratory. Olatz Idigoras and Abhijeet Sangle are acknowledged for help with machining.

Central to the design (Figures 3.10-3.11) was a dumbbell shaped piece of copper, comprising two disks of diameter 5 cm, and thickness 1 cm, connected by a solid rod of diameter 1 cm. The dumbbell was mounted vertically on a small aluminium platform of area 16.5 cm x 15 cm and height 12.5 cm, such that the upper disk of the dumbbell formed the sample table and the lower disk was suspended underneath to be immersed in a polystyrene bucket filled with liquid N_2 . Perspex sheeting supported the sides of

the aluminium platform to enclose the bucket. A PVC tube was threaded through the top of the platform into the bucket to enable liquid N_2 to be poured in without having to lift the platform. A nozzle was also added to the top of the aluminium platform to attach the dry N_2 line. To monitor the level of liquid in the bucket, six K-type thermocouples were attached onto a 7 cm-long PCB strip, forming an equally spaced array that extended almost the full depth of the bucket. Contacts were placed on top of the aluminium platform to enable the operator to monitor each thermocouple with a voltmeter and thus deduce the level of liquid.

Above the aluminium platform, a strip heater was fabricated with constantan heater wire and kapton tape, and placed around the circumference of the upper disk of the dumbbell (i.e. the sample table), enabling electronic control of temperature. A flat Pt-100 RTD (type M213, area 1.7 mm x 1.25 mm, height 1 mm, Heraeus) was also mounted on the sample stage. To keep the sample space free from moisture, a small open-bottomed perspex box of dimensions 8.5 cm x 6.0 cm x 2.7 cm was placed over. A hole of dimensions ~ 0.7 cm x ~ 1.5 cm was made in the roof of this box to permit access for the tungsten tips of the micropositioners. When the flow of dry N_2 was switched on, gas would flow around the sample and out of this hole, such that there was no back-flow of air into the sample space, which remained free of ice (Figure 3.11b).

View from top



View from front

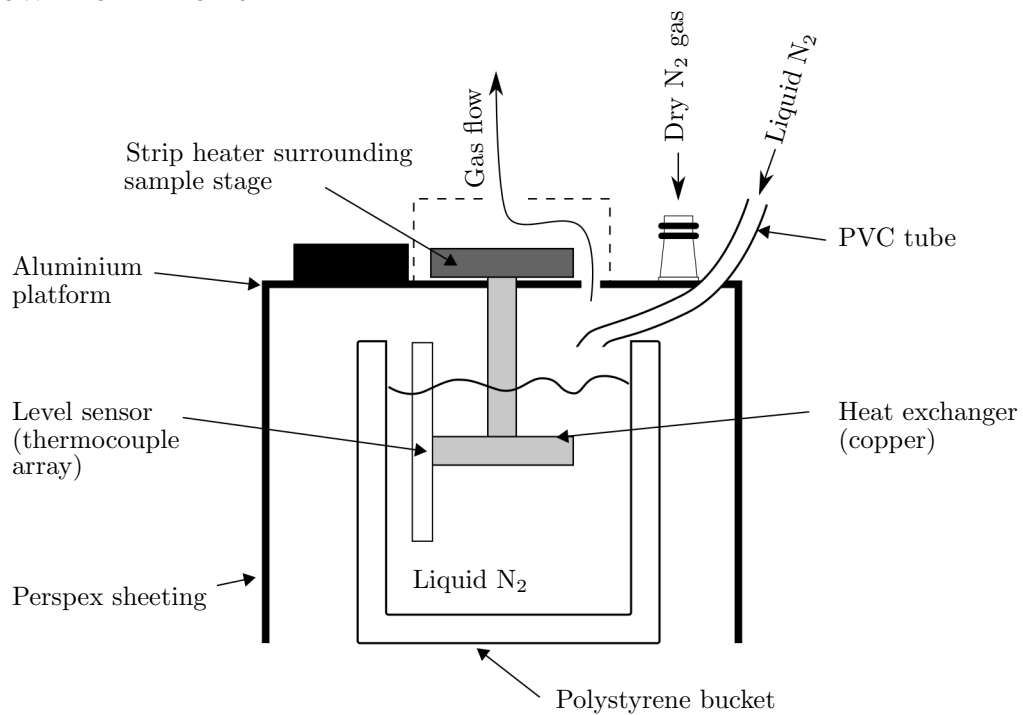
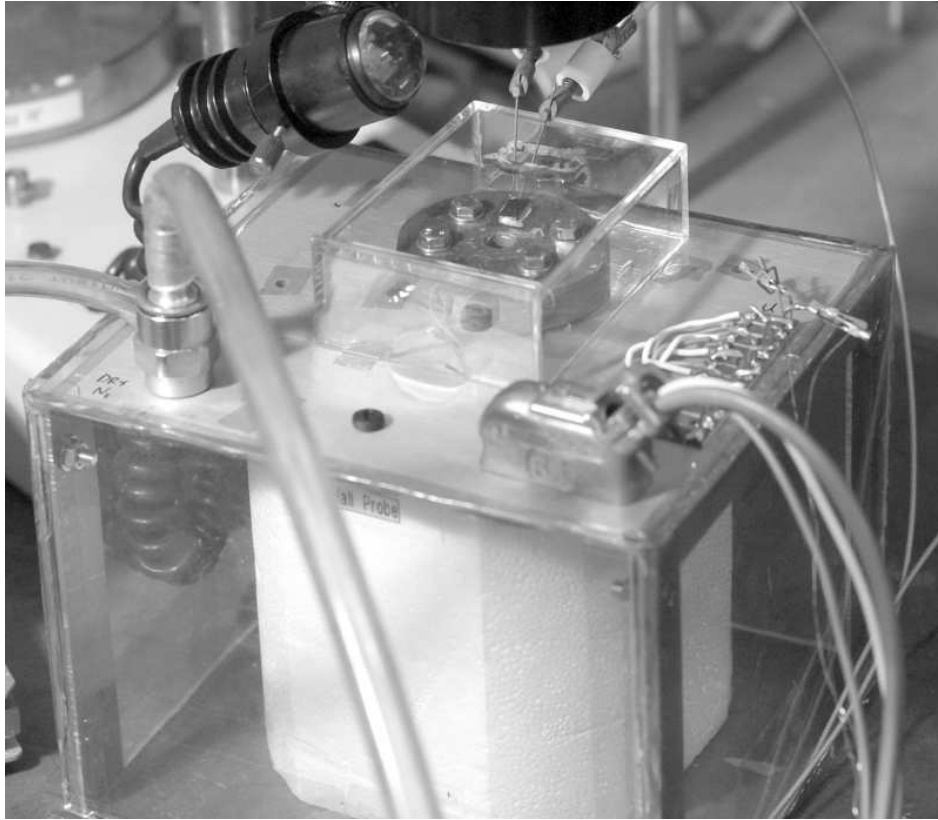


Figure 3.10: Schematic of cryogenic stage. Scale bars are accurate to within 10 %.

(a)



(b)

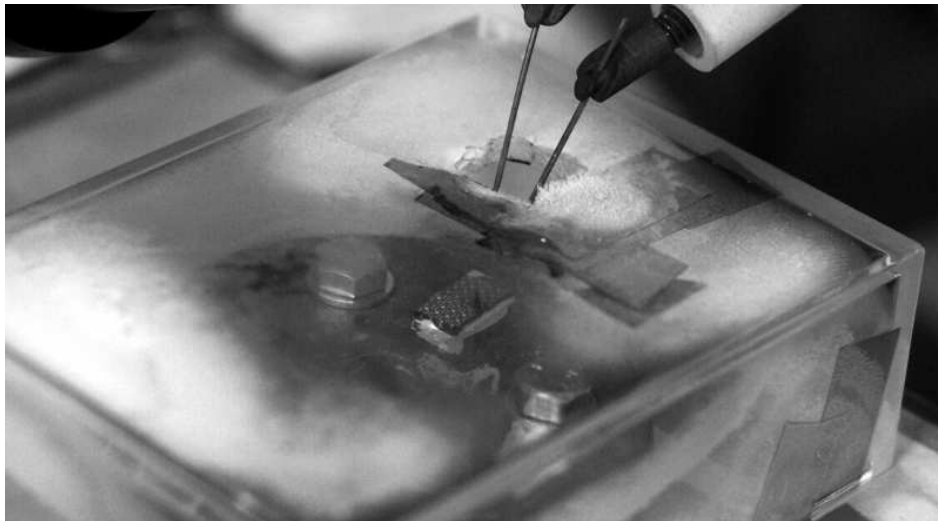


Figure 3.11: (a) Photograph of cryogenic stage, showing all components. (b) Close-up photograph of cryogenic stage under low-temperature operation. Moisture has condensed around the exterior of the enclosure, but the sample space remains free of ice due to the slight positive pressure of dry N_2 . Two micropositioner tips are visible in (a) and (b).

3.3.1 Temperature control

Addition of liquid N₂ into the bucket would cause rapid cooling to the base temperature of ~ 110 K within a few minutes. A full bucket would start to boil off after 5-10 minutes, so this was the maximum time the sample stage could be stabilised at base temperature without adding extra liquid N₂ through the PVC tube. When adding liquid N₂ in this way, some mechanical disturbance of the micropositioner tips was almost inevitable.

After cooling to base temperature, it was possible to maintain a temperature ramp from 110-400 K, at a rate of 5 ± 1 K min⁻¹ or greater, by supplying a current to the strip heater around the sample stage. Liquid N₂ would boil off during this process and tend to increase the rate of heating, but the Lakeshore PID controller was able to automatically compensate for this by reducing heater power. Stabilisation within ~ 1 K for $\sim 3 - 10$ mins was also possible, using the strip heater and the PID controller.

3.4 Software

Both control and data-processing software were written in Labview (v9f3, National Instruments) for Microsoft Windows.

A bespoke binary file format with the extension .ect was developed for storage of data. An unlimited number of .ect-format files could be stored in a single master file. Each individual file could contain an unlimited number of data curves, and could also be ‘stamped’ with singular pieces of information, such as the measurement type, the date, the sample name or a physical quantity such as temperature or bias field. By storing *multiple* measurement files in a *single* master file, it was straightforward to apply identical mathematical operations on all measurements in the master file consecutively, without prompting. This saved a great deal of time at the data-processing stage, particularly with large datasets of $P(E)$ loops that were used to estimate isothermal electrocaloric ΔS via the Maxwell relation $(\partial P/\partial T)_E = (\partial S/\partial E)_T$.

3.4.1 Measurement control

The measurement software (Figure 3.12) used multithreading³ to isolate the subroutines responsible for interfacing with instruments, for file input/output, and for the user interface. Various measurement definitions were supported as ‘high-level’ threads. The purpose of the ‘high-level’ threads was to send commands to the ‘low-level’ threads which were in direct communication with instrumentation. Thus the ‘high-level’ threads associated with particular types of measurement were not directly concerned with interfacing to instrumentation, making debugging much easier and improving the scalability of the program. Figure 3.13 shows a screenshot of the measurement software running. The following instruments were supported, each in their own ‘low-level’ thread:

- Direct current and voltage sourcemeters (type 2400 and 2410, Keithley Instruments) via GPIB.

³In a single-threaded program, the subroutines run in *series* which means that if one part of the program encounters a delay, all the remaining parts of the program must wait for the problem to be resolved. In a multi-threaded program, the subroutines each run in their own individual ‘thread’, with available computing resources divided between the threads such that each functions independently of the others.

- PID temperature controller (type 336, Lakeshore Cryotronics) via TCP/IP. A pre-programmed series of temperature ramps could be uploaded, and optionally repeated in a loop until terminated by the user.
- Lock-in amplifier (type 7265, Amatek INC, 19312 Pennsylvania) via GPIB.
- Digital multimeter (type 196, Keithley Instruments) via GPIB.
- Heater current source (type ITC4, Oxford Instruments) via RS232.
- Digital-analogue and analogue-digital converter (type 3116, Keithley Instruments) via USB.
- K-type thermocouple reader (type 3216, Eurotherm LTD, RH10 9SJ UK) via RS232.
- Impedance analyser (type 4294A, Agilent Technologies INC, 95051 California) via GPIB.
- Ferroelectric tester (type Precision Premier II, Radiant Technologies) by interfacing with Radiant ‘Vision’ software⁴.

⁴The manufacturer of the Precision Premier II have provided no meaningful programmatic control of this instrument. To work around this, Vision would be configured to write data to a text file, and the present measurement software would query the computer file system to see if this text file had appeared. When the query was raised, the measurement software would interpret the file to recover the data from the Radiant, and then delete the file, to prevent it being read multiple times by accident. Programmatic triggering of Vision measurements was possible by programmatically simulating mouse clicks.

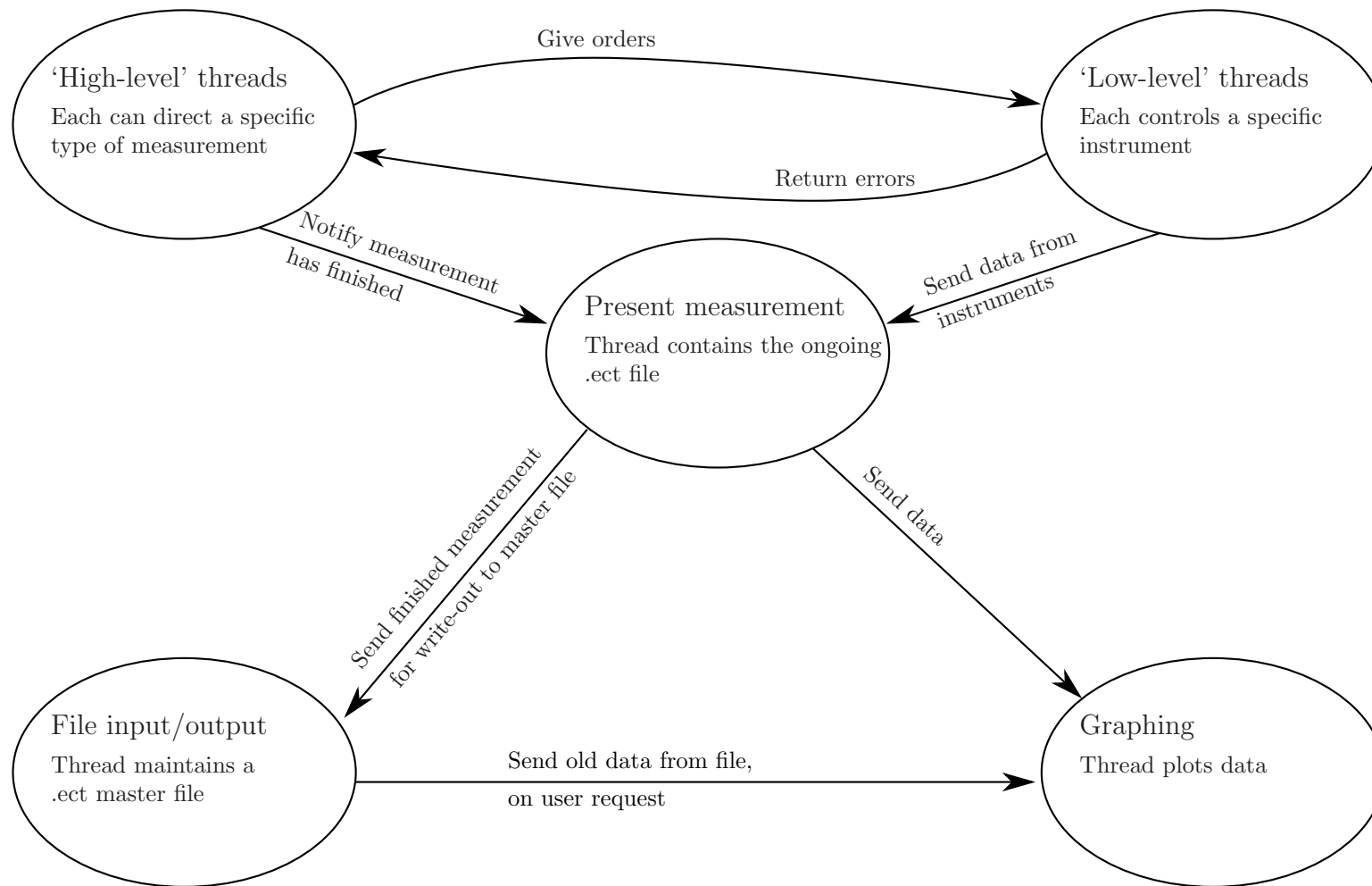


Figure 3.12: Schematic of measurement software showing the multithreaded design.

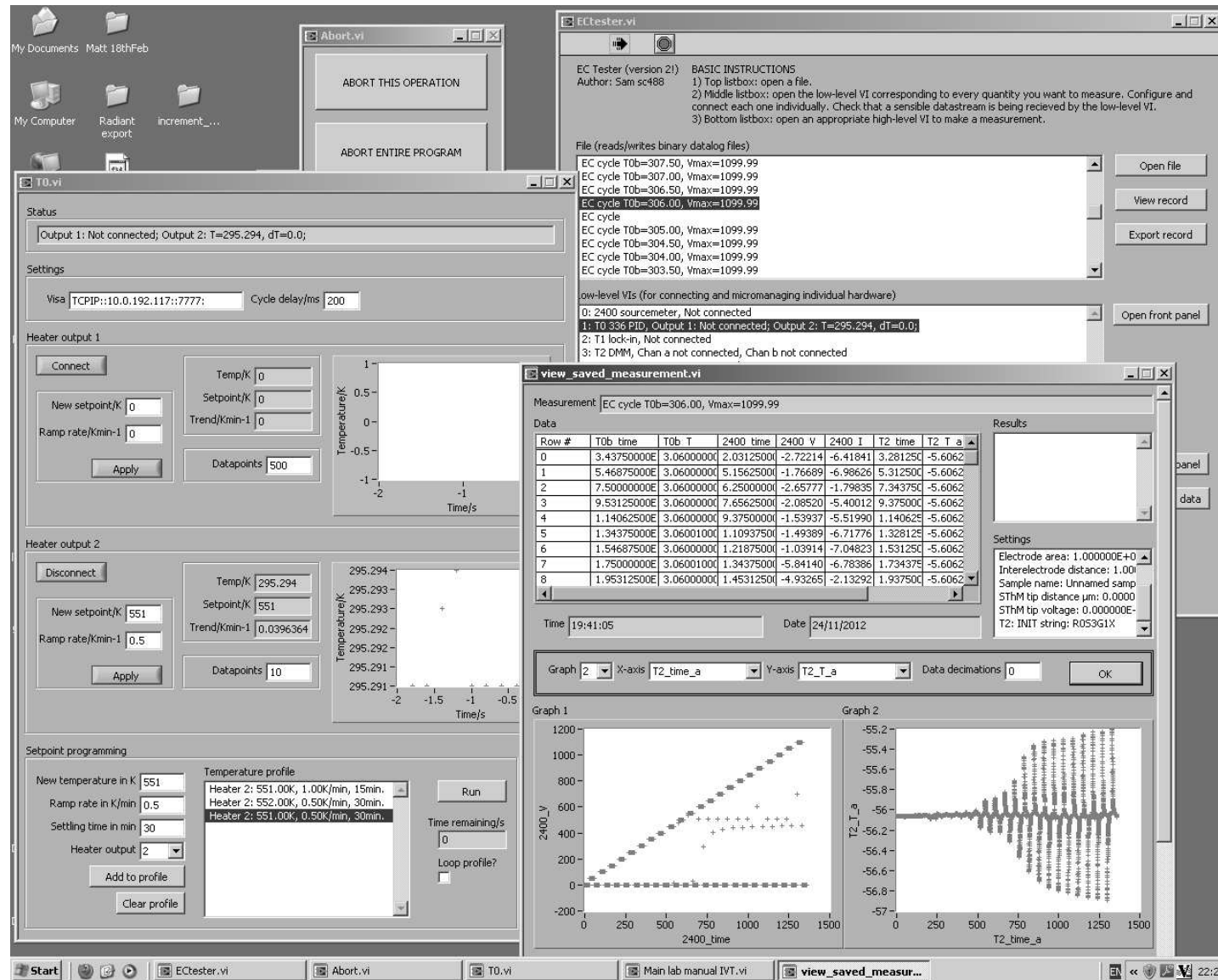


Figure 3.13: Screenshot of measurement software running.

3.4.2 Data processing

Data processing software was written to read .ect master files directly, avoiding the need for time-consuming interpretation of ASCII text files. Measurements from multiple files could be concatenated, merged, and have spurious sections removed with a few mouse-clicks. The data processing capabilities included:

- All mathematical functions that appear on standard scientific calculators.
- Normalisation of data, i.e. subtraction of the mean value.
- Statistical operations on data arrays, such as taking the average value, n^{th} value, standard deviation, etc.
- Interpolation of data arrays, e.g. to synchronise arbitrary $P(E)$ datasets so that the E values are identical, for later transposition to $P(T)$.
- Smoothing of data arrays by fitting a cubic spline to the data. The number of nodes was adjusted by eye to achieve the desired balance between smoothness and fidelity.
- Numerical differentiation and integration.

Use was made of standard Labview mathematical functions and algorithms. A large $P(E)$ dataset of several hundred loops could be processed into an estimate for electrocaloric isothermal entropy change via the Maxwell relation $(\partial P/\partial T)_E = (\partial S/\partial E)_T$, within five to ten minutes, depending on the speed of the computer.

Chapter 4

Electrocaloric effects in inorganic salts

Single crystals of $(\text{NH}_4)_2\text{SO}_4$, KNO_3 and NaNO_2 were obtained. This Chapter begins with a discussion of the large zero-field ΔS often seen in order-disorder ferroelectrics such as these. Electrical and electrocaloric measurements on each material will then be described consecutively.

Isothermal electrocaloric entropy change ΔS is a factor in the amount of isothermal heat $Q \sim T_C \Delta S$ that could be pumped by an electrocaloric cycle. Although Q is of greater practical interest than ΔS , it is ΔS that has been quoted more in literature, particularly since the publication of the paper of Neese *et al.* (2008) whose key result was that ΔS for 1 μm -thick PVDF-TrFE was $\sim 55 \text{ J K}^{-1} \text{ kg}^{-1}$ [21] — far higher than the corresponding value for 350 nm-thick Zr-rich PZT of $\sim 8 \text{ J K}^{-1} \text{ kg}^{-1}$ [20], despite the corresponding adiabatic temperature change for both materials being similar at $\Delta T \sim 12 \text{ K}$. It was later noted that these two systems showed less disparate values of volume-normalised entropy change: $62 \text{ J K}^{-1} \text{ dm}^{-3}$ and $106 \text{ J K}^{-1} \text{ dm}^{-3}$ respectively [54]. Nonetheless, these examples demonstrate that a large value of ΔS is no guarantee of a large value of ΔT for a given driving field. Accurate interconversion between the two is only possible by mapping entropy in the relevant section of $E - T$ space, as described in Section 2.5. As entropy is not a measurable quantity, such a map can only be constructed indirectly.

Many of the most entropic ferroelectric phase transitions occur in systems with order-disorder transitions, often inorganic salts. Some examples (along with some

common displacive ferroelectrics) are tabulated in Table 4.1, which is adapted primarily from Scott [39]. Table 4.1 contains zero-field entropy changes normalised by mole, by mass and by volume. Normalisation by mole can be convenient for discussing transition mechanisms because each ordering event has an associated entropy per mole of $-R \ln \Omega$ (the Boltzmann formula for entropy), where R is the molar gas constant and Ω is the number of states of the formula unit that become thermally randomised.

Normalisations by mass and by volume are more relevant when considering cooling applications. The inverse right-hand side of the Clausius-Clapeyron equation has also been evaluated in Table 4.1. This quantity approximates, the size of the electric field which would be required to drive the paraelectric-ferroelectric transition.

At $17.6 \text{ J K}^{-1} \text{ mol}^{-1}$, $(\text{NH}_4)_2\text{SO}_4$ (ammonium sulphate) shows the largest molar entropy change, near its 223 K transition. Normalising by mass or by volume, this entropy change becomes $133.2 \text{ J K}^{-1} \text{ kg}^{-1}$ or $235.7 \text{ J K}^{-1} \text{ dm}^{-3}$ respectively, which is still larger than all the other values in Table 4.1 except the 98 K transition of HCl ($\Delta S = 367 \text{ J K}^{-1} \text{ kg}^{-1}$ or $514 \text{ J K}^{-1} \text{ dm}^{-3}$). However, NaNO_2 ($\Delta S = 76.8 \text{ J K}^{-1} \text{ kg}^{-1}$ or $170.0 \text{ J K}^{-1} \text{ dm}^{-3}$) shows the second largest mass-normalised, and largest volume-normalised zero-field transition heat¹ $Q \sim T_C \Delta S$, due to its large Curie temperature of 433 K. Another factor favouring NaNO_2 is its larger spontaneous polarisation, granting it a relatively small value of $dE/dT = \Delta S/P_S = 21.25 \text{ [kV cm}^{-1}] \text{ K}^{-1}$, implying that the transition might be driven more readily with lower fields.

Other notable materials from Table 4.1 include KNO_3 ($\Delta S = 53.4 \text{ J K}^{-1} \text{ kg}^{-1}$ or $112.7 \text{ J K}^{-1} \text{ dm}^{-3}$) and NH_4HSO_4 ($\Delta S = 67.8 \text{ J K}^{-1} \text{ kg}^{-1}$ or $117.2 \text{ J K}^{-1} \text{ dm}^{-3}$). The latter is one of the few inorganic salts to have been investigated for electrocaloric effects, but it was found to be unpromising due to large ionic conductivity in the sample studied [77].

As predictors of electrocaloric performance, the data in Table 4.1 are indirect and incomplete. For example, electrocaloric materials must support large driving fields without breaking down or transmitting too much leakage current. The purpose of the present work was to obtain data with special relevance to electrocalorics on some of these materials.

¹Zero-field Q is approximately equal to zero-field $T_C \Delta S$ as all transitions occur, to some extent, over a finite range of T .

Material (family)	Formula	$ \Delta S $ (J K ⁻¹ mol ⁻¹)	$ \Delta S $ (J K ⁻¹ kg ⁻¹)	ϱ (kg dm ⁻³)	$ \Delta S $ (J K ⁻¹ dm ⁻³)	T_C (K)	Q (kJ kg ⁻¹)	Q (kJ dm ⁻³)	P_S (μC cm ⁻²)	$ \Delta S /P_S$ (kV cm ⁻¹ K ⁻¹)
Barium titanate (perovskite)	BaTiO ₃	0.60	2.6	6.1	15.7	393	1	6.2	26	0.6
Potassium niobate	KNbO ₃	0.28	1.6	4.59	7.14	435	0.7	3.1	30	0.24
Potassium nitrate	KNO ₃	5.4	53.4	2.11	112.7	401	21.4	45	8.1	13.9
Cadmium niobium oxide (pyrochlore)	Cd ₂ Nb ₂ O ₇	0.43	0.8	6.24	5.13	185	0.15	0.95	5.5	0.93
Antimony sulphoiodide	SbSI	0.87	3.1	5.19	16	295	0.9	4.7	25	0.64
Potassium dihydrogen phosphate	KH ₂ PO ₄	4.01	29.5	2.34	69	123	3.6	8.5	5	13.8
Triglycine sulphate	(NH ₂ CH ₂ COOH) ₃ ·H ₂ SO ₄	2.31	7.15	1.69	12	323	2.3	3.9	2.8	4.3
Ammonium sulphate	(NH ₄) ₂ SO ₄	17.6	133.2	1.77 [97]	235.7	223	29.7	52.6	0.62	380.2
Ammonium hydrogen sulphate	(NH ₄)HSO ₄	7.8	67.8	1.73	117.2	270	18.3	31.6	0.8	146.6
Sodium trihydroselenite	NaH ₃ (SeO ₃) ₂	4.1	14.6	3.20	46.87	194	2.8	9.1	3	15.6
Rochelle salt	KNaC ₄ H ₄ O ₆ ·4H ₂ O	0.034	0.12	1.83	0.22	296	0.03	0.07	0.025	8.8
Sodium nitrite	NaNO ₂	5.3 [75]	76.8	2.16	170.0	433 [98]	33.3	73.6	8	21.25
Methylammonium aluminium alum	CH ₆ AlNO ₈ S ₂ ·12H ₂ O	9.7	20.8	1.59	33	174	3.6	5.7	1	33
Hydrogen chloride	HCl	13.4 [71]	367	1.4 [71]	514	98 [72]	36	50.4	1.2 [72]	428

Table 4.1: Properties of selected ferroelectric phase transitions, where ΔS is the zero-field entropy change for the entire transition (measured via e.g. differential scanning calorimetry), ϱ is density, T_C is Curie temperature, $Q \sim T_C \Delta S$ is zero-field transition heat and P_S is spontaneous polarisation. Except where stated otherwise, data are adapted from the compilation of Scott [39].

4.1 $(\text{NH}_4)_2\text{SO}_4$

Ammonium sulphate $[(\text{NH}_4)_2\text{SO}_4]$ is a common inorganic salt which has mass-market application as a fertiliser for agriculture. German and Japanese studies from the 1930s observed a calorimetric anomaly near 223 K [99,100]. Shomate (1944) conducted the first accurate determination of the zero-field entropy change ΔS ($16.7 \text{ J K}^{-1} \text{ mol}^{-1}$) [101]. In 1956, Matthias and Remeika [102] reported that the low-temperature phase was a uniaxial ferroelectric with $P_S = 0.25 \text{ } \mu\text{C cm}^{-2}$. A more detailed study by Hoshino *et al.* in 1958 gave revised values of P_S ($0.45 \text{ } \mu\text{C cm}^{-2}$) and zero-field ΔS ($17.6 \text{ J K}^{-1} \text{ mol}^{-1}$), and also measured $\varepsilon'(T)$, revealing a relatively low peak value of $\varepsilon' \sim 165$ at T_C with a Curie-Weiss constant of several 10s of K. Unruh (1970) revised P_S to $0.62 \text{ } \mu\text{C cm}^{-2}$ by measuring pyroelectric charge², and further revealed that P_S *decreases* as the temperature is reduced from $\sim (T_C - 10) \text{ K}$, taking a negative value below $\sim 80 \text{ K}$ [103]. This observation (carefully confirmed by Sawada *et al.* [104]) led to the hypothesis by Unruh and Rudiger [105] that the low-temperature phase of $(\text{NH}_4)_2\text{SO}_4$ is ferrielectric. This was confirmed by the observation of faint triple $P(E)$ loops just below T_C by Sawada *et al.* in 1980 [106]. A notably detailed calorimetric study also took place in the 1980s, by Higashigaki and Chihara [107] (albeit on a deuterated sample, but the deuteration was shown to make little difference) who reported that $\sim 40 \%$ of the zero-field entropy change occurs at a single temperature, with the remainder evolving continuously over a few 10s of K below T_C .

The process of reconciling the complex phenomenology of $(\text{NH}_4)_2\text{SO}_4$ with structural and spectroscopic measurements began well before the discovery of ferrielectricity in 1970. The first X-ray study was in 1916 [108]. The room-temperature structure is orthorhombic with $a = 7.782 \text{ } \text{\AA}$, $b = 10.636 \text{ } \text{\AA}$ and $c = 5.993 \text{ } \text{\AA}$, and space group $Pnam$ (Figure 4.1). The crystal structure below 223 K is orthorhombic with $a = 7.837 \text{ } \text{\AA}$, $b = 10.610 \text{ } \text{\AA}$ and $c = 5.967 \text{ } \text{\AA}$ and space group $Pna2_1$ with the polar axis in the c -direction. In the ferroelectric phase the two ammonium groups are not in equivalent positions. Schlemper and Hamilton (1966) suggested a displacive mechanism based on hydrogen bonding [109], but this proved inconsistent with NMR experiments of O'Reilly and Tsang that indicated an order-disorder transition involving all three ionic groups in the molecular formula [110]. O'Reilly and Tsang pointed out that a triple-ion order-disorder model has an entropy change $3R \ln 2 = 17.2 \text{ J K}^{-1} \text{ mol}^{-1}$, in good agreement with experimental values. Around this time, $(\text{NH}_4)_2\text{SO}_4$ was also considered

²High coercive fields precluded $P(E)$ data at temperatures lower than a few 10s of K below T_C .

in the framework of improper ferroelectricity³ due to the anomalously small Curie-Weiss constant [111, 112].

³Ferroelectrics in which the order parameter of the transition is not P .

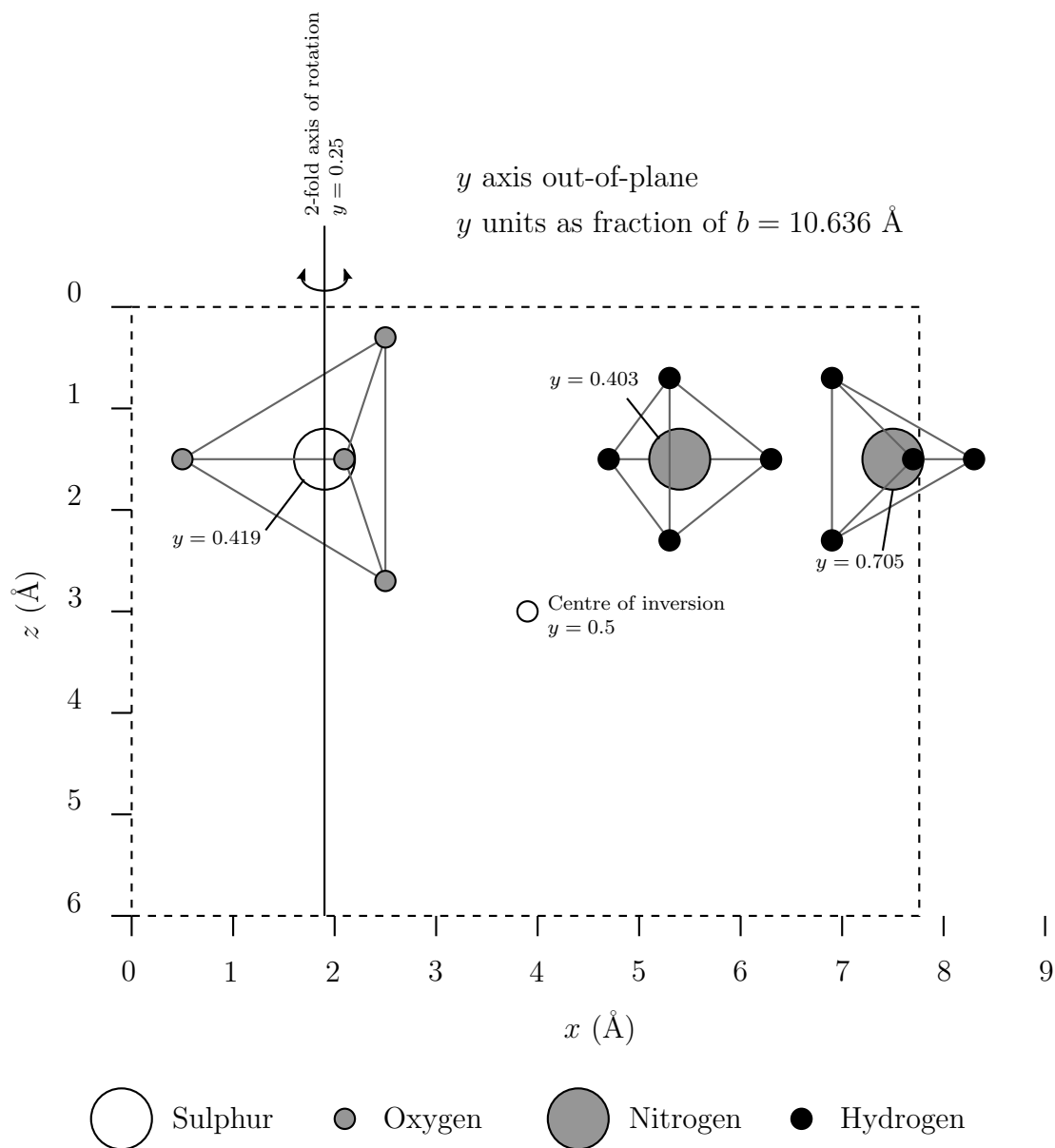


Figure 4.1: Room-temperature paraelectric $(\text{NH}_4)_2\text{SO}_4$ has an orthorhombic cell (dotted line) with $a = 7.782 \text{ \AA}$, $b = 10.636 \text{ \AA}$ and $c = 5.993 \text{ \AA}$. One of the four formula units per unit cell is shown. The remaining formula units follow via symmetry operations of the space group $Pnam$ (a subset of these operations is shown). The sulphate is centred at $(0.244, 0.419, 0.250)$ [fractional coordinates], ammonium A (left) at $(0.6895, 0.4025, 0.250)$ and ammonium B (right) at $(0.9677, 0.7050, 0.250)$ [109]. The in-plane displacements of the tetrahedral H and O species inform the out-of-plane displacements. The c -direction becomes polar on cooling below $\sim 223 \text{ K}$.

After the discovery of ferrielectricity the focus shifted to two-sublattice models [104,105]. Dvorak and Ishibashi [113] gave a modified Landau free-energy expansion for such a system:

$$\begin{aligned}
G = & \frac{1}{2}a_1P_1^2 + \frac{1}{4}b_1P_1^4 + \frac{1}{6}c_1P_1^6 \\
& + \frac{1}{2}a_2P_2^2 \\
& + \gamma_1P_1P_2 + \gamma_2P_1^3P_2 \\
& - EP
\end{aligned} \tag{4.1}$$

where the subscripts ‘1’ and ‘2’ refer to the first and second sublattices and γ_1 and γ_2 are inter-sublattice coupling constants. Thus sublattice 1 is assumed to drive the transition, and as a result, high-order terms in P_2 are not required, and only the a_1 Landau coefficient has a temperature dependence. Such a free energy was qualitatively consistent with the small Curie-Weiss constant and negative value of P_S observed at low temperatures [103]. In an alternative treatment by Onodera, the two sublattices were each given separate order parameters [114,115].

Disagreements in the literature persist to the present day. In the 1980s, some argued that an instability of the sulphate group was responsible for driving the phase transition [116,117], whereas others were in favour of a more passive role for the sulphate group [104,118–121]. For example, a 1988 study by Kozlov *et al.* found spectroscopic evidence supportive of both models, and was unable to reach a firm conclusion [122]. In the 1990s De Sousa Meneses argued that one of the two competing components of polarisation has an order-disorder mechanism, and the other displacive [123], with the order-disorder component driving the transition and involving all three ionic groups. Thus the excellent agreement with between the entropy of a triple-ion disordering via the Boltzmann formula, and the experimental zero-field entropy change, first noted by O’Reilly and Tsang in the 1960s [110], is preserved in the De Sousa Meneses model.

The electrocaloric properties of $(\text{NH}_4)_2\text{SO}_4$ have not been studied, and predicting them is not straightforward as the ferroelectric properties of this material are complex and still not fully understood. Summarising what is known:

- The molar zero-field entropy change of the phase transition at 223 K is $17.6 \text{ J K}^{-1} \text{ mol}^{-1}$ [124], the largest of any known ferroelectric material. However

only $\sim 40\%$ of this occurs at a single temperature [107], the remainder being evolved continuously over a few 10s of K below T_C . The large zero-field ΔS is consistent with disorder of all three ionic groups, by the Boltzmann formula [110].

- The material is ferrielectric and has a complex phase transition whose order parameter is strongly coupled to P_S . Many mechanisms have been suggested without any clear consensus emerging.

4.1.1 Crystal growth

Growth of $(\text{NH}_4)_2\text{SO}_4$ single crystals was performed by Thirumurugan Alagarsamy in the group of Anthony K. Cheetham (Materials Science, University of Cambridge). Crystals were grown at room temperature in H_2O with precursors of sulphuric acid ($> 95\%$) and ammonium hydroxide (aq. 35%). Crystals were of mixed morphologies, with some thin and rod-like, and others plate-like. Crystals were up to ~ 1.5 mm thick in the polar c -direction of interest.

4.1.2 Device preparation

An eleven-step process was used to fabricate capacitors of $(\text{NH}_4)_2\text{SO}_4$ with thicknesses in the tens of μm range, from the bulk single crystals (Figure 4.2).

- i A large uncut single crystal was picked out and indexed with a parallel-beam X-ray diffractometer (type D8 Advance, Bruker) by holding 2θ at 29.56° , the value for the 004 Bragg reflection, and rotating the crystal until a signal was observed.
- ii A plane normal to the c -axis was flattened out by dry polishing. This polishing used 1200 grade sandpaper (type 734, 3M) to remove significant amounts of material, then 4000 grade sandpaper (type P4000, Buehler) to achieve a smooth, shiny finish. During this process, the sample was normally superglued to a glass slide to ensure that the resulting polished surface was flat. The superglue was removed with acetone, which did not attack the $(\text{NH}_4)_2\text{SO}_4$ as H_2O would have done.
- iii A ~ 70 nm-thick layer of platinum was deposited onto the flattened face of the sample using an automated commercial sputter deposition system (type K575, Emitech) with a sputter current of ~ 40 mA.
- iv A substrate was prepared by cutting a thin slab of copper metal with dimensions approx 1 cm x 1 cm by 1 mm. One surface was covered with electrically insulating kapton tape, and a smear of silver epoxy adhesive (type 186-3616, Radiospares) was added. The viscosity of the silver epoxy was adjusted by adding variable amounts of isopropanol.
- v The sample was placed on the substrate, platinised surface facing down. The substrate was heated to $\sim 100^\circ\text{C}$ to cure the silver epoxy and permanently join the sample with the substrate.

- vi Because the cured silver epoxy had far superior adhesive properties than ordinary silver dag, it was now possible to polish down the (001) face of the crystal without the crystal detaching from the substrate. Polishing followed the same process as for the first face, except that this time great care was required not to overpolish and destroy the crystal. Despite frequent checking for cracks in an optical microscope, it was very difficult to judge when a sample was near breaking point, and many samples ($\sim 50\%$) did not make it to stage vii.
- vii An improvised deposition mask for the top electrode was formed from the top lid of an ordinary laboratory membrane storage box (type AGG3319, Agar Scientific). The storage box was dismantled with a power drill in such a way as to form a free-standing membrane of thick clingfilm in a rigid plastic frame. The frame would ensure that the membrane was held taut against the top of the sample, which was important to achieve a sharply-defined edge for the electrode. The clingfilm membrane was pierced with a hot stainless-steel sewing needle to form a neat hole in the centre with typical dimensions of 0.5 mm x 0.5 mm (in practice, several sample boxes were often wasted before a suitable hole could be made in this way). The purpose of using small electrodes was to ensure that the largest possible fields could be applied with the smallest chance of breakdown. Unlike opaque metallic masks, this mask was transparent and could be accurately positioned over the sample, to ensure that there would be significant clearance between the edge of the top electrode and the edge of the crystal.
- viii Platinum was again sputtered, through the improvised membrane-mask, to form the top electrode. The sample was annealed at $\sim 100^\circ\text{C}$, as is standard practice after the deposition of platinum electrodes.
- ix A thin copper wire was attached to the top electrode using silver epoxy, which was then cured at $\sim 100^\circ\text{C}$. This step was delicate due to the small wire and small top electrode, and the need to prevent silver epoxy from leaking over the edge of the top electrode. The top electrode was to be the high-voltage electrode, with the bottom electrode at ground.
- x The as-prepared sample would be ready for testing, but the tendency for arcing and breakdown could be dramatically reduced by coating both the sample surface, and the end of the high-voltage wire, with electrically resistive vacuum grease. A suitable grease (type N, Apiezon) was liberally applied around the top of the sample.

xi To achieve a smooth continuous coating of grease, the substrate was heated again to ~ 100 °C. This caused the grease to become liquid and coat the entire surface of the sample uniformly. Thus the high-voltage electrode was entirely encased in electrically resistive grease.

The thickness of the $(\text{NH}_4)_2\text{SO}_4$ films, and the area of each top electrode, were measured in an optical microscope (type Optiphot, Nikon) with a computer interface. Because the $(\text{NH}_4)_2\text{SO}_4$ crystals were transparent with a finely polished upper surface, it was possible to focus on both the lower and upper surfaces by moving the sample stage of the microscope up and down. Thus the thickness of the samples could be deduced by reading off the travel involved, and multiplying it by the 1.53 refractive index of $(\text{NH}_4)_2\text{SO}_4$ [125] (Figure 4.3a). For the electrode area calculation, an image of the entire top electrode could be taken in the microscope, and an irregular polygon drawn around the electrode in a vector graphics program (Inkscape, open-source software) [Figure 4.3b].

After the samples were prepared and their geometries measured, they were mounted in probe head 2 (Section 3.1) for electrical measurements at cryogenic temperatures.

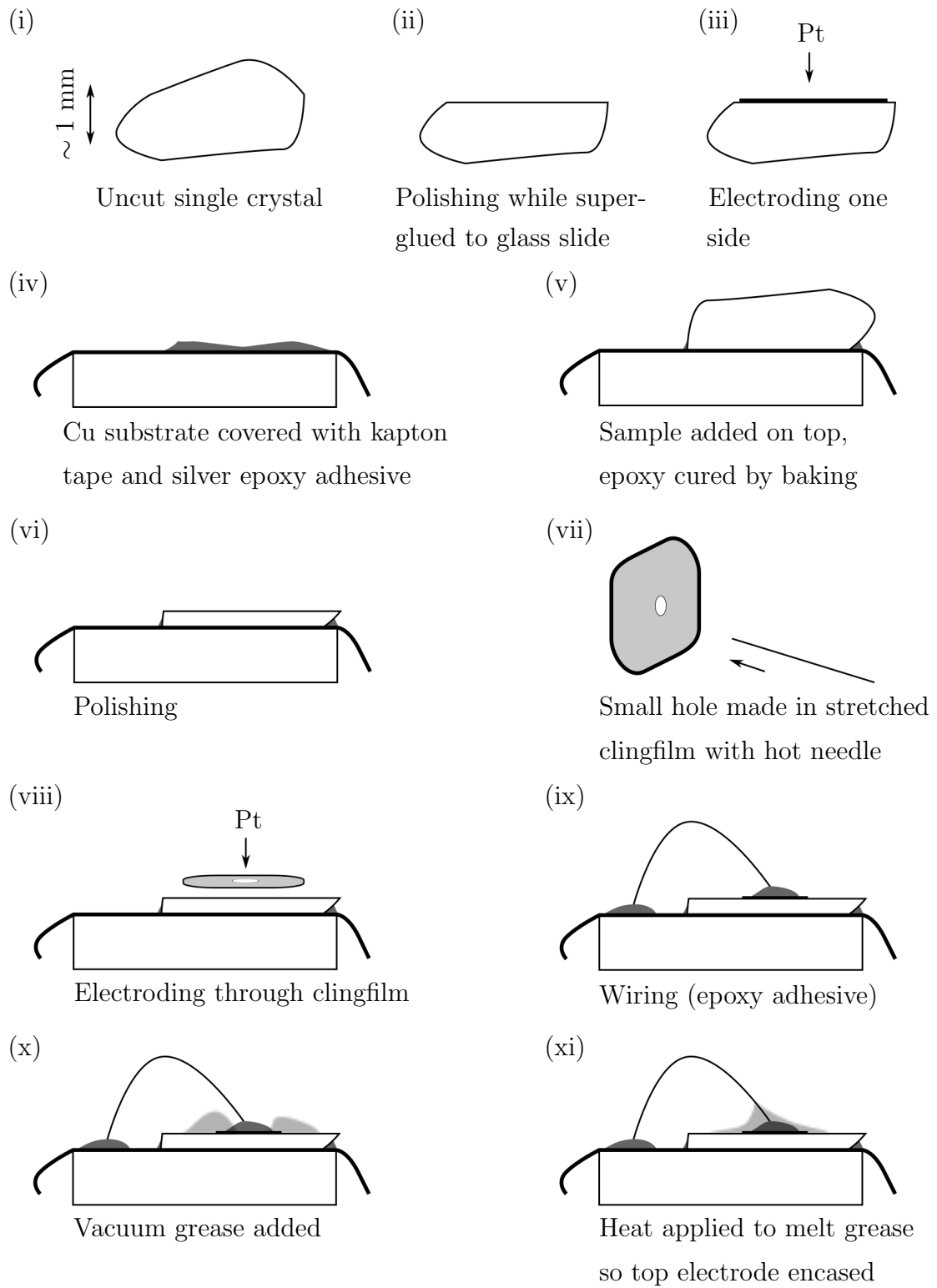


Figure 4.2: Procedure for thinning of $(\text{NH}_4)_2\text{SO}_4$ crystals to obtain devices with thicknesses in the 10s of μm range.

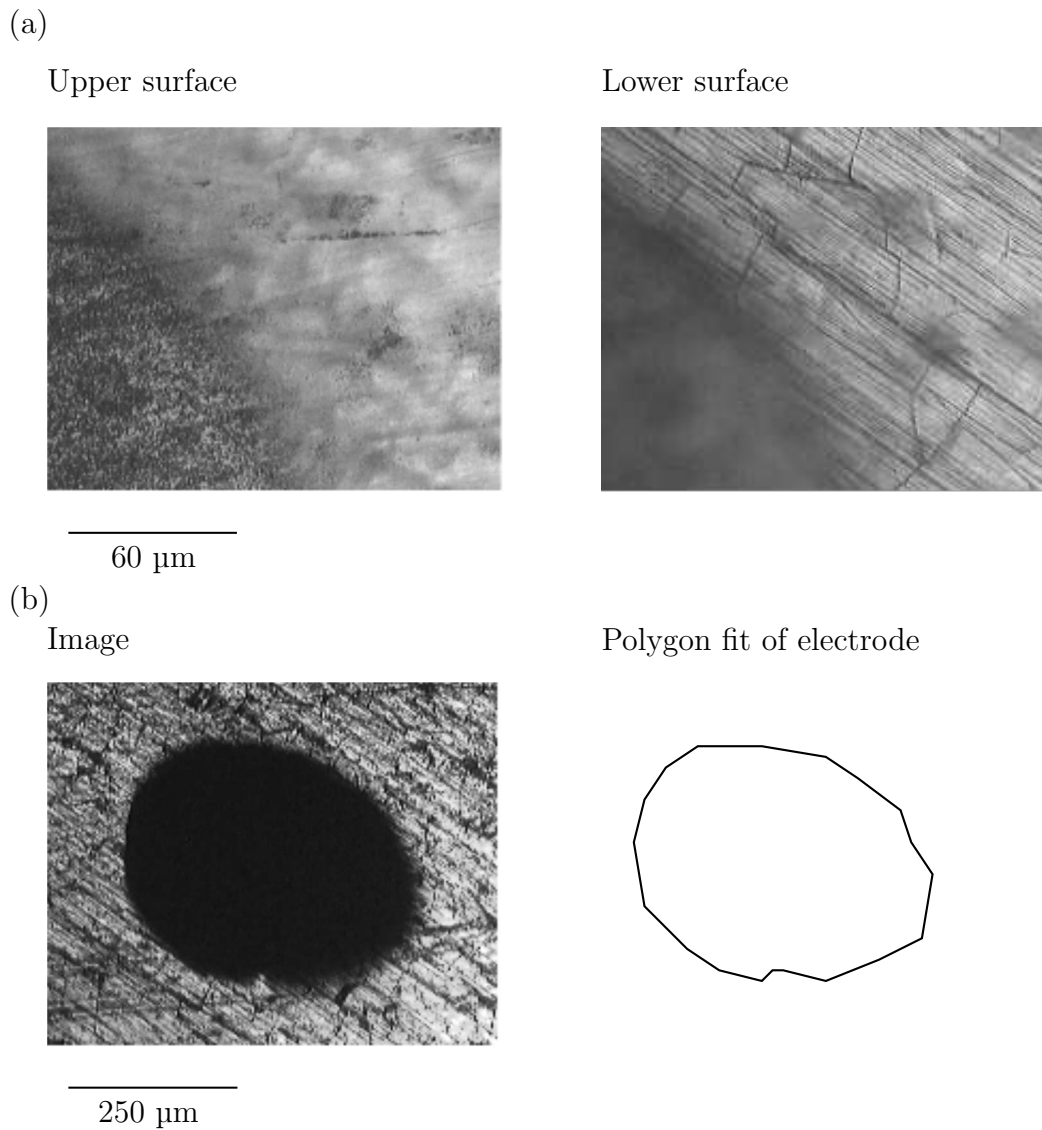


Figure 4.3: **(a)** Measuring thickness of a mounted, transparent crystal of $(\text{NH}_4)_2\text{SO}_4$. The focal plane of a microscope was used as a reference point and moved between the upper and lower surfaces. The travel distance between the two images, multiplied by the refractive index of the crystal, was equal to the crystal thickness. These images show part of the top electrode in the lower left corners. **(b)** Measuring the area of the top electrode of the same $(\text{NH}_4)_2\text{SO}_4$ crystal. An irregular polygon (right) was drawn around the image of the electrode (left), and its area was computed by an algorithm built into the Inkscape vector graphics editor. A polarising filter was used to obtain this image, in order to reduce the reflectivity of the platinum top electrode to zero and thus enhance contrast.

Data are presented on three samples, A, B and C. Crystal A was 50 μm thick and had an electrode area of 0.47 mm^2 . Crystal B was 53 μm thick and had an electrode area of 42.5 mm^2 . Crystal C was 37 μm -thick and had an electrode area of 0.45 mm^2 .

4.1.3 Dielectric constant

Figure 4.4a shows the dielectric constant of Crystal A as a function of temperature at 1 kHz, using the equivalent parallel capacitance model (Section 2.2). The temperature was ramped down then up at $\pm 0.2 \text{ K min}^{-1}$. The data showed a peak at $T_C = 220.5 \text{ K}$. This peak was asymmetric, decaying faster above the transition than below it, as also observed by Hoshino *et al.* [124]. However the highest value of $\varepsilon' \sim 75$ was lower than the corresponding value of Hoshino *et al.* (~ 150). A thermal hysteresis of $\sim 2 \text{ K}$ between heating and cooling was apparent. The Curie-Weiss constant above T_C on heating (ignoring the non-linear region immediately above T_C) was ~ 67 (Figure 4.4b), which is larger than the literature value of ~ 26 . However the present value was very approximate as the impedance measurement was very close to the noise level above T_C . Dielectric losses were unmeasurably small above the transition temperature, and ~ 0.05 just below the transition, rising to ~ 0.2 as temperature was reduced to 200 K (Figure 4.4c).

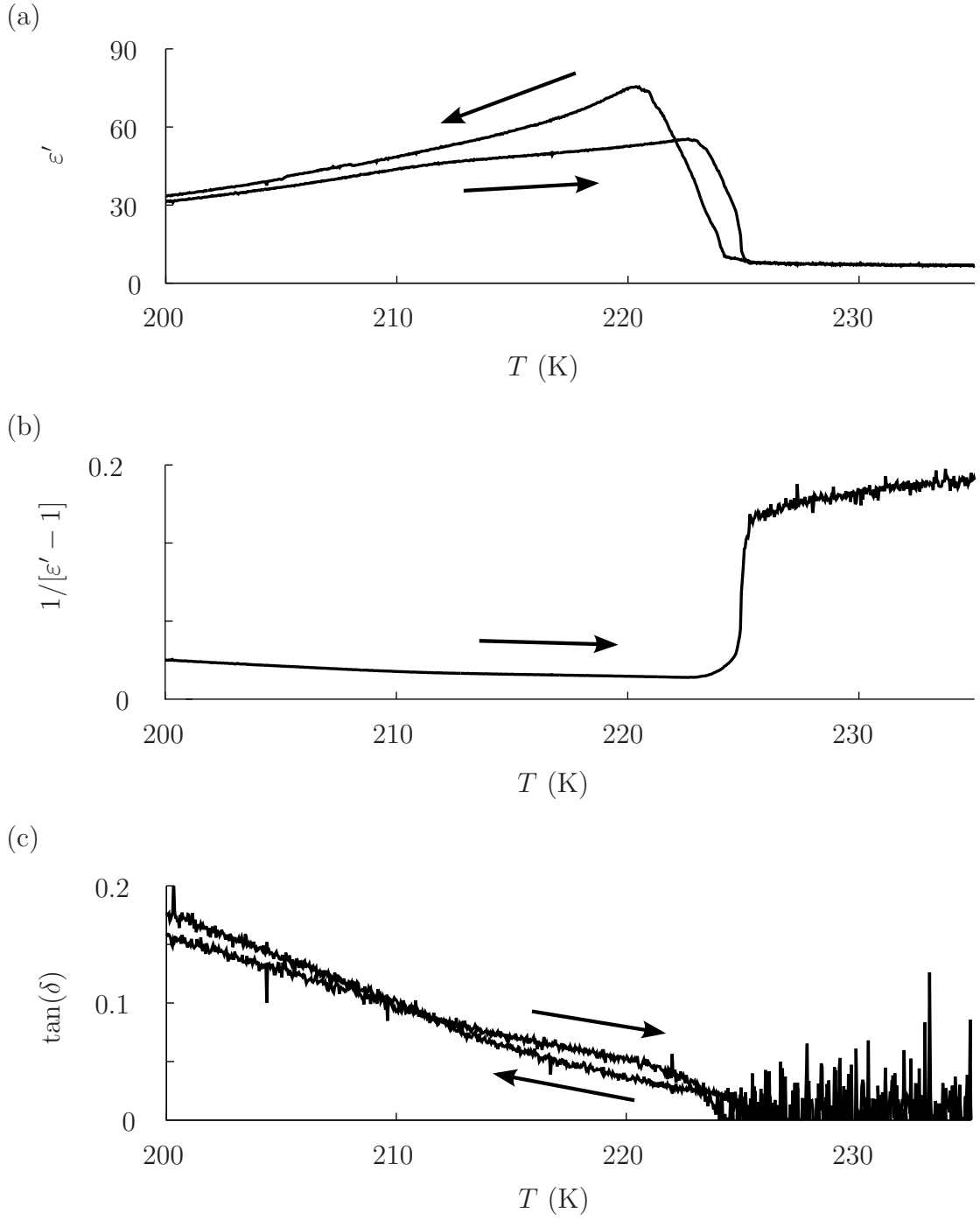


Figure 4.4: Dielectric data derived from an impedance dataset for $(\text{NH}_4)_2\text{SO}_4$ Crystal A. The amplitude and frequency of the driving field were 1 V RMS and 1 kHz respectively. A known parasitic capacitance of 1.8 pF was subtracted from the measured equivalent parallel capacitance, which was ~ 2.2 pF at high temperatures. Data for heating and cooling are indicated by arrows. The magnitude of the thermal ramp rate was $\sim 0.2 \text{ K min}^{-1}$. **(a)** Dielectric constant, **(b)** reciprocal dielectric susceptibility, and **(c)** loss tangent, as functions of temperature.

4.1.4 Zero-field ΔS

Heat-flow vs temperature measurements were performed on heating and cooling an uncut 9.429 mg single crystal of $(\text{NH}_4)_2\text{SO}_4$ at $\pm 2 \text{ K min}^{-1}$ as described in Section 2.5. Measurements were performed by Robert Cornell. Figure 4.5a shows specific heat capacity as evaluated from raw data, which contained an offset in heat flow between heating and cooling. The specific heat capacity was therefore estimated by forcing c_E on heating and cooling to be equal at 233 K, giving an offset of $928 \text{ J K}^{-1} \text{ kg}^{-1}$, which was added to the heating curve and subtracting from the cooling curve (Figure 4.5b-c). The specific heat capacity above the transition temperature was $\sim 1000 \text{ J K}^{-1} \text{ kg}^{-1}$, slightly smaller than the $\sim 1250 \text{ J K}^{-1} \text{ kg}^{-1}$ value measured by Hoshino *et al.* [124]. Due to latent heat, the specific heat capacity showed a very large peak value of $\sim 20000 \text{ J K}^{-1} \text{ kg}^{-1}$ at the transition temperature (Figure 4.5c). The entropy change in the immediate vicinity of the transition was $\sim 50 \text{ J K}^{-1} \text{ kg}^{-1}$ (Figure 4.5d), and the specific heat capacity did not return to the high-temperature value below T_C , indicating that transitional entropy was still evolved in this temperature range. These observations were both in agreement with the data of Higashigaki on $(\text{ND}_4)_2\text{SO}_4$, which showed that of the $133 \text{ J K}^{-1} \text{ kg}^{-1}$ zero-field entropy change associated with the transition, around 40 % (i.e. $53.2 \text{ J K}^{-1} \text{ kg}^{-1}$) occurs at a single temperature, and that the remainder evolves over a few 10s of K below T_C [107].

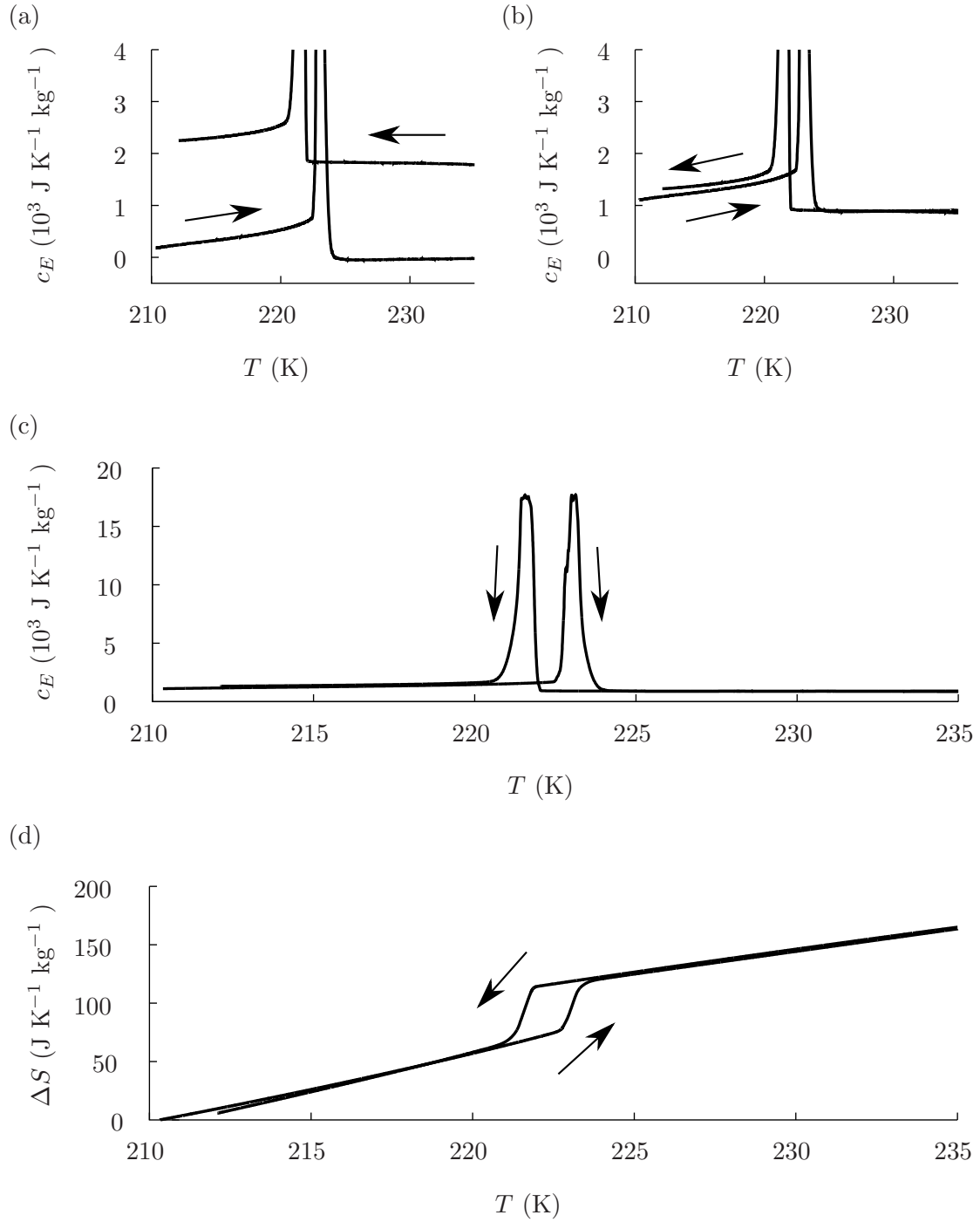


Figure 4.5: Calorimetry results for $(\text{NH}_4)_2\text{SO}_4$ taken on heating and cooling at $\pm 2 \text{ K min}^{-1}$. **(a)** Specific heat capacity c_E for $(\text{NH}_4)_2\text{SO}_4$ evaluated from raw heat flow data, which contained an offset between heating and cooling data. **(b)** Specific heat capacity with offset averaged out. In (a) and (b), the y -axis has been cropped to better show the values away from T_C . **(c)** Specific heat capacity with offset averaged out, showing full height of peak at T_C . **(d)** Zero-field $\Delta S(T)$ with respect to the initial entropy at 210 K. Derived from the specific heat capacity plot with offset averaged out.

4.1.5 $P(E)$ loops

Due to the small dielectric constant of $(\text{NH}_4)_2\text{SO}_4$, the intrinsic linear parasitic capacitance of the ceramic-insulated wiring of the probe was large in comparison with that of the samples. For experiments on Crystal B, this parasitic contribution was subtracted, leading to noisy data. For Crystal C, a superior wiring configuration permitted the high-voltage line to be used only for applying the driving voltage, and one of the coaxial lines to be used for the signal-return wire from the sample. This configuration was only employed for one sample because it presented the danger that if a sample were to break down, the expensive coaxial return line would be exposed to high voltages, causing damage. The probe chassis was carefully grounded to eliminate AC pickup.

Figures 4.6a-e show $P(E)$ loops at selected temperatures taken on Crystal B, with a driving frequency of 10 Hz and a field amplitude of 380 kV cm^{-1} . The equivalent parallel resistivity ϱ was extracted from the $P(E)$ loops using the method described in Section 2.3, and was found to have an almost constant value of $\sim 0.33 \text{ G}\Omega \text{ m}$ throughout the temperature range (Figure 4.6f). For each temperature in Figure 4.6, both raw and compensated data are shown. The compensated data had the spurious contribution from ϱ subtracted (ϱ was conservatively set at $0.4 \text{ G}\Omega \text{ m}$ for all loops). Major (switching) and minor (non-switching) loops are shown. The major $P(E)$ loops from below $T_C \sim 223 \text{ K}$ appeared very slim because the coercive field of $\sim 10 \text{ kV cm}^{-1}$ was small in comparison with the driving field amplitude of 380 kV cm^{-1} . The major and minor loops below T_C featured high-field discontinuities in dP/dE at around $\pm 200 \text{ kV cm}^{-1}$ which combined with the main loop at the origin to form a ferrielectric triple loop (Figures 4.6a-b). In literature, only the 1980 paper of Sawada *et al.* reported a ferrielectric triple loop in $(\text{NH}_4)_2\text{SO}_4$ [106]. In that study, the triple loops were observed at 60 Hz, measured at 11 kV cm^{-1} , within a narrow 10 mK window below the Curie temperature. In contrast, the triple loops here were observed at 10 Hz, measured at 380 kV cm^{-1} , over a broad range of temperatures.

The high-field discontinuities in dP/dE observed in Crystal B persisted in a near-identical form *above the transition temperature*, even after the main ferroelectric loop had vanished (Figures 4.6c-e and 4.7). Double loops corresponding to a field-induced phase transition are commonly observed just above first-order transitions, but these double loops are different, as they persisted below T_C , and did not evolve with temperature as expected for a field-induced transition obeying the Clausius-Clapeyron

equation. This observation may be of interest for future discussions of the transition mechanism.

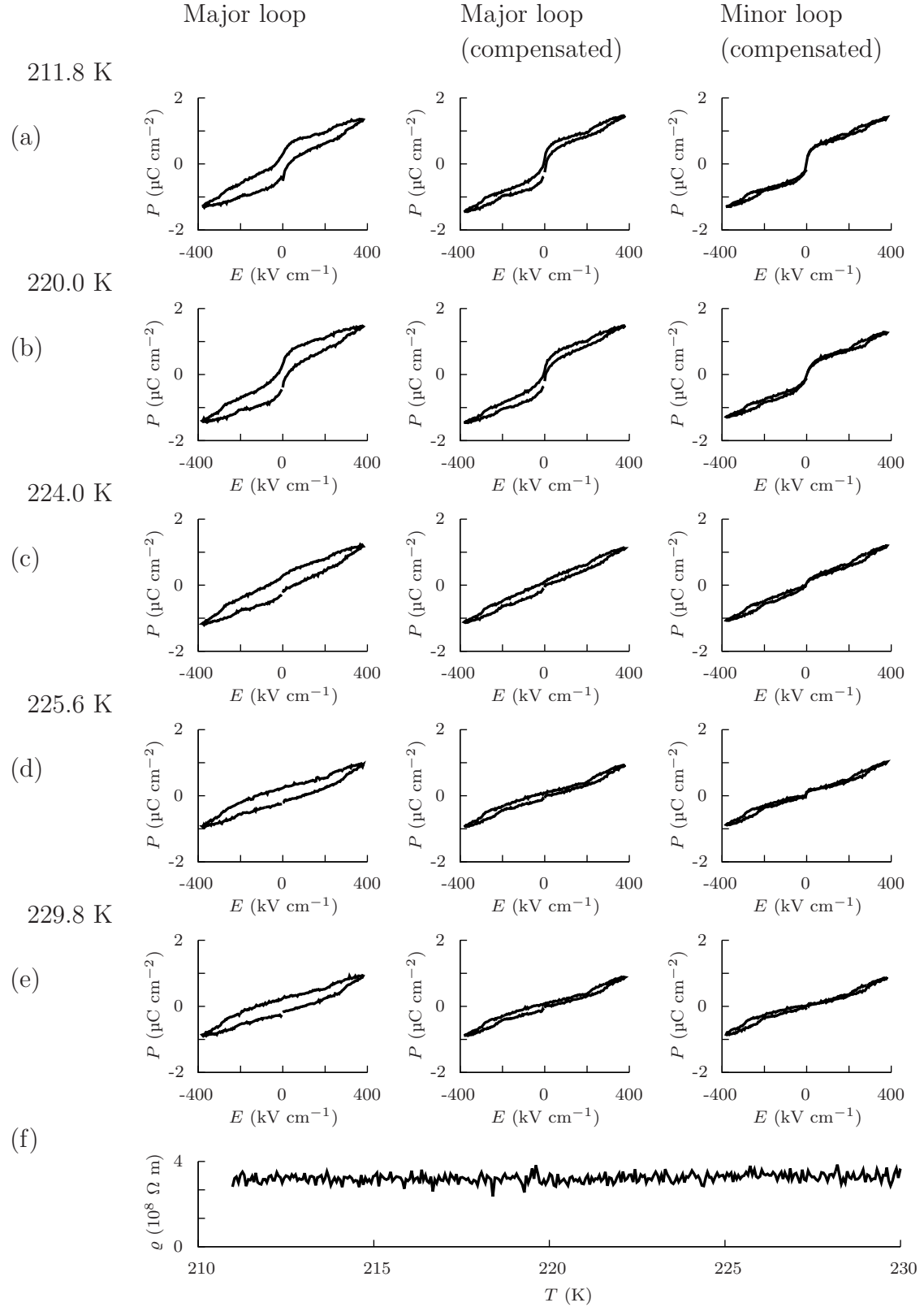


Figure 4.6: **(a)-(e)** $P(E)$ loops at 10 Hz for $(\text{NH}_4)_2\text{SO}_4$ Crystal B. Major (switching), and minor (non-switching) loops are shown. For the major loop, raw data is shown, in addition to data compensated for an equivalent parallel resistivity of $0.4 \text{ G}\Omega \text{ m}$. **(f)** Equivalent parallel resistivity ρ extracted from the $P(E)$ measurement.

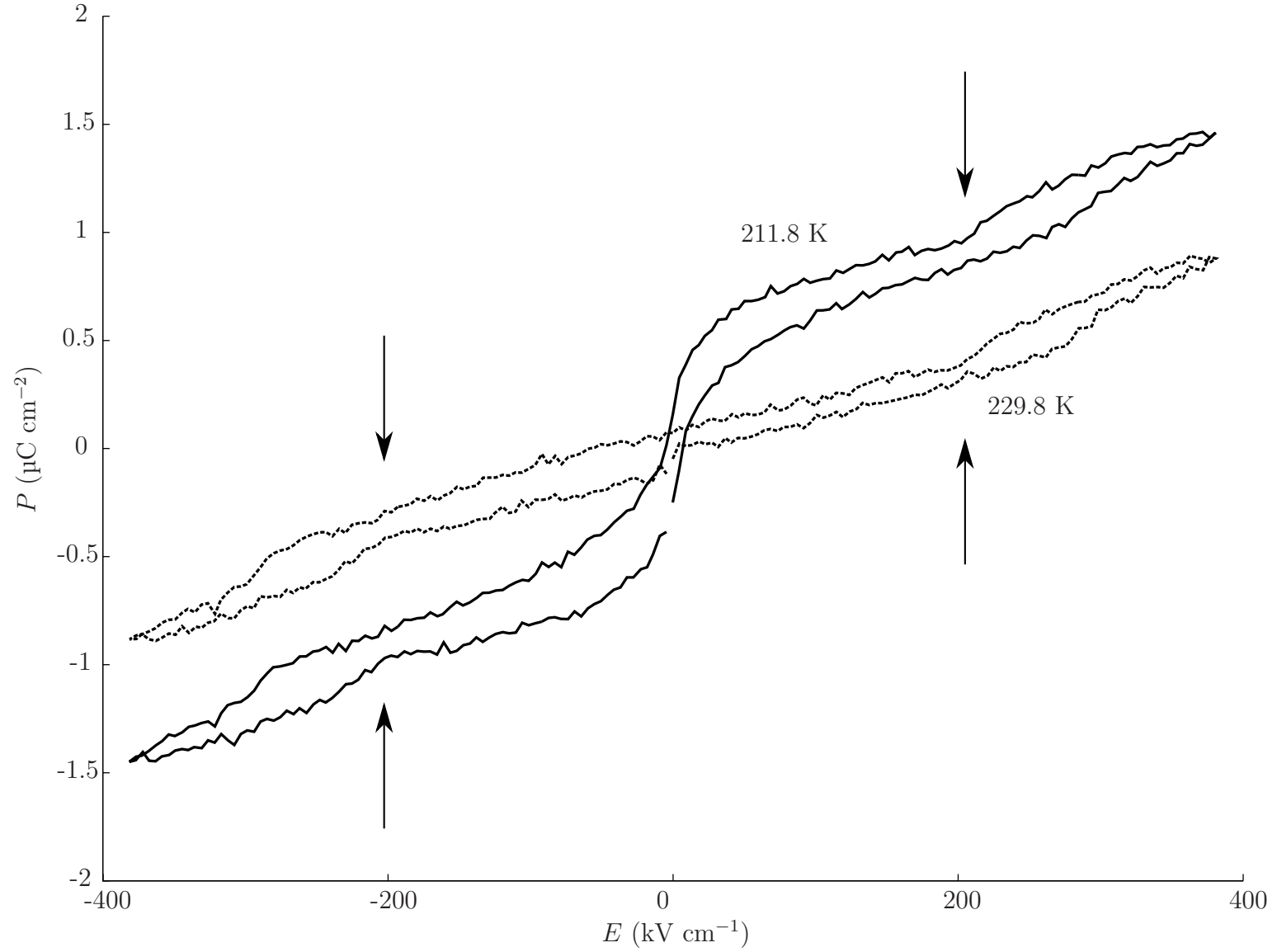


Figure 4.7: Major, compensated $P(E)$ loops at 10 Hz for $(\text{NH}_4)_2\text{SO}_4$ Crystal B, at 211.8 K and 229.8 K. High-field discontinuities in dP/dE are indicated with arrows. Data reproduced from Figure 4.6 panels (a) and (e).

Figures 4.8a-d show $P(E)$ loops at various temperatures for Crystal C with a driving frequency of 10 Hz and a field amplitude of 400 kV cm^{-1} . No parasitic resistivity could be measured here. Ferroelectric $P(E)$ loops were observed below $T_C = 223 \text{ K}$, and linear paraelectric behaviour above T_C . Thus, the ferrielectric triple loops of Crystal B were not reproduced for Crystal C.

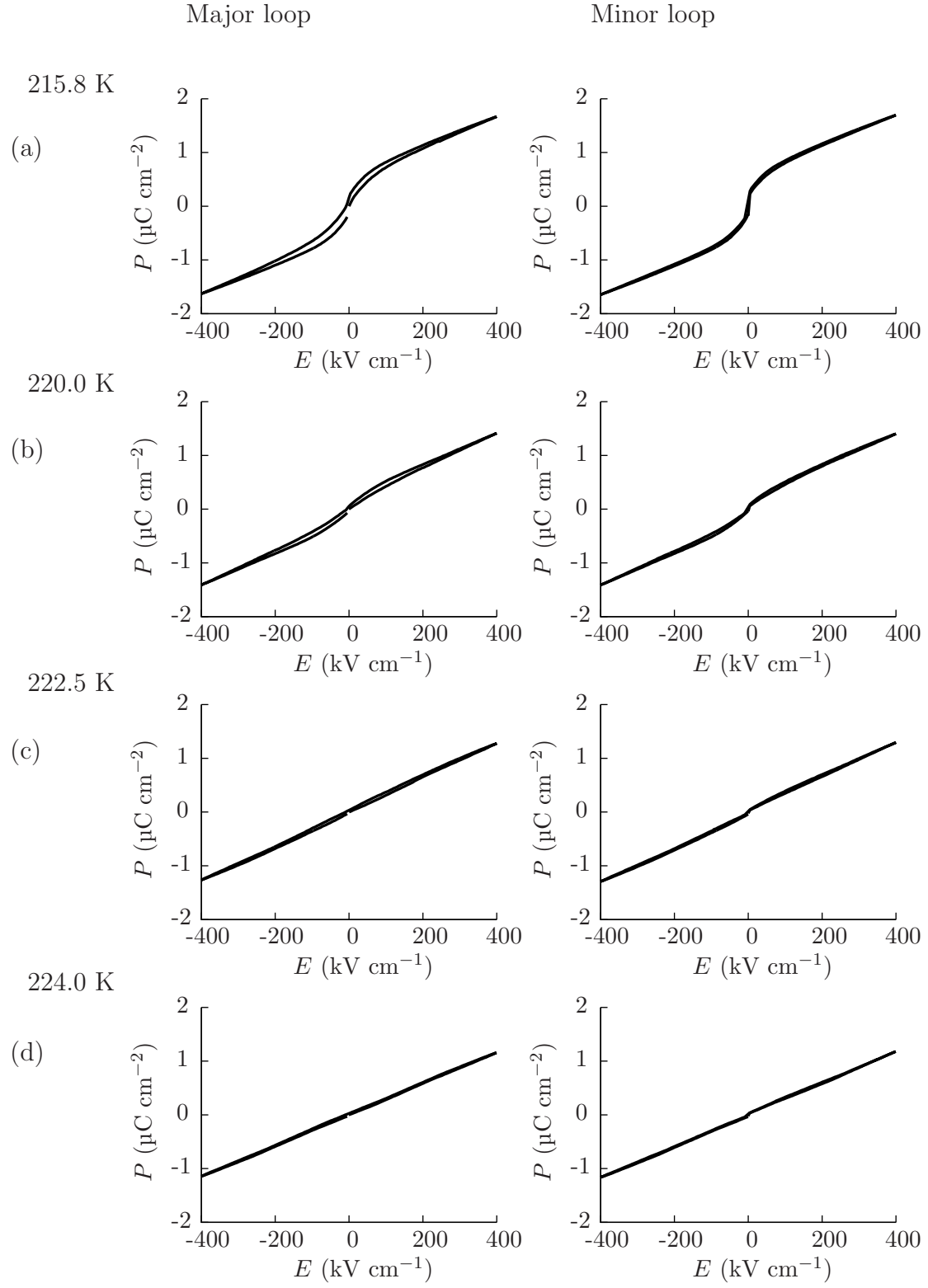


Figure 4.8: $P(E)$ loops at 10 Hz for $(\text{NH}_4)_2\text{SO}_4$ Crystal C, at various temperatures near $T_C = 223$ K. Major (switching), and minor (non-switching) loops are shown.

4.1.6 Isothermal $|\Delta S|$

The differences between the ‘standard’ and ‘resetting’ methods for accessing isothermal ΔS via $P(E)$ loops and the Maxwell relation $(\partial P/\partial T)_E = (\partial S/\partial E)_T$ have been described in detail in Section 2.4. In the ‘standard’ method, $P(E)$ loops are obtained sequentially during a temperature ramp, whereas for the ‘resetting’ method, temperature is ‘reset’ to well above the transition temperature, in between each successive loop. To summarise what was written in Section 2.4, certain magnetocaloric materials with thermally hysteretic, entropic, first-order transitions cannot be characterised using the ‘standard’ method [92], as a spurious, large⁴, sharp and symmetric peak appears in isothermal ΔS at T_C . For such systems the ‘resetting’ method should be used, leading to a lower, broader peak that may decay gradually to zero above T_C . An analogous situation is expected for thermally hysteretic, entropic, first-order ferroelectric transitions, such as that of $(\text{NH}_4)_2\text{SO}_4$.

To evaluate isothermal ΔS via the ‘standard’ indirect method, major and minor $P(E)$ loops were obtained every ~ 15 s during temperature ramps at around ± 0.2 K min^{-1} . The minor loops were transposed to $P(T)$, and cubic splines were fitted to eliminate spurious fluctuations (Figure 4.9 [Crystal B] and Figures 4.11a-b [Crystal C]). The fitted splines were differentiated with respect to T , yielding $\partial P/\partial T$ at various fields E , which was numerically integrated to give volume-normalised and mass-normalised values of isothermal $|\Delta S|$ via the Maxwell relation $(\partial P/\partial T)_E = (\partial S/\partial E)_T$ and the literature value for density of 1770 kg m^{-3} [97] (Figure 4.10 [Crystal B] and Figures 4.11c-d [Crystal C]). Due to sample failure only data on heating were obtained for Crystal C.

A dataset was also obtained for Crystal C using the ‘resetting’ method (Figure 4.12). The resetting temperature was 228 K, and the crystal was cooled to the measurement temperature at -1 K min^{-1} . The thermodynamic analysis was performed on the initial branch of the loop only, as required by the ‘resetting’ method (Section 2.4).

Crystal B: ‘standard’ method

Figure 4.9 shows the $P(T)$ for Crystal B from transposing $P(E)$ data obtained via the ‘standard’ method, for selected fields only. Plots are shown for heating, cooling, applying a field (i.e. derived from the lower branch of the minor $P(E)$ loops) and removal of a field (from the upper branch of the minor loops). The raw data points and

⁴Often greater than the zero-field ΔS .

the spline fit are both shown. The plots suggested a transition region of $\sim 217 - 224$ K on cooling and $\sim 219 - 225$ K on heating. Figure 4.10 shows the corresponding values of isothermal $|\Delta S|$ as a function of temperature and field, again for heating, cooling, applying a field and removing a field. The plots in $E - T$ space are mirrored to show low-field behaviour more clearly. The plots show peaks in isothermal $|\Delta S|$ slightly above $T_C = 223$ K. The maximum isothermal $|\Delta S|$ on cooling ($\sim 28 \text{ J K}^{-1} \text{ kg}^{-1}$) was smaller than that on heating ($\sim 43 \text{ J K}^{-1} \text{ kg}^{-1}$), but for temperatures slightly below this peak both datasets showed a similar ‘shoulder’ feature ($\sim 20 - 25 \text{ J K}^{-1} \text{ kg}^{-1}$).

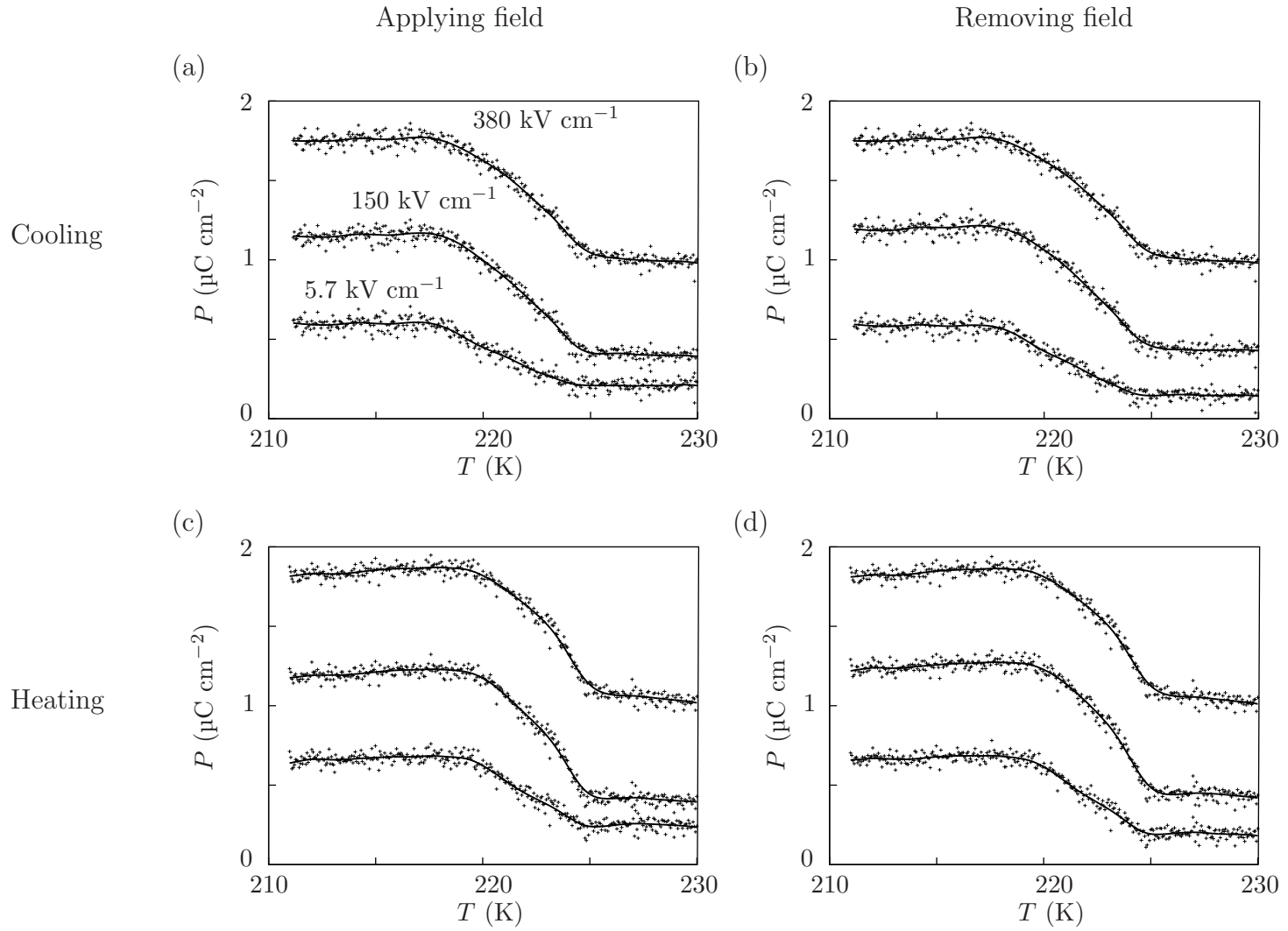


Figure 4.9: Selected $P(T)$ plots derived from $P(E)$ loops taken with the ‘standard’ method for $(\text{NH}_4)_2\text{SO}_4$ Crystal B. The four graphs correspond to applying and removing a field (i.e. lower and upper branches of the minor loops) on heating and cooling. The three plots of each graph correspond to 380 kV cm^{-1} (upper line), 150 kV cm^{-1} (middle line) and 5.7 kV cm^{-1} (lower line) as indicated in (a). Points: raw (measured) data, lines: cubic spline fit.

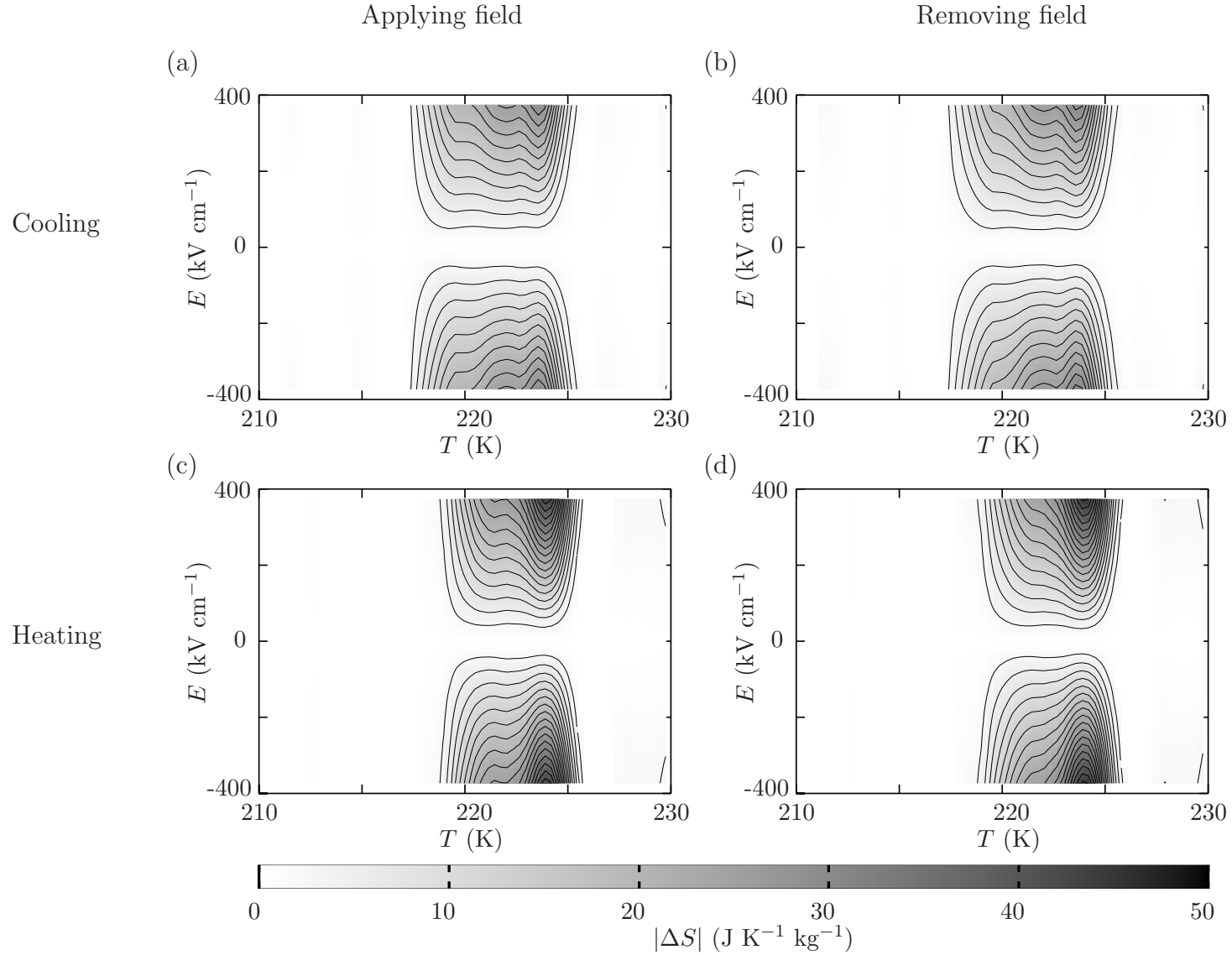


Figure 4.10: Isothermal $|\Delta S|$ for $(\text{NH}_4)_2\text{SO}_4$ Crystal B evaluated via ‘standard’ indirect method. The four graphs correspond to applying and removing a field (i.e. lower and upper branches of the minor loops) on heating and cooling. Data for negative E : ‘mirror image’ of those for positive E . Contour spacing: 2.5 $\text{J K}^{-1} \text{kg}^{-1}$.

Crystal C: ‘standard’ method

Figures 4.11a-b show the $P(T)$ for Crystal C from transposing $P(E)$ data obtained via the ‘standard’ method, for selected fields only, and for heating only. Figure 4.11a corresponds to applying a field and Figure 4.11b to removal of a field. The raw data points and the spline fit are both shown. The plots suggest a transition region of $\sim 215 - 224$ K which is broader than that observed for Crystal B (Figure 4.9). Figures 4.11c-d show the corresponding values of isothermal $|\Delta S|$ as a function of temperature and field. The plots show peaks in isothermal $|\Delta S|$ slightly above $T_C = 223$ K, as was also observed for Crystal B (Figure 4.10). However, the maximum isothermal $|\Delta S|$ (~ 22 J K $^{-1}$ kg $^{-1}$) was almost 50 % smaller than the corresponding value for Crystal B on heating (~ 43 J K $^{-1}$ kg $^{-1}$). The low-temperature ‘shoulder’ to the peak observed in Crystal B was observed again here, but the magnitude of isothermal $|\Delta S|$ was $\sim 10 - 15$ J K $^{-1}$ kg $^{-1}$ as opposed to $\sim 20 - 25$ J K $^{-1}$ kg $^{-1}$ for Crystal B.

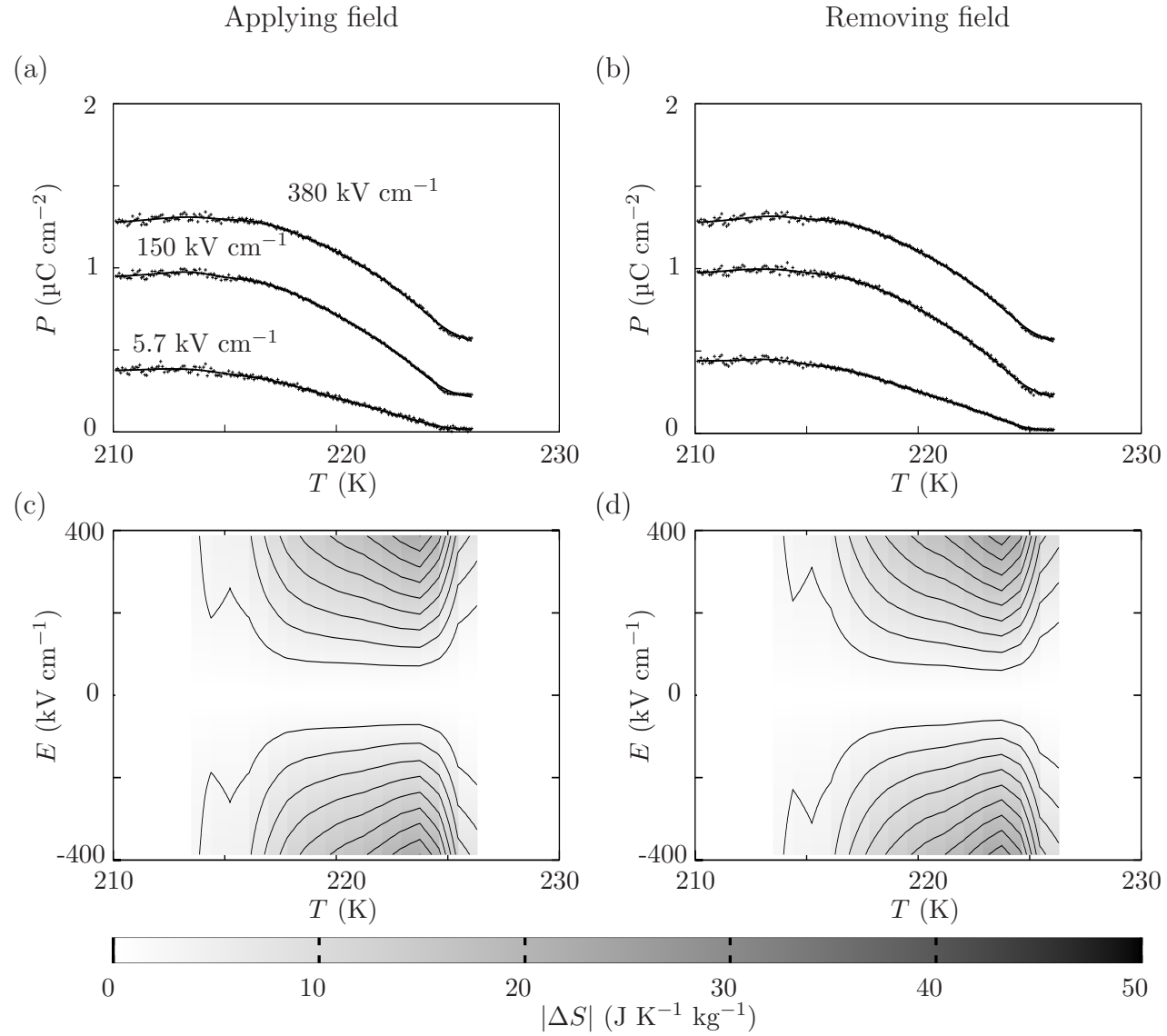


Figure 4.11: Plots for **(a)-(b)** selected $P(T)$ for applying and removing a field (i.e. lower and upper branches of the minor loops) and **(c)-(d)** isothermal $|\Delta S|$ for $(\text{NH}_4)_2\text{SO}_4$ Crystal C evaluated via the ‘standard’ indirect method for applying and removing a field. Data were taken on heating. **(a)-(b)** Points: raw (measured) data, lines: cubic spline fit. **(c)-(d)** Data for negative E : ‘mirror image’ of those for positive E . Contour spacing: $2.5 \text{ J K}^{-1} \text{ kg}^{-1}$.

Crystal C: ‘resetting’ method

Figure 4.12a shows the $P(T)$ for Crystal C from transposing $P(E)$ data obtained via the ‘resetting’ method, for selected fields only, and for cooling only. The raw data points and the spline fit are both shown. The plot suggests a transition region of at least $\sim 214 - 224$ K (the lower limit cannot be confirmed without $P(E)$ data for $T < 214$ K, which were not obtained). This range is slightly larger than that observed on Crystal C using the ‘standard’ method (Figures 4.11a-b) but broader than that observed for Crystal B (Figure 4.9). Figure 4.12b shows the corresponding values of isothermal $|\Delta S|$ as a function of temperature and field. The peak in isothermal $|\Delta S|$ slightly above $T_C = 223$ K that was previously observed in plots for the ‘standard’ method (Figure 4.10 and 4.11c-d), is almost absent here. Instead, isothermal $|\Delta S|$ is almost uniform from 214 K to 225 K, at $\sim 10 \text{ J K}^{-1} \text{ kg}^{-1}$.

Given that the ‘resetting’ dataset lacked the peak of isothermal $|\Delta S|$ at T_C that was present in all of the ‘standard’ datasets, and furthermore, given that the peak in the ‘standard’ datasets was large and sharp and thus qualitatively consistent with the spurious results from magnetocalorics measured with the ‘standard’ method, it may be concluded that the ‘resetting’ dataset is correct, and the ‘standard’ datasets at least partially spurious.

The plot for isothermal $|\Delta S|$ of Figure 4.12b in the region $222 < T < 225$ shows a slope in $E - T$ space that could represent the lower reach of the paraelectric-ferroelectric phase boundary. To investigate this on a preliminary basis, the gradient was read off approximately (as shown by the dotted line in Figure 4.12b), and found to be $dE/dT \sim 193 \text{ [kV cm}^{-1}] \text{ K}^{-1}$, which is in order-of-magnitude agreement with the Clausius-Clapeyron prediction of $dE/dT = \varrho |\Delta S| / P_S \sim 148$ (using $P_S = 0.62 \text{ } \mu\text{C cm}^{-2}$ [103], $\varrho = 1770 \text{ kg m}^{-3}$ [97] and $\Delta S = 50 \text{ J K}^{-1} \text{ kg}^{-1}$ [Figure 4.5]).

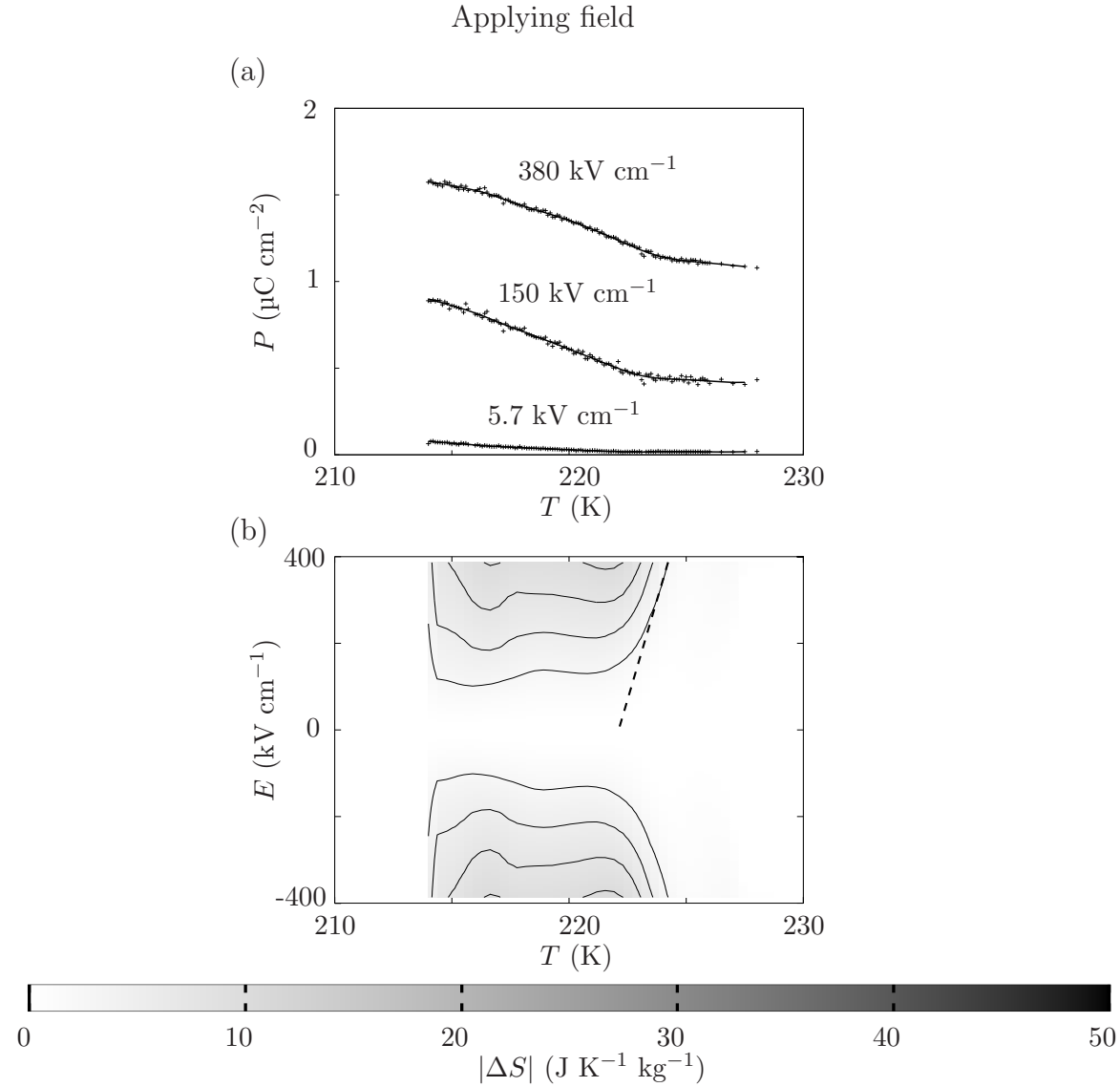


Figure 4.12: Plots for **(a)** selected $P(T)$ for applying a field (i.e. initial branch of the $P(E)$ loop) and **(b)** isothermal $|\Delta S|$ for $(\text{NH}_4)_2\text{SO}_4$ Crystal C evaluated via ‘resetting’ indirect method, for applying a field. Data were taken on cooling. Dotted line: slope in $E - T$ space used in main text discussion of Clausius-Clapeyron phase boundary. **(a)** Points: raw (measured) data, lines: cubic spline fit. **(b)** Data for negative E : ‘mirror image’ of those for positive E . Contour spacing: $2.5 \text{ J K}^{-1} \text{ kg}^{-1}$.

Comparison of the ‘standard’ and ‘resetting’ data

Figure 4.13 shows four plots — three via the ‘standard’ indirect method and one via the ‘resetting’ method — corresponding to isothermal $|\Delta S(T)|$ for the maximum field change of 380 kV cm^{-1} . These plots were compiled using the same datasets as previously shown in Figures 4.10-4.12. It is again apparent that, in the immediate vicinity of T_C , the ‘standard’ curves showed a large peak in $|\Delta S|$, but this peak was largely absent for the ‘resetting’ curve. However, the ‘standard’ datasets could nonetheless be valid in the temperature region $215 < T < 220 \text{ K}$, below the temperature of the main (spurious) peak, suggesting that isothermal entropy changes of $\sim 20 \text{ J K}^{-1} \text{ kg}^{-1}$ were driven in Crystal B.

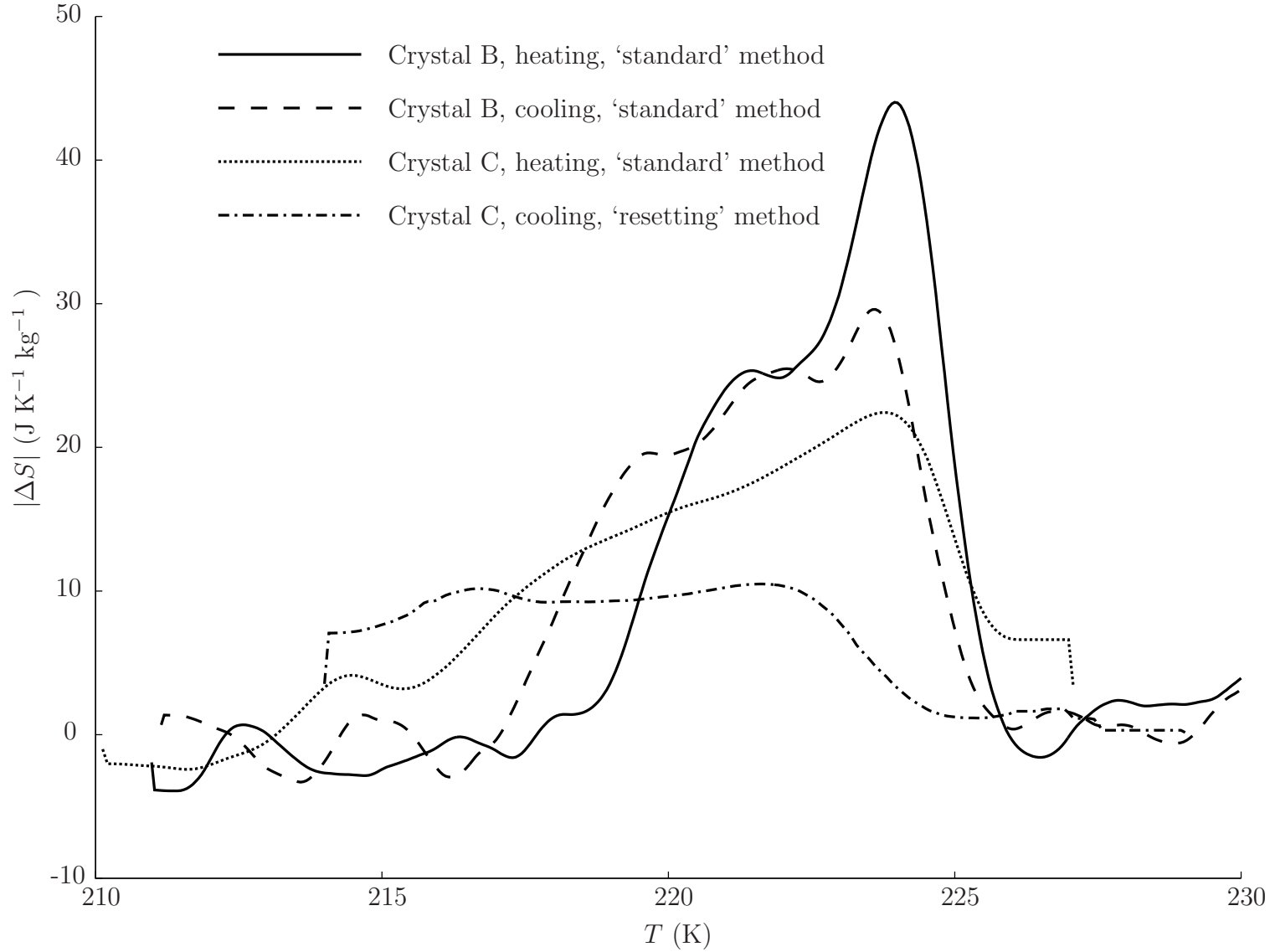


Figure 4.13: Comparison of isothermal $|\Delta S(T)|$ for $(\text{NH}_4)_2\text{SO}_4$ crystals due to application of an electric field of $\sim 380 \text{ kV cm}^{-1}$ near $T_C \sim 223 \text{ K}$. These plots were compiled using the same datasets as previously shown in Figures 4.10-4.12.

4.1.7 Adiabatic $|\Delta T|$

Having evaluated *zero-field* ΔS for $(\text{NH}_4)_2\text{SO}_4$ (Figure 4.5d), and having independently evaluated *isothermal* $|\Delta S(E)|$ at various temperatures via the Maxwell analysis on $P(E)$ data (Figures 4.10-4.12), it was possible to construct a *map* of ΔS in $E - T$ space by subtracting the isothermal $|\Delta S(E)|$ from the zero-field $\Delta S(T)$. This was performed on the ‘standard’ indirect dataset for Crystal B for isothermal ΔS for applying a field on heating (Figure 4.10c), and the ‘resetting’ dataset for Crystal C for removing a field on cooling (Figure 4.12b). Small systematic errors in T were expected when combining data taken with two different cryostats. To account for this error, the temperature scale of the zero-field ΔS was shifted such that the peak point of specific heat capacity lay at the peak dielectric constant had been measured in probe head 2 (Figure 4.4). For heating, the temperature axis of the zero-field ΔS was reduced by 0.5 K, and for cooling it was reduced by 1 K.

Figure 4.14a shows zero-field ΔS on heating, Figure 4.14b shows isothermal $|\Delta S|$ via the ‘standard’ indirect method on heating Crystal B, and Figure 4.14c shows adiabats that result from combining these two datasets. The region of greatest change in T is $\sim 218 < T < 222$ K, which is away from the spurious peak in isothermal $|\Delta S|$ at ~ 224 K. The adiabats just above ~ 222 K are unsafe as they coincide with the spurious peak in isothermal $|\Delta S|$.

Figure 4.15a shows zero-field ΔS on cooling, Figure 4.15b shows isothermal $|\Delta S|$ via the ‘resetting’ indirect method on cooling Crystal C, and Figure 4.14c shows adiabats that result from combining these two datasets. The adiabats show less variation in T than the dataset for Crystal B (Figure 4.14), however they were not affected by any spurious peak in isothermal $|\Delta S|$, owing to the use of the ‘resetting’ method for acquiring $P(E)$ loops.

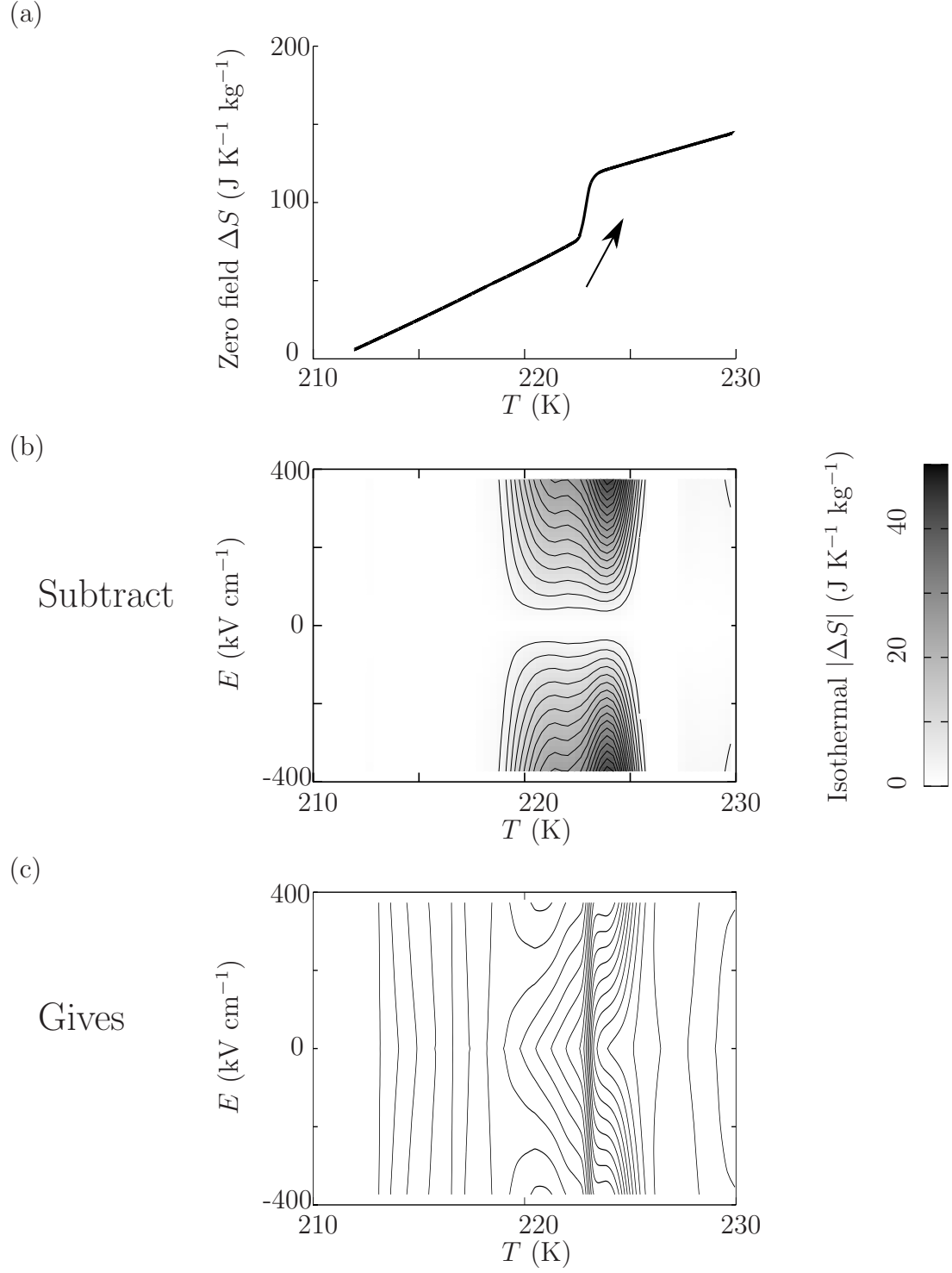


Figure 4.14: **(a)** Plot of zero-field ΔS evaluated from calorimetry data (Figure 4.5d). **(b)** Isothermal $|\Delta S|$ evaluated from ‘standard’ Maxwell analysis on Crystal B (Figure 4.10c). **(c)** Subtracting the plot of (b) from that of (a) gives a map of ΔS in $E - T$ space. The contour lines (spacing $5 \text{ J K}^{-1} \text{ kg}^{-1}$) are adiabats.

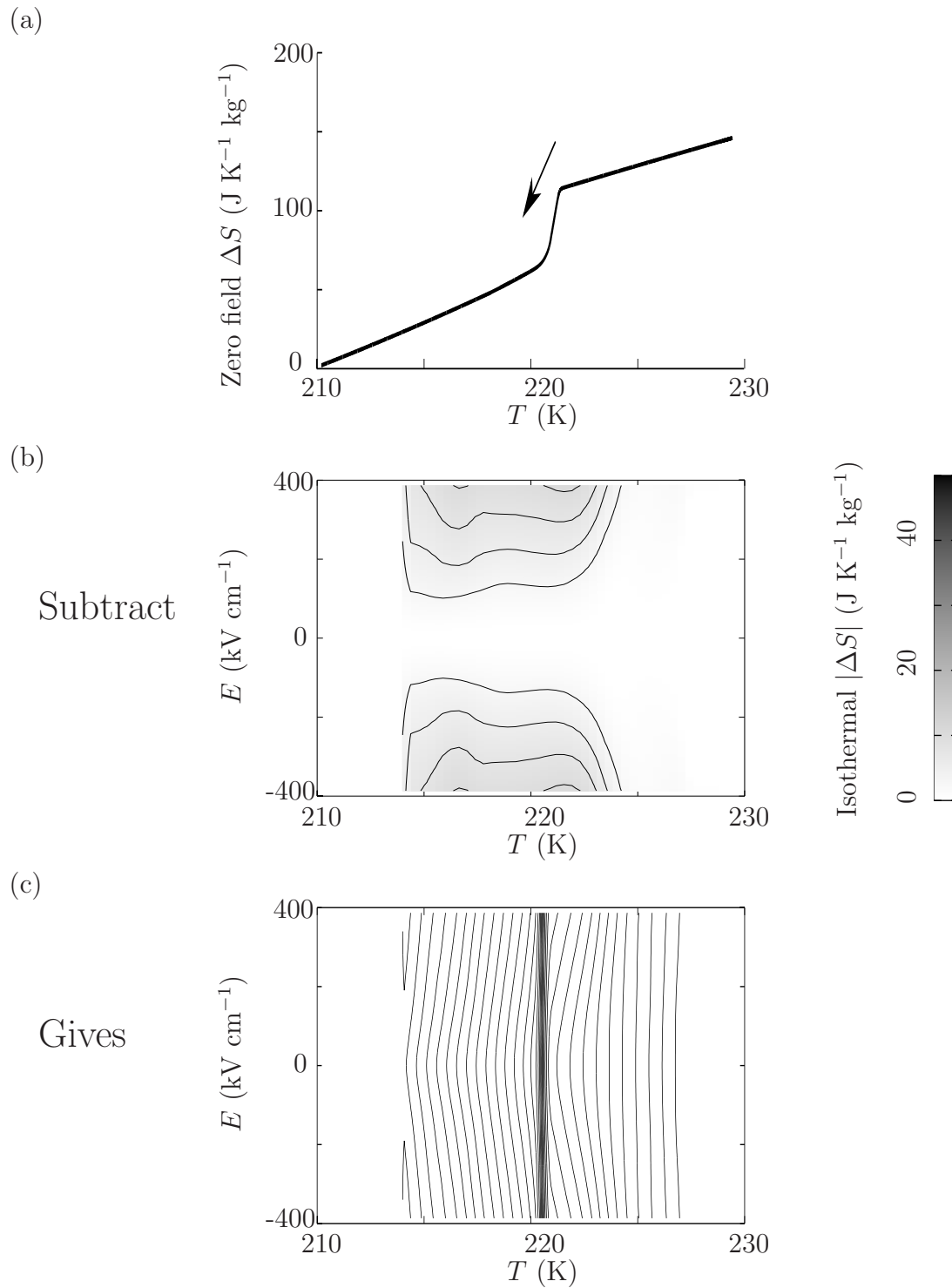


Figure 4.15: **(a)** Plot of zero-field ΔS evaluated from calorimetry data (Figure 4.5d). **(b)** Isothermal $|\Delta S|$ evaluated from ‘resetting’ Maxwell analysis on Crystal C (Figure 4.12b). **(c)** Subtracting the plot of (b) from that of (a) gives a map of ΔS in $E - T$ space. The contour lines (spacing $5 \text{ J K}^{-1} \text{ kg}^{-1}$) are adiabats.

Adiabatic application of an electric field ΔE will drive the system along an adiabatic path, resulting in a temperature change ΔT . The adiabatic paths for Crystal B (from a ‘standard’ dataset on heating) and Crystal C (from a ‘resetting’ dataset on cooling) were plotted in Figure 4.14c and Figure 4.15c. Figure 4.16 shows the corresponding adiabatic temperature change $|\Delta T|$ for Crystal B and C as a function of temperature, for the case of a field $E \sim 380 \text{ kV cm}^{-1}$ for Crystal B and $\sim 400 \text{ kV cm}^{-1}$ for Crystal C. The maximum adiabatic $|\Delta T|$ was $\sim 4 \text{ K}$ in Crystal B and $\sim 1.25 \text{ K}$ in Crystal C.

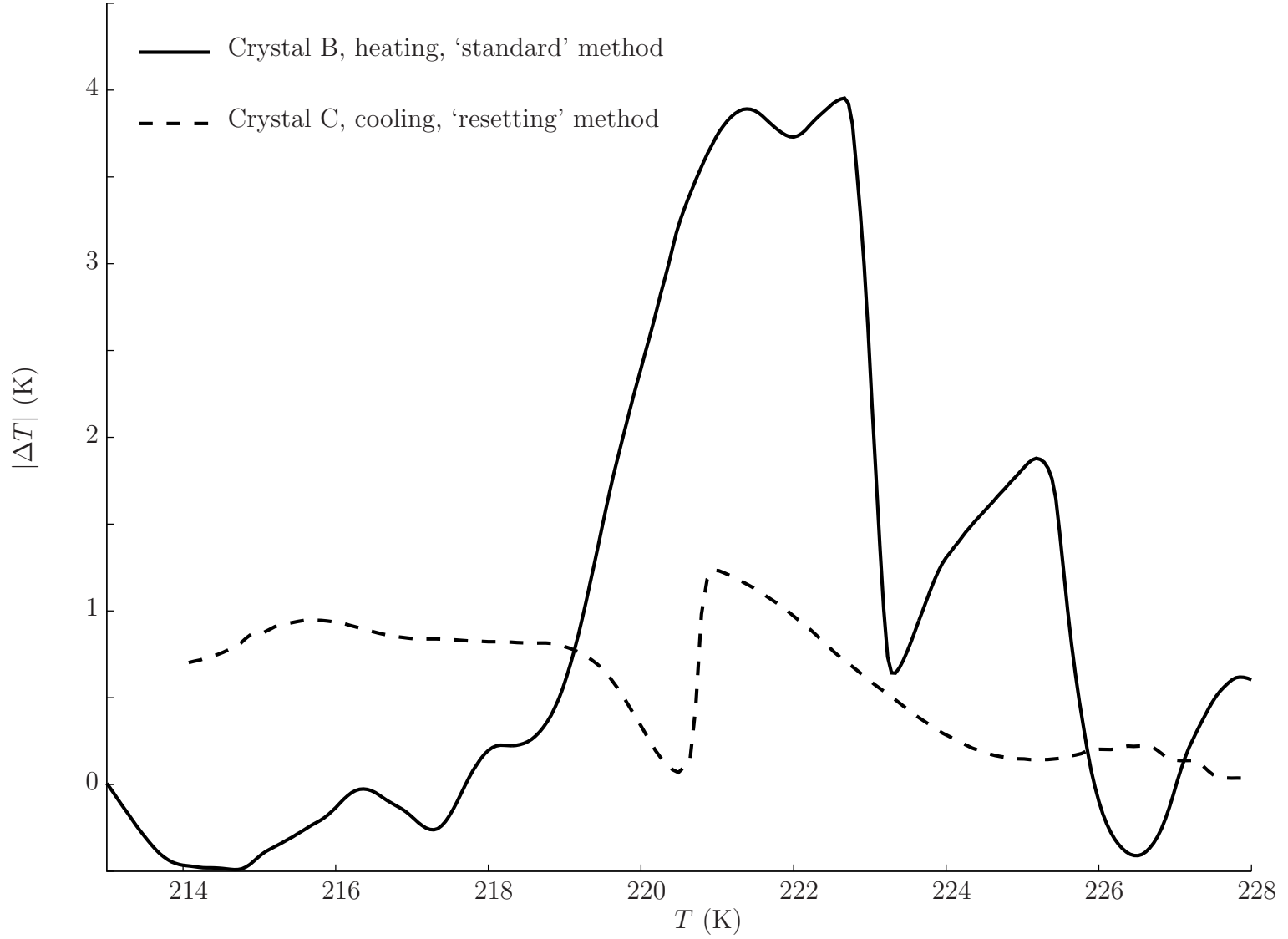


Figure 4.16: Adiabatic $|\Delta T|$ for $(\text{NH}_4)_2\text{SO}_4$ Crystal B (from a ‘standard’ dataset on heating) and Crystal C (from a ‘resetting’ dataset on cooling) for a field change of $\sim 380 \text{ kV cm}^{-1}$ (Crystal B) and $\sim 400 \text{ kV cm}^{-1}$ (Crystal C).

4.1.8 Conclusions

$(\text{NH}_4)_2\text{SO}_4$ has many unusual properties, such as a very large entropy change of $133.2 \text{ J K}^{-1} \text{ kg}^{-1}$ near $T_C = 223 \text{ K}$, and ferrielectricity. Electric fields of up to 400 kV cm^{-1} were applied across samples with thicknesses of a few tens of microns. Such large fields are associated with ‘giant’ electrocaloric effects in other materials such as Zr-rich PZT [20]. The ‘resetting’ indirect method revealed an electrically driven entropy change of $\sim 10 \text{ J K}^{-1} \text{ kg}^{-1}$ or $17.7 \text{ J K}^{-1} \text{ dm}^{-3}$ under a field of 400 kV cm^{-1} , with the ‘standard’ method spuriously predicting up to $45 \text{ J K}^{-1} \text{ kg}^{-1}$ under a similar field (Figure 4.13). The ‘standard’ method did, however, predict entropy changes of $\sim 20 \text{ J K}^{-1} \text{ kg}^{-1}$ or $35.4 \text{ J K}^{-1} \text{ dm}^{-3}$ just below T_C , away from the temperature where the ‘standard’ method results were spurious. The entropy change of $\sim 20 \text{ J K}^{-1} \text{ kg}^{-1}$ was larger than the $\sim 8 \text{ J K}^{-1} \text{ kg}^{-1}$ of Zr-rich PZT thin films, however the corresponding electrocaloric heat Q would be less disparate because the Curie temperature of Zr-rich PZT is $\sim 490 \text{ K}$, approximately double that of $(\text{NH}_4)_2\text{SO}_4$. The maximum predicted adiabatic temperature change $|\Delta T|$ was $\sim 4 \text{ K}$ over a narrow temperature range $\sim 220.5 < T < 222.5 \text{ K}$ for the ‘standard’ method on heating. The ‘resetting’ method on cooling predicted a maximum value of $|\Delta T| \sim 1.25 \text{ K}$, but on a different crystal.

4.2 KNO₃

Potassium nitrate (KNO₃) is a common inorganic salt known historically as ‘saltpetre’, the oxidant of gunpowder. Bulk samples of KNO₃ are ferroelectric only on cooling, from 395 K to ~ 380 K. The high-temperature paraelectric phase is normally labelled I, the low-temperature phase II and the ferroelectric phase III (Table 4.2). Kracek’s 1929 study [126] was the first to report the latent entropy for all three phase transitions, with the more modern study of Westphal *et al.* (1993) [127] giving slightly revised values (Table 4.3). Of these transitions, only I-III occurs on both heating and cooling and is thus of interest for electrocalorics.

	Phase II	Phase I	Phase III
Type	Paraelectric	Paraelectric	Ferroelectric
Space group	$Pnma$	$R\bar{3}A$	$R3A$
Lattice	Orthorhombic	Hexagonal	Hexagonal
a (Å)	5.414	5.425	5.487
b (Å)	9.166	$= a$	$= a$
c (Å)	6.431	9.836	9.156 (polar)

Table 4.2: Phases of bulk KNO₃ at atmospheric pressure. Data from Nimmo and Lucas (1976) [128].

Transition	Temperature (K)	Entropy change (J K ⁻¹ kg ⁻¹)	Entropy change (J K ⁻¹ dm ⁻³)	Occurrence
II \rightarrow I	401	123.6	260	Heating only
I \leftrightarrow III	395	65.3	137.5	Heating and cooling
III \rightarrow I	~ 380	52.4	110.3	Cooling only

Table 4.3: Transitions of bulk KNO₃ at atmospheric pressure. Data from Westphal *et al.* (1993) [127].

The structure of the ferroelectric phase III of KNO₃ is shown in Figure 4.17. The permanent dipole is due to the NO₃⁻ ion being displaced along the c -axis by $\delta \sim 0.4$ Å from the centre of the unit cell. Sawada *et al.* (1958) [98] were the first to measure a ferroelectric $P(E)$ loop in this material, on a polycrystalline sample prepared from melt.

The same authors presented a detailed ferroelectric and dielectric study on a single-crystal sample in 1961 [129]. The spontaneous polarisation was $8 \mu\text{C cm}^{-2}$ as measured by $P(E)$ loops, and $10 \mu\text{C cm}^{-2}$ as measured by pyroelectric current. An order-disorder transition was suggested such that above T_C , the NO_3^- ions oscillate about the centre of the unit cell due to thermal excitation, leading to a net dipole moment of zero. Order-disorder has been confirmed by spectroscopic measurements [130] and also via crystallography [128, 131]. Measurements of the temperature of the lower transition from phase III to phase II show poor agreement, and this transition has been shown to be sensitive to factors such as moisture [132]. It is well established that the ferroelectric phase III remains stable down to room temperature in thin films of KNO_3 . This was initially linked to strain, but Scott *et al.* [133] showed it to be due to surface electric fields.

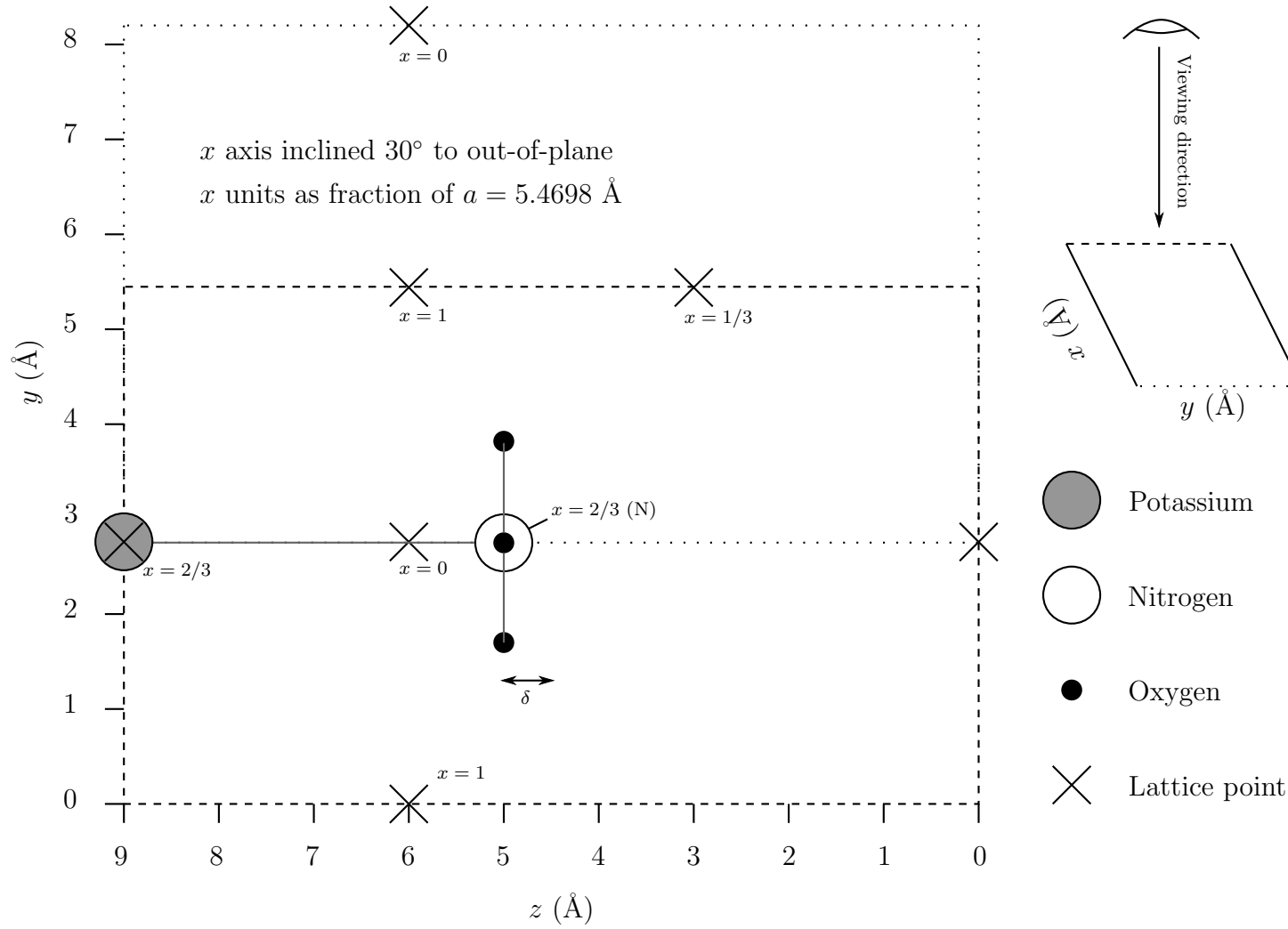


Figure 4.17: Structure of ferroelectric phase III of KNO_3 (space group $R3m$). Six lattice points are shown, the atomic motif for $x = 2/3$ only. Viewing direction perpendicular to $y - z$ plane (see top right). The x -axis of this hexagonal structure is thus inclined at 30° to the direction out of the plane of the page. Dashed lines denote boundary of the upper surface of the unit cell, and dotted lines denote boundary of the lower surface. Above $T_C = 395$ K, the mean displacement of the NO_3 groups shifts to the centre of the z -axis as denoted by δ . In-plane O displacements inform the out-of-plane displacements of the trigonal planar NO_3 groups. Crystallographic data: Freney *et al.* (2009) [134].

4.2.1 Crystal growth

Single crystals of KNO_3 were prepared by Wei Li in the group of Anthony K. Cheetham (Materials Science, University of Cambridge). Crystals were grown at room temperature in H_2O via slow evaporation. The crystals were rod-like with lengths of order 1 cm and cross-sectional areas of order 1 mm^2 . The ferroelectric axis pointed along the length of the rod.

4.2.2 Device preparation

KNO_3 crystals were prepared for measurement on copper substrates with Pt electrodes using the same 11 step process as described in Section 4.1.2 for $(\text{NH}_4)_2\text{SO}_4$. However, it was not possible to prepare samples with thicknesses in the 10s of μm range, because the crystals of KNO_3 were fragile and prone to disintegration on polishing. Thus, once samples were glued to the copper substrate, they were polished to a thickness of a few 100s of μm . Thicknesses were measured with a digital calliper, and electrode areas with a microscope image as described in Section 4.1.2.

Data will be presented on two samples, A and B. Crystal A was $\sim 310 \mu\text{m}$ -thick and had an electrode area of 0.28 mm^2 . Crystal B was $\sim 250 \mu\text{m}$ -thick and had an electrode area of 0.54 mm^2 . The two crystals showed slightly different transition temperatures between phases I and III — Crystal A showed a 395 K transition on cooling and Crystal B showed a 400 K transition on cooling.

Dielectric measurements were conducted in the bespoke high-temperature stage (Section 3.2). Measurements of $P(E)$ were conducted in probe head 2 (Section 3.1).

4.2.3 Dielectric constant

Figure 4.18a shows the dielectric constant of Crystal A as a function of temperature at 1 kHz, as deduced using the equivalent parallel capacitance model (Section 2.2). The sample was mounted on the bespoke high-temperature stage and temperature was ramped at around $\pm 0.5 \text{ K min}^{-1}$. The phase transition sequence of this material was revealed by anomalies in the dielectric constant corresponding to the II \rightarrow I transition at $\sim 400 \text{ K}$ on heating, the I \rightarrow III transition at $\sim 395 \text{ K}$ on cooling and the III \rightarrow II transition at $\sim 380 \text{ K}$ on cooling. The Curie-Weiss constant above T_C on cooling

(ignoring the non-linear region immediately above T_C) was ~ 4900 , which agreed with the literature value of 5600 within error (Figure 4.18b) [39]. Losses were small (<0.1) in phase II and ~ 0.2 in both phase III and phase I below 400 K (Figure 4.18c). Losses increased to ~ 0.4 for phase I at 410 K. When Crystal A was measured multiple times on cooling at ~ 0.2 K min $^{-1}$, the temperature of the III \rightarrow II phase transition was observed to vary from ~ 385 K to ~ 376 K (Figure 4.19). In contrast, the temperature of the I \rightarrow III transition did not change from run to run.

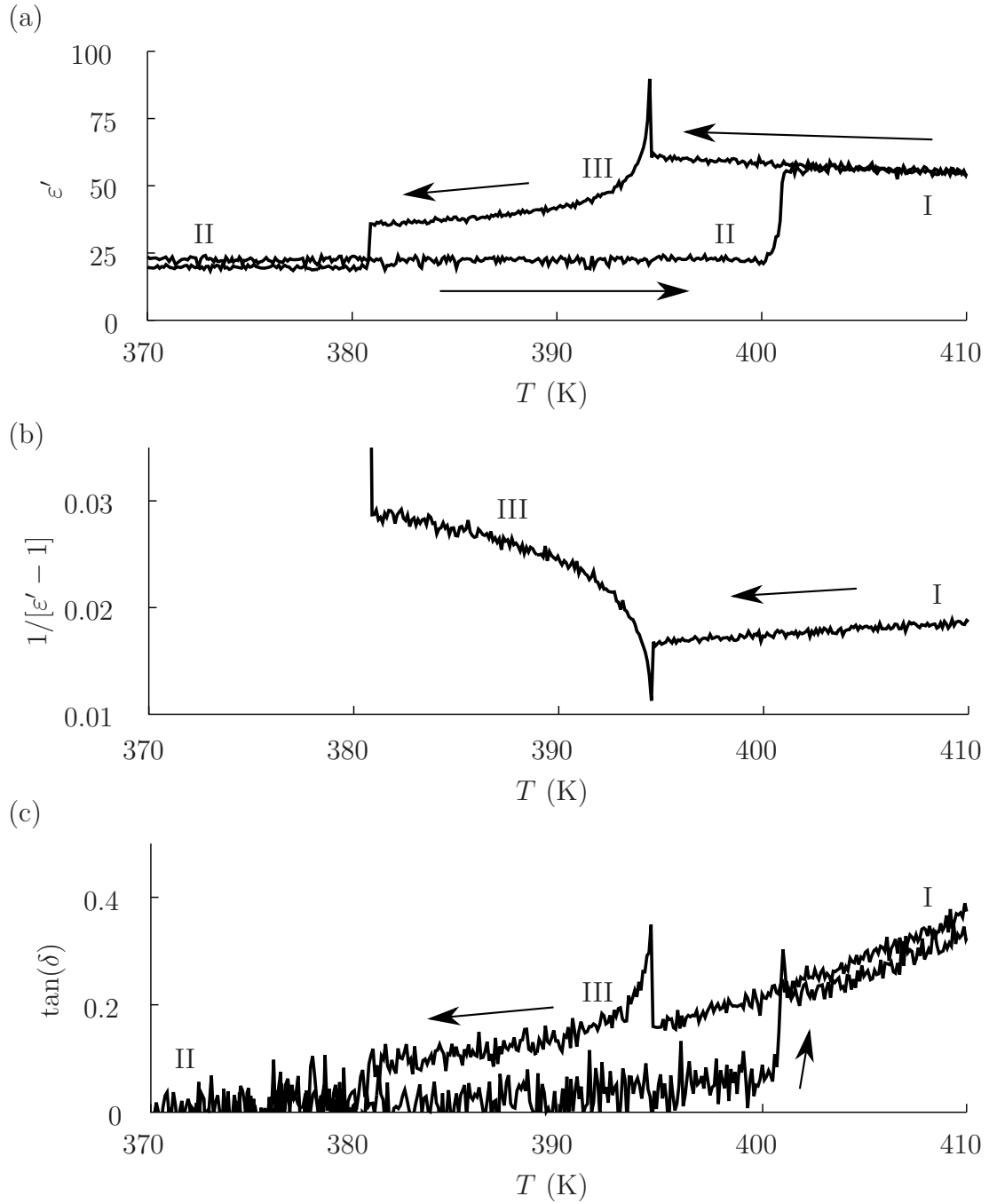


Figure 4.18: Dielectric data derived from an impedance dataset on KNO₃ Crystal A. The amplitude and frequency of the driving field were 1 V RMS and 1 kHz respectively. A known parasitic capacitance of 0.7 pF was subtracted from the measured equivalent parallel capacitance of ~ 0.85 pF at low temperatures. Data for heating and cooling are indicated by arrows. The thermal ramp rate was around ± 0.5 K min⁻¹. The sections of the plots corresponding to phases I, II and III are labelled. **(a)** Dielectric constant, **(b)** reciprocal dielectric susceptibility, and **(c)** loss tangent, as functions of temperature.

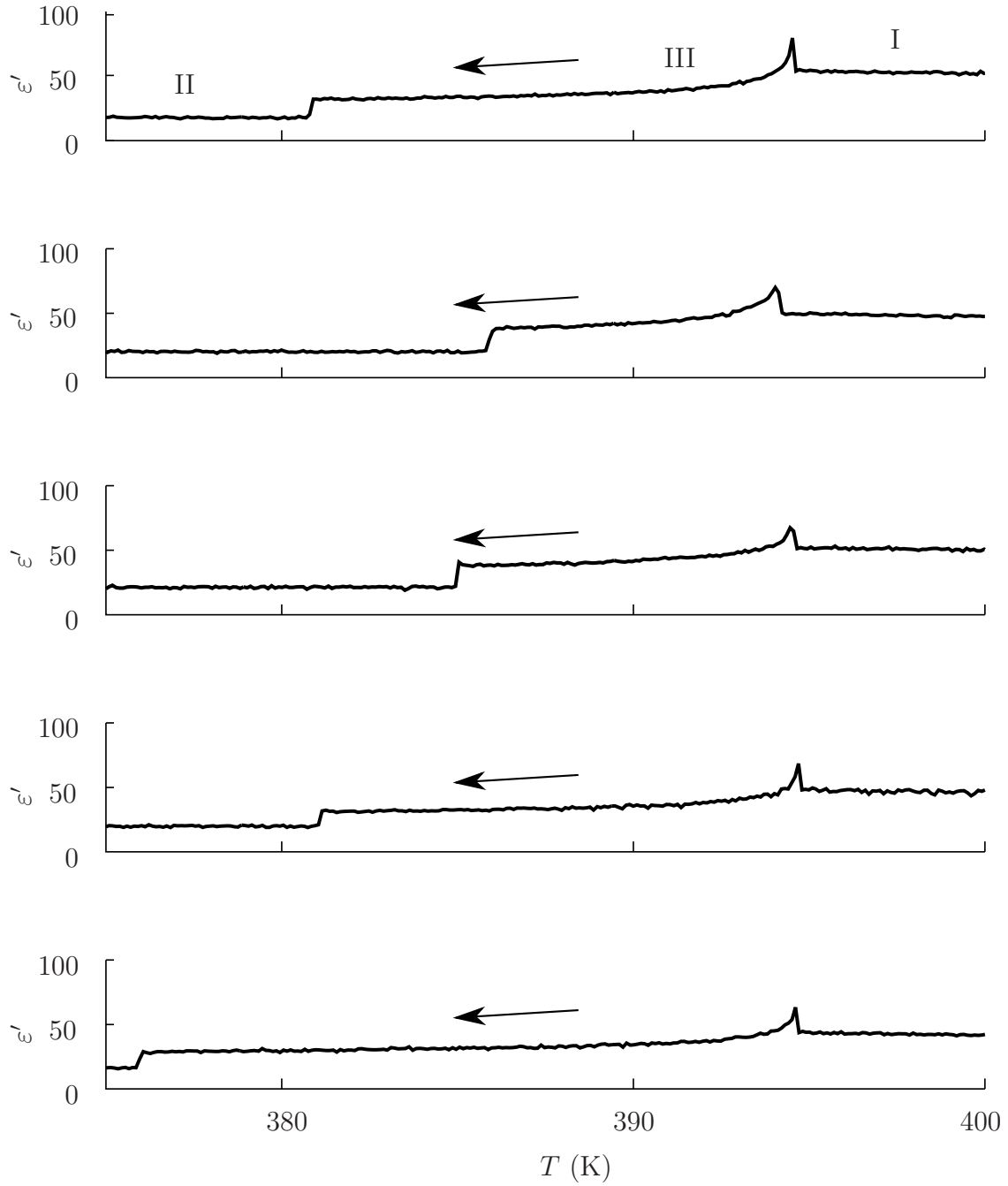


Figure 4.19: To investigate the reproducibility of the III \rightarrow II phase transition, dielectric data were obtained for KNO₃ Crystal A, on multiple cooling runs at ~ -0.5 K min⁻¹, using identical measurement conditions with respect to the previous figure. The x -axis of all plots is common. For the uppermost plot, the sections corresponding to phases I, II and III are labelled.

4.2.4 Zero-field ΔS

Heat-flow vs temperature measurements were performed as described in Section 2.5 on heating and cooling a 1.527 mg single crystal of KNO_3 at $\pm 2 \text{ K min}^{-1}$. These measurements were performed by Robert Cornell. Figure 4.20a shows specific heat capacity as evaluated from the raw heat-flow data which contained an offset. The true specific heat capacity was estimated by forcing c_E on heating and cooling to be equal at 419 K, yielding an offset of $3597 \text{ J K}^{-1} \text{ kg}^{-1}$ which was added to the heating curve and subtracting from the cooling curve (Figure 4.20b). The specific heat capacity above the transition temperature was $\sim 2000 \text{ J K}^{-1} \text{ kg}^{-1}$. The value measured by Westphal *et al.* (who measured powder samples) was $\sim 1300 \text{ J K}^{-1} \text{ kg}^{-1}$, i.e. $\sim 35\%$ smaller [127]. The II \rightarrow I and I \rightarrow III transitions both showed clear signals in the specific heat capacity traces on heating and cooling respectively, but there was no unambiguous anomaly with which to identify to the III \rightarrow II transition (Figure 4.20c). Due to latent heat, the specific heat capacity at the I \rightarrow III transition showed a very large peak value of $\sim 60000 \text{ J K}^{-1} \text{ kg}^{-1}$. The entropy change in the immediate vicinity of the I \rightarrow III transition was $\sim 62 \text{ J K}^{-1} \text{ kg}^{-1}$ (Figure 4.20d), in good agreement with the literature value of $65.3 \text{ J K}^{-1} \text{ kg}^{-1}$ [127]. However, the evaluated zero-field ΔS was not conserved at 370 K following the thermal excursion to 420 K. This problem, and possibly also the discrepancy between the present data and those of Westphal, could reflect poor measurement accuracy due to the small size of the sample used, or could indicate some irreversible thermodynamic ageing process. Owing to the uncertainty, the results of Figure 4.20 should be regarded as preliminary.

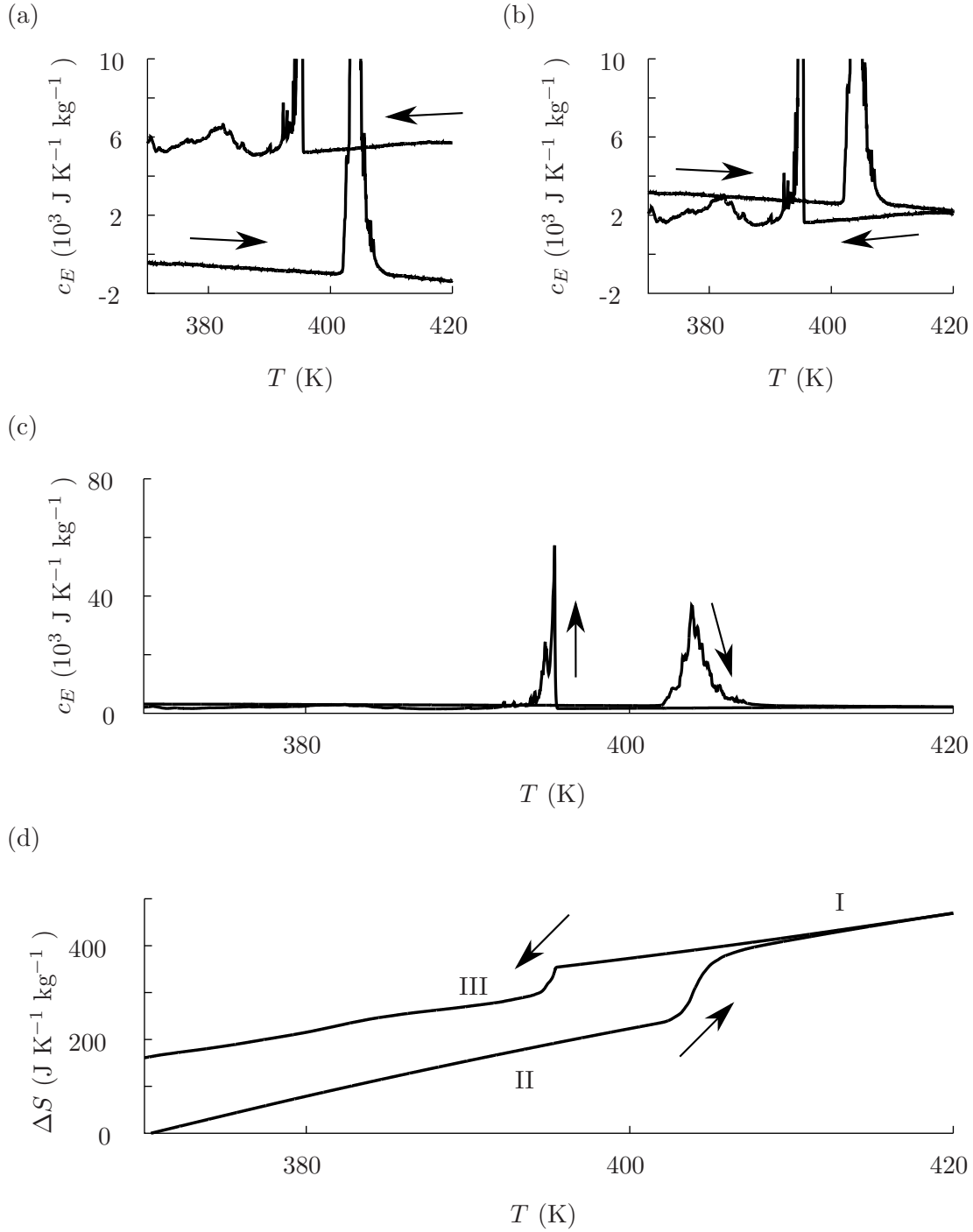


Figure 4.20: Calorimetry results for KNO₃ taken on heating and cooling at $\pm 2 \text{ K min}^{-1}$. **(a)** Specific heat capacity c_E for KNO₃ as evaluated from raw heat-flow data, which contained an offset between heating and cooling data. **(b)** Specific heat capacity with offset averaged out. In (a) and (b), the y -axis has been cropped to better show the values away from T_C . **(c)** Specific heat capacity with offset averaged out, showing full height of peak at T_C . **(d)** Zero-field $\Delta S(T)$ with respect to the initial entropy at 370 K. Derived from the specific heat capacity data with offset averaged out.

4.2.5 $P(E)$ loops

Figures 4.21a-d show $P(E)$ loops taken on Crystals A and B using a driving field frequency of 10 Hz and amplitude of 47 kV cm^{-1} . Uncompensated and compensated major loops are shown, along with compensated minor loops. Compensation was performed using an estimate of equivalent parallel resistivity ϱ , simultaneously obtained from the raw data as described in Section 2.3.

Figure 4.21 (a) and (b) show $P(E)$ loops on Crystal B, in phases I and III respectively. Ferroelectric hysteresis is visible in phase III (b) but not in phase I (a). The spontaneous polarisation of phase III was $\sim 9.6 \text{ } \mu\text{C cm}^{-2}$, somewhat larger than the value of $8 \text{ } \mu\text{C cm}^{-2}$ reported by Sawada *et al.* from $P(E)$ loops, but similar to the value of $10 \text{ } \mu\text{C cm}^{-2}$ measured by the same authors via pyroelectric current [129].

Figure 4.21c, like Figure 4.21b, shows $P(E)$ data on Crystal B in phase III, but (c) was taken ~ 16 hours after (b) during which time several additional loops had been taken (not shown), and several thermal excursions through the $\text{I} \leftrightarrow \text{III}$ phase transition had taken place. One or more of these temporal, thermal or electrical stresses led to significant changes in the form of the loops. The ‘aged’ loops in (c) showing a less sharp ferroelectric switching transition and a lower susceptibility than the less ‘aged’ loops in (b). Similar ‘ageing’ behaviour was observed in Crystal A (Figure 4.21d).

Once settled in the ‘aged’ state, the $P(E)$ behaviour continued to degrade, but much more slowly. After Crystal A had been subjected to a large number of thermal and electrical cycles, no ferroelectric loop at all could be observed on cooling.

All of the $P(E)$ loops in Figures 4.21a-d were significantly affected by electrical losses. The equivalent parallel resistivity ϱ showed a small anomaly at $T_C \sim 396 \text{ K}$ and was lower in phase I ($\sim 1 - 2 \text{ M}\Omega \text{ m}$) than phase III ($\sim 2.5 \text{ M}\Omega \text{ m}$) [Figure 4.21e]. Resistivity in phase I became lower as temperature was increased, as might have been anticipated from the increased dielectric loss (Figure 4.18c).

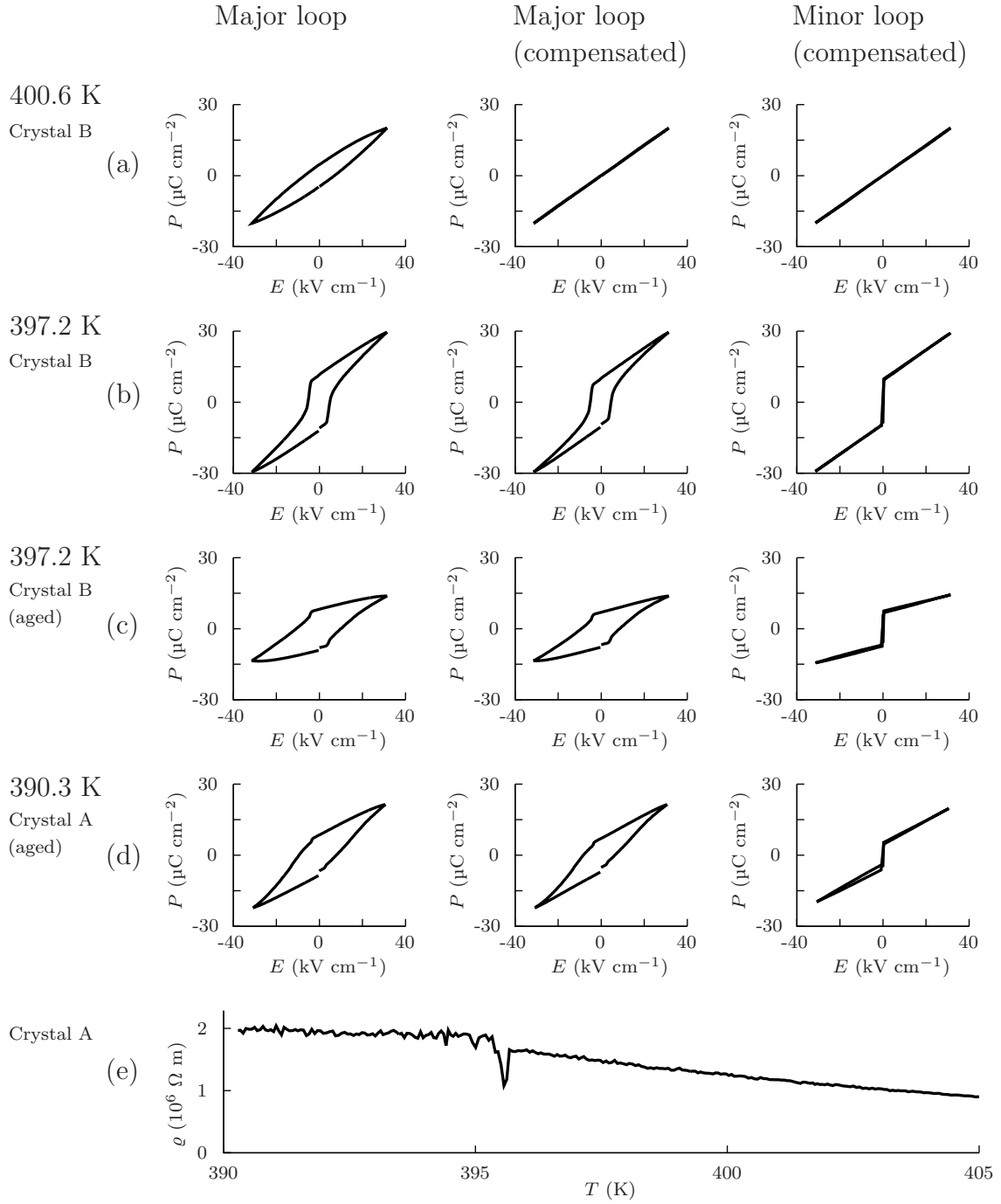


Figure 4.21: **(a)-(d)** $P(E)$ loops at 10 Hz for KNO₃ Crystals A and B at various temperatures near the Curie temperature. Major (switching), and minor (non-switching) loops are shown. **(f)** Equivalent parallel resistivity ϱ for Crystal A deduced from $P(E)$ data taken on cooling.

4.2.6 Isothermal $|\Delta S|$

To evaluate isothermal $|\Delta S|$ via the ‘standard’ (ramping) method, $P(E)$ loops were obtained on Crystal A every ~ 15 s during temperature ramps at around ± 0.2 K min $^{-1}$. These loops were not compensated for losses, and were processed into $P(T)$ data, and thus a prediction of isothermal ΔS in the same way as for $(\text{NH}_4)_2\text{SO}_4$ (Section 4.1), using the CRC value of 2105 kg m $^{-3}$ for the density of KNO_3 [97]. Figure 4.22 shows $P(T)$, and Figure 4.23 shows mass-normalised isothermal $|\Delta S|$ as a function of E for various T . The maximum value of isothermal $|\Delta S|$ evaluated from these ‘standard’ datasets was ~ 450 J K $^{-1}$ kg $^{-1}$, an order-of-magnitude larger than the 62 J K $^{-1}$ kg $^{-1}$ zero-field ΔS of the phase transition (Figure 4.20b). Furthermore, the anomalies in isothermal $|\Delta S|$ were highly localised and symmetric about T_C , and thus matched the expected profile of spurious datasets from an invalid application of the ‘standard’ indirect method (Section 2.4). It was therefore concluded that the results of Figure 4.23 were spurious, exemplifying the failure of the ‘standard’ indirect method near entropic and thermally hysteretic first-order phase transitions.

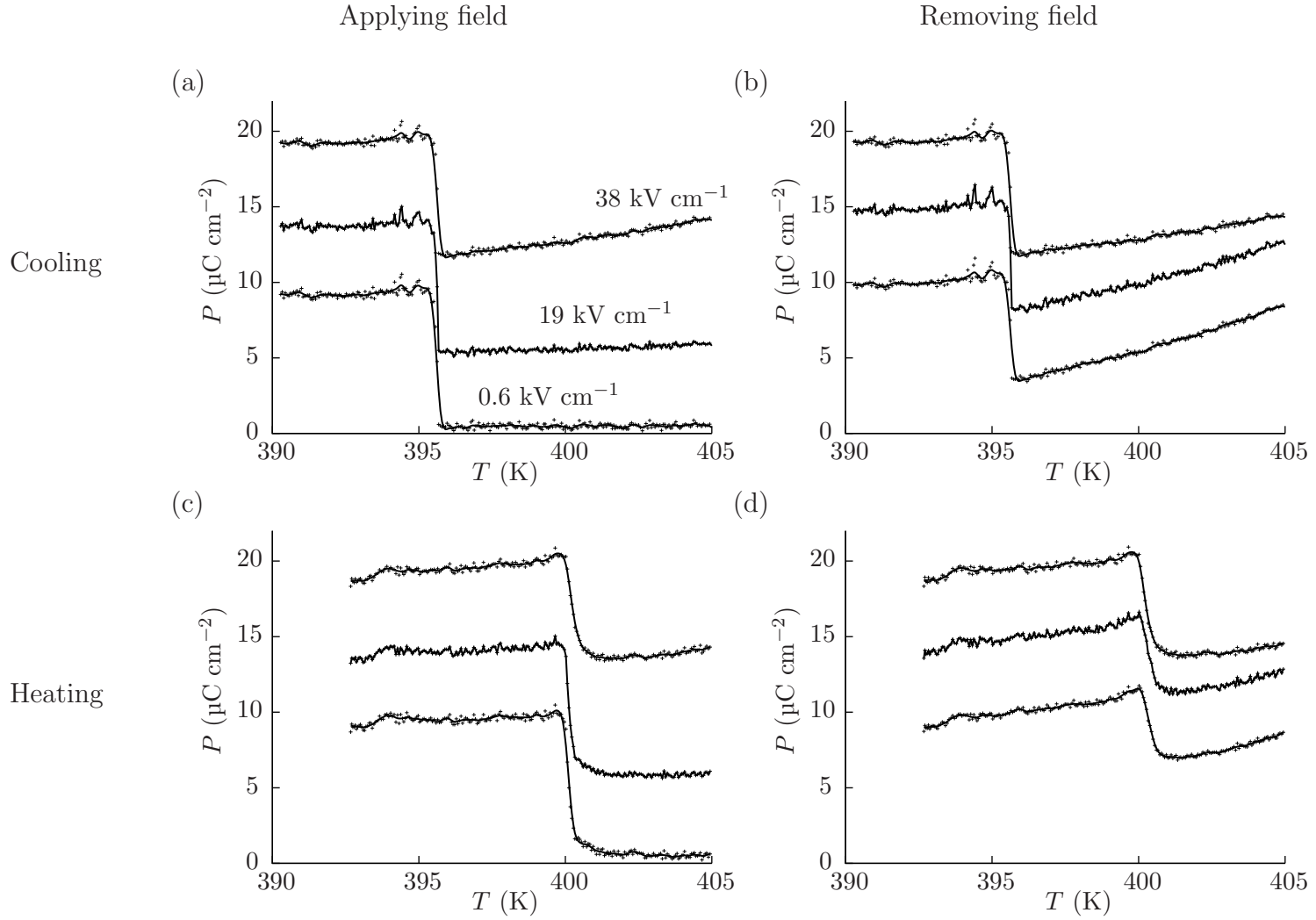


Figure 4.22: Selected $P(T)$ curves derived from minor $P(E)$ loops taken with the ‘standard’ method for KNO_3 Crystal A. The four graphs correspond to applying and removing a field (i.e. lower and upper branches of the minor loops) on heating and cooling. The three plots of each graph correspond to 38 kV cm^{-1} (upper line), 19 kV cm^{-1} (middle line) and 0.6 kV cm^{-1} (lower line) as indicated in (a). Points: raw (measured) data, lines: cubic spline fit.

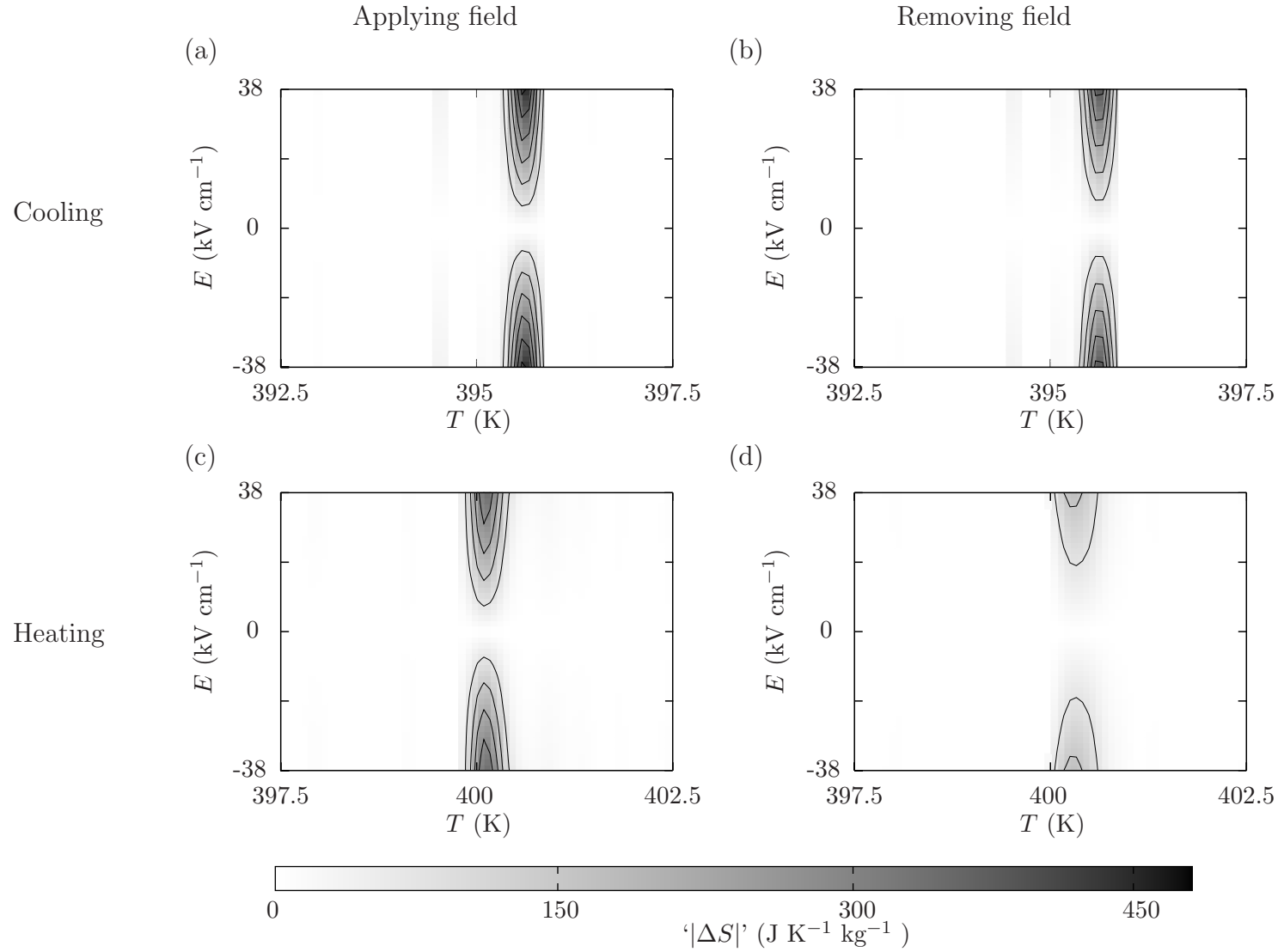


Figure 4.23: Spurious isothermal $|\Delta S|$ for KNO_3 Crystal A evaluated via ‘standard’ indirect method. The four graphs correspond to applying and removing a field (i.e. lower and upper branches of the minor loops) on heating and cooling. Data for negative E : ‘mirror image’ of those for positive E . Contour spacing: $75 \text{ J K}^{-1} \text{kg}^{-1}$.

Plots for $P(T)$ and isothermal $|\Delta S|$ were also evaluated using the ‘resetting’ method, whereupon the sample was reset to a temperature known to lie above T_C (in this case 410 K) before cooling to the measurement temperature for each $P(E)$ loop, as described fully in Section 2.4. For this dataset, the thermodynamic analysis was performed on the initial branch of the loop. A temperature ramp rate of $\pm 1 \text{ K min}^{-1}$ was used to move between 410 K and the measurement temperature. The resulting $P(T)$ (Figure 4.24a) were somewhat noisy just above T_C , as certain datapoints (circled) corresponded to $P(E)$ loops (not shown) similar to those observed in the paraelectric phase (i.e. similar to Figure 4.21a), despite occurring at temperatures *lower* than the start of the nominal transition. The origin of this noise could be the fact that thermal stabilisation was not attained at measurement temperatures, as stabilisation necessarily involved a small thermal excursion to a few 100s of mK below the measurement temperature, which was considered unacceptable for such a sharp transition.

In comparison with the values of isothermal $|\Delta S|$ obtained using the ‘standard’ indirect method (Figure 4.23), the values obtained via the ‘resetting’ method (Figure 4.24b) showed an anomaly that was broader and asymmetric, as it extended further above T_C than below. Furthermore, the maximum predicted value of isothermal $|\Delta S|$ for the ‘resetting’ dataset was $\sim 75 \text{ J K}^{-1} \text{ kg}^{-1}$ (Figure 4.25), which is still larger than the zero-field value of $\sim 62 \text{ J K}^{-1} \text{ kg}^{-1}$, but possibly consistent within error. Nonetheless, these results should be regarded as preliminary due to the underlying noisy $P(T)$ curves.

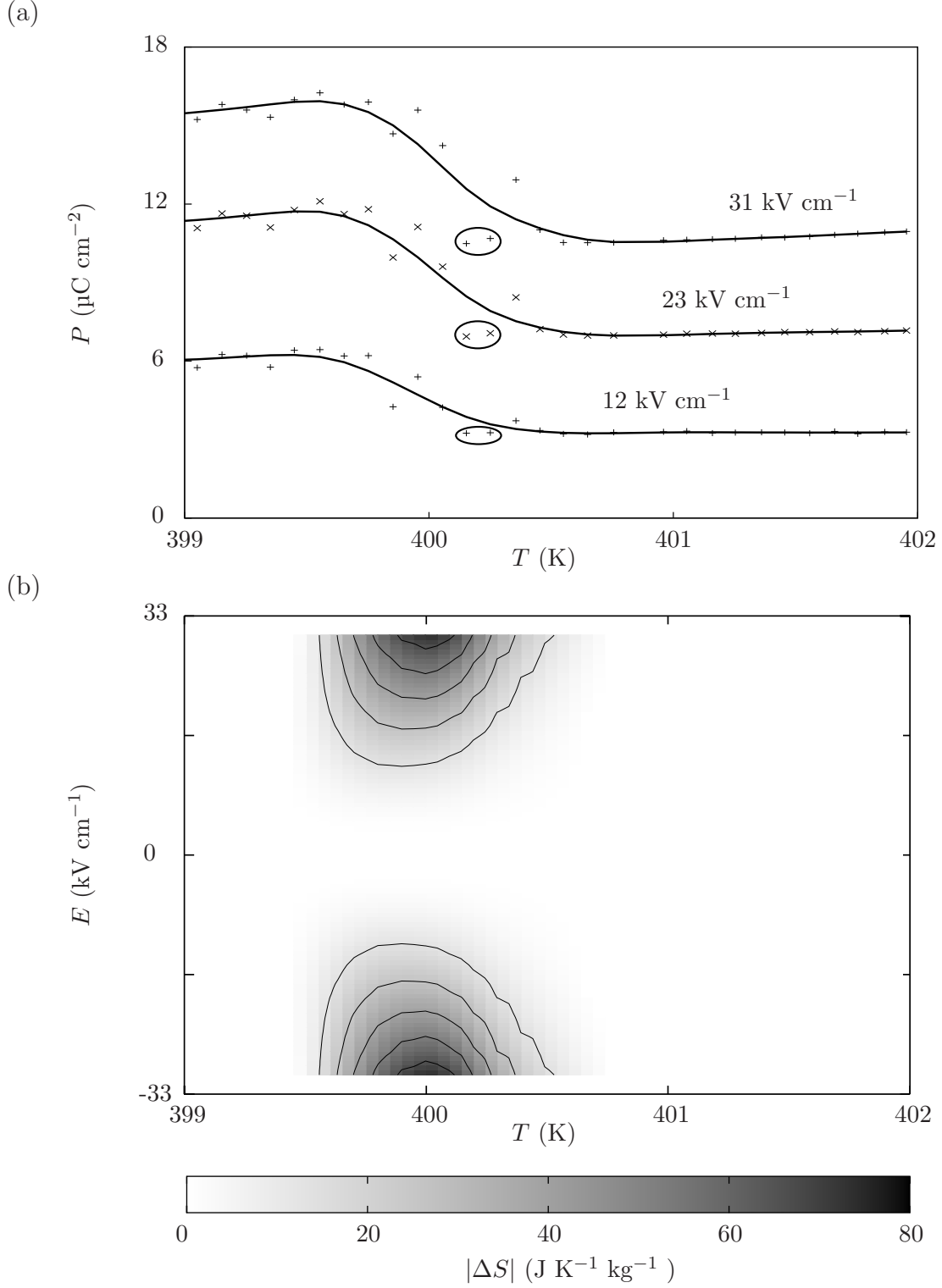


Figure 4.24: Plots for **(a)** selected $P(T)$ for applying a field (i.e. initial branch of the $P(E)$ loop) and **(b)** isothermal $|\Delta S|$ for KNO_3 Crystal B evaluated via ‘resetting’ indirect method, for applying a field. Data were taken on cooling. **(a)** Points: raw (measured) data, lines: cubic spline fit. Circled points: referred to in main text. **(b)** Data for negative E : ‘mirror image’ of those for positive E . Contour spacing: $20 \text{ J K}^{-1} \text{ kg}^{-1}$.

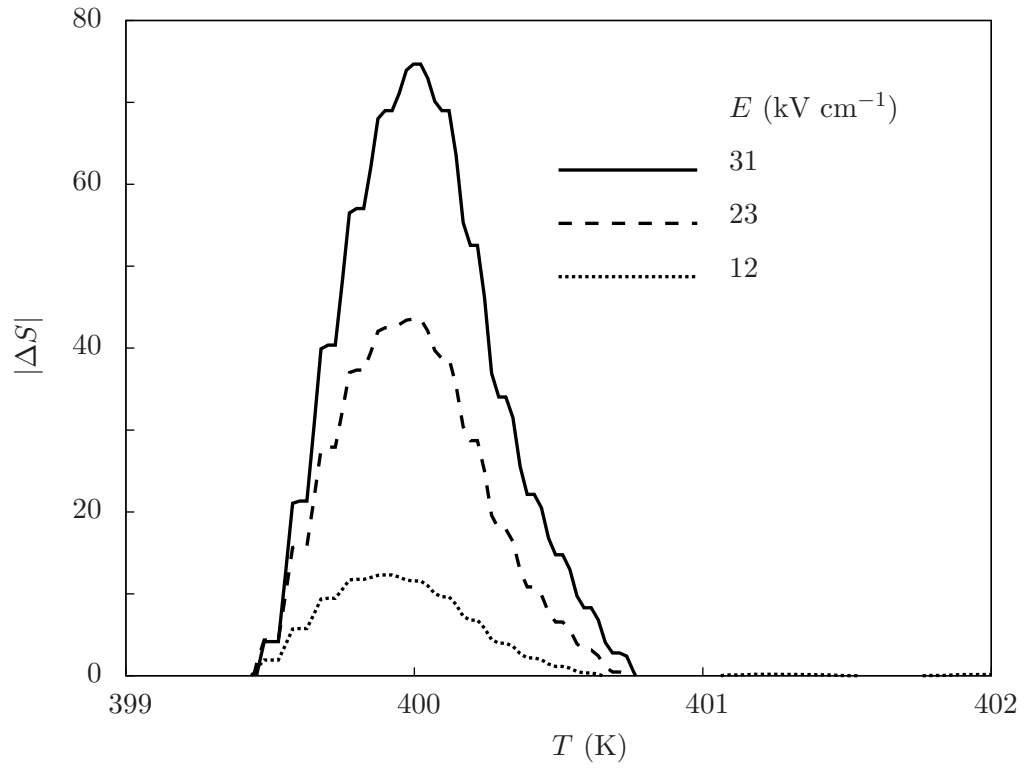


Figure 4.25: Isothermal $|\Delta S|$ for KNO_3 Crystal B evaluated via the ‘resetting’ indirect method. Same dataset as for Figure 4.24. The ‘step’ like features in the data are an artifact from binning.

4.2.7 Conclusions

Preliminary and indirect experiments on bulk single crystals of KNO_3 suggested an isothermal entropy change of $\sim 75 \text{ J K}^{-1} \text{ kg}^{-1}$ or $\sim 158 \text{ J K}^{-1} \text{ dm}^{-3}$ could be driven with an electric field of $\sim 31 \text{ kV cm}^{-1}$, at a temperature just above the $T_C \sim 400 \text{ K}$. This entropy change was somewhat larger than the calorimetric value for the zero-field entropy change of this transition of $\sim 62 \text{ J K}^{-1} \text{ kg}^{-1}$, but possibly consistent within error. The calorimetric dataset obtained was of preliminary quality, and furthermore the values of isothermal $|\Delta S|$ could have been affected by ageing effects, so adiabatic $|\Delta T|$ was not evaluated for the present work. KNO_3 appears to exemplify the danger of using the ‘standard’ indirect method near an entropic, hysteretic first-order phase transition.

Thinner devices would be desirable to achieve larger fields. This could be accomplished by growing large single crystals which would have sufficient mechanical strength for thinning, by developing a system for thin-film deposition, such as that used in [133].

4.3 NaNO₂

Sodium nitrite (NaNO₂) is a common inorganic salt with various industrial applications. It is added in small quantities to meat, although it is toxic if ingested in large quantities. It is ferroelectric with a Curie temperature of 436.5 K. The ferroelectric phase has an orthorhombic crystal structure in space group $Im2m$. The b -axis is ferroelectric due to alignment of the polar NO₂ groups (Figure 4.26). In the paraelectric phase (space group $Immm$), the orientation of the polar NO₂ groups becomes rotationally disordered [75]. Ferroelectricity was first observed in NaNO₂ by Sawada *et al.* (1958) [98], who measured a sharp peak in $\varepsilon'(T)$ at T_C and a $P(E)$ loop showing ferroelectric hysteresis. The value of P_S at room temperature was measured to be $7 \mu\text{C cm}^{-2}$ using a pyroelectric method, and $6.4 \mu\text{C cm}^{-2}$ using a $P(E)$ loop. Several studies around the early 1960s reported double $P(E)$ loops just above the transition temperature, which was originally attributed to a field-driven transition [98, 135]. However, it was soon shown that the double loops were the result of an incommensurate antiferroelectric phase, which is stable in a ~ 1 K interval above T_C [75, 136].

Nomura (1961), Sakiyama *et al.* (1965), Hatta and Ikushima (1973) and Kourkova *et al.* (2009) performed thermal measurements on NaNO₂ [75, 137–139]. The results all show a specific heat capacity anomaly stretching from ~ 360 K to ~ 448 K, with a major peak at the ferroelectric-incommensurate transition temperature of ~ 436.5 K and a minor peak at the incommensurate-paraelectric transition temperature of ~ 437.3 K. The total zero-field molar ΔS (given by Sakiyama *et al.*) is $5.3 \text{ J K}^{-1} \text{ mol}^{-1}$ which is close to $R \ln 2$, i.e. consistent with monoaxial rotational disordering of the NO₂ group. Neutron diffraction studies confirmed rotational disorder about the a -axis as the driving instability of the phase transition [140]. The mass and volume-normalised zero-field ΔS of $76.8 \text{ J K}^{-1} \text{ kg}^{-1}$ or $170.0 \text{ J K}^{-1} \text{ dm}^{-3}$ is among the largest of all known ferroelectrics (Table 4.1). The ferroelectric-incommensurate transition is weakly first-order, i.e. thermal hysteresis is small [138, 139].

Chemical decomposition of the liquid state of NaNO₂ is slow, enabling devices to be prepared from melt. An interesting study by Kutnjak *et al.* (2005) used a glass matrix to constrain the volume of a sample prepared from melt, with the result that the transition became broad and second-order with a lower value of T_C of ~ 420 K, such that the incommensurate phase was no longer observed [141].

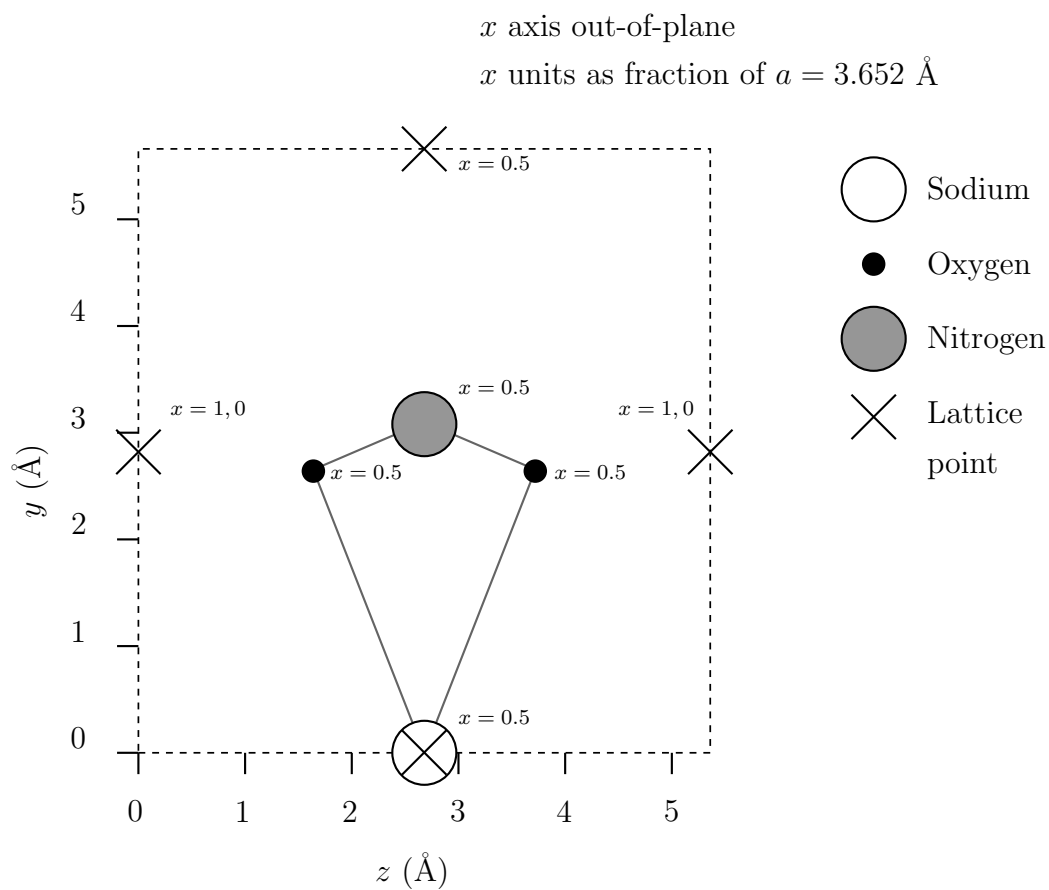


Figure 4.26: At room temperature NaNO_2 has an orthorhombic cell (dotted line) with $a = 3.652 \text{ \AA}$, $b = 5.652 \text{ \AA}$ and $c = 5.362 \text{ \AA}$. Six lattice points are shown, but only one atomic motif is shown only at $x = 0.5$. Crystallographic data: Kay *et al.* (1975) [140].

4.3.1 Crystal growth

Single crystals of NaNO_2 were prepared by Wei Li and Anthony K. Cheetham (Materials Science, University of Cambridge). Crystals were grown at room temperature in H_2O via slow evaporation. The crystals were rod-like with lengths of order 2.5 mm and cross-sectional areas of order 2 mm^2 . The ferroelectric b -axis pointed along the length of the rod.

4.3.2 Device preparation

As for the case of the KNO_3 crystals, the small size and fragility of the NaNO_2 crystals prevented preparation samples with thicknesses in the 10s of μm range, as had been accomplished for $(\text{NH}_4)_2\text{SO}_4$. Electrodes of silver dag was applied directly to the crystal surfaces, without a layer of platinum. This was because the small cross sectional area of the crystals made deposition of platinum electrodes of a well-defined area difficult. To measure the electrode area, a photograph was taken of the sample with a ruler in the frame for calibration, and a polygon fit was made in a vector graphics program (Inkscape). In all other respects, sample preparation was the same as previously described for KNO_3 .

Electrical measurements were performed in the bespoke high-temperature stage (Section 3.2). One crystal was tested, with an electrode area of $\sim 0.5 \text{ mm}^2$ and thickness of $620 \mu\text{m}$. The crystal showed high equivalent parallel conductivity, such that $P(E)$ loops could be obtained only at frequencies of $\sim 1 \text{ kHz}$. This was likely due to problems with the sample as studies on this material from literature did not report such issues [98,135]. All the data presented here should thus be considered preliminary.

4.3.3 Dielectric constant

Figure 4.27a shows dielectric constant for the NaNO_2 crystal, evaluated at 1 kHz using the equivalent parallel capacitance model (Section 2.2), on heating and cooling at around $\pm 1 \text{ K min}^{-1}$. On both heating and cooling, the ferroelectric-incommensurate transition was observed as a large peak in ϵ' at $\sim 437 \text{ K}$, and the incommensurate-paraelectric transition as a smaller shoulder to that peak at $\sim 439 \text{ K}$. The Curie-Weiss constant above T_C was $\sim 6300 \text{ K}$, in order-of-magnitude agreement with the literature value of 5000 K (Figure 4.18b) [39]. Dielectric loss was large, ranging

from 0.4 at low temperatures to 1.5 at T_C . The observed thermal hysteresis could be the result of the relatively fast ramp rate of ± 1 K that was used for this preliminary measurement.

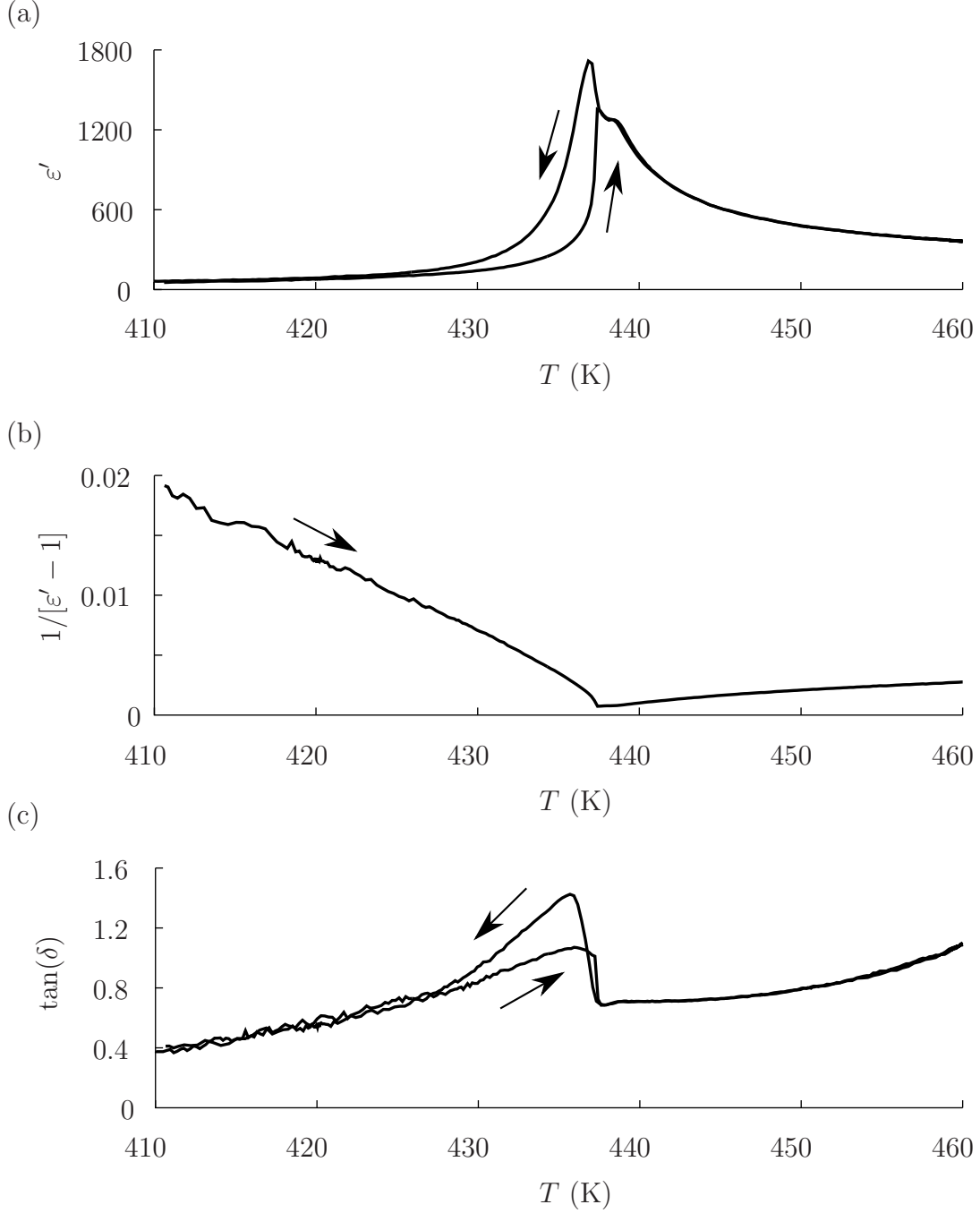


Figure 4.27: Dielectric data derived from an impedance dataset on the NaNO_2 crystal. The amplitude and frequency of the driving field were 1 V RMS and 1 kHz respectively. A parasitic capacitance of 0.7 pF was subtracted from the evaluated equivalent parallel capacitance, which was ~ 0.88 pF at low temperatures. Data for both heating and cooling are represented as indicated by arrows. The thermal ramp rate was around $\pm 1.0 \text{ K min}^{-1}$. **(a)** Dielectric constant, **(b)** reciprocal dielectric susceptibility, and **(c)** loss tangent, as functions of temperature.

4.3.4 $P(E)$ loops

Figures 4.28a-d show $P(E)$ loops for the NaNO_2 crystal, taken at 1 kHz, at various temperatures. Uncompensated and compensated major loops are shown, along with compensated minor loops. Compensation was performed using an estimate of equivalent parallel resistivity ϱ , simultaneously obtained from the raw data as described in Section 2.3. The spontaneous polarisation at 431 K was $\sim 4.4 \mu\text{C cm}^{-2}$, somewhat smaller than the literature value of $\sim 6.4 \mu\text{C cm}^{-2}$ [98]. The coercive field of $\sim 10 \text{ kV cm}^{-1}$ was large on account of the high driving frequency that was used to reduce the effect of losses on the data. Double loops corresponding to the antiferroelectric incommensurate phase were not seen. Equivalent parallel resistivity ϱ ranged from 10 – 35 $\text{k}\Omega \text{ m}$ (higher in the paraelectric phase) which was approximately two orders of magnitude smaller than the values measured for KNO_3 in Section 4.2.3.

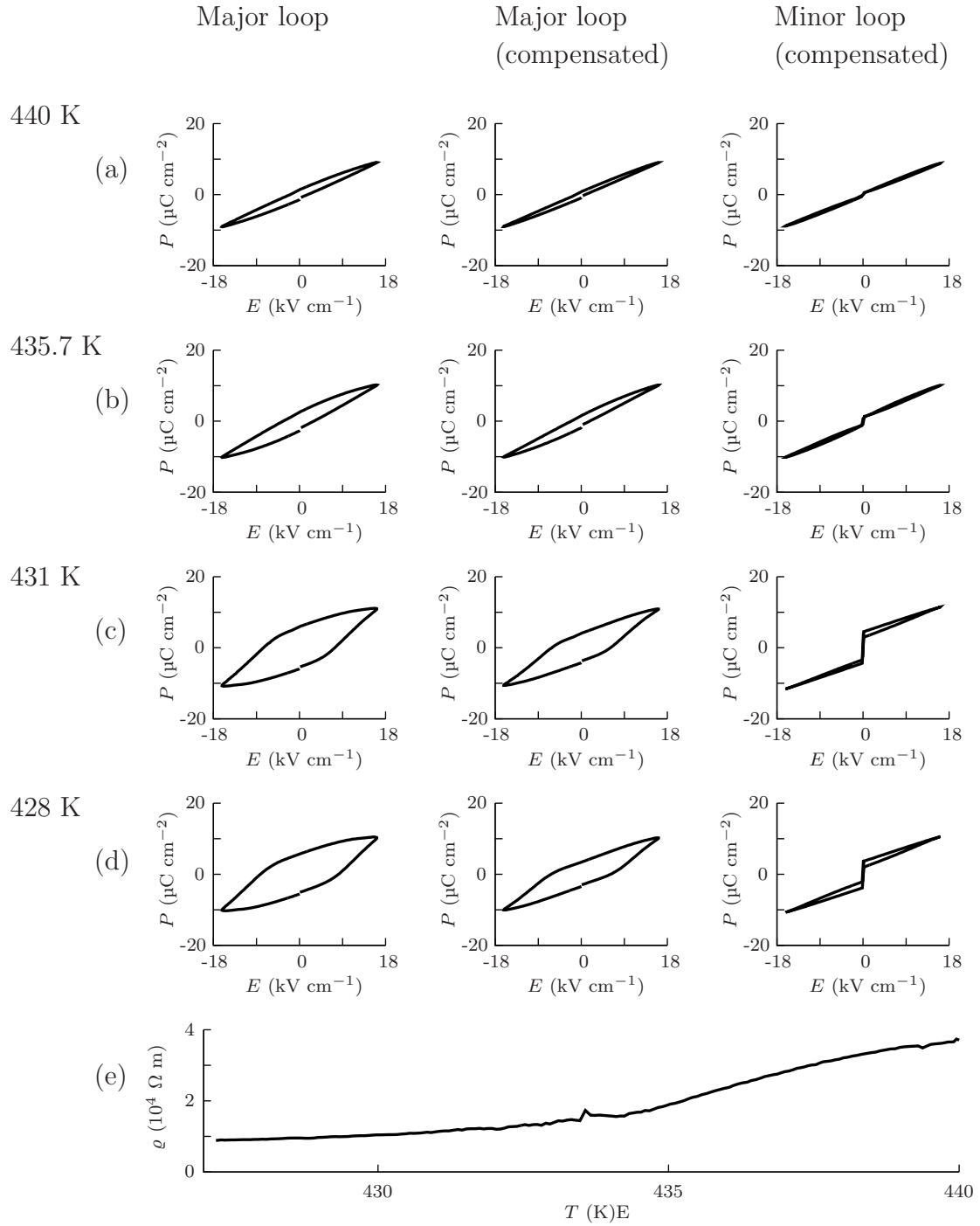


Figure 4.28: (a)-(d) $P(E)$ loops at 1 kHz on the NaNO₂ crystal at various temperatures near the Curie temperature. Major (switching), and minor (non-switching) loops are shown. (f) Equivalent parallel resistivity ϱ for Crystal A deduced from $P(E)$ data taken on cooling.

4.3.5 Isothermal $|\Delta S|$

To evaluate isothermal $|\Delta S|$ via the ‘standard’ method (Section 2.4), $P(E)$ loops were obtained for the NaNO_2 crystal every ~ 15 s during a temperature ramps at around ± 0.5 K min^{-1} . These loops were not compensated for losses, and were processed into $P(T)$ plots for evaluation of isothermal ΔS in the same way as for $(\text{NH}_4)_2\text{SO}_4$ (Section 4.1), using the CRC value of 2170 kg m^{-3} for the density of NaNO_2 [97]. It was not possible to perform the ‘resetting’ method due to time constraints, but because the phase transition of NaNO_2 is only weakly first-order and not strongly thermally hysteretic, the ‘standard’ method was considered likely to be valid.

The $P(T)$ plots (Figure 4.29) showed a gradual decline of P with temperature in the transition region. The largest value of isothermal $|\Delta S|$ was ~ 14 J K^{-1} kg^{-1} or 34.7 J K^{-1} dm^{-3} under a relatively small applied field of 15 kV cm^{-1} , representing an electrocaloric strength of ~ 0.9 J K^{-1} kg^{-1} $[\text{kV cm}^{-1}]^{-1}$. The peaks of isothermal $|\Delta S|$ were not highly symmetric and localised about T_C , as might be expected when applying the ‘standard’ indirect method to transitions that are thermally hysteretic, e.g. as seen for KNO_3 (Figure 4.23).

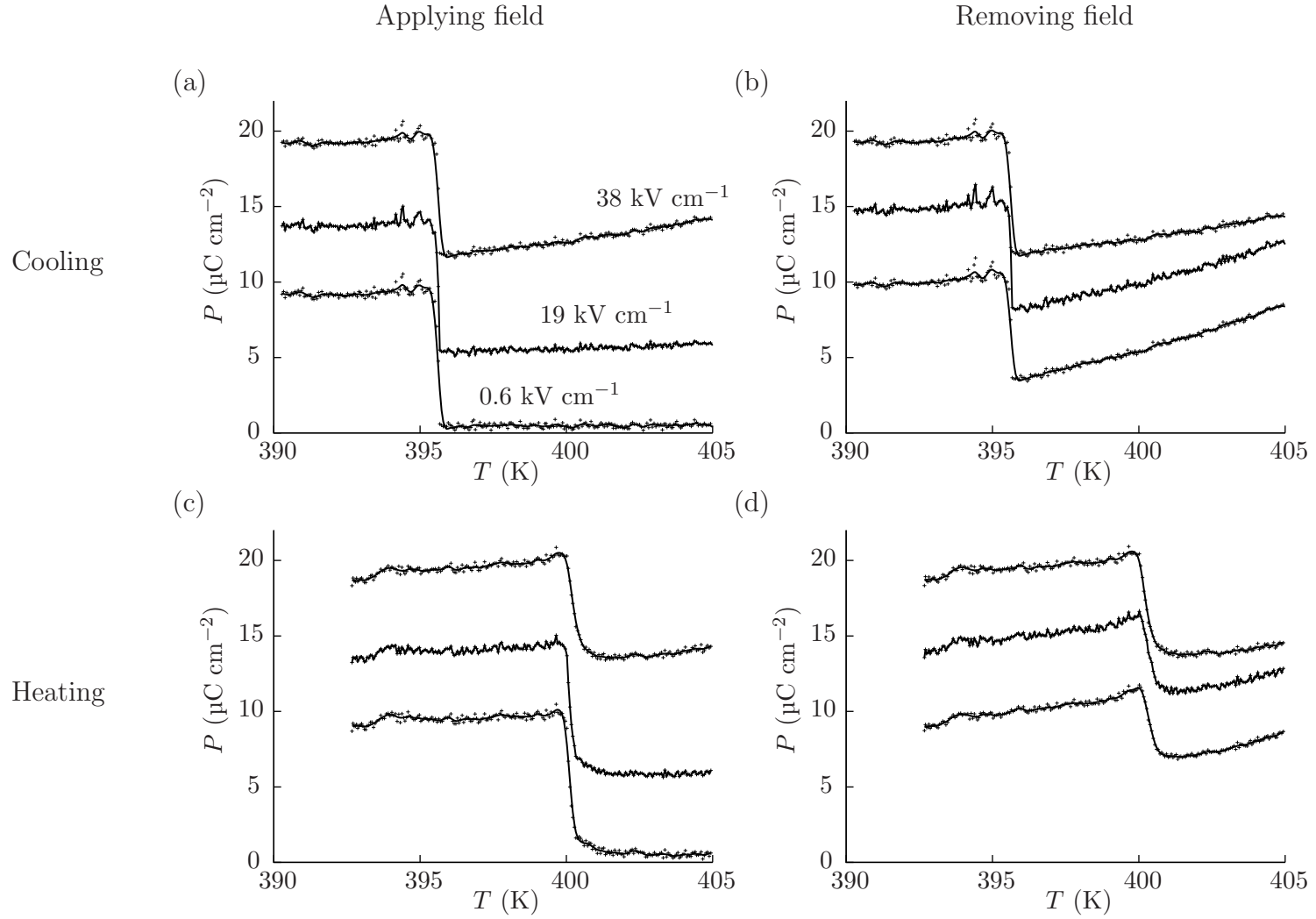


Figure 4.29: Selected $P(T)$ curves derived from $P(E)$ loops taken with the ‘standard’ method the NaNO_2 crystal. The four plots correspond to applying and removing a field (i.e. lower and upper branches of the minor loops) on heating and cooling. The three curves of each plot correspond to 16 kV cm^{-1} (upper line), 8 kV cm^{-1} (middle line) and 0.24 kV cm^{-1} (lower line) as indicated in (a). Points: raw (measured) data, lines: cubic spline fit.

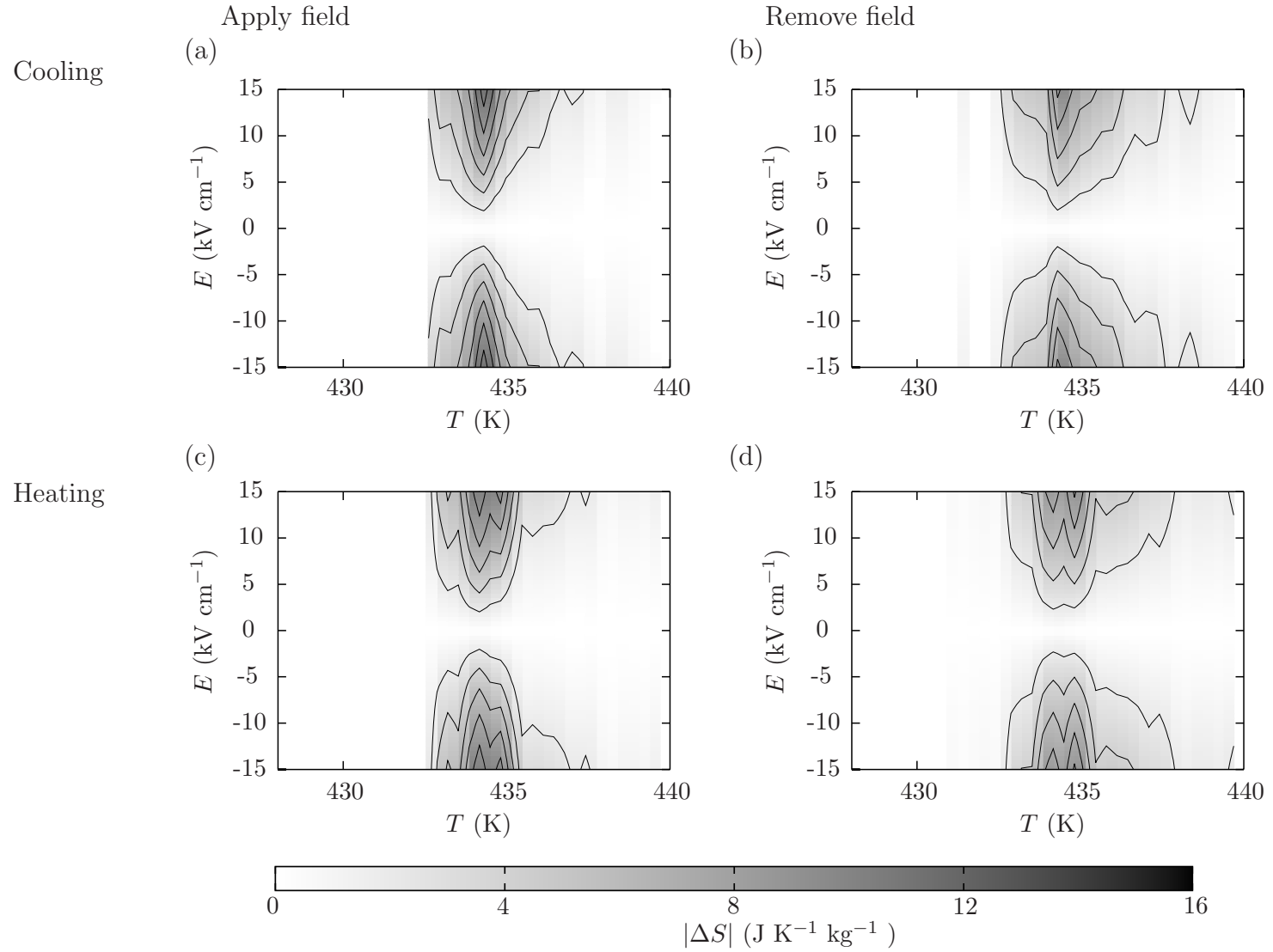


Figure 4.30: Isothermal $|\Delta S|$ for the NaNO_2 crystal evaluated via ‘standard’ indirect method. The four graphs correspond to applying and removing a field (i.e. lower and upper branches of the minor loops) on heating and cooling. Data for negative E : ‘mirror image’ of those for positive E . Contour spacing: 2 $\text{J K}^{-1} \text{kg}^{-1}$.

4.3.6 Conclusions

Preliminary and indirect experiments on a lossy bulk single crystal of NaNO_2 suggest an isothermal $|\Delta S|$ of $\sim 14 \text{ J K}^{-1} \text{ kg}^{-1}$ or $\sim 30 \text{ J K}^{-1} \text{ dm}^{-3}$ could be driveable with an electric field of $\sim 15 \text{ kV cm}^{-1}$ at temperatures near $T_C \sim 435 \text{ K}$. This corresponds to a ‘giant’ electrocaloric strength of $\sim 0.9 \text{ J K}^{-1} \text{ kg}^{-1} [\text{kV cm}^{-1}]^{-1}$. An electrocaloric strength of $\sim 0.5 \text{ J K}^{-1} \text{ kg}^{-1} [\text{kV cm}^{-1}]^{-1}$ in single crystals of BaTiO_3 was recently hailed by Moya *et al.* [10]. The initial focus of any future research on this material should be on growth of a sample with lower electrical conductivity.

Chapter 5

Electrocaloric effects in $\text{PbSc}_{0.5}\text{Ta}_{0.5}\text{O}_3$ ceramics

Oxides containing lead with perovskite-based crystal structures (or simply ‘lead-based perovskites’) have been a key focus in ferroelectrics since the 1950 discovery of ferroelectricity in PbTiO_3 [29]. The $\text{PbZr}_x\text{Ti}_{1-x}\text{O}_3$ (PZT) system has seen mass-market commercial exploitation in devices such as transducers, pyroelectric sensors and ferroelectric memories. Bulk PZT was one of the first materials to be measured for electrocaloric effects. Adiabatic temperature changes of $\Delta T = 1.6$ K were reported by Thacher (1968) [31] and $\Delta T = 2.4$ K was reported in a Nb- and Sn-doped bulk ceramic sample by Tuttle and Payne (1981) [34]. The first report of ‘giant’ electrocaloric effects of 12 K by Mischenko *et al.* (2006) was in 350 nm-thick films of $\text{PbZr}_{0.95}\text{Ti}_{0.05}\text{O}_3$ (Zr-rich PZT).

Perovskites have a molecular formula of ABX_3 , with *A*- and *B*-site cations, and anion *X* (often oxygen). The cubic perovskite structure (Figure 5.1) is normally drawn with the *A*-site cations in the corner positions, the *B*-site cations in the cube centre and the anions in centres of the cube faces [3]. This structure has a centre of inversion at the cube centre, so it corresponds to the paraelectric phase. The structure of the ferroelectric is traditionally considered to be a displacive distortion of the cubic structure [3]. The cubic structure is sometimes referred to as the ‘prototype’ structure [3]. Perovskite ferroelectrics can be poled locally along any high-symmetry axis of the unit cell.

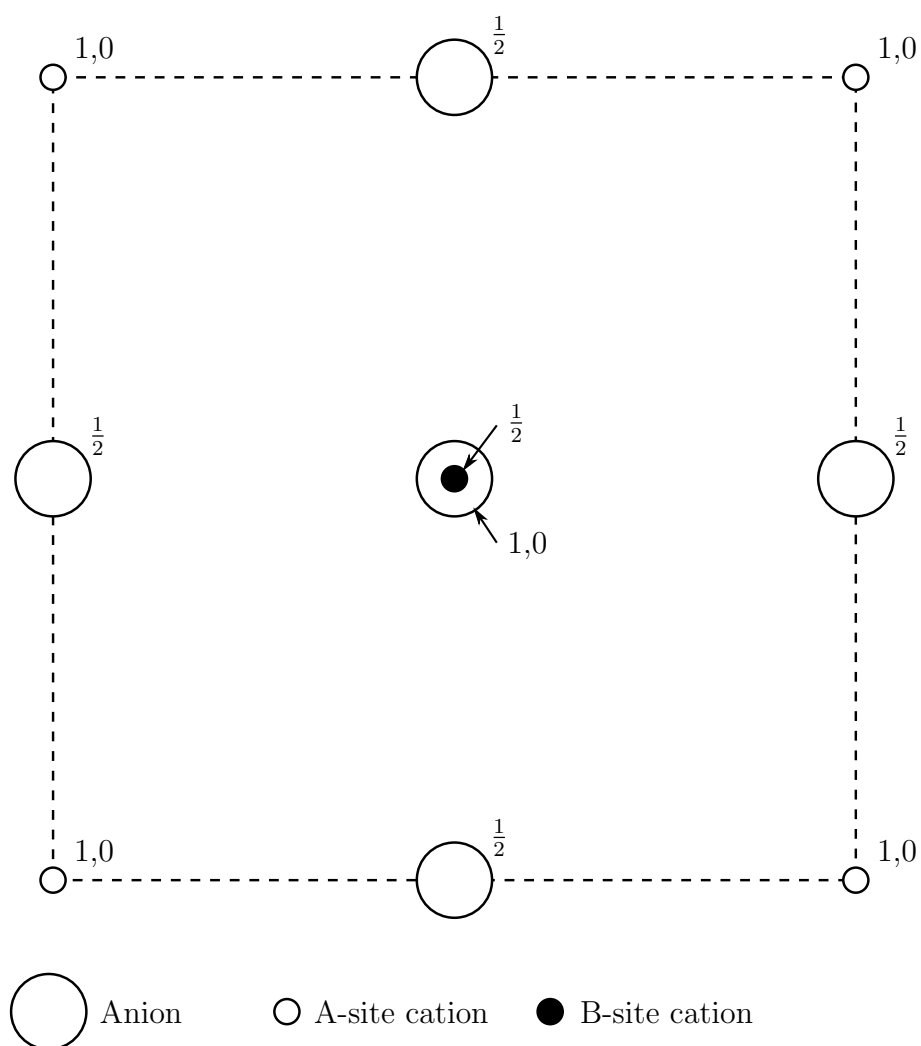


Figure 5.1: Many (but by no means all) ferroelectric materials have the cubic perovskite crystal structure (pictured) above T_C [3]. The ferroelectric phase is traditionally considered to be a displacive distortion of this ‘prototype’ cubic perovskite structure.

A key drawback of all lead-containing materials is toxicity. There is now a broad global consensus, increasingly reflected in legislation, that superior properties of lead-containing materials rarely, if ever, justify the impact or potential for impact on public health. With recent studies proposing a link between pre-school blood lead levels and the level of social violence, this trend is unlikely to reverse [142] [143].

5.1 Lead scandium tantalate

Stenger *et al.* (1979-80) [144–146] were the first to provide a full description of the ferroelectric properties of lead scandium tantalate ($\text{PbSc}_{0.5}\text{Ta}_{0.5}\text{O}_3$, ‘PST’) for various levels of cation ordering. A widely-cited paper of Setter and Cross (1980) [147] reporting similar findings, followed shortly after. PST has a perovskite structure at high temperatures, with Pb as the *A*-site cation, O as the anion and Sc and Ta distributed in equal proportions over the *B*-sites. A distribution where Sc and Ta are each arranged in alternating *B*-site positions throughout the lattice is termed ‘cation ordered’, whereas a random distribution is termed ‘cation disordered’. Cation ordering Ω is quantified as $2n - 1$, where n is the fractional occupation of alternating *B*-sites with a particular cation, Sc or Ta. Thus $\Omega = 1$ corresponds to full ordering, and $\Omega = 0$ to minimum ordering. Cation-ordered PST is a ferroelectric with a first-order displacive transition at ~ 295 K, whereas lower levels of cation ordering lead to relaxor behaviour [147]. The value of Ω is readily measured via X-ray diffraction [15, 144]. PST has been extensively studied as a prototypical relaxor ferroelectric because it is straightforward to modify the degree of cation ordering with annealing.

The electrocaloric properties of PST were studied in a series of papers from 1988 to 2001 by L. A. Shebanovs and coworkers. Their paper of 1988 [35] described the field-driven paraelectric-ferroelectric phase transition for $\Omega = 0.8$ observed via X-ray diffraction. Adiabatic $|\Delta T|$ was directly measured, showing a peak value of 1.7 K with a field change of $|\Delta E| = 25 \text{ kV cm}^{-1}$ near the transition temperature¹. The Shebanovs paper of 1992 [36] reported the effect on electrocaloric properties of substituting $\sim 5\%$ of the Ta ions in $\Omega = 0.85$ PST with various dopants — In, Ga, Mn, Ni, Fe, Co, Zn, Y, V, Sb, Nb, Ti, Zr, Hf and Sn. The best performing dopant was Sb, giving $|\Delta T| \sim 2$ K

¹There is an apparent contradiction with respect to [35] in that the transition temperature given of ~ 275 K corresponds to cation disordered PST, but the X-ray and electrocaloric data suggested that the sample was highly cation ordered. This issue was not addressed in the paper and could imply an error.

for a field change of 50 kV cm^{-1} . Electrocaloric effects in relaxor PST with nominal values of $\Omega = 0.34$ and $\Omega = 0.0$ were also investigated and found to show broader, smaller peaks in $|\Delta T(T)|$ than for $\Omega = 0.85$ (the largest effects were $|\Delta T| = 0.6 \text{ K}$ for $\Omega = 0.34$ and $|\Delta T| = 0.25 \text{ K}$ for $\Omega = 0.0$). In the Shebanovs paper of 1995 [37], effects of $|\Delta T| \sim 2.3 \text{ K}$ were reported in a pure $\Omega = 0.85$ sample that was subjected to a field change of 50 kV cm^{-1} . In the final Shebanovs paper of 2001 [38], the $|\Delta T| \sim 2.3 \text{ K}$ effects were also observed in Co- and Sb-doped PST ceramics, and multilayer capacitors with a dielectric layer thickness of $\sim 70 \text{ }\mu\text{m}$ and Pt electrodes ($|\Delta E| = 138 \text{ kV cm}^{-1}$).

Thin films of PST have also been studied for electrocaloric effects. Correia *et al.* [50] reported effects of up to $|\Delta T| = 6.9 \text{ K}$ at $\sim 390 \text{ K}$ evaluated via the indirect method, in 350 nm -thick films of polycrystalline $\Omega = 0.32$ PST under a large field change of 774 kV cm^{-1} and at a temperature of $\sim 100 \text{ }^\circ\text{C}$. The corresponding results at room temperature showed $|\Delta T| \sim 3.5 \text{ K}$.

5.2 Samples

Ceramic samples of $\Omega = 0.65$ PST were provided by Roger W. Whatmore. The samples were made in the 1980s and 90s by Osbond and Whatmore (GEC Marconi). The following description of the fabrication process was given by Whatmore:

‘The PST ceramic samples were fabricated using the mixed-oxide method described by Osbond and Whatmore (1992) [148]. Sc_2O_3 and Ta_2O_5 powders were milled together and then pre-reacted at 900 °C to form a wolframite ScTaO_4 phase. This was then reacted with PbO at 900 °C to form a single-phase perovskite powder, which was subsequently hot-pressed in Si_3N_4 tooling and an alumina grit packing medium at 40 MPa and 1200 °C for 6 hours.’

The dielectric properties of comparable PST ceramics for various DC bias fields were reported by Shorrocks, Whatmore and Osbond [149]. The permittivity at zero DC bias rose to ~ 10000 at the Curie temperature of ~ 298 K. Application of a DC bias broadened and lowered the peak, and shifted it to higher temperatures as expected for a first-order phase transition obeying the Clausius-Clapeyron equation $dT/dE = P_S/|\Delta S|$.

The PST ceramic samples had a plate-like geometry with thickness of order ~ 1 mm and area of several square centimeters. The rough surface was opaque and light yellow-green, but samples became almost transparent if polished flat with 4000 grade sandpaper. Samples with a thickness of several 100s of microns were fabricated by polishing by hand with 1200 grade sandpaper, with the sample superglued to a glass slide (after polishing, samples were freed with acetone). Rough surfaces were used because they were observed to be more resistant to electrical arcing at high voltages. Pt electrodes were deposited by sputtering as described in Section 4.1.2. The thickness of the samples was measured using a digital caliper. A clearance of at least 0.5 mm was left between the edge of the top electrodes and the edge of each sample to suppress arcing. A typical electrode area was $\sim 0.25 \text{ cm}^2$.

5.3 Measurement strategy

Electrical and electrocaloric data will be presented on four samples. Sample A had a thickness of 420 μm and an electrode area of 0.29 cm^2 . Sample B had a thickness of 450 μm and an electrode area of 0.27 cm^2 . Sample C had a thickness of 390 μm and an electrode area of 0.35 cm^2 . The collaboration of Olatz Idigoras is acknowledged in preparing and electroding samples B-C.

For electrical and electrocaloric measurements, an insulating layer of kapton tape was laid on the surface of probe head 2 (see Section 3.1), and samples were mounted flat on top with silver paste adhesive and electrically resistive grease around the upper high-voltage electrode to suppress arcing. Arcing nonetheless imposed an upper limit on the voltages that could be applied. For qualitative measurements of ΔT , a K-type thermocouple was used as described in Section 2.1. For quantitative measurements of ΔT , scanning thermal atomic force microscopy (SThM) and infra-red thermometry were used.

SThM was performed in collaboration with Sohini Kar-Narayan. The use of SThM for direct electrocaloric measurements on multilayered capacitors has been described by Kar-Narayan *et al.* [52]. The tips for SThM (type DM-GLA-1, Anasys Instruments) were supplied patterned with a ~ 1 μm -scale platinum thermometer. Because of the small size and small thermal mass of these thermometers, SThM has been suggested for direct thermometry of micro or nano-scale electrocaloric devices [52]. A Wheatstone bridge (type nano-TA2, Anasys Instruments) was used to monitor the ~ 270 Ω resistance of the SThM tip. The tip was mounted in a tip-scanning AFM (type Dimension with Nanoscope V controller, Veeco). The SThM tip was pre-calibrated using a Pt-100 thermometer as a simultaneous thermometer and heater, as described in [52].

Infra-red thermometry was also suggested and demonstrated for electrocaloric measurements by Kar-Narayan *et al.* [52]. Infra-red sensors can deduce the temperature of a black body by measuring the intensity of its radiation at various wavelengths. The temperature of non black-bodies can also be measured via an emissivity correction. The instrument described in the relevant part of [52] was an infra-red camera which provided spatially-resolved thermal images of a sample. In contrast, the device used for the present work was a point-detector (type CS LT 15, Optris GmbH). The detector was supplied in a rod-shaped metal enclosure of length 9 cm and diameter 12 mm. The spectral range was 8-14 μm in wavelength. A close-focus lens was fitted (type

ACCTCF, Optris) giving a spot size of diameter 0.8 mm on the sample which lay at the focal point, 1 cm from the lens. Data acquisition was via a USB interface supplied with the sensor. The surface of each PST sample was coated in silver paint, and therefore, for calibration purposes, the copper heat reservoir of the bespoke high-temperature stage (Section 3.2) was also coated with silver paint and heated to 330 K in air. The temperature of this surface was then measured with the infra-red sensor, allowing the calibration factor for silver paint to be deduced.

5.4 Dielectric constant

Figure 5.2a shows the dielectric constant of Sample A as a function of temperature, measured at 1 kHz using the equivalent parallel capacitance model (Section 2.2). The sample was mounted in probe head 2 (Section 3.1) and temperature was ramped at around $\pm 0.5 \text{ K min}^{-1}$. The data reveal a $\sim 4 \text{ K}$ thermal hysteresis on heating or cooling through T_C . The peak value of ϵ' was $\sim 11,000$, in agreement with published data on these samples from the 1990s [149]. The Curie-Weiss constant above T_C was $\sim 300 \text{ kK}$ (Figure 5.2b). The dielectric loss tangent was very small above $\sim 320 \text{ K}$, rising to a peak value of ~ 0.05 at T_C , and then falling to ~ 0.04 as temperature was further reduced to 240 K (Figure 5.2c).

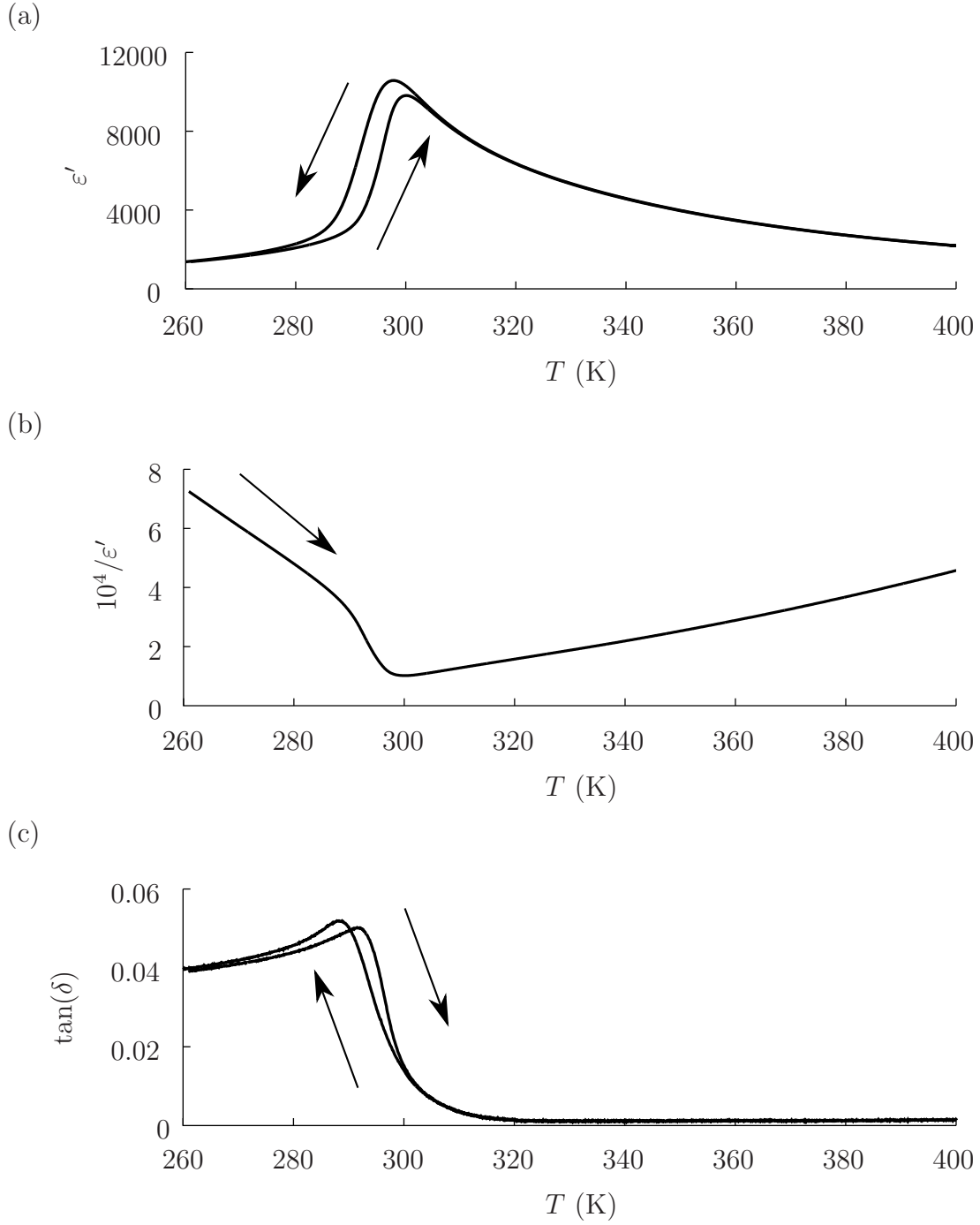


Figure 5.2: Dielectric data on PST Sample A (equivalent parallel capacitance model). The amplitude and frequency of the driving field were 1 V RMS and 1 kHz respectively. Data for heating and cooling are represented as indicated by arrows. The thermal ramp rate was around $\pm 0.5 \text{ K min}^{-1}$. **(a)** Dielectric constant as a function of temperature. **(b)** Reciprocal of dielectric susceptibility as a function of temperature. **(c)** Loss tangent as a function of temperature.

5.5 Zero-field ΔS

Heat-flow vs temperature measurements were performed on heating and cooling a 13.249 mg sample of ceramic PST at 5 K min⁻¹ as described in Section 2.5.

Measurements were performed by Robert Cornell. The specific heat capacity anomaly on heating was integrated to give a transition heat Q of 924 J kg⁻¹, and associated transition entropy ΔS of 3.13 J K⁻¹ kg⁻¹ or 28.4 J K⁻¹ dm⁻³, using the value for density of 9071 kg m⁻³ given by Shebanov *et al.* [35] (Figure 5.3a). Figure 5.3b shows specific heat capacity data that contained an offset in heat flow. The specific heat capacity was therefore estimated by requiring c_E on heating and cooling to be equal at 330 K, giving an offset of ~ 136 J K⁻¹ kg⁻¹ which was added to the heating curve and subtracting from the cooling curve (Figure 5.3c). The specific heat capacity above the transition temperature was ~ 400 J K⁻¹ kg⁻¹. Figure 5.3d shows the calculated entropy change with respect to the entropy at 280 K on heating and cooling. The latent entropy of the transition is barely discernable over the background.

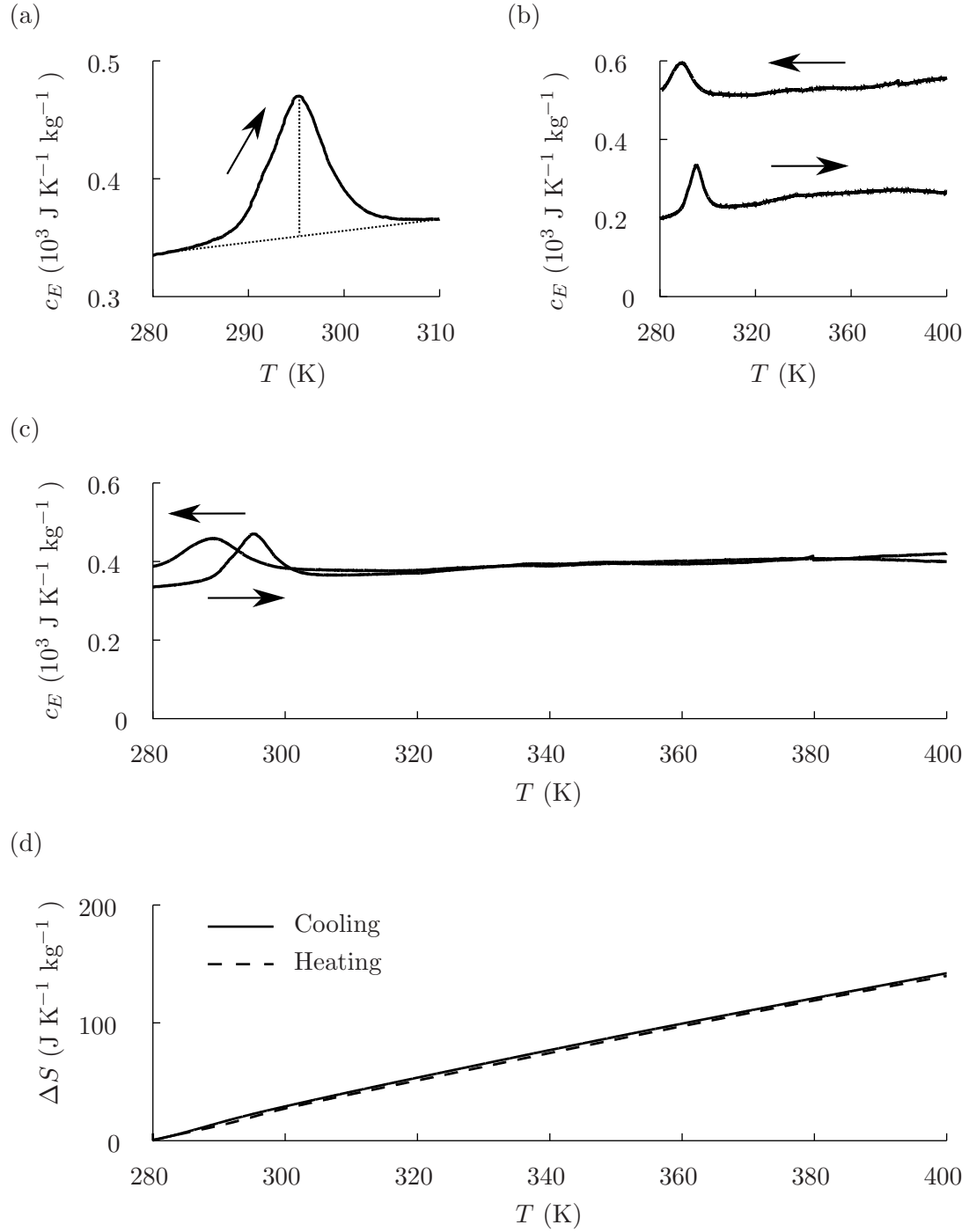


Figure 5.3: Calorimetry results for PST taken on heating and cooling at $\pm 5 \text{ K min}^{-1}$. **(a)** Specific heat capacity anomaly c_E on heating, which was integrated to give the total transition heat. **(b)** Specific heat capacity c_E for PST evaluated from raw heat-flow data that contained an offset. **(c)** Specific heat capacity with offset averaged out. **(d)** Zero-field $\Delta S(T)$ with respect to the entropy at 280 K, derived from the specific heat capacity curve with offset subtracted. Transition seen in (c) is barely perceptible in (d).

5.6 $P(E)$ loops

Figure 5.4 shows $P(E)$ data on the 420 μm -thick PST Sample A taken at 1 Hz and at various temperatures near T_C . At 280 K an open major loop was observed, which became slightly slimmer when temperature was increased to 292.5 K. At 295 K offset subloops became noticeable in the minor loop, corresponding to a transition partially driven by field to completion. By 297.5 K, the subloops were also visible in the major loop. Just above 300 K, in the paraelectric phase, the subloops represented a completely driven paraelectric-ferroelectric phase transition, and formed the dominant feature of both the major and minor loops. As temperature was increased further, the offset of the subloops progressed to higher fields as expected from the inverse Clausius-Clapeyron equation $dE/dT = |\Delta S|/P_S$. At 320 K, only a linear paraelectric signal remained.

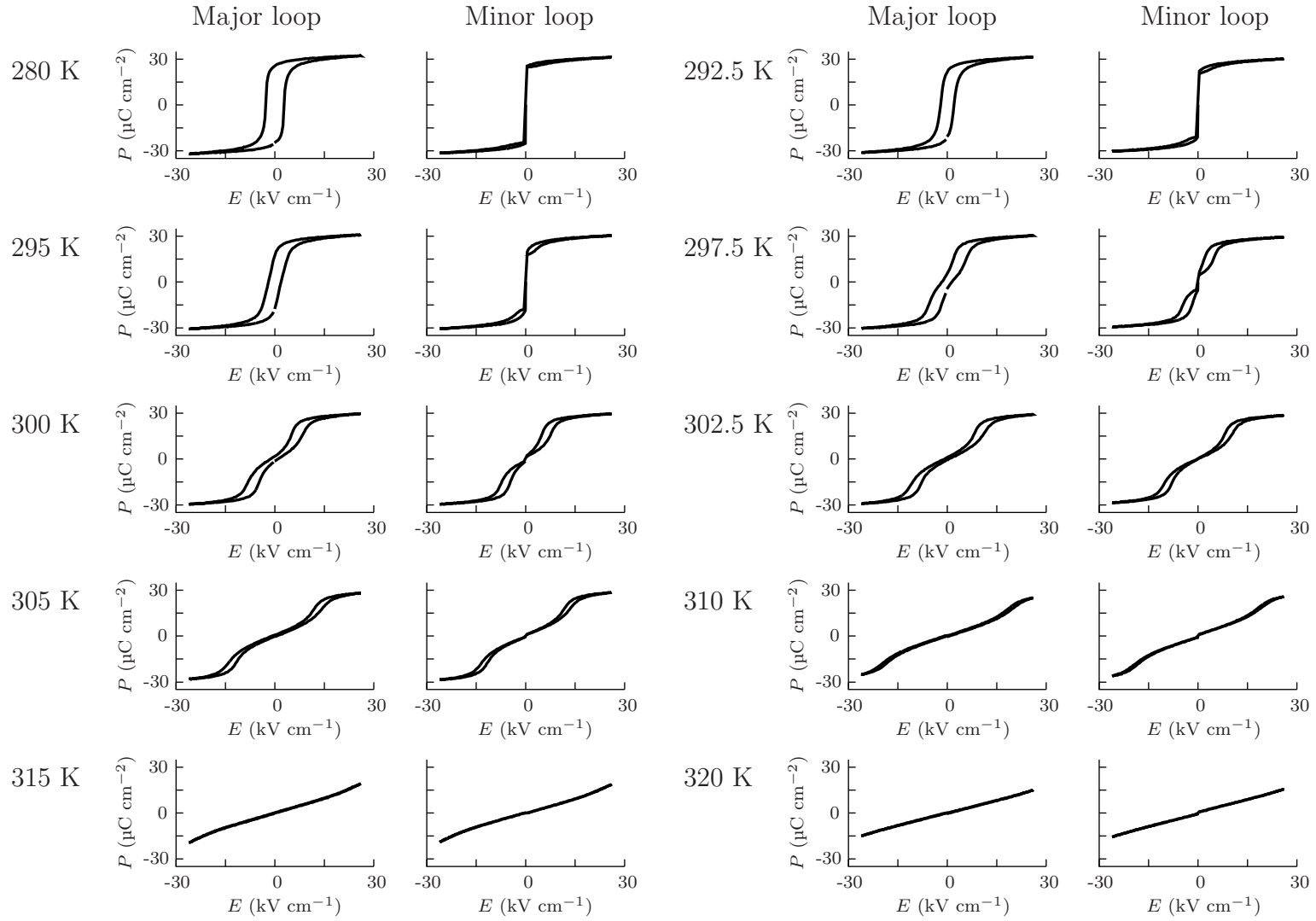


Figure 5.4: $P(E)$ loops at 1 Hz for PST Sample A (420 μm -thick) at various temperatures. For each temperature, both major and minor loops are shown.

5.7 Isothermal $|\Delta S|$

To evaluate isothermal $|\Delta S|$ via the ‘standard’ indirect method, $P(E)$ loops were obtained for Crystal A, as described in Section 5.6, every ~ 15 s during temperature ramps at around ± 0.5 K min^{-1} . These data were transposed to $P(T)$ (Figure 4.9), and cubic splines were fitted to eliminate spurious fluctuations (Figure 5.5). The fitted splines were differentiated with respect to T , yielding $\partial P/\partial T$ at various fields E , which was numerically integrated to give volume-normalised and mass-normalised values of isothermal $|\Delta S|$ via the Maxwell relation $(\partial P/\partial T)_E = (\partial S/\partial E)_T$ and the literature value for density of 9071 kg m^{-3} [35].

Figure 5.6 shows the evaluated isothermal $|\Delta S|$ as a function of T and $|E|$ for applying a field (i.e. using the lower branch of the minor loops) and removing a field (i.e. the upper branches of the minor loops) for $P(E)$ data obtained on heating and cooling. A finite-width line in $E - T$ space corresponding to a paraelectric-ferroelectric phase boundary obeying the Clausius-Clapeyron equation $dE/dT = |\Delta S|/P_S$ was observed, in all cases. The field-driven transition broadened as temperature was increased from $T_C \sim 295$ K. The gradient of the field-driven transition line was $dE/dT \sim 1.2$ kV cm^{-1} K^{-1} , in reasonable agreement with the value of $|\Delta S|/P_S \sim 28.4/32 \sim 0.9$ kV cm^{-1} K^{-1} .

From ~ 300 K to ~ 312 K under a 26 kV cm^{-1} driving field, the evaluated isothermal $|\Delta S|$ showed a sloped plateau from ~ 3.25 J K^{-1} kg^{-1} to ~ 2.25 J K^{-1} kg^{-1} (or ~ 30 J K^{-1} dm^{-3} to ~ 20 J K^{-1} dm^{-3}) before falling off more steeply at higher temperatures (Figure 5.7a). The maximum isothermal $|\Delta S|$ of ~ 3.25 J K^{-1} kg^{-1} showed good agreement with the zero-field entropy change of 3.13 J K^{-1} kg^{-1} (Figure 5.3). A small hysteresis in $|\Delta S(E)|$ was observed. The hysteresis was ~ 2.5 kV cm^{-1} at 305 K (Figure 5.7b). It was unsurprising to observe hysteresis in E when the transition was driven electrically, given that the transition was hysteretic in T when driven thermally (Figure 5.2).

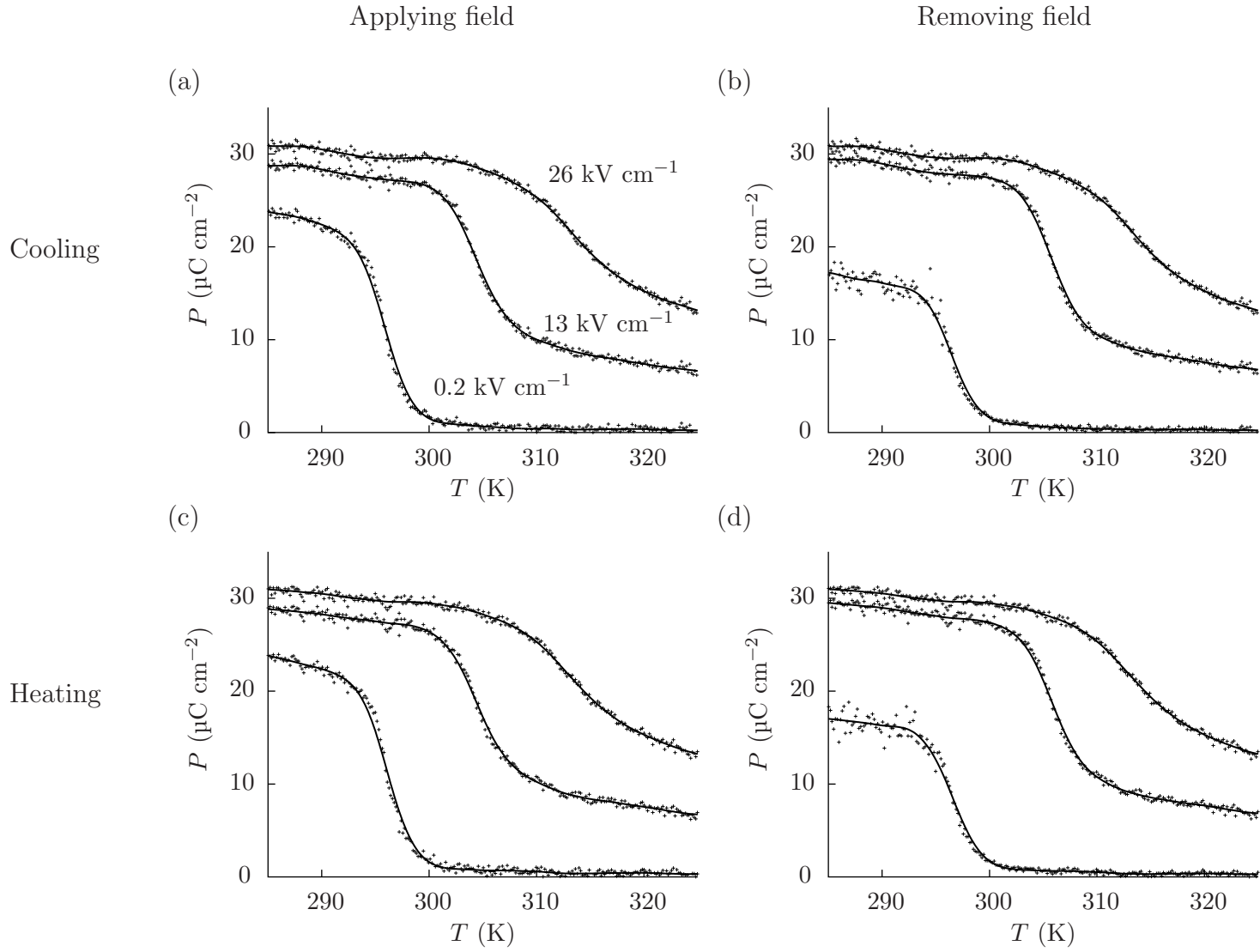


Figure 5.5: Selected $P(T)$ derived from $P(E)$ loops for PST Sample A. The four graphs correspond to applying and removing a field (i.e. lower and upper branches of the minor loops) on heating and cooling. The three plots of each graph correspond to 26 kV cm^{-1} (upper line), 13 kV cm^{-1} (middle line) and 0.25 kV cm^{-1} (lower line) as indicated in (a). Points: raw (measured) data, lines: cubic spline fit.

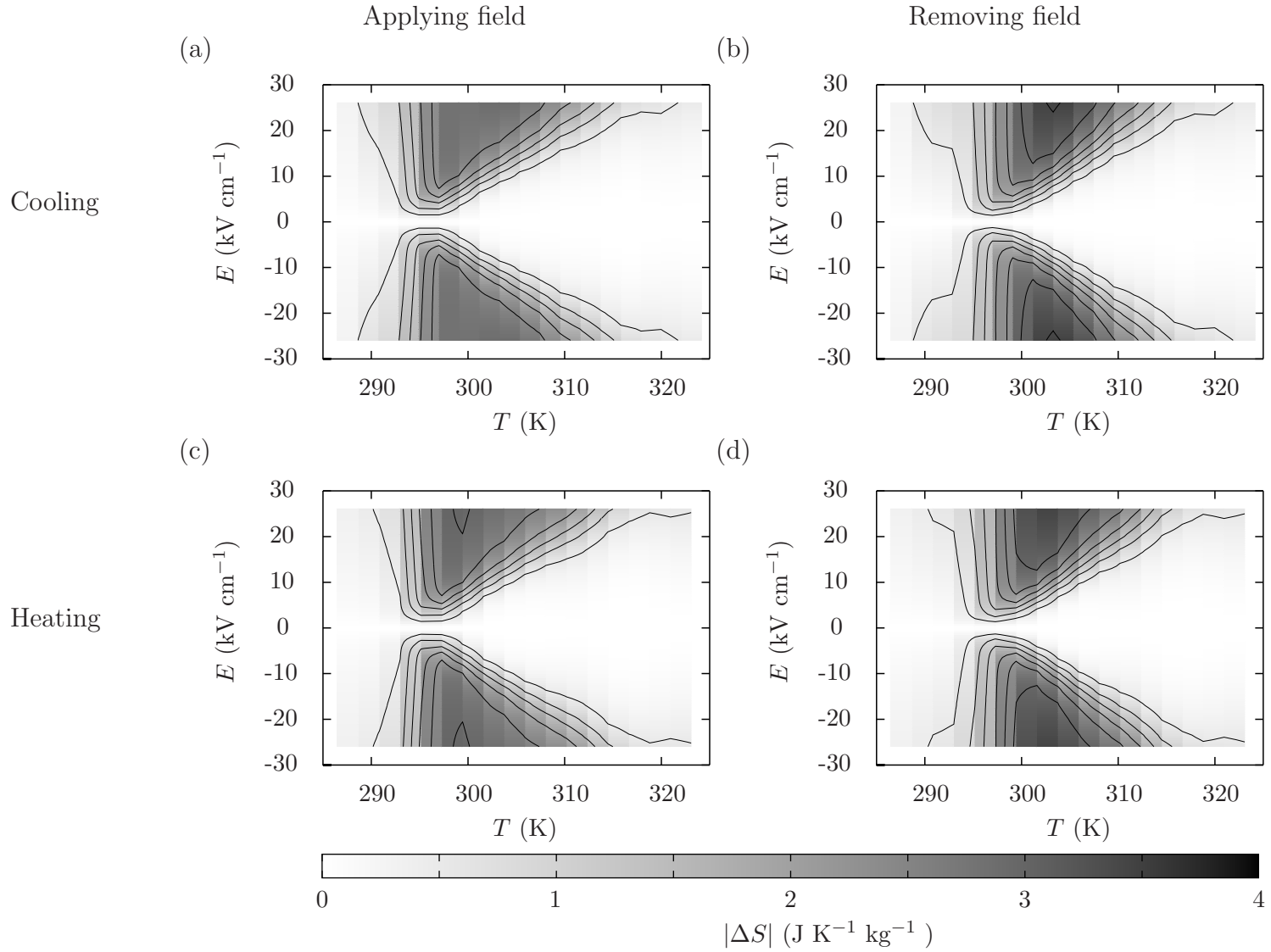


Figure 5.6: Isothermal $|\Delta S|$ for for PST Sample A evaluated via ‘standard’ indirect method. The four graphs correspond to applying and removing a field (i.e. lower and upper branches of the minor loops) on heating and cooling. Data for negative E : ‘mirror image’ of those for positive E . Contour spacing: $0.5 \text{ J K}^{-1} \text{kg}^{-1}$.

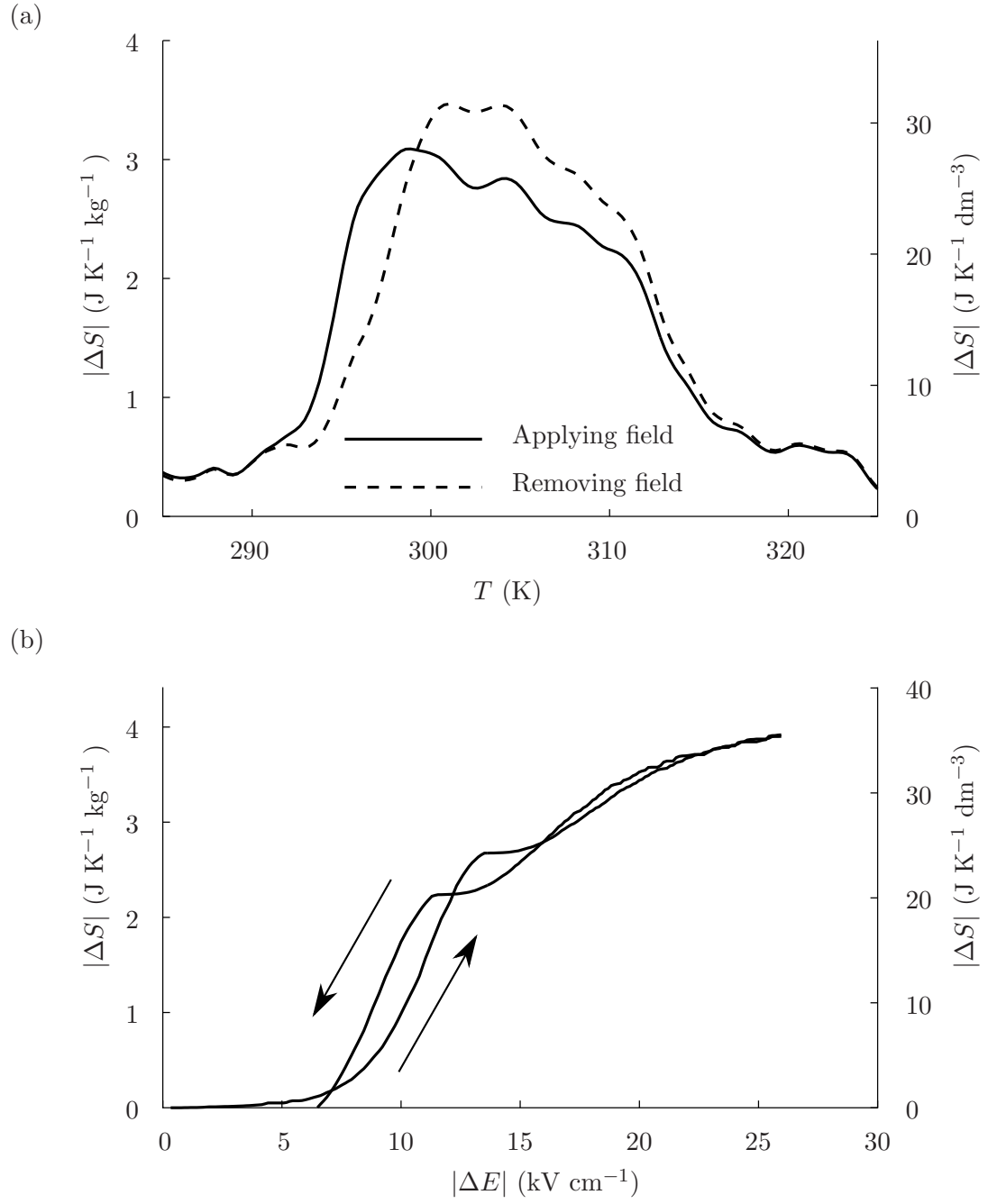


Figure 5.7: Isothermal $|\Delta S|$ for PST Sample A evaluated via ‘standard’ indirect method. as a function of **(a)** T for $|\Delta E| = 26 \text{ kV cm}^{-1}$, and **(b)** $|\Delta E|$ for $T = 305 \text{ K}$.

5.8 Adiabatic $|\Delta T|$ (via indirect method)

Having evaluated *zero-field* ΔS for PST (Figure 5.3d), and having independently evaluated *isothermal* $|\Delta S(E)|$ at various temperatures via the Maxwell analysis on $P(E)$ data (Figure 5.6), it was possible to construct a *map* of ΔS in $E - T$ space by subtracting the isothermal $|\Delta S(E)|$ from the zero-field $\Delta S(T)$. This was performed on the ‘standard’ indirect datasets of isothermal $|\Delta S|$ for applying a field on heating (Figure 5.6c), and removing a field on heating (Figure 5.6d). Small systematic errors in T were expected when combining data taken with two different cryostats. To account for this error, the temperature scale of the calorimetric dataset was shifted up by 5 K such that the peak point of specific heat capacity lay at 300 K, i.e. the temperature at which the peak in dielectric constant on heating had been measured in probe head 2 (Figure 5.2).

Figure 5.8 shows lines of constant S — adiabats — in $E - T$ space from the compiled $\Delta S(E, T)$ dataset. Adiabatic application of an electric field ΔE will drive the system along a path that results in temperature change ΔT . The adiabats diverged slightly from isotherms below T_C , and this divergence became more pronounced above ~ 293 K. Above ~ 300 K, the transition required a non-zero ‘critical field’ to drive it. This ‘critical field’ was an almost linear function of temperature, as previously observed for isothermal $|\Delta S(E)|$ (Figure 5.6) and again consistent with a field-driven transition obeying the Clausius-Clapeyron equation.

For the maximum field change of 26 kV cm^{-1} , the evaluated $|\Delta T(T)|$ is shown in Figure 5.9. A plateau was observed from ~ 298 K to ~ 310 K, corresponding to the regime in which the full paraelectric-ferroelectric transition was driven with the applied field. The value of $|\Delta T|$ was ~ 2.2 K in this range of temperatures. Outside of the plateau region, smaller values of $|\Delta T|$ were observed corresponding to partial driving of the phase transition.

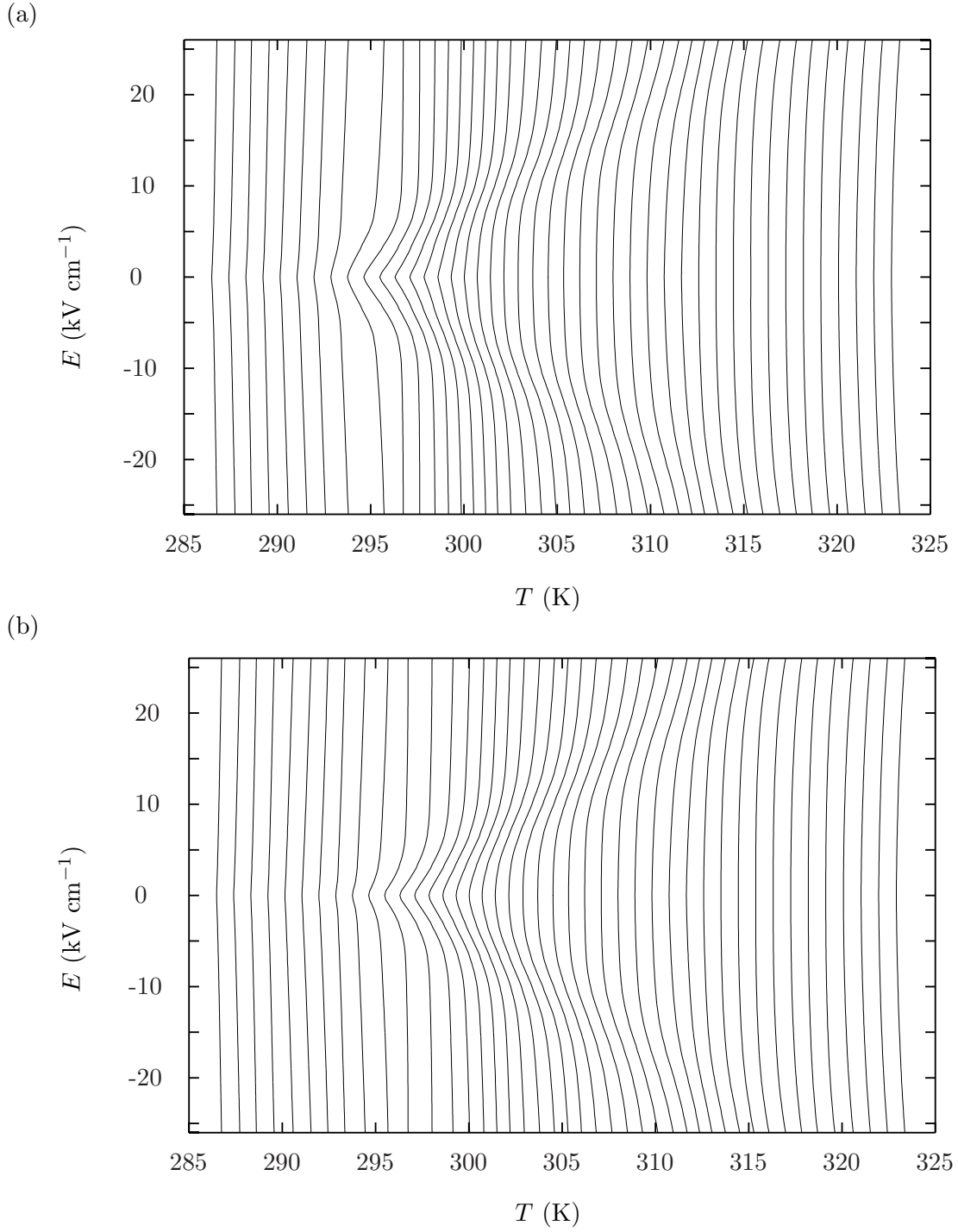


Figure 5.8: Adiabats in $E - T$ space for PST Sample A (420 μm -thick) for **(a)** applying a field and **(b)** removing a field. Data were compiled from two separate measurements, zero-field $\Delta S(T)$ from calorimetry data (Figure 5.3), and isothermal $|\Delta S(E)|$ (Figure 5.6c-d) evaluated via the Maxwell relation from a dataset of $P(E)$ loops taken on heating.

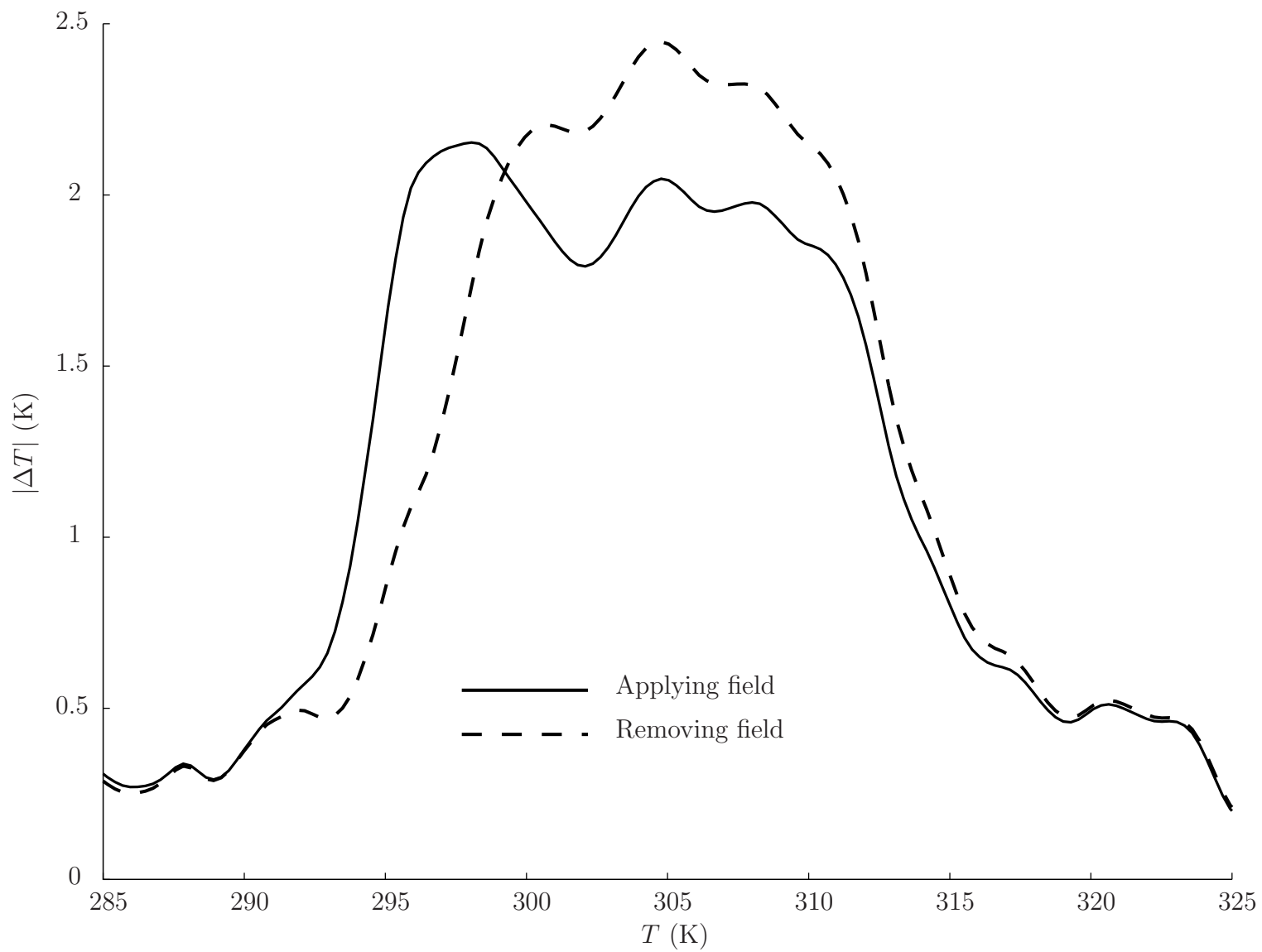


Figure 5.9: Indirectly evaluated adiabatic $|\Delta T|$ for PST Sample A (420 μm -thick) on applying or removing a field of 26 kV cm^{-1} .

5.9 Adiabatic $|\Delta T|$ (via direct method)

Various direct measurements of nominally adiabatic ΔT were performed. Sample B was mounted flat on probe head 2, and ΔT was measured as a function of applied field and starting temperature via a K-type thermocouple, as described in Section 2.1. Due to flat-mounting on copper and also the fact that only $\sim 40\%$ of Sample B was electroded, the measurement was affected by unknown heat leaks. Thus, the measured values of ΔT were reduced by an unknown factor, and are accordingly quoted in ‘arbitrary units’. Quantitative measurements were performed via scanning thermal atomic force microscopy (SThM) and infra-red (IR) thermometry, on Samples A and C, at room temperature. The SThM and IR measurements complemented those of the flat-mounted experiment which had the advantage of high resolution in T and E .

The plots shown in Figure 5.10, corresponding to the flat-mounted experiment for PST Sample B, were each compiled in a three-step cycle:

- Temperature was ramped to 320 K, thus ‘resetting’ the sample to the paraelectric phase.
- Temperature was stabilised at the measurement temperature indicated on the *inner y-axis*.
- ΔT (shown on the outer *y-axis*, in arbitrary units) was monitored as a function of time (inner *x-axis*), while a 24 kV cm^{-1} driving field was applied for 30 s and removed for 30 s, twice in succession (outer *x-axis*).

The data showed that small electrocaloric temperature changes occurred at the highest starting temperature of 320 K, but the maximum changes occurred from $\sim 298 \text{ K}$ to $\sim 310 \text{ K}$. Below $\sim 298 \text{ K}$, the *initial* field change resulted in a larger temperature change than subsequent field changes, as these temperatures corresponded to the zero-field phase-coexistence regime, and the initial field-driven paraelectric-ferroelectric transition was not fully reversible in field.

Figure 5.11, compiled from the same dataset as Figure 5.10, shows the temperature dependence of the directly measured $|\Delta T|$ (in arbitrary units) for a field change of magnitude 24 kV cm^{-1} . The $|\Delta T|$ below $\sim 298 \text{ K}$ was larger for applying a field than for removing a field, as the initial field-driven paraelectric-ferroelectric transition was not fully reversible. Above $\sim 297 \text{ K}$, the data were in good qualitative agreement with the

corresponding data obtained indirectly (Figure 5.9). A future ‘resetting’ indirect measurement might be able to observe the asymmetry of $|\Delta T|$ on applying and removing a field, seen at $T < 297$ K in direct data (Figure 5.11).

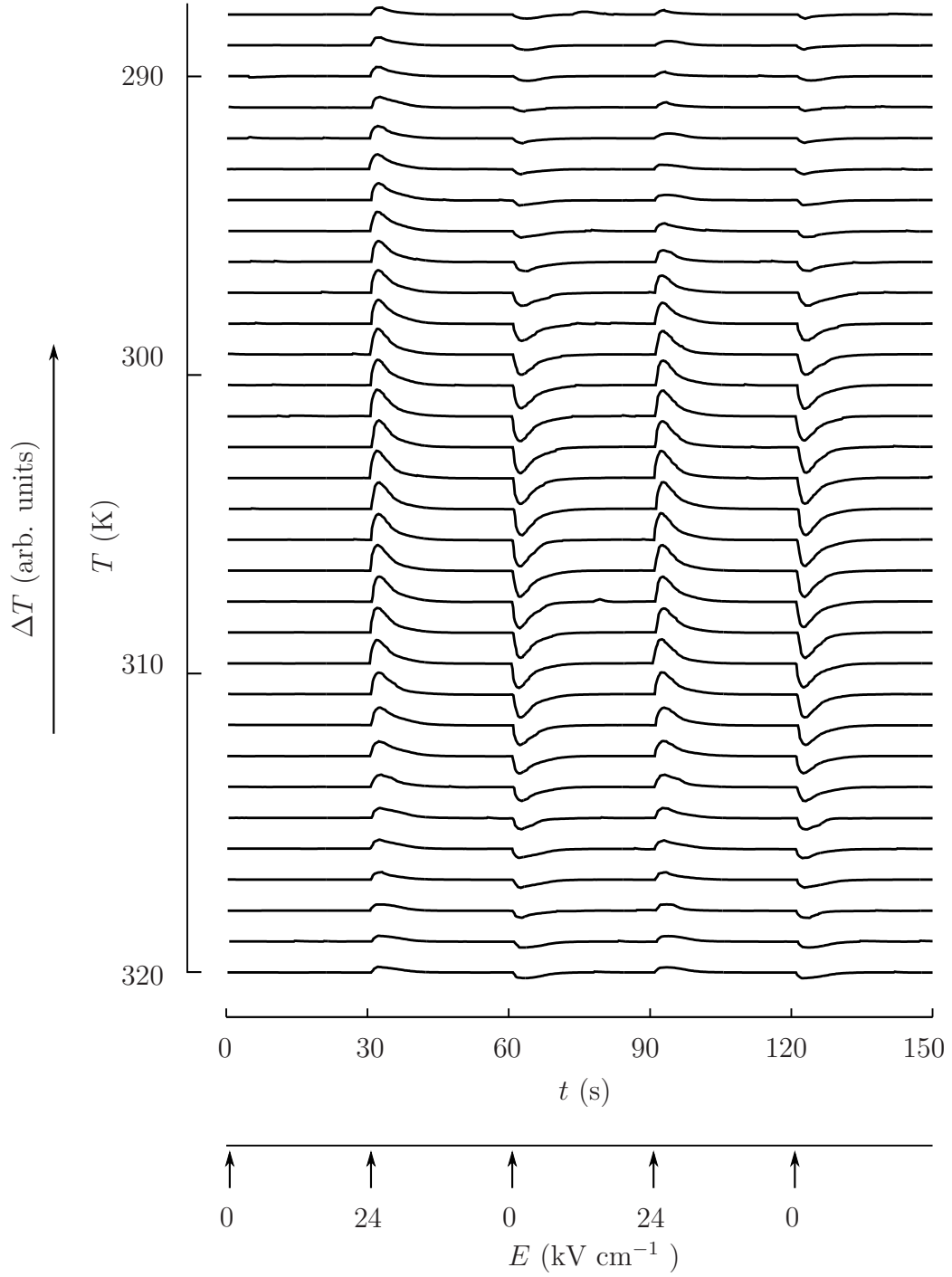


Figure 5.10: Nominally adiabatic ΔT for PST Sample B (450 μm -thick). The sample was flat-mounted on probe head 2 and stabilised at the starting temperature T given on the inner y -axis, after having reset the sample via an excursion to 320 K. The applied field was changed to the values indicated (outer x -axis) at the arrowed times (inner x -axis). The units of ΔT (outer y -axis) were not calibrated due to the difficulty of quantifying heat leaks.

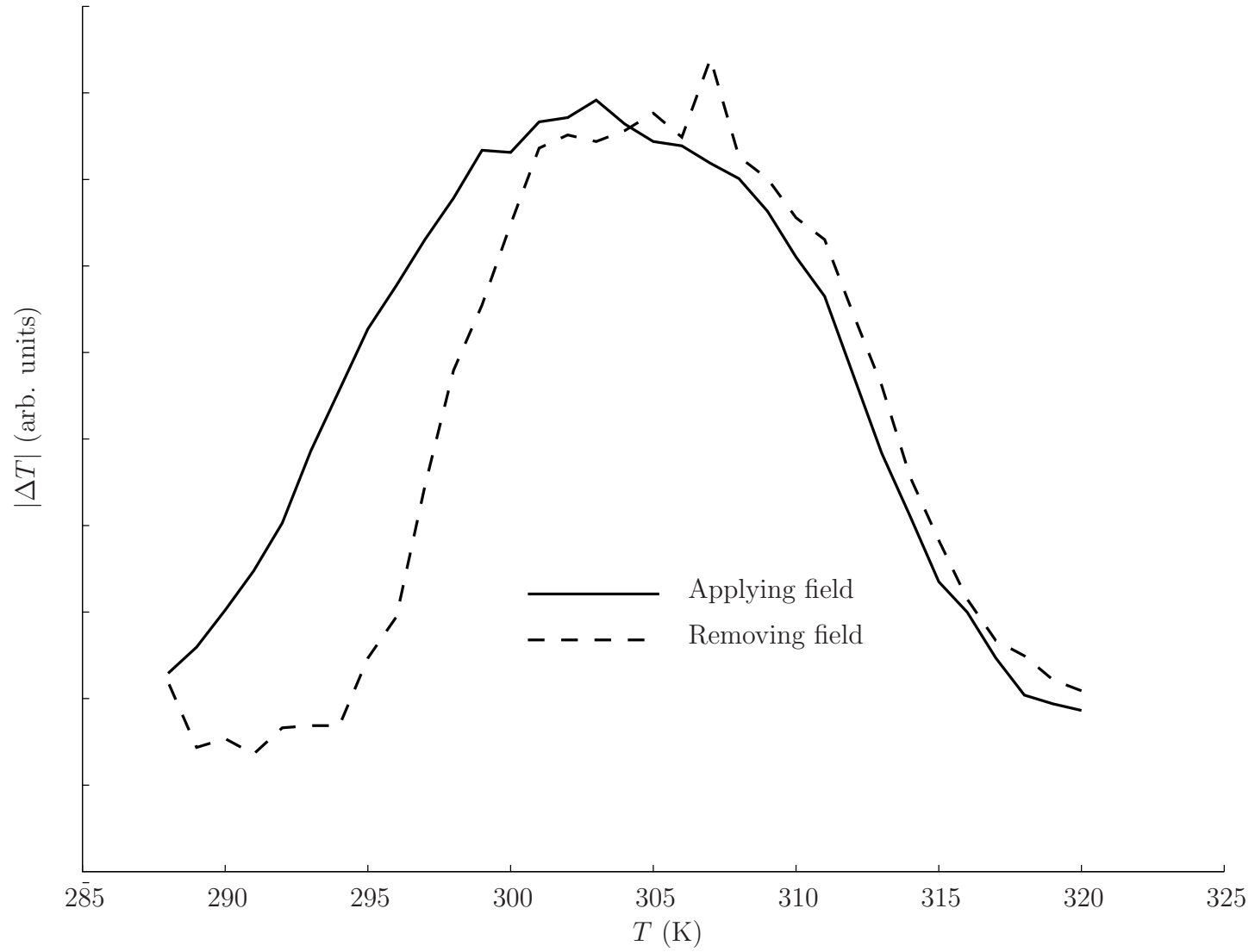


Figure 5.11: Directly measured, nominally adiabatic $|\Delta T|$ for PST Sample B (450 μm -thick) on applying or removing a field of 24 kV cm^{-1} . The units of ΔT have not been calibrated due to the difficulty of quantifying heat leaks.

The plots shown in Figure 5.12, corresponding to a second flat-mount experiment on PST Sample B to probe both field and temperature-dependence of $|\Delta T|$, were each compiled in a two-step cycle:

- Temperature was stabilised at the measurement temperature indicated on the *inner y-axis*, without ‘resetting’ the sample into the paraelectric phase.
- As a function of time (inner *x-axis*), ΔT (outer *y-axis*, in arbitrary units) was monitored. During this time, electric fields of *variable* magnitude were applied and *subsequently removed*. The initial field that was applied was 1.1 kV cm^{-1} , and for each subsequent application the field was increased by 1.1 kV cm^{-1} up to a maximum value of 24 kV cm^{-1} (outer *x-axis*).

As the sample was not reset to the paraelectric phase prior to each measurement, irreversible driving of the phase transition from the phase coexistence regime was not probed (this was a purpose of the previous Figure 5.10).

Thus, Figure 5.10 represents a map of nominally adiabatic ΔT as a function of both ΔE and starting temperature T , at least for $T > T_C$. The data showed excellent qualitative agreement with the adiabatic map that was measured indirectly (Figure 5.8). The temperatures in which a field of $< 24 \text{ kV cm}^{-1}$ was able to drive the phase transition was $\sim 298 \text{ K}$ to $\sim 310 \text{ K}$ in both datasets. A small remanent ΔT was observed away from the transition region, at 320 K and 290 K , in both datasets. The temperature dependence of the ‘critical field’ to drive the transition was qualitatively very similar in both datasets.

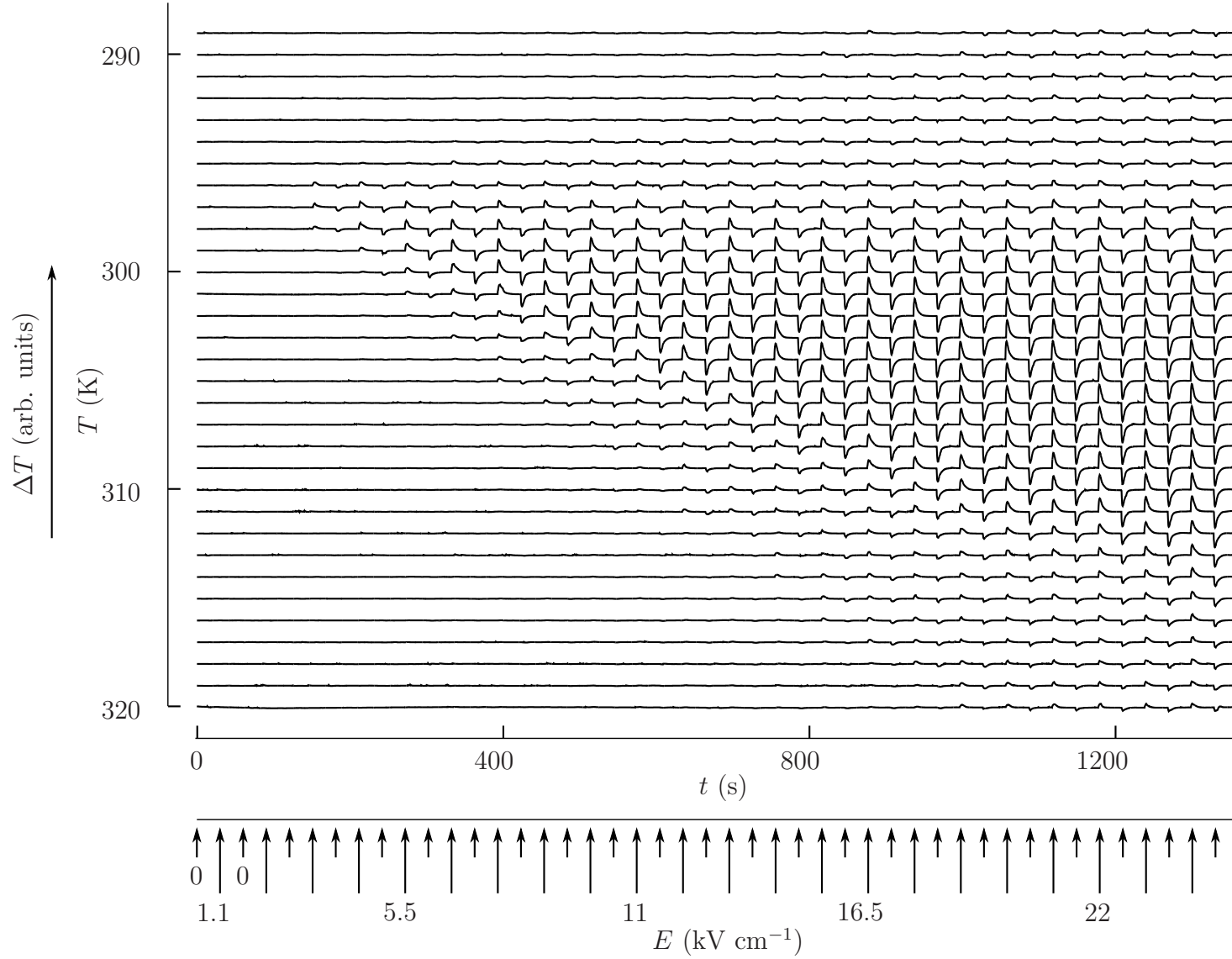


Figure 5.12: Temperature and field dependence of electrocaloric ΔT for PST Sample B (450 μm -thick). The sample was flat-mounted on probe head 2 and stabilised at the starting temperature T given on the inner y -axis. The applied field was changed to the values indicated (outer x -axis) at the arrowed times (inner x -axis), where small arrows denote a field of 0 kV cm^{-1} , and large arrows denote successively larger finite fields. The units of ΔT (outer y -axis) have not been calibrated due to the difficulty of quantifying heat leaks.

The values of $|\Delta T|$ measured on Sample B in probe head 2 were uncalibrated and quoted in arbitrary units. For calibrated thermometry, Sample C was flat-mounted on a thermally insulating glass slide. The temperature of the grounded top electrode was then measured via an SThM tip at a height of $\sim 20\text{ }\mu\text{m}$, while fields were successively applied and removed. Sample A was similarly flat-mounted on a glass slide and its temperature monitored via the infra-red temperature sensor, as described previously in Section 5.3. These experiments were conducted at room temperature due to limitations of the equipment. The SThM experiment was conducted in collaboration with Sohini Kar-Narayan.

The maximum temperature changes were $\sim 2\text{ K}$ for both the SThM (Figure 5.13a) and IR (Figure 5.13a) experiments, which was in good agreement with the indirect results (Figure 5.9). Both the SThM and IR experiments exhibited a ‘critical’ field change of $\sim 9.5\text{ kV cm}^{-1}$ to drive temperature changes $> 0.5\text{ K}$. The SThM experiment detected a small temperature change of $< 0.4\text{ K}$ for a field change of 5 kV cm^{-1} , but the IR experiment detected no response to the comparable field change of 4.8 kV cm^{-1} .

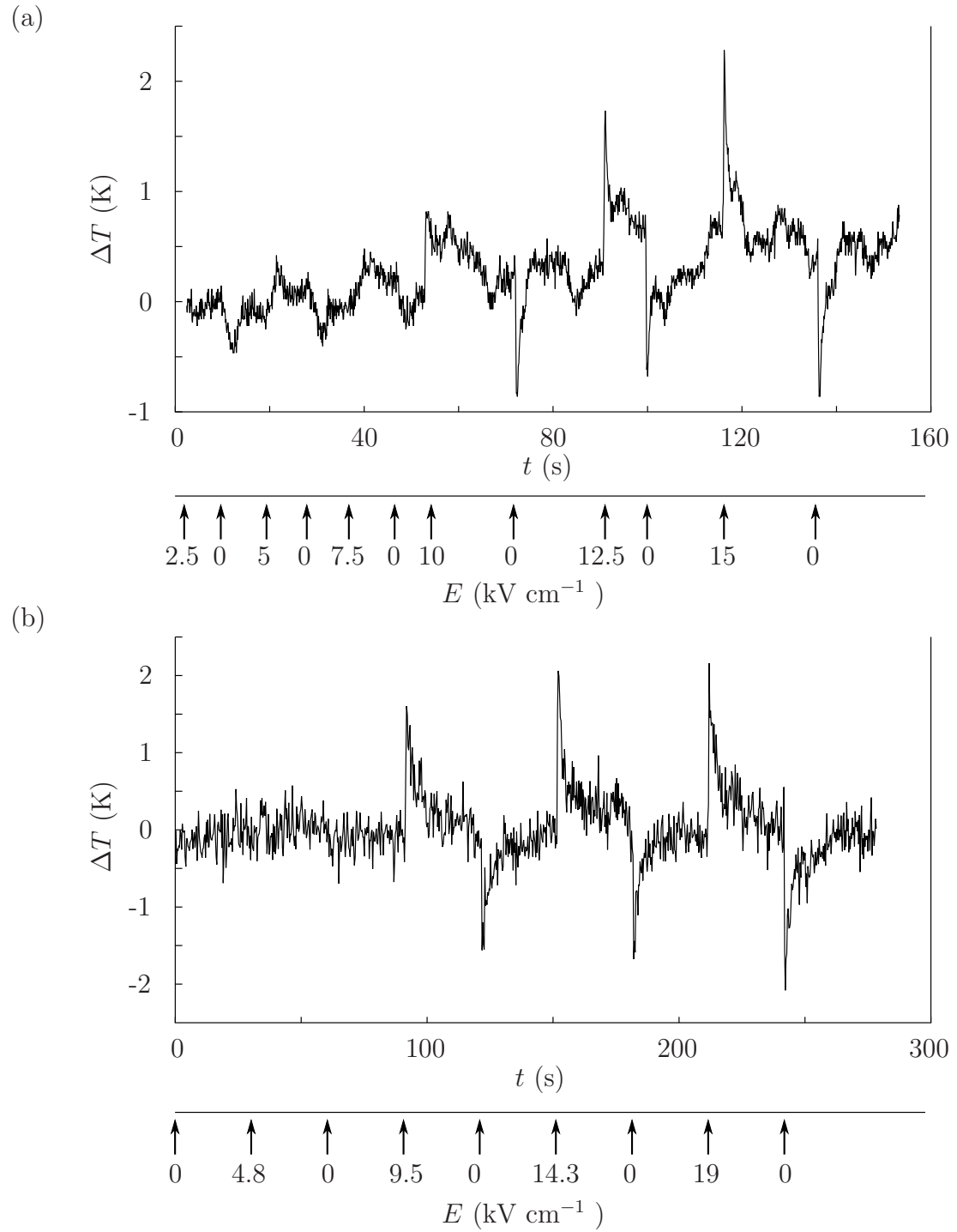


Figure 5.13: Nominally adiabatic ΔT for PST at room temperature. The applied field was changed to the values indicated (outer x -axis) at the arrowed times (inner x -axis). **(a)** Sample C, temperature monitored via scanning thermal microscopy (SThM). This measurement was conducted in collaboration with Sohini Kar-Narayan. **(b)** Sample A, temperature monitored by infra-red thermometry.

5.10 Thinned $\text{PbSc}_{0.5}\text{Ta}_{0.5}\text{O}_3$

A 95 μm -thick device of ceramic PST on a copper substrate was fabricated using the same 11-stage method as for $(\text{NH}_4)_2\text{SO}_4$ (Section 4.1.2). The sample was polished with 4000 grade sandpaper until it had a smooth, transparent surface. Thickness was measured (retrospectively) by demounting the sample and embedding it vertically in plasticine, such that its edge could be viewed in a microscope. The platinum electrode in the centre of the sample initially had an area of 0.66 mm^2 , but the first $P(E)$ loops showed a series of sudden drops consistent with electrode damage due to high voltages. These drops ceased after a few cycles, enabling experiments to continue, with electrode area re-evaluated at the end. However due to the high-voltage damage, the final measured area of 0.28 mm^2 , and thus all measurements of polarisation, should be regarded as approximate.

There was some evidence of ageing in this sample, with ferroelectric switching becoming noticeably more diffuse in E . Due to this, and the fact that the electrode area was only approximately measured, the results for the thinned sample should be regarded as preliminary.

5.10.1 $P(E)$ loops

The $P(E)$ loops for the 95 μm -sample, measured out to 160 kV cm^{-1} at 10 Hz (Figure 5.14), were markedly different from those shown previously for the 420 μm -thick sample measured out to 26 kV cm^{-1} at 1 Hz (Figure 5.4). For the previous data, the major loops showed clear ferroelectric hysteresis below $T_C \sim 295 \text{ K}$, and double loops above T_C corresponding to a field-driven transition. In contrast, for the present data, major loops appear nominally ‘ferroelectric’ well above the nominal Curie temperature of 295 K, and show a steady decay of spontaneous polarisation and coercive field. There was a hint of the field-driven transition in the minor loops for the thinned sample, but the offset sub-loops were slimmer and more diffuse than those for the unthinned sample.

The suggested explanation for the difference between the two samples relates to different degrees of mechanical clamping. The 420 μm -thick PST sample was electroded over a much larger area fraction than the 95 μm -thick sample (Figure 5.15). A small electrode area for the PST sample thinned to 95 μm was used in order to maximise the fields that could be applied without breakdown or arcing. Therefore the electrically-addressed

material in the 95 μm -thick sample was placed under greater mechanical stress during the field-driven transition (which involves a change in unit cell volume), i.e. it was more strongly clamped. This hypothesis should be confirmed via further work focussing on measuring high-field electrocaloric effects in an *unclamped* thinned sample of PST.

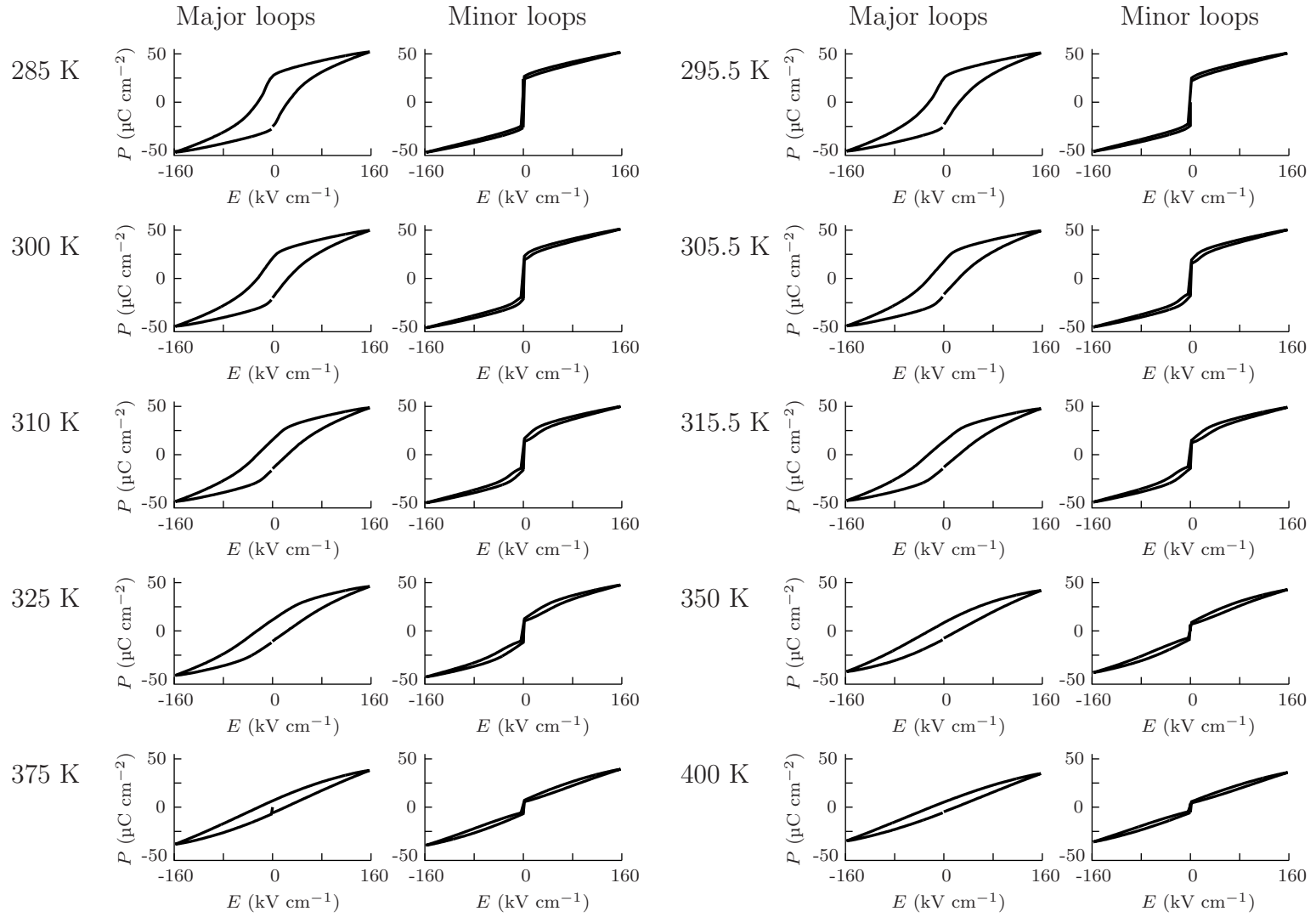


Figure 5.14: $P(E)$ loops at 10 Hz for the PST sample thinned to $95\ \mu\text{m}$ at various temperatures. Both major and minor loops are shown.

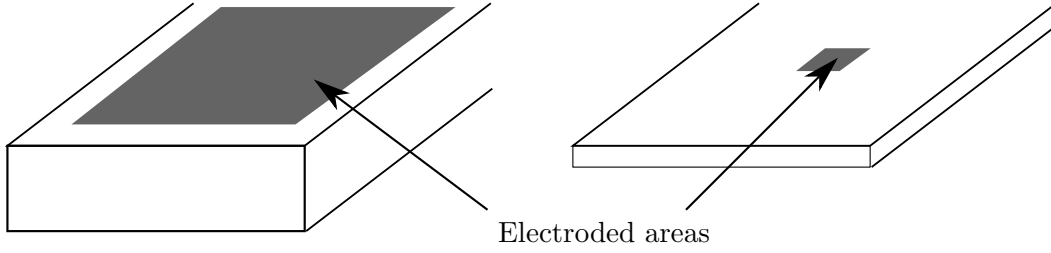
420 μm -thick PST95 μm -thick PST

Figure 5.15: Illustration of the approximate relative geometries for the 420 μm -thick PST sample and the sample thinned to 95 μm . A smaller electrode area was used for the 95 μm -thick sample to mitigate the risk of arcing or dielectric breakdown.

5.10.2 Isothermal $|\Delta S|$

To evaluate isothermal $|\Delta S|$ via the ‘standard’ indirect method, $P(E)$ loops were obtained on the PST sample thinned to 95 μm , as described in Section 5.10.1, every ~ 15 s on heating at 0.5 K min^{-1} from 280 K to 400 K. These data were transposed to $P(T)$ for processing into isothermal $|\Delta S|$, as described in Section 5.7.

Figure 5.16 shows $P(T)$ for the thinned sample, for (a) applying a field (i.e. using the lower branches of the minor loops) and (b) removing a field (upper branches). For the lowest field shown of 2 kV cm^{-1} , the greatest variation in $P(T)$ occurred near the expected T_C of 295 K. For the highest field shown of 155 kV cm^{-1} , the variation of $P(T)$ was relatively unchanged throughout the temperature range shown.

Figure 5.17 shows the evaluated isothermal $|\Delta S|$ as a function of E and T for the thinned sample, for (a) applying a field and (b) removing a field. The maximum entropy change was $\sim 4.5 \text{ J K}^{-1} \text{ kg}^{-1}$, slightly higher than the value of $\sim 3.25 \text{ J K}^{-1} \text{ kg}^{-1}$ obtained for the previous 420 μm -thick sample with a field change of 26 kV cm^{-1} (Figure 5.6). However, this entropy change of $\sim 4.5 \text{ J K}^{-1} \text{ kg}^{-1}$ occurred only for large fields $> 100 \text{ kV cm}^{-1}$. As such, the electrocaloric strength $|\Delta S|/|\Delta E|$ was much smaller for the thinned sample ($0.028 \text{ J K}^{-1} \text{ kg}^{-1} [\text{kV cm}^{-1}]^{-1}$) than for the 420 μm -thick sample ($0.125 \text{ J K}^{-1} \text{ kg}^{-1} [\text{kV cm}^{-1}]^{-1}$). This could relate, again, to differing degrees of mechanical clamping.

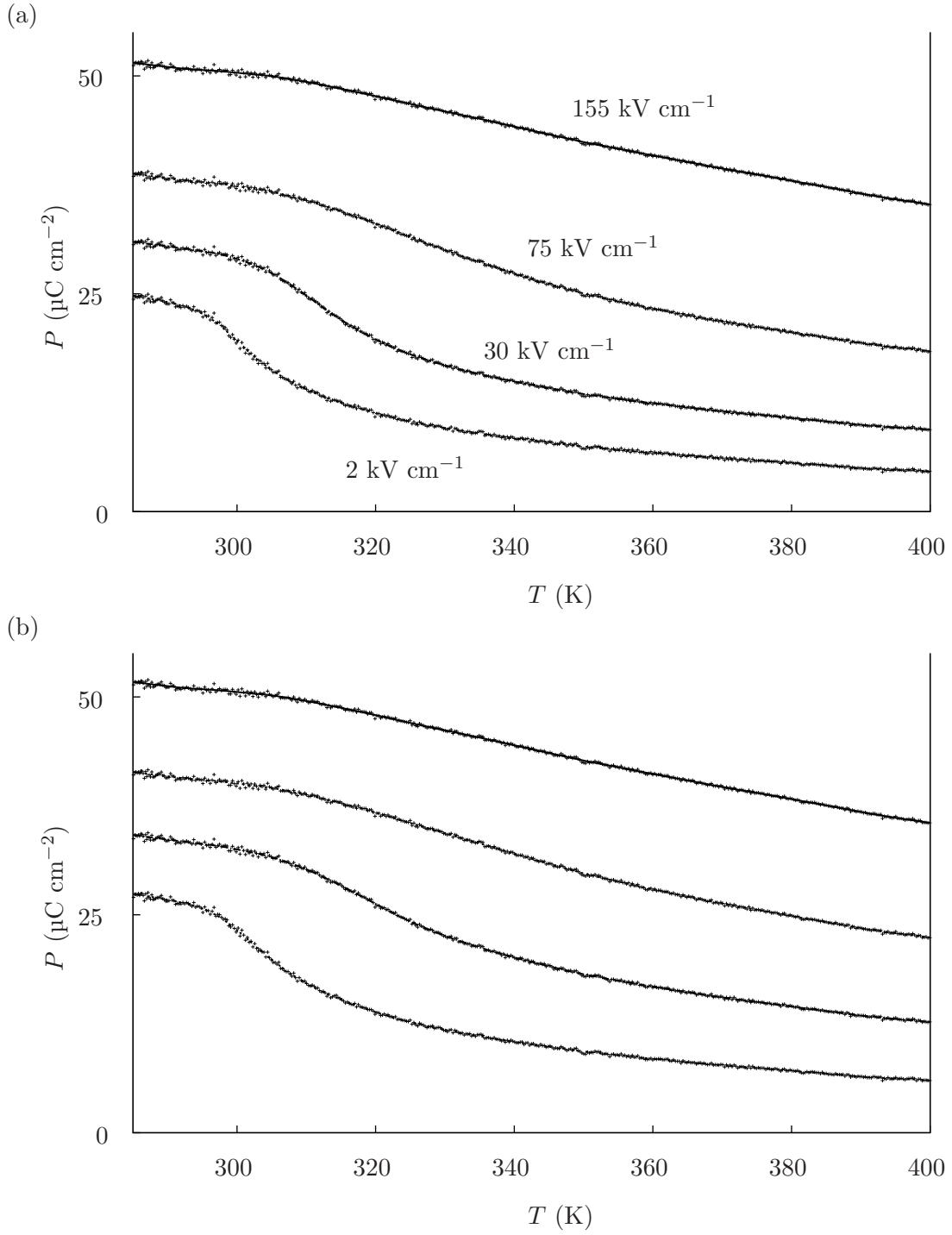


Figure 5.16: Selected $P(T)$ derived from $P(E)$ loops for 95 $\mu\text{-m}$ thick PST sample, for **(a)** applying a field (i.e. lower branches of minor $P(E)$ loops) and **(b)** removing a field (upper branches). The three plots of each graph correspond to 155 kV cm^{-1} (upper line), 75 kV cm^{-1} (middle line), 30 kV cm^{-1} (middle line) and 2 kV cm^{-1} (lower line) as indicated in (a). Points: raw (measured) data, lines: cubic spline fit.

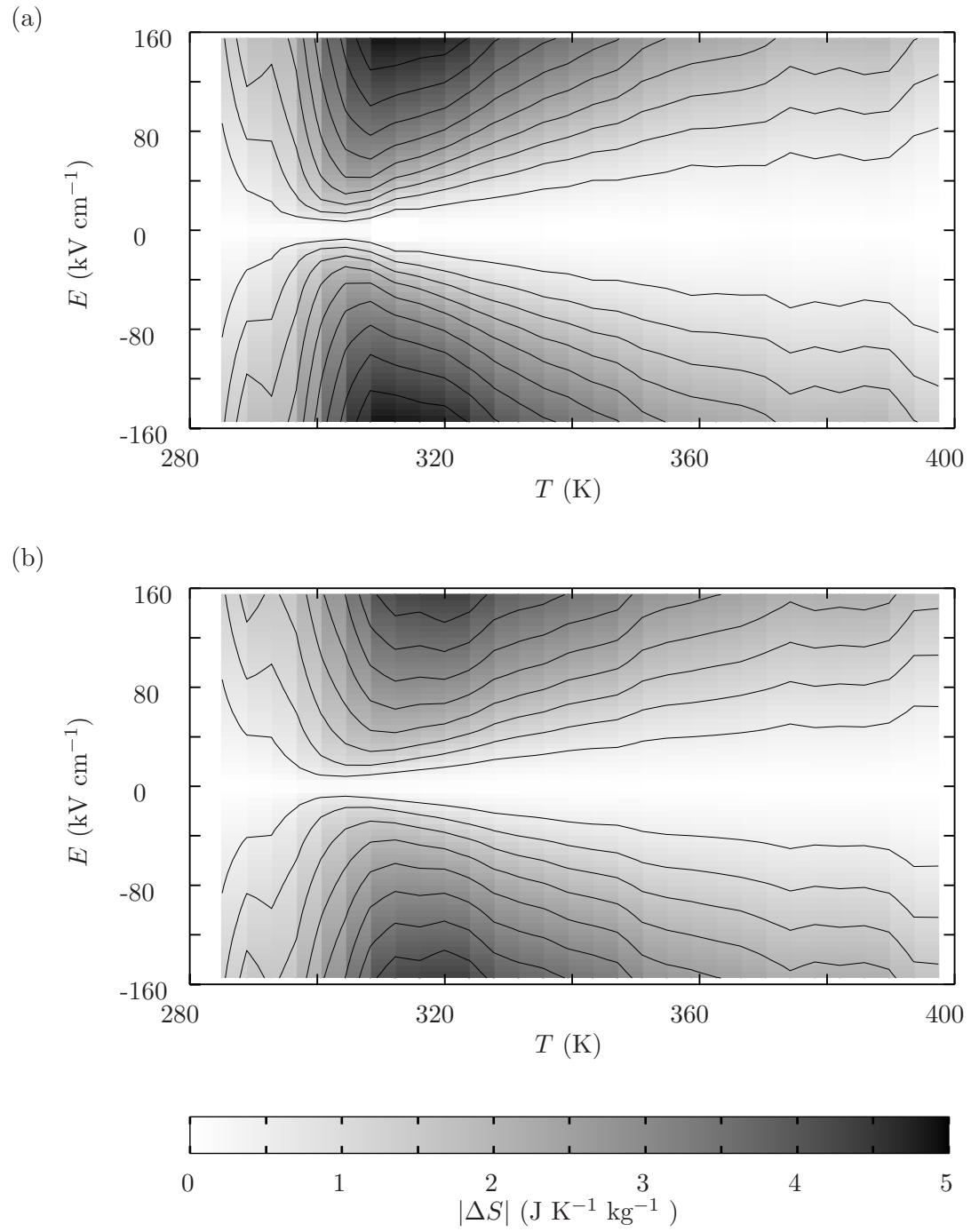


Figure 5.17: Evaluated isothermal $|\Delta S|$ derived from $P(T)$ plots (Figure 5.5) for the PST sample thinned to 95 μm , for **(a)** applying a field (i.e. lower branches of the minor loops) and **(b)** removing a field (upper branches). Data for negative E : ‘mirror image’ of those for positive E .

5.11 Conclusions

Samples of PST can vary from first-order ferroelectric materials to relaxor-like systems, depending on the degree of cation order [147]. The $P(E)$ experiments to $\pm 26 \text{ kV cm}^{-1}$ on a $420 \text{ }\mu\text{m}$ -thick sample of PST ceramic with $\sim 65 \%$ order revealed a sharp first-order phase transition, with clear double loop features corresponding to a field-driven phase transition just above T_C , and no evidence of relaxor-like behaviour (Figure 5.4).

Performing the indirect Maxwell analysis on these data, and mapping isothermal electrocaloric entropy change $|\Delta S|$ in $E - T$ space, confirmed a Clausius-Clapeyron relation for the phase boundary (Figure 5.6). Combining these data with a determination of zero-field ΔS via calorimetry enabled the mapping of adiabats in $E - T$ space (Figure 5.8), and these showed excellent qualitative agreement with direct measurements of field and temperature-resolved adiabatic $|\Delta T|$ (Figure 5.12). The magnitude of adiabatic $|\Delta T|$ for the full field-driven transition was $\sim 2 \text{ K}$ when measured via adiabatic mapping, and $\sim 2 \text{ K}$ when measured directly via SThM and infra-red thermometry (Figure 5.13). Owing to the clear, high-resolution and consistent data obtained, the PST ceramic with a thickness of several 100s of microns represents a case study in the thermodynamics of electrocaloric effects associated with field-driven first-order ferroelectric phase transitions.

In contrast, when a thinned $95 \text{ }\mu\text{m}$ -thick sample was tested at much larger fields of 160 kV cm^{-1} , $P(E)$ loops showed a diffuse decay of ferroelectric character on changing temperature (Figure 5.14). The isothermal $|\Delta S|$ evaluated from a subsequent Maxwell analysis showed that the field-driven phase transition was also more diffuse in E (Figure 5.17). It was suggested that the diffuse transition of the thinned sample could be linked to greater levels of mechanical clamping. The maximum isothermal entropy change was slightly larger for the thinned sample ($\sim 4.5 \text{ J K}^{-1} \text{ kg}^{-1}$) than the $420 \text{ }\mu\text{m}$ -thick sample ($\sim 3.25 \text{ J K}^{-1} \text{ kg}^{-1}$) but the quantitative results for the thinned sample were preliminary and approximate. The temperature range of the electrocaloric effect was larger for the thinned sample, as a result of the much larger field that could be applied. However, the electrocaloric strength $|\Delta S|/|\Delta E|$ was ~ 4.5 times smaller for the thinned sample. Future work should focus on fabricating samples with thicknesses in the 10s of μm range, and conducting a systematic investigation into the effect of mechanical clamping, with the aim of confirming the above hypothesis.

Chapter 6

Electrocaloric effects in strained epitaxial films of SrTiO_3

6.1 Electrocaloric effects in thin films

A key milestone in the field of electrocalorics was the paper of Mischenko *et al.* (2006) reporting, for the first time, indirect observation of ‘giant’ electrocaloric effects of $|\Delta T| \sim 12$ K in 350 nm-thick films of ceramic $\text{PbZr}_{0.95}\text{Ti}_{0.05}\text{O}_3$ near $T_C \sim 490$ K [20]. This was the first electrocaloric report on a thin-film sample, and the ‘giant’ effects were a direct result of the high breakdown fields of thin films (100s to 1000s of kV cm^{-1}), enabling the electrocaloric effect to be driven far harder than had been possible in bulk materials. Neese *et al.* (2008) followed up with a report of $|\Delta T| \sim 12$ K effects in a 1 μm -thick film of poly(vinylidene fluoride-trifluoroethylene) (55/45 mol %) [PVDF-TrFE] near $T_C \sim 350$ K [21]. These seminal papers inspired further indirect measurements on thin films of various ferroelectric materials (see Chapter 1). At the time of writing, the largest $|\Delta T|$ claimed was 45 K, in 350 nm-thick films of the relaxor ceramic $\text{Pb}_{0.8}\text{Ba}_{0.2}\text{ZrO}_3$ near room temperature [53].

6.2 Epitaxial films

Epitaxial films are thin single-crystal films grown on polished single-crystal substrates. The in-plane lattice parameters of the film are strained to fit the lattice parameters of the substrate material, at least for the first few 10s of nm. For epitaxial growth to

occur, the native lattice parameters of the film material should match those of the substrate material within a few percent. Thicker films and larger lattice mismatches tend to lead to strain relaxation via lattice defects [150]. Nonetheless, epitaxial strain can greatly exceed the maximum strain in bulk without fracture, so many exciting discoveries have been made in the last few decades relating to new or transformed physical properties caused by epitaxial strain. For example:

- Choi *et al.* (2004) [151] grew BaTiO_3 epitaxially on DyScO_3 and GdScO_3 substrates. As a result of epitaxial compression, the out-of-plane spontaneous polarisation was enhanced by a factor of 2.5 over values for bulk single crystals, and the Curie temperature was increased from the bulk value of 120 °C to 540 °C.
- Haeni *et al.* (2004) [59] grew 50 nm-thick SrTiO_3 epitaxially on DyScO_3 substrates. Bulk SrTiO_3 is an incipient ferroelectric. As a result of epitaxial strain, the SrTiO_3 film showed in-plane ferroelectricity with a Curie temperature of ~ 295 K.
- Moya *et al.* (2013) [152] grew $\text{La}_{0.7}\text{Ca}_{0.3}\text{MnO}_3$ (a material which shows small magnetocaloric effects in bulk near its Curie temperature of 259 K) epitaxially on BaTiO_3 substrates. As a result of strain-mediated feedback between the film and the interfacial regions of the BaTiO_3 substrate, giant magnetocaloric effects were observed in the *film* near the 190 K structural phase transition of the *substrate*.

Various deposition methods may be used to fabricate epitaxial films, such as pulsed laser deposition, sputter deposition, chemical vapour deposition and molecular beam epitaxy. A much larger variety of materials have been used as films than substrates, as substrates must be prepared as large single crystals with atomically flat surfaces [150]. Furthermore, in order to optimise growth conditions, a large supply of substrates must be available. A small industry has developed around the mass/batch fabrication of a limited range of substrates for laboratories working on epitaxial films. A few such laboratories are themselves actively involved in substrate fabrication, or the development of new substrate materials.

The effect of epitaxial strain on electrocaloric effects has not been investigated experimentally. The high levels of crystalline perfection associated with epitaxial films could lead to enhanced electrocaloric properties. Furthermore, epitaxial films are oriented and can thus enable fields to be applied exclusively across the polar axis. The

objective of the present work was to grow epitaxial films of SrTiO_3 with in-plane compressive strain, in order to investigate the electrocaloric properties of the strain-induced ferroelectric phase transition first observed by Haeni *et al.* [59]. The substrate was (001)-oriented NdGaO_3 , with an epitaxial layer of the conductive perovskite oxide $\text{La}_{0.67}\text{Sr}_{0.33}\text{MnO}_3$ as a bottom electrode. The fabrication method was pulsed laser deposition.

6.3 Materials

6.3.1 SrTiO_3

SrTiO_3 has a perovskite structure with cubic cell parameter $a = 3.901 \text{ \AA}$ [153]. The epitaxial SrTiO_3 films of SrTiO_3 of Haeni *et al.* [59] were grown on substrates of (110)-oriented DyScO_3 which is orthorhombic with cell parameters $a = 5.449 \text{ \AA}$, $b = 5.726 \text{ \AA}$ and $c = 7.913 \text{ \AA}$ [154]. The $[001]$ and $[1\bar{1}0]$ directions lie in plane and define the ‘pseudo-cubic’ cell of DyScO_3 (110), which has a lattice parameter of $a = 3.952 \text{ \AA}$ (Figure 6.1). Thus fully strained epitaxial films of SrTiO_3 grown on (110) DyScO_3 experience a $\sim 1.3 \%$ tensile in-plane strain¹.

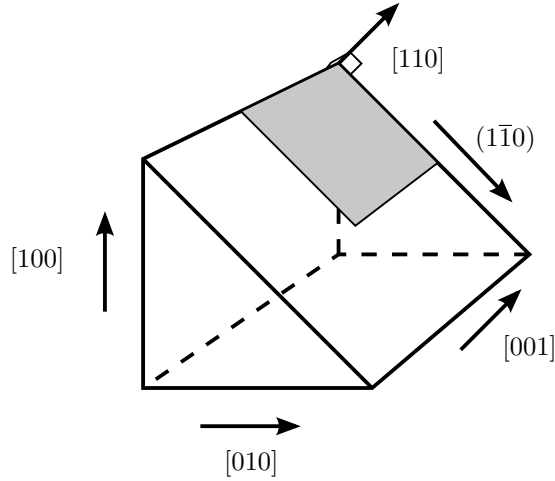


Figure 6.1: Part of orthorhombic unit cell of DyScO_3 , showing pseudo-cubic cell (shaded area). Not to scale.

¹Haeni *et al.* [59] report a 1 % in-plane strain, but quoted different lattice parameters for DyScO_3 .

The dielectric constant of bulk strontium titanate (SrTiO_3) rises to some tens of thousands at liquid helium temperatures, as has been known since at least the early 1950s [155,156]. Spectroscopic studies in the 1960s showed that the frequencies of the zone-centre soft phonons soften but remain finite at low temperatures [157]. An antiferrodistortive transition occurs at ~ 110 K, which coincides with the softening of $< 111 >$ zone-boundary phonons [158–160]. Small amounts of uniaxial stress [161,162], applied electric field [163,164] or chemical impurities [165,166] are sufficient to induce the ferroelectric phase at low temperatures. Thus, SrTiO_3 is a system in which ferroelectric, antiferroelectric and paraelectric phases are in close thermodynamic proximity at low temperatures. Weakly hysteretic ‘ferroelectric’ $P(E)$ loops have been observed below 45 K [167], and ‘antiferroelectric’ double loops have been observed below 50 K on samples annealed to reduce internal stresses [168].

The observation of room temperature ferroelectricity in strained epitaxial SrTiO_3 films was anticipated by a Landau-Ginsburg-Devonshire theoretical treatment of Pertsev *et al.* [169,170] which predicted a rich phase diagram in strain-temperature space, shown here as Figure 6.2. Four orthorhombic ferroelectric phases were predicted FOI-IV, two tetragonal ferroelectric phases FTI-II, two ‘structural’ (non-ferroelectric) phases ST and SO, and a paraelectric high temperature phase HT. The transition observed by Haeni *et al.* [59], via an in-plane dielectric trace at 10 GHz, was nominally $\text{FOI} \leftrightarrow \text{HT}$.

Biegalski *et al.* [171] grew epitaxial SrTiO_3 films under ~ 1 % tensile strain on DyScO_3 (101) substrates, and measured $P(E)$ loops, and dielectric constant at kHz frequencies, as a function of temperature. A large peak in ϵ' was observed at ~ 250 K, and a hysteretic $P(E)$ loop was measured at 77 K. The dielectric measurements showed a frequency dispersion, suggesting that the SrTiO_3 film was behaving as a relaxor ferroelectric, possibly due to surface ferroelectricity in the substrate, inhomogeneous strain, a small structural coherence length, or point defects.

Yamada *et al.* [172] grew epitaxial films of SrTiO_3 with a ~ 1 % compressive in-plane strain, on NdGaO_3 (110) substrates. Infra-red spectroscopy provided evidence for a ferroelectric phase transition at ~ 150 K. However, Nuzhnyy *et al.* [173] grew similar films but found no evidence for this transition, or any ferroelectric transition between 5 K and 300 K, in infra-red spectroscopy using polarised light. The authors postulated that the phonon mode observed by Yamada *et al.* (who used unpolarised light) was an artifact related to substrate anisotropy. It was further suggested that substrate anisotropy could suppress the ferroelectric phase transition expected from theory [173].

Electrocaloric properties of bulk SrTiO_3 were measured at cryogenic temperatures in the 1960s [174] and 1970s [33]. The measured effects were small, with $|\Delta T|$ in the range of 10s-100s of mK for a field change in the range of 10s of kV cm^{-1} . Thin films of SrTiO_3 have not been studied experimentally for electrocaloric properties. However, such properties have been predicted in theoretical papers by Qiu (2009) [175] and Zhang (2012) [176]. With reference to the phase diagram of Pertsev (Figure 6.2), the Qiu study predicted adiabatic $|\Delta T| \sim 2.2$ K for the $\text{FTI} \leftrightarrow \text{HT}$ transition (2 % compressive in-plane strain), and $|\Delta T| \sim 3.0$ K for the $\text{FOI} \leftrightarrow \text{HT}$ transition (2 % tensile in-plane strain), for field changes of 300 kV cm^{-1} . The Zhang study predicted $|\Delta T| \sim 4$ K at room temperature for the $\text{FTI} \leftrightarrow \text{HT}$ transition (2 % compressive in-plane strain), and $|\Delta T| \sim 5$ K at room temperature for the $\text{FOI} \leftrightarrow \text{HT}$ transition (1.5 % tensile in-plane strain), for field changes of 1000 kV cm^{-1} .

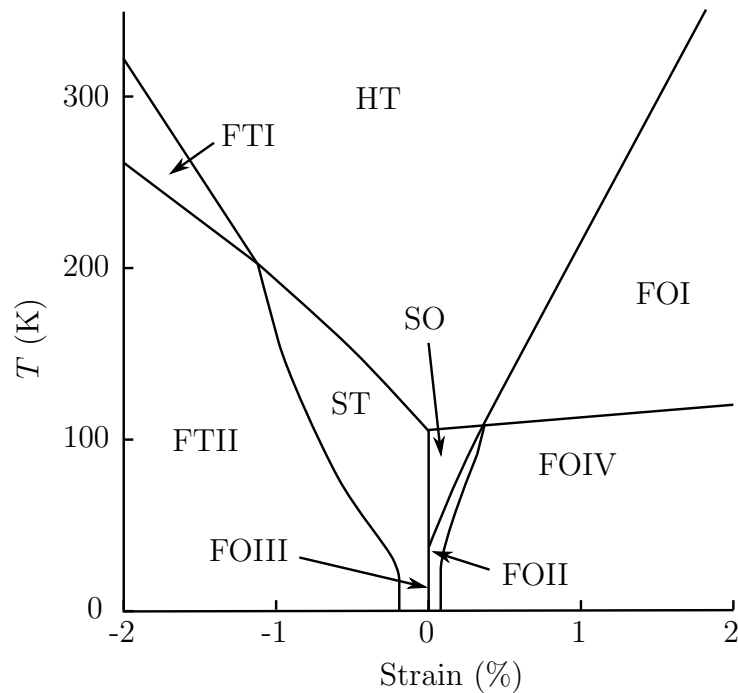


Figure 6.2: Phase diagram of epitaxial SrTiO_3 , according to theoretical calculations of Pertsev *et al.* [169, 170]. FOI-IV: orthorhombic ferroelectric phases, FTI-II: tetragonal ferroelectric phases, ST and SO: ‘structural’ (non-ferroelectric) tetragonal and orthorhombic phases, HT: high-temperature paraelectric phase. Figure: after Pertsev *et al.* [170].

6.3.2 NdGaO₃

NdGaO₃ (001) is a commercially-available substrate with an orthorhombic structure with cell parameters $a = 5.4276 \text{ \AA}$, $b = 5.4979 \text{ \AA}$, $c = 7.7078 \text{ \AA}$ [177]. The $[110]$ and $[1\bar{1}0]$ directions lie in plane and define the ‘pseudo-cubic’ cell of NdGaO₃ (001) with lattice parameter of $a = 3.863 \text{ \AA}$ (Figure 6.3). Thus SrTiO₃ with a unit cell parameter of 3.901 \AA [153] was expected to grow epitaxially with a 1 % compressive strain (Figure 6.3) with a polar axis parallel to the out-of-plane direction.

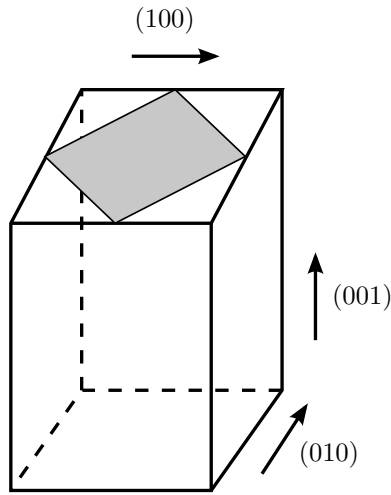


Figure 6.3: Orthorhombic unit cell of NdGaO₃, showing pseudo-cubic cell (shaded area). Not to scale.

6.3.3 Electrodes: $\text{La}_{0.67}\text{Sr}_{0.33}\text{MnO}_3$ and Pt

A thin bottom electrode of the conductive perovskite oxide material $\text{La}_{0.67}\text{Sr}_{0.33}\text{MnO}_3$ (LSMO) was deposited between the substrate and the film, and top electrodes of platinum were sputtered through a hard mask, to form electrode pads of 100 μm , 200 μm and 500 μm diameter.

As explained by Scott [9], band structure can profoundly influence the performance of ferroelectric thin-film capacitors, as it determines whether undesirable charge injection into the conduction band of the ferroelectric will occur from the Fermi level of the electrode [9]. The energy difference between the vacuum level and the Fermi level of a metal is the work function Φ . The energy difference between the vacuum level and the conduction band of a ferroelectric is the electron affinity χ . Unfortunately, determining whether charge injection will occur is not a simple matter of comparing these quantities numerically, due to factors such as an expected difference between the vacuum levels of the two materials, charge depletion layers in the interfacial regions of the ferroelectric, and the presence of donors or acceptors in the ferroelectric (for full details see [9]). It is safe, however, to state that ‘good’ electrodes such as Pt and SrRuO_3 have large work functions, in these cases 5.3 eV and 4.8 eV respectively [9]. For this reason, SrRuO_3 has been widely used as a bottom electrode for epitaxial ferroelectric thin films. However, the deposition of SrRuO_3 presented difficulties for the present work, due to a structural phase transition at $\sim 680^\circ\text{C}$ which places an upper limit on the deposition temperature of the SrTiO_3 film [178]. Furthermore, SrRuO_3 only grows uniformly on substrates which have a single chemical termination, usually achieved via an HF etching process [178], which is challenging and unpleasant.

LSMO was used for the bottom electrode as a result of the issues with SrRuO_3 . LSMO was chosen because it is known to form smooth, epitaxial films on NdGaO_3 (001) substrates, in the deposition system used for the present work [179]. LSMO has a resistivity of $\sim 10^{-3} \Omega \text{ m}$ at room temperature (approximately ten times less than SrRuO_3 [180]) which increases to $\sim 10^{-2}$ above the magnetic transition temperature at $\sim 370 \text{ K}$ [181]. However, the temperature range of interest was expected to lie significantly below this temperature. No information concerning the work function of LSMO could be found, but it has previously been used successfully as a bottom electrode for epitaxial ferroelectric BiFeO_3 [182]. The side of the LSMO pseudocubic unit cell is 1.11 % larger than for NdGaO_3 [179].

6.4 Pulsed laser deposition

Pulsed laser deposition (PLD) is a popular method of fabricating epitaxial thin films. Posadas *et al.* [150] have written a useful review focussing on PLD of ferroelectric materials. In PLD, high-intensity laser pulses may be used to heat the surface of a ‘target’ material to plasma temperatures. At low ambient pressures, a plasma plume is created. The substrate is normally positioned on a heating stage with a direct line of sight to the plasma plume, allowing the plasma to condense on the surface of the substrate to form the film. A key strength of PLD is that the stoichiometry of the target material is usually preserved in the film. The target can be a high-density sintered ceramic or a single crystal. Because PLD is a relatively simple deposition process, multilayers are usually straightforward to fabricate by mounting multiple targets on a carousel and switching between them. Close control over film thickness is straightforward, as thickness is a linear function of the number of laser pulses fired at the target.

For the present work, the ‘Mark X’ (Mk X) PLD system was used, which was assembled in Cambridge during the 1990s. The system features a ~ 25 l high-vacuum chamber, tubomolecular vacuum pump (type Ext250M 100CF, Edwards), two-stage 18 l rotary vane pump (Edwards), six-target carousel (Neocera) and a 2 inch diameter 25-950 °C inconel substrate heater (Neocera). The laser is a KrF gas excimer (type Compex 201, Lambda Physik) with a maximum pulse energy of ~ 700 mJ at the laser aperture, wavelength of 248 nm, pulse duration ~ 25 ns, beam dimensions 24 mm (vertical) by ~ 12 mm (lateral), beam divergence ~ 3 mrad (vertical) and ~ 1 mrad (lateral) and pulse frequency 1-10 Hz.

Figure 6.4 is a scale drawing showing the geometry of the beam path and interior of the deposition chamber. The laser beam passes via two mirrors, 1 and 2, whose purpose is to rotate the beam profile by 90° , such that the long axis lies horizontal. The purpose of mirrors 3 and 4 is to direct the beam into the deposition chamber. The beam path contains two optical boxes which are empty by default, but may be used for placing optical components. A lens outside the chamber focusses the beam through a window in the chamber onto a small spot of area ~ 6.5 mm² at the target. The optical path between the laser aperture and the lens extends ~ 200 cm, and the distance between the lens and the target extends ~ 40 cm. The mirrors, lens and window reduce the energy of the laser pulses by ~ 55 %, of which ~ 10 % is due to the window. The exact transparency of the window varies due to steady build-up of film material, which is

removed by occasional cleaning (1-2 times per year). The mirrors and lens also degrade with pulses, but at a much slower rate. Before and after each deposition, the energy of the laser pulses at the target is calibrated by placing the window into optical box 1, and measuring the laser energy after the lens with an energy meter (type LM-P10, Coherent).

Within the chamber, the target carousel is suspended from the top flange, and the substrate heater is positioned 6.5 cm vertically below the target surfaces. Targets are rotated via a motor attached to the carousel, so that the laser spot is distributed over the target surface. A metal shutter can be positioned between the target and the substrate, enabling targets to be ‘cleaned’ with laser pulses without depositing on the substrate. The shutter and the target carousel are manipulated via mechanical feedthroughs on the top flange. Substrates are attached to the heater using silver paste, and removed by careful prising with a razor blade.

For the present work, the laser beam profile of ~ 24 mm x ~ 12 mm was cropped to a smaller central section of dimensions 15 mm x 4.5 mm to achieve a more uniform fluence, which is standard practice for gas excimer lasers [150]. The cropping was accomplished by placing an improvised mask of Cu tape stretched over a steel frame in optical box 1 (Figure 6.4). The use of the mask resulted in a 2.6-fold reduction in the total pulse energy, and a ~ 1.7 -fold reduction in the laser spot size to ~ 3.8 mm² at the target. As a result, longer deposition times were required with the mask in place, but this was not unduly onerous as the films were thin.

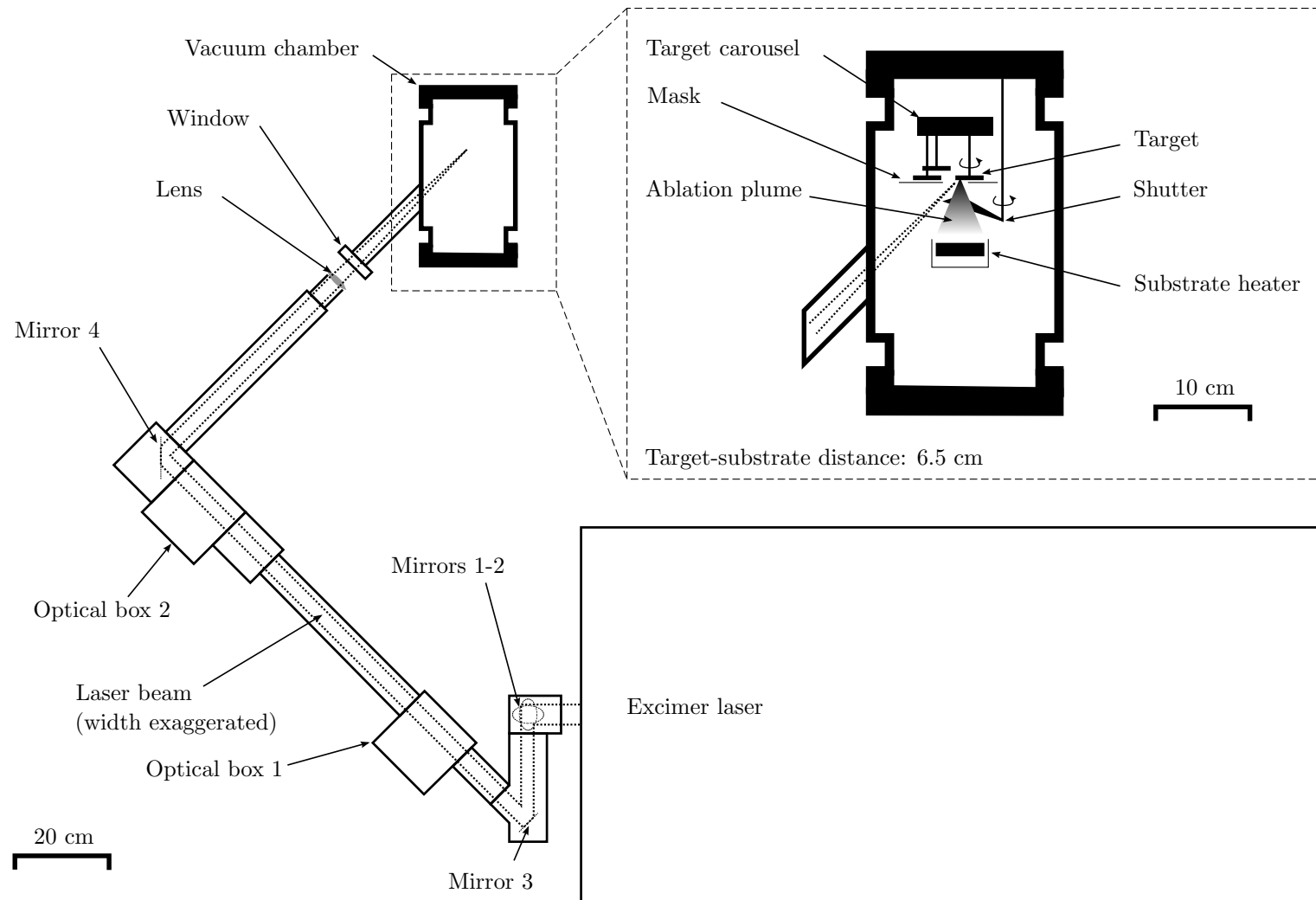
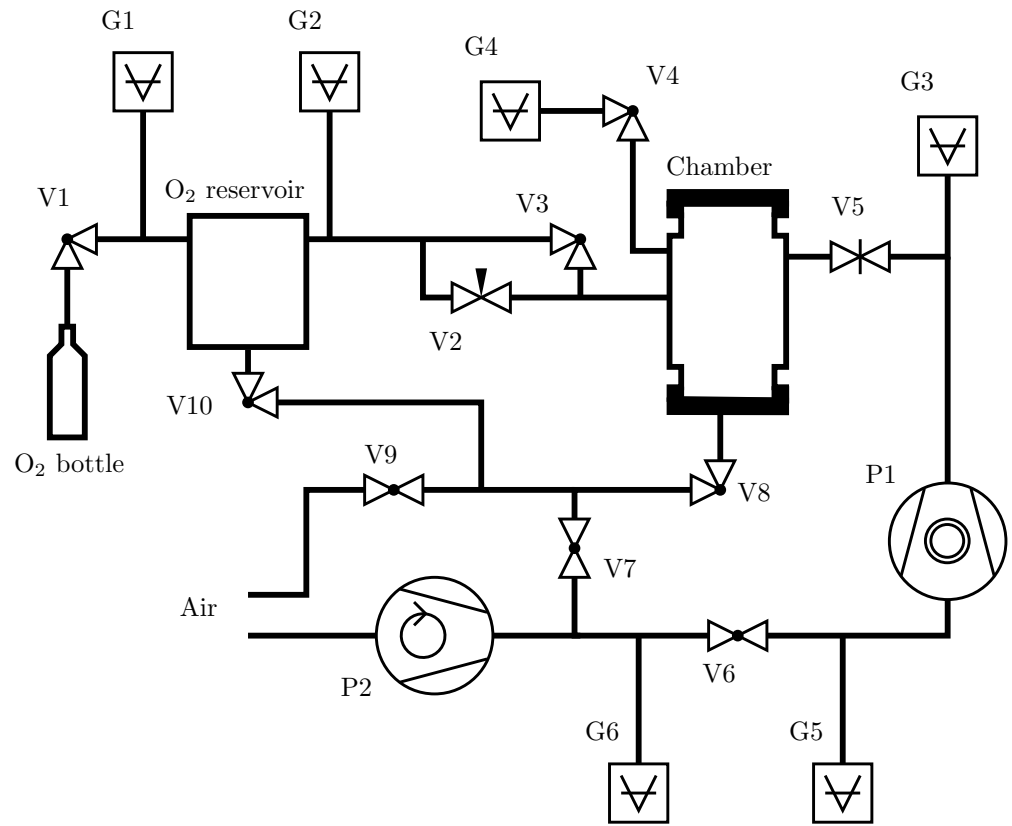


Figure 6.4: Schematic of the 'Mark X' system for pulsed laser deposition. Scale bars accurate to within 10 %.

Figure 6.5 is a diagram of the principle vacuum components of the Mk X system. Where known, the manufacturer of each component is shown in the table. The turbomolecular pump P1 can be isolated for short periods of time by closing gate valve V5 and diaphragm valve V6, so it is never necessary to power down this pump. The chamber can be vented to air by opening valves V8 and V9. Once loaded, the chamber can be evacuated to rough vacuum with rotary vane pump P2, by opening valves V7 and V8. Subsequent evacuation to high vacuum is accomplished by closing valves V7 and V8 and connecting the turbomolecular pump by opening valves V5 and V6. The evacuation process can be monitored using Pirani gauges G5 and G6. Base pressure can be accurately measured using a small mass spectrometer G3. A typical base pressure after overnight pumping is $2 * 10^{-6}$ atm. The O₂ reservoir can be evacuated to rough vacuum by isolating the turbomolecular pump, and opening valves V7 and V10.

Prior to deposition, 105 kPa of O₂ gas (ultrapure grade, Air Products) is admitted to the O₂ reservoir by opening valve V1. The pressure of the O₂ reservoir can be monitored with a resolution of 0.1 kPa using Baratron gauge G2. Needle valve V2 and gate valve V5 are opened slightly to allow a small flow of O₂ from the O₂ reservoir to the turbomolecular pump via the deposition chamber. By manual adjustment of these two valves, the pressure of flowing O₂ inside the deposition chamber can be manipulated in the range $\sim 1 - 30$ Pa with an accuracy of $\sim 0.1 - 0.5$ Pa. The pressure inside the deposition chamber is monitored using Baratron gauge G4. For post-deposition annealing in ~ 55 kPa of O₂, valves V2, V4 and V5 are closed, and valve V3 opened to equilibrate the pressure in the O₂ reservoir and the deposition chamber.



Component	Description	Manufacturer
V1	Right-angle valve	VAT
V2	Needle valve	
V3	Right-angle valve	
V4	Right-angle valve	
V5	Gate valve	
V6	Diaphragm valve	
V7	Diaphragm valve	
V8	Right-angle valve	
V9	Leak valve	
V10	Right-angle valve	
G1	Pirani gauge	VG Scienta
G2	Baratron gauge	MKS
G3	Mass spectrometer	VG Arga
G4	Baratron gauge	MKS
G5	Pirani gauge	Edwards
G6	Pirani gauge	Edwards
P1	Turbomolecular pump	Edwards
P2	2-stage rotary vane pump	Edwards

Figure 6.5: Vacuum diagram of the ‘Mark X’ system for pulsed laser deposition showing vacuum components. Where known, the manufacturer of each component is given.

6.5 Atomic force microscopy and X-ray diffraction

Once grown, films were characterised with atomic force microscopy and X-ray diffraction.

Atomic force microscopy (AFM) probes the surfaces of samples by bringing a small tip very close to them or into contact with them. The deflection of the cantilever-mounted tip due to atomic-scale forces is measured via the reflection of a laser beam from the cantilever as the sample or tip is scanned in-plane, enabling a topographical image of the sample surface to be constructed. Tips can operate in ‘contact mode’ or ‘tapping mode’. For the latter, the tip displacement oscillates just above the sample surface and phase-sensitive detection is used to deduce topography [183]. The AFM used for the present work was a sample-scanning model, i.e. the tip was stationary above the sample, which was scanned to generate the topographical image. Topography was measured in tapping mode. The AFM controller was a Nanoscope V (Bruker).

X-ray diffraction (XRD) may be used to explore reciprocal space in crystals and polycrystals [184]. The scattering vector \mathbf{s} for a particular plane is defined in terms of the angles 2ϑ and ω (Figure 6.6). If \mathbf{s} coincides with a reciprocal lattice vector \mathbf{q} for the crystal, diffraction occurs and intensity is measured at the X-ray detector. X-rays penetrate up to several microns into a crystalline material, so when a thin film is characterised by XRD, the reciprocal lattices of both substrate and film may be detected. As $\arg(\mathbf{s})$ is specified by $\vartheta - \omega$ (Figure 6.6) and $|\mathbf{s}| = 2 \sin(\vartheta)/\lambda$ (Bragg’s law), a scan at constant $\arg(\mathbf{s})$ requires *simultaneous* variation of ϑ and ω , often referred to as a $2\vartheta - \omega$ scan. Two-dimensional scans in any two of 2ϑ , ω and $2\vartheta - \omega$ are known as ‘reciprocal space maps’ [185]. These are particularly useful for characterising epitaxial films, as the relative positions of the film and substrate peaks in the map allow the level of epitaxial strain to be quantified. For the present work, reciprocal space maps were measured by Mary E. Vickers using a Panalytical PW3050/65 X’Pert PRO diffractometer. The incident beam was from a Cu $K\alpha$ ($\lambda = 1.5418 \text{ \AA}$) radiation source. It was first passed through a graded mirror to produce a parallel beam, and then passed via a Ge (220) 4-bounce monochromator to remove parasitic wavelengths. The diffracted beam was measured with a scintillation counter, via a 3-bounce analyser crystal that removed diffracted X-rays not in $2\vartheta \pm 0.006^\circ$.

At small values of 2ϑ between $\sim 0.5^\circ$ and $\sim 5^\circ$, X-rays reflected from a substrate-film interface can interact with those reflected from the top surface of the film to produce

interference fringes, from which film thickness can be deduced [185]. Such a measurement is termed a ‘reflectivity’ measurement as it is not strictly a diffraction process. For the present work, these measurements were performed with a Bruker D8 Advance diffractometer with a parallel Cu K α incident beam and scintillation counter detector with automatic absorber. The incident beam was cropped with a 0.05 mm-thick slit to reduce the illuminated area of the sample at low angles, and thus improve resolution. Simulated data was fitted to the measured data using Panalytical Reflectivity software.

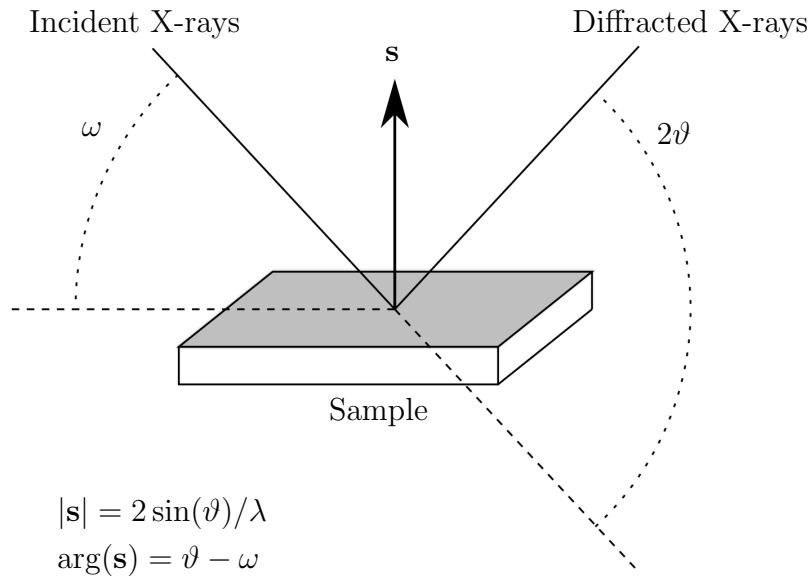


Figure 6.6: Geometry for X-ray diffraction (assumes parallel incident beam). The scattering vector \mathbf{s} is defined for a particular plane by diffraction angle 2ϑ and orientation angle ω . The wavelength of the X-rays is $\lambda = 1.5418 \text{ \AA}$ for a standard Cu K α radiation source.

6.6 Film growth and characterisation

Josée Kleibeuker is acknowledged for providing the recipe for growth of high-quality SrTiO_3 films, and the furnace for pre-annealing substrates. The recipe for growth of high-quality LSMO films in the Mk X PLD system had been established by Neil D. Mathur and co-workers, over the previous decade.

The SrTiO_3 target was a commercial single-crystal (Surfacenet GmbH, Germany), and the LSMO target was a commercial single-phase stoichiometric ceramic (Praxair). Prior to all depositions, targets were polished with 800-1200 grade sandpaper and isopropanol, until all laser damage from the previous deposition was barely visible. Commercially grown single-crystal (001)-oriented NdGaO_3 substrates were obtained (Crystal GmbH). Prior to all depositions, substrates were cleaned for approximately 10 minutes in acetone and then a further 10 minutes in isopropanol, in an ultrasonic bath. The substrates were then annealed at 950 °C for 90 minutes in a quartz tube-furnace under a continuous flow of O_2 at atmospheric pressure. AFM was performed on substrates at this point to assess surface topography. For each deposition, a substrate was mounted on the PLD heater using liberal amounts of silver paste to ensure good thermal contact. Targets were mounted via a target holder on the target carousel. The deposition chamber was evacuated to $\sim 2 \times 10^{-6}$ atm overnight.

Before fabricating a $\text{SrTiO}_3|\text{LSMO}||\text{NdGaO}_3$ bilayer, $\text{SrTiO}_3||\text{NdGaO}_3$ and $\text{LSMO}||\text{NdGaO}_3$ monolayers were deposited to demonstrate epitaxial growth of each material individually.

6.6.1 $\text{SrTiO}_3||\text{NdGaO}_3$ monolayer

The heater temperature was ramped to 750 °C at 35 °C min⁻¹, and a flowing O_2 pressure of 10 Pa was then established as described in Section 6.4. The laser energy was set to give a fluence at the target of 1.3 J cm⁻² per pulse. The rotating target was cleaned by firing pulses at 1 Hz for 5 minutes, with the shutter positioned between the target and the substrate. For deposition, the shutter was withdrawn and 3600 pulses were fired at 1 Hz. After deposition, the temperature was reduced to 600 °C at -10 °C min⁻¹, and O_2 was admitted to the chamber to establish a pressure of ~ 55 kPa for post-annealing. The sample was left annealing under these conditions for one hour, before cooling to room temperature at -10 °C min⁻¹.

AFM and X-ray reflectivity were performed on the deposited SrTiO₃ film. AFM data on the surface of the blank substrate showed atomically flat terracing (Figure 6.7a-b). The topography of the SrTiO₃ film was similar (Figure 6.7a-b). Simulated X-ray reflectivity data assuming a film thickness of 35.4 nm (corresponding to an average of 101.6 laser pulses per nm of film thickness) showed an excellent match to the data (Figure 6.7c).

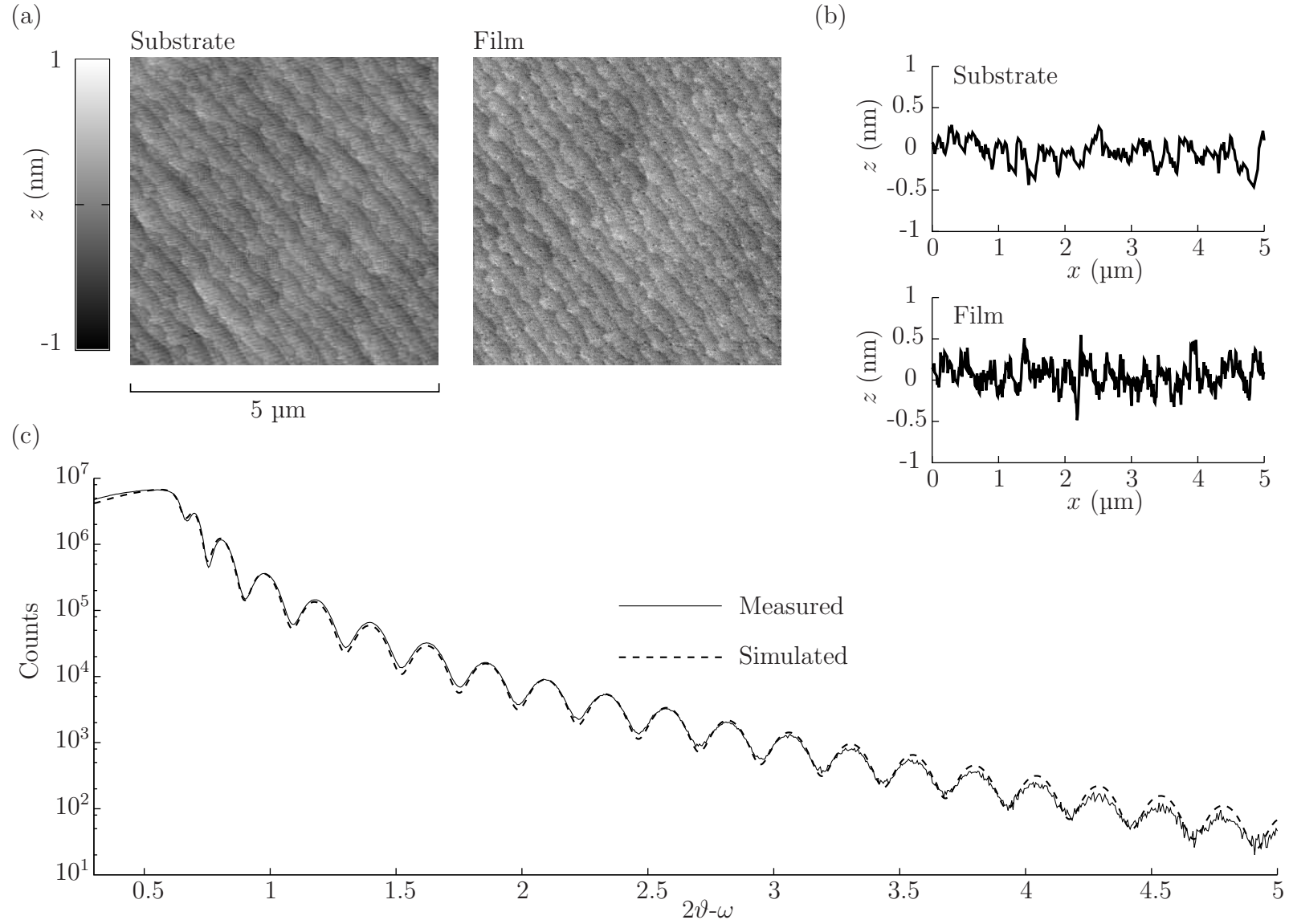


Figure 6.7: AFM and X-ray reflectivity for epitaxial SrTiO_3 monolayer on an (001)-oriented NdGaO_3 substrate. **(a)** AFM topographical measurement of the surface of the bare substrate (measured before deposition) and the surface of the film. **(b)** Single AFM traces from (a), i.e. surface height z as a function of lateral distance x for the bare substrate and the film. **(c)** Low-angle X-ray reflectivity on the film and substrate. Simulated data computed for a film thickness of 35.4 nm.

6.6.2 LSMO||NdGaO₃ monolayer

LSMO was deposited on the (001)-oriented NdGaO₃ substrates using the same procedure as for SrTiO₃, except that the laser fluence was 1.7 J cm⁻² per pulse, the deposition temperature was 775 °C and the deposition O₂ pressure was 15 Pa. These conditions were known to be optimal for growth of LSMO in the Mk X system from previous work by others.

As previously, AFM data on the surface of the blank substrate showed atomically flat terracing (Figure 6.8a-b). The surface of the LSMO film was similarly flat, although the atomic terraces appeared somewhat wider (Figure 6.8a-b). The small identical ‘white’ features in the AFM data for the LSMO film were artifacts, but they did reoccur in the same position on rescanning, and therefore reveal surface defects of an unknown nature. Simulated X-ray reflectivity data using a film thickness of 24.0 nm (corresponding to an average of 150 laser pulses per nm of film thickness) showed an excellent match to the experimental data (Figure 6.8c).

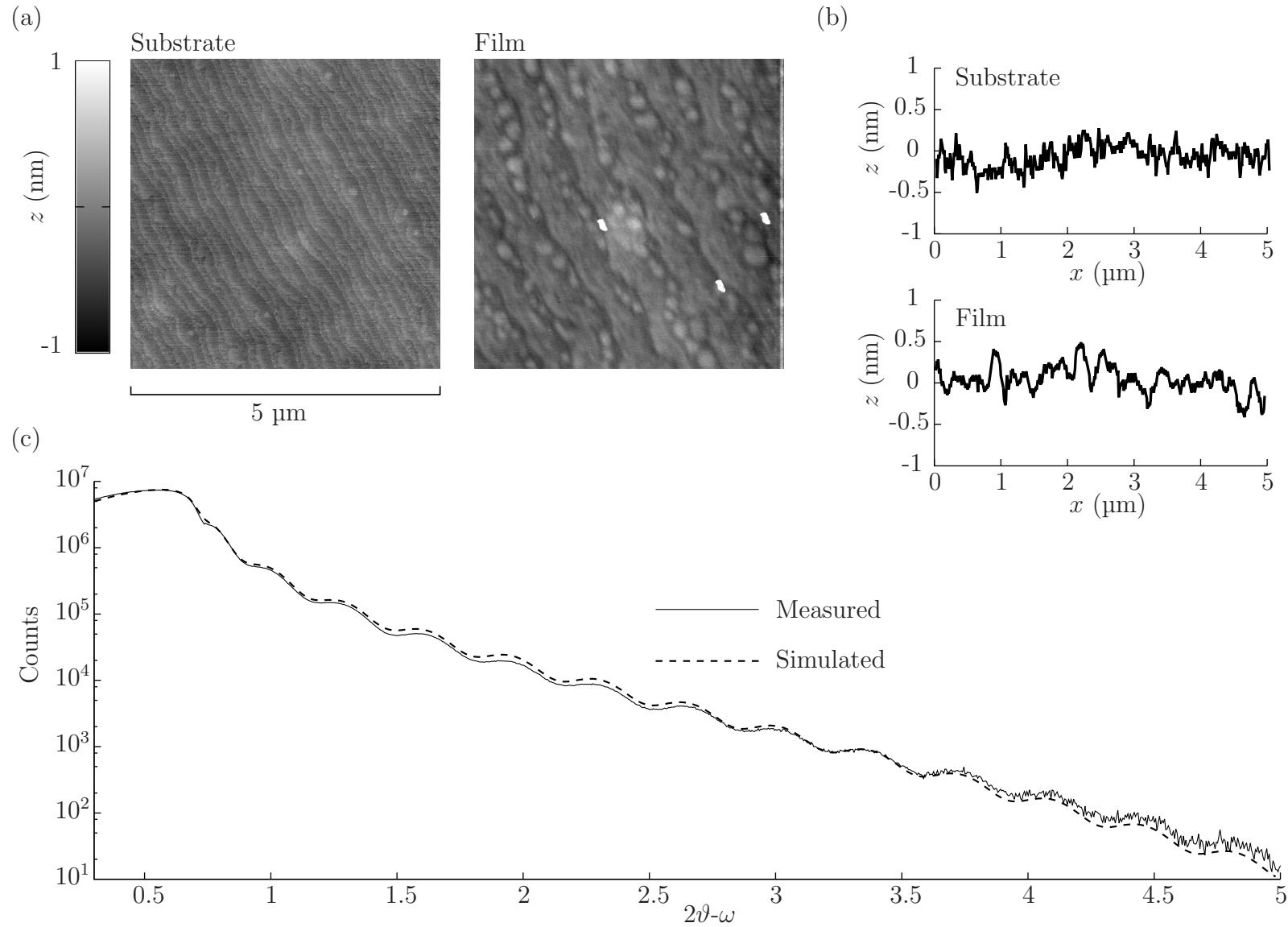


Figure 6.8: AFM and X-ray reflectivity for epitaxial LSMO monolayer on an (001)-oriented NdGaO_3 substrate. **(a)** AFM topographical measurement of the surface of the bare substrate (measured before deposition) and the surface of the film. **(b)** Single AFM traces from (a), i.e. surface height z as a function of lateral distance x for the bare substrate and the film. **(c)** Low-angle X-ray reflectivity on the film and substrate. Simulated data computed for a film thickness of 24.0 nm.

6.6.3 SrTiO₃|LSMO||NdGaO₃ bilayer

Having demonstrated the growth of epitaxial films of SrTiO₃ and LSMO on NdGaO₃ (001) substrates, a bilayer was fabricated with an LSMO bottom electrode and an overlying film of SrTiO₃. For each component of the bilayer, the deposition conditions were the same as those described previously. The number of pulses was 3600 for LSMO, and 7200 for SrTiO₃. Post-annealing was performed at 750 °C.

As previously, AFM data on the surface of the blank substrate showed atomically flat terracing (Figure 6.8a-b). The surface of the SrTiO₃/LSMO bilayer also showed atomically flat terraces, but a superimposed ‘criss-cross’ pattern was also observed (Figure 6.8a-b). This was likely due to a lattice interaction at the interface between the SrTiO₃ and LSMO. Simulated X-ray reflectivity data using a film thickness for SrTiO₃ of 63.8 nm (corresponding to an average of 112.9 laser pulses per nm of film thickness) and a film thickness for LSMO of 24.04 nm (corresponding to an average of 150 laser pulses per nm of film thickness) showed the best match to the experimental data at lower values of 2θ (Figure 6.8c). The expected thicknesses of the films given the previously determined growth rates were used as a starting point for the two parameter fit. The overall quality of the fit was questionable, however the *positions* of the peaks, which are determined by film thickness, were in reasonable agreement, so the film thicknesses quoted are credible. The growth rate of the SrTiO₃ film here was lower than the growth rate for the SrTiO₃ film grown alone, which showed an average of 101.6 laser pulses per nm of film thickness.

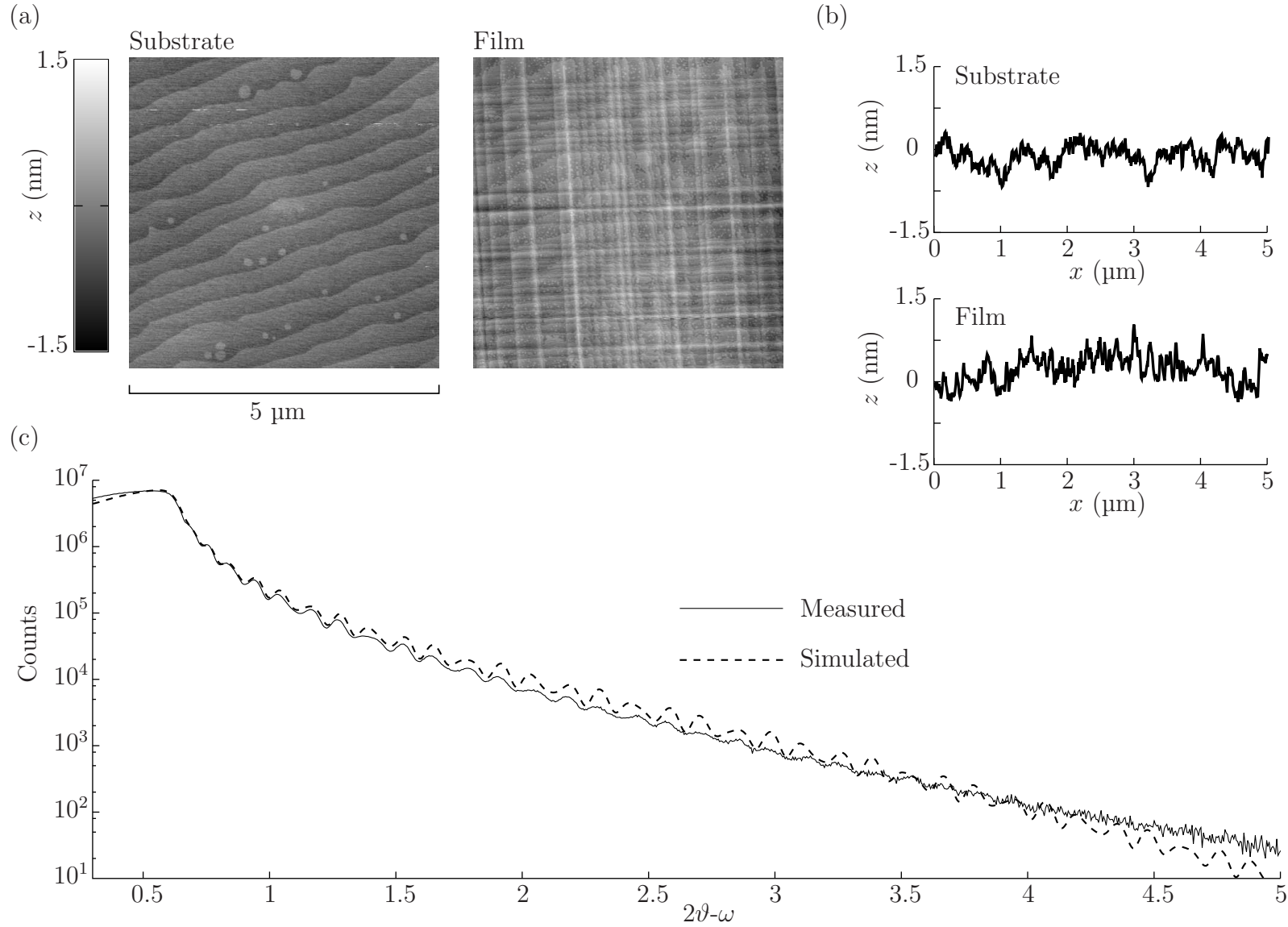


Figure 6.9: AFM and X-ray reflectivity for epitaxial $\text{SrTiO}_3|\text{LSMO}$ bilayer on an (001)-oriented NdGaO_3 substrate. **(a)** AFM topographical measurement of the surface of the bare substrate (measured before deposition) and the surface of the bilayer. **(b)** Single AFM traces from (a), i.e. surface height z as a function of lateral distance x for the bare substrate and the bilayer. **(c)** Low-angle X-ray reflectivity on the bilayer and substrate. Simulated data computed for a SrTiO_3 film thickness of 63.8 nm and a LSMO film thickness of 24.0 nm.

X-ray diffraction was also used to investigate the SrTiO₃/LSMO bilayer. These measurements were by Mary E. Vickers. A two-dimensional scan in ω and $2\vartheta - \omega$ about the NdGaO₃ pseudo-cubic 103 reflection or 116 orthorhombic reflection (Figure 6.10) revealed secondary peaks attributed to SrTiO₃ 103 and LSMO 103 pseudo-cubic reflections.

The two-dimensional scan in ω and $2\vartheta - \omega$ was converted into reciprocal space units (Figure 6.11). The film and substrate peaks coincide along the in-plane reciprocal space axis Q_x , confirming that the SrTiO₃ and LSMO films were fully strained to the lattice of the NdGaO₃ substrate.

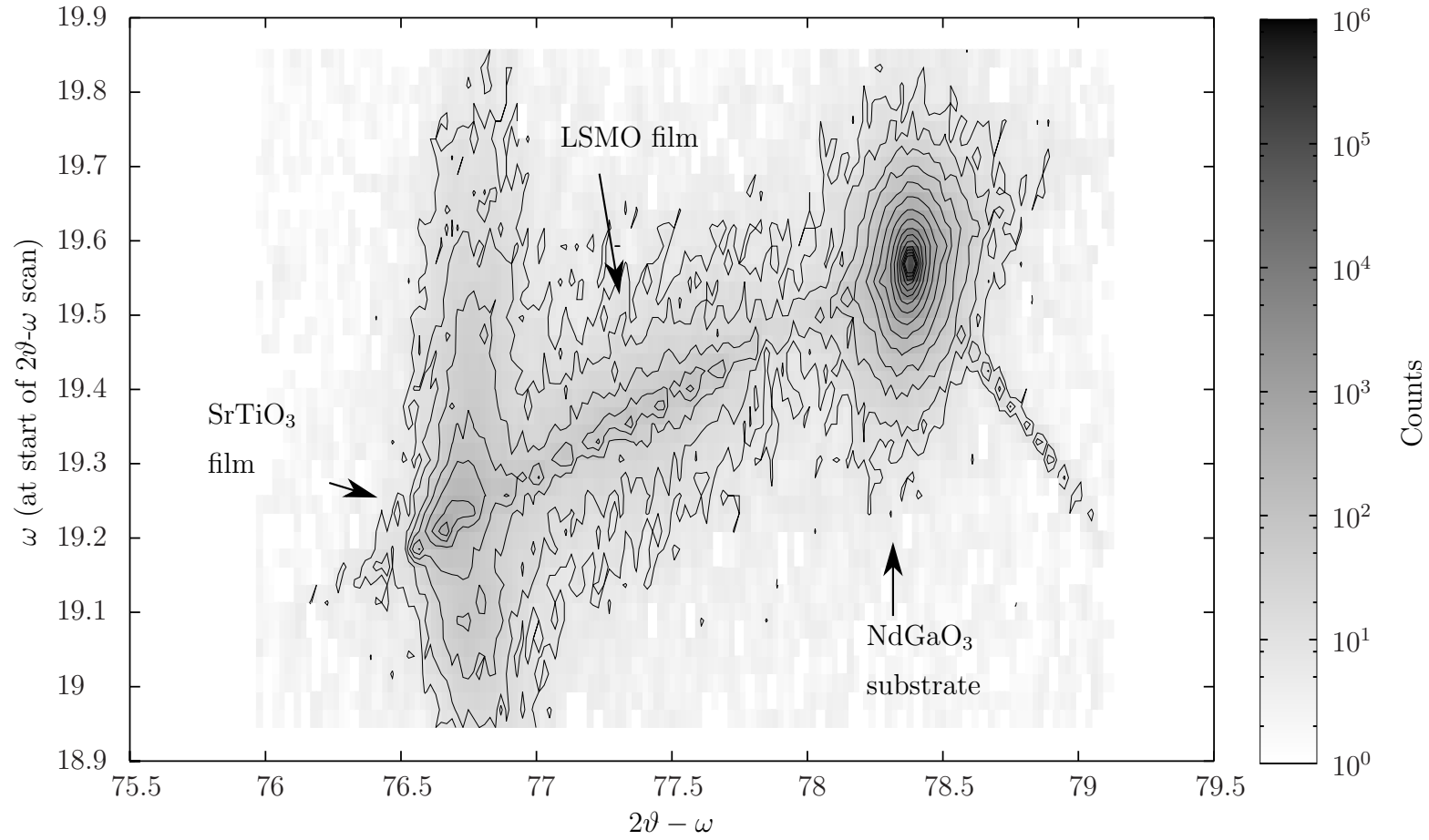


Figure 6.10: XRD for epitaxial SrTiO₃|LSMO bilayer on an NdGaO₃ (001) substrate, showing the NdGaO₃ 103 pseudo-cubic or 116 orthorhombic reflection, the SrTiO₃ 103 pseudo-cubic reflection and the LSMO 103 pseudo-cubic reflection in a two-dimensional scan. Measurement by Mary E. Vickers.

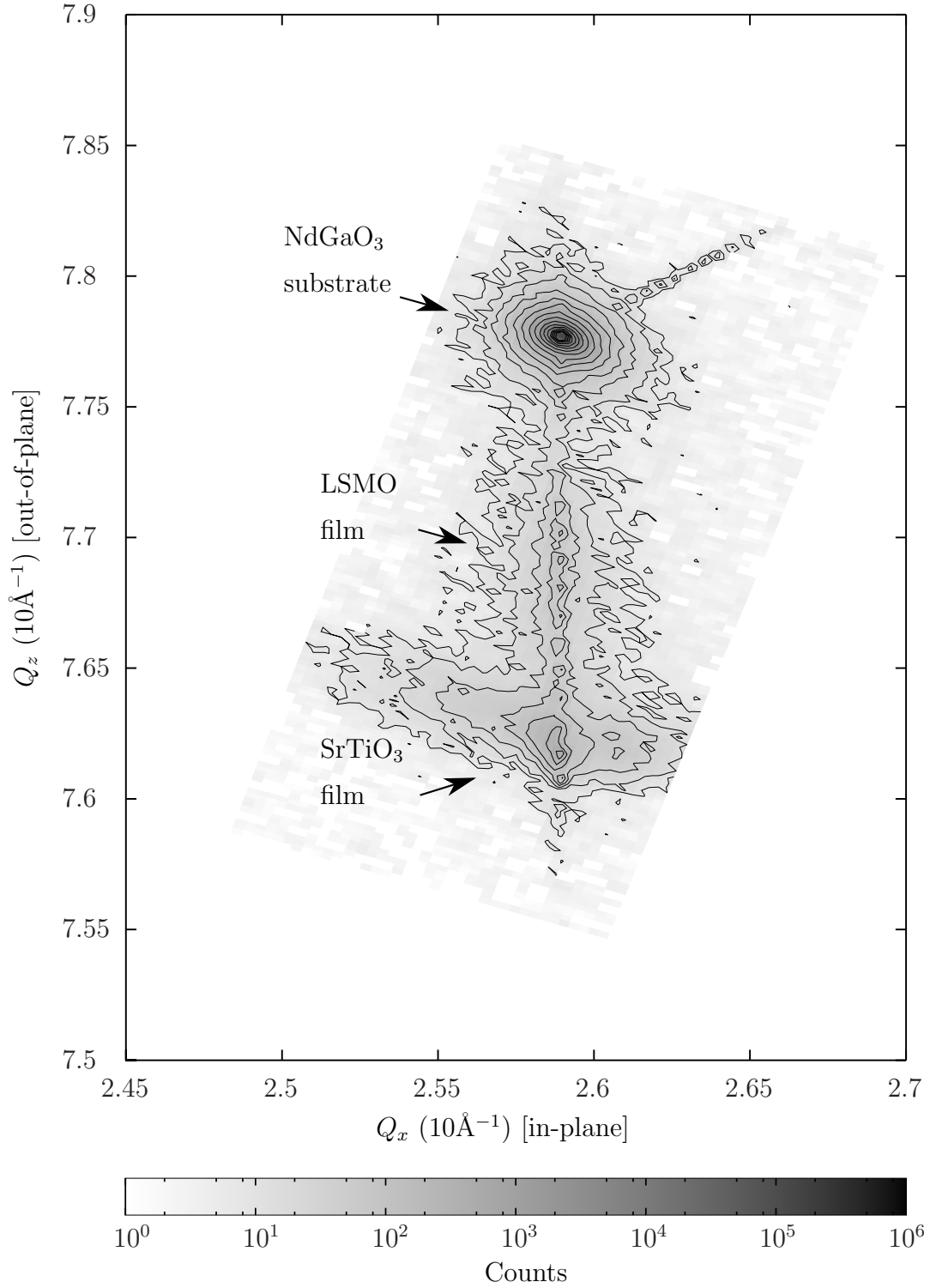


Figure 6.11: Reciprocal space map for epitaxial SrTiO₃/LSMO bilayer on NdGaO₃ (001) substrate, showing the NdGaO₃ 103 pseudo-cubic or 116 orthorhombic reflection, the SrTiO₃ 103 reflection and the LSMO 103 pseudo-cubic reflection in a two-dimensional scan. Computed from raw dataset of Figure 6.10. Measurement by Mary E. Vickers.

6.7 Measurement strategy

The 63.8 nm/24.0 nm thick SrTiO₃/LSMO bilayer was electrically characterised via dielectric and $P(E)$ measurements. Fields were applied out-of-plane by sputtering Pt electrodes on the top surface of the SrTiO₃ film through a hard mask, to form electrode pads of diameter 100 μm , 200 μm and 500 μm . An automated commercial sputter deposition system was used (type K575, Emitech), with a low sputter current of 15 mA for the first half of the deposition to reduce the risk of ion damage, and a higher sputter current of 40 mA for the second half of the deposition. Evaporation would have been preferable to sputtering as it presents no risk of ion damage, but it was not available. After electrode deposition, the sample was annealed on a benchtop hot plate for ~ 1 hour at ~ 100 °C.

The sample was mounted on the bespoke cryogenic stage described in Section 3.3. Contact with the bottom LSMO electrode was made via a smear of silver paste on the side of the substrate. Contact with the top Pt pads was made via tungsten tips attached to micropositioners. All measurements were performed during heating ramps from 120 K at ~ 5 K min⁻¹. The data should be considered preliminary for several reasons. Only a single sample was tested, no comparable dataset was available on cooling (due to limitations of the cryogenic stage), the micropositioner probes occasionally required repositioning mid-measurement causing minor damage to the top electrode pads, ion damage from depositing the top electrode has not been ruled out, and non-strain related mechanisms of ferroelectricity in SrTiO₃ (such as oxygen vacancies or chemical impurities) have not been fully considered or ruled out.

6.8 Dielectric constant

Figure 6.12a shows the dielectric constant of the 63.8 nm-thick epitaxial SrTiO₃ film as a function of temperature, at 1 kHz, using the equivalent parallel capacitance model (Section 2.2). A 200 μm -diameter Pt pad was used as the top electrode. The data showed relatively little variation in the temperature range 120 K to 320 K, with no clear peak to identify a ferroelectric phase transition. There was a small change in the slope of ϵ' at ~ 240 K (Figure 6.12b). The dielectric loss tangent was ~ 0.12 at 120 K, rising to ~ 0.22 at 320 K (Figure 6.12c).

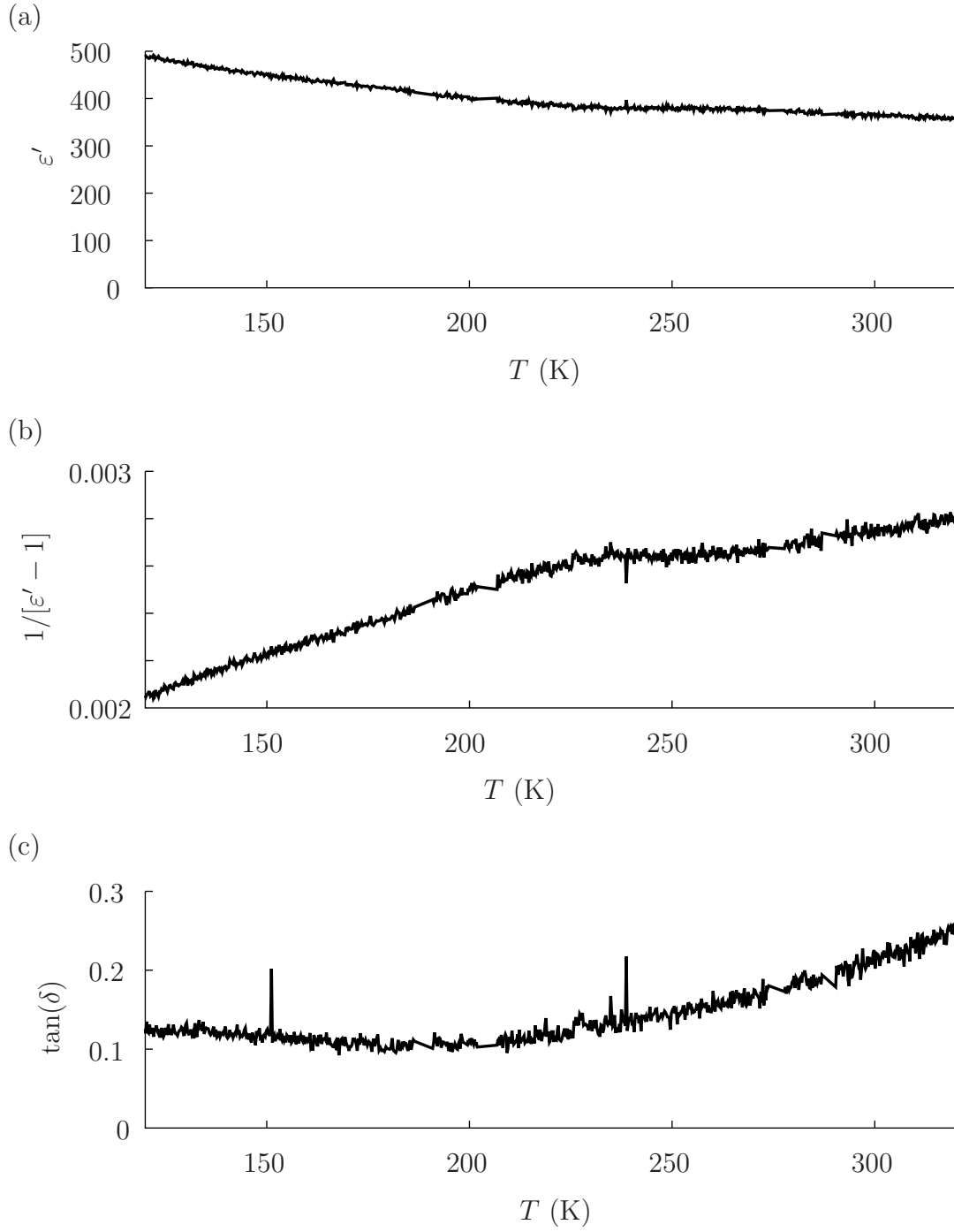


Figure 6.12: Preliminary dielectric data derived from an impedance dataset on the 63.8 nm-thick epitaxial SrTiO_3 film. The amplitude and frequency of the driving field were 30 mV RMS and 1 kHz respectively. Data taken on heating at $\sim 5 \text{ K min}^{-1}$. **(a)** Dielectric constant, **(b)** reciprocal of dielectric susceptibility and **(c)** loss tangent, as functions of temperature.

6.9 $P(E)$ loops

Figure 6.13 shows $P(E)$ loops for the 63.8 nm-thick epitaxial SrTiO₃ film, at 10 kHz and various temperatures. A 100 μm -diameter Pt pad was used as the top electrode. In contrast to all other $P(E)$ datasets shown in this dissertation, these $P(E)$ loops were taken using a ‘traditional’ triangular driving field to yield single major loop with no minor loop. Minor loops could be investigated in a future study.

Electric fields of $\sim 1500 \text{ kV cm}^{-1}$ could be applied without breakdown. However, the $P(E)$ loops out to such high fields appeared asymmetric and lossy, especially at higher temperatures. Accordingly, a lower maximum field of 780 kV cm^{-1} was used for Figure 6.13. All the loops are slim, but the loops at 130 K appear nominally ‘ferroelectric’, as there is no negative curvature. As the temperature was increased, the qualitative ‘ferroelectric’ character declined gradually and the loops became more lossy. Asymmetry between positive and negative field was perceptible throughout, but particularly at higher temperatures, possibly due to the different materials used for the top and bottom electrodes.

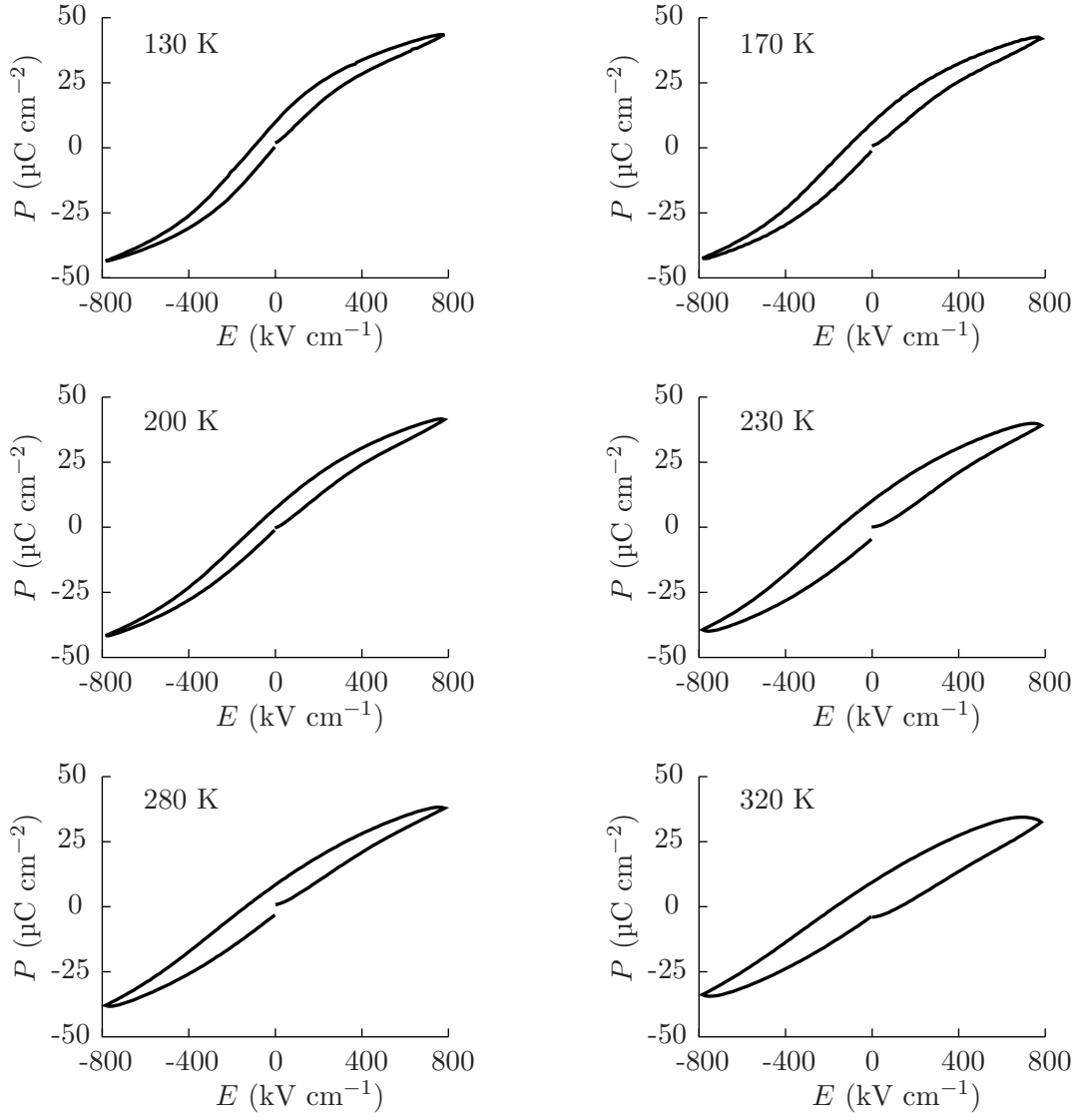


Figure 6.13: Preliminary $P(E)$ loops at 10 kHz for the 63.8 nm-thick epitaxial SrTiO_3 film, at various temperatures.

6.10 Isothermal $|\Delta S|$

To evaluate isothermal $|\Delta S|$ via the ‘standard’ indirect method, $P(E)$ loops were obtained every ~ 6 s during a heating ramp at 5 K min^{-1} . The upper positive branches of these $P(E)$ data were transposed to $P(T)$, and cubic splines were fitted to eliminate spurious fluctuations (Figure 6.14a). The fitted splines were differentiated with respect to T , yielding $\partial P/\partial T$ at various fields E , which was numerically integrated to give volume-normalised and mass-normalised values of isothermal $|\Delta S|$ via the Maxwell relation $(\partial P/\partial T)_E = (\partial S/\partial E)_T$ and the literature value for density of 5100 kg m^{-3} [97] (Figure 6.14b).

The evaluated isothermal $|\Delta S|$ shows a broad anomaly near $\sim 180 \text{ K}$, where an applied field of 780 kV cm^{-1} induces an isothermal $|\Delta S| \sim 8 \text{ J K}^{-1} \text{ kg}^{-1}$ or $\sim 41 \text{ J K}^{-1} \text{ dm}^{-3}$. At first glance the anomaly appears consistent with a diffuse second-order phase transition at $\sim 180 \text{ K}$, but a closer look at the $P(T)$ results (Figure 6.14a) reveals localised fluctuations (possibly related to electrode damage) that could have adversely affected the spline fit to localise a broader peak about $\sim 180 \text{ K}$.

It seems plausible that the high-temperature ‘tail’ of a phase transition with $T_C < 120 \text{ K}$ was observed, and not the transition itself. It is also possible that there is no well defined phase transition, even at significantly lower temperatures than 120 K , due to the anisotropy of the cell parameters of the NdGaO_3 substrate, as was suggested by Nuzhnyy *et al.* [173]. Either of these explanations would be consistent with the observed dielectric data which showed no peak to correspond to a ferroelectric transition in the temperature range $120 - 320 \text{ K}$ (Figure 6.12).

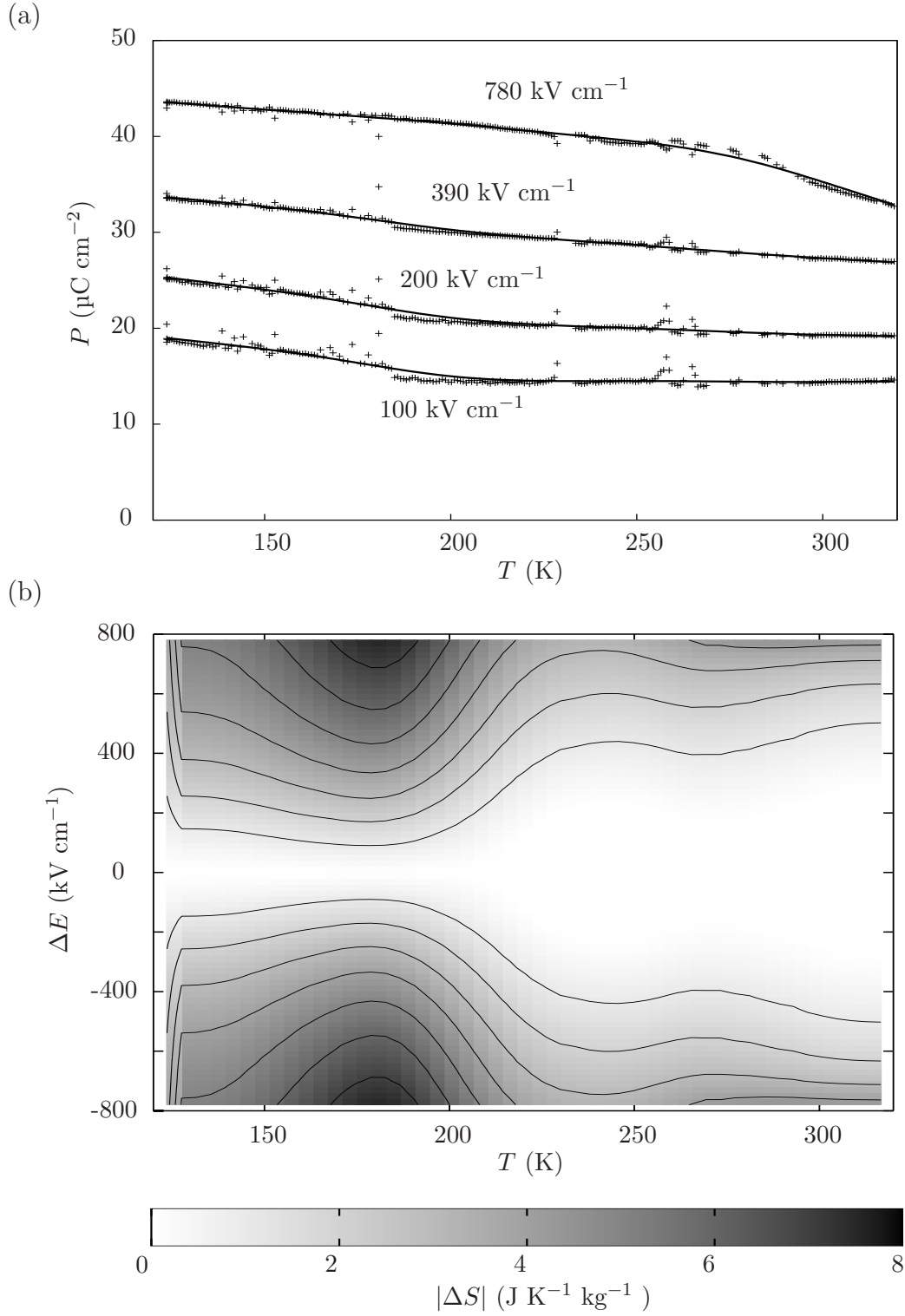


Figure 6.14: Plots for (a) selected $P(T)$ and (b) evaluated isothermal $|\Delta S|$ for the 63.8 nm-thick SrTiO_3 epitaxial film. Data were taken on heating, and are derived from the upper positive branch of major $P(E)$ loops. (a) Points: raw (measured) data, lines: cubic spline fit. (b) Data for negative E : ‘mirror image’ of those for positive E . Contour spacing: $1 \text{ J K}^{-1} \text{kg}^{-1}$.

6.11 Conclusions

Epitaxial ~ 1 % compressively in-plane strained and ~ 64 nm-thick SrTiO_3 films were grown on NdGaO_3 (001) substrates with a 24 nm-thick $\text{La}_{0.67}\text{Sr}_{0.33}\text{MnO}_3$ bottom electrode and Pt top electrodes. The films showed atomically flat terraces, and X-ray diffraction confirmed epitaxy and crystallinity. Dielectric data in 120-320 K did not reveal any ferroelectric phase transition (Figure 6.12). Nominally ‘ferroelectric’ $P(E)$ loops were observed at low temperatures, but having failed to determine a transition temperature, a conclusion that the SrTiO_3 films are ferroelectric is premature.

The preliminary isothermal entropy change of $\sim 8 \text{ J K}^{-1} \text{ kg}^{-1}$ is of the same order or magnitude as the entropy change in Zr-rich PZT [20]. The corresponding adiabatic temperature change was $|\Delta T| \sim 3.5 \text{ K}$ (using $|\Delta T| \sim T|\Delta S|/c_E$, where $T = 180 \text{ K}$ and specific heat capacity $c_E = 410 \text{ J K}^{-1} \text{ kg}^{-1}$, the value for a single crystal [186]), at a starting temperature of 180 K. This is smaller than the 12 K predicted for Zr-rich PZT. However, there are no reports of ‘giant’ electrocaloric effects at cryogenic temperatures, and the predicted effect in the epitaxial SrTiO_3 films did not appear to be saturated (Figure 6.14b). Larger driving fields could be achieved in future, perhaps in a thinner sample.

The question of whether there is a phase transition below 120 K, or whether the phase transition is suppressed by anisotropy of the pseudo-cubic unit cell of the NdGaO_3 substrate (as suggested by Nuzhnyy *et al.* [173]), could perhaps be resolved by a follow-up measurement at liquid helium temperatures.

At ~ 64 nm-thick, the SrTiO_3 films are amongst the thinnest ever successfully characterised, if on a preliminary basis, for electrocaloric properties. This was likely a result of the high crystalline quality of the epitaxial films.

Chapter 7

Modelling of multilayered capacitors for cooling

Multilayered capacitors (MLCs) (Figure 7.1) were proposed as electrocaloric coolers by Kar-Narayan and Mathur in 2010 [45], who reported serendipitous adiabatic temperature changes of ~ 0.5 K in commercial MLCs with 5 μm -thick Y5V¹ dielectrics and 2 μm -thick nickel electrodes. These commercial MLCs were since used to demonstrate a prototype electrocaloric cooler [51].

MLCs are attractive for three reasons:

- The layers of dielectric are thin and thus associated with large electrocaloric effects.
- The large number of stacked layers collectively have sufficient thermal mass to cool macroscopic loads.
- The thermal conductivity of the MLC is large as it is dominated by the metallic electrodes, enabling rapid input and extraction of electrocaloric heat.

¹Based on doped BaTiO₃.

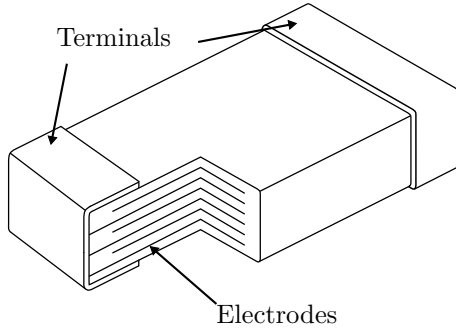


Figure 7.1: Illustration of multilayered capacitor. Adapted from [187].

Kar-Narayan and Mathur developed a model based on a lumped thermal circuit to predict cooling powers for hypothetical MLCs with materials optimised for electrocaloric cooling [19]. This is superseded in the present work by a model using the computational finite element method. The finite element method gives more accurate predictions for MLC cooling power, enabling MLCs to be geometrically optimised for electrocaloric cooling. It has

also been used to create a new lumped thermal circuit model.

The collaboration of James McGinnigle is acknowledged in developing a preliminary FEM model of an MLC, which was superseded by the model described here.

7.1 Lumped thermal circuit model

The lumped thermal circuit model of Kar-Narayan and Mathur [19] was constructed of interdigitated layers of electrode (thickness d_e , thermal conductivity κ_e , density ρ_e and specific heat c_e) and electrocaloric material (thickness d_{EC} , thermal conductivity κ_{EC} , density ρ_{EC} and specific heat c_{EC}) with overall length D and width w (Figure 7.2). Each half-length of electrode was represented as a thermal resistor $R_e = \frac{D}{2} / [\kappa_e w d_e]$ with no thermal capacitance². Each half-thickness of electrocaloric material was modelled as a thermal capacitor $C_{EC} = w D [d_{EC}/2] \rho_{EC} c_{EC}$. Thus it was assumed that EC heat originates from points in the centre of each electrocaloric layer. The MLC terminals and the short sections of electrically unaddressed electrocaloric material at the ends of the layers were ignored. The time period for a complete electrocaloric cycle of the model MLC was set at 20τ to allow a time of 5τ for each of the four stages of the cycle, namely:

- Electrocaloric heating of the MLC.
- Rejection of the heat from the MLC to a heat reservoir.

²Although an electrode thermal capacitance was discussed in the paper, it was not used for calculating cooling powers. It was used erroneously for calculating a secondary result of the paper, the thermal time constant of an MLC based on a Y5V dielectric and Ni electrodes.

- Electrocaloric cooling of the MLC.
- Withdrawal of heat from a load.

Outward heat flow $\phi(t)$ was taken to follow an exponential decay of form $\phi = \phi_{\max} e^{-t/\tau}$. Evaluating ϕ_{\max} as $\Delta T/R_{\text{total}}$, average cooling power may be calculated as $P = (1/20\tau) \int_0^{5\tau} \phi_{\max} e^{-t/\tau} dt = \phi_{\max}/20$. Cooling power per unit area is then given by:

$$P_A = n\Delta T/20R_e = \frac{2\kappa_e w d_e n \Delta T}{20DA} \quad (7.1)$$

where A is the sheet area of the MLC.

Six model MLCs were considered. The electrocaloric materials were 6.5 μm -thick Y5V ($\Delta T = 0.74$ K, from the commercial MLC whose electrocaloric properties were measured experimentally [45]), 350 nm-thick $\text{PbTi}_{0.05}\text{Zr}_{0.95}\text{O}_3$ ($\Delta T = 12$ K [20]) and 1 μm -thick poly(vinylidene fluoride-trifluoroethylene) (55/45 mol %) [PVDF-TrFE] ($\Delta T = 12$ [21]). The electrode materials were Ni ($\kappa = 94$ W m $^{-1}$ K $^{-1}$) and Ag ($\kappa = 428$ W m $^{-1}$ K $^{-1}$), with the ratio of the thickness of the electrode to that of the electrocaloric material fixed at around 1:3, the value from the commercial MLC measured in [45]. The geometries, material parameters and predicted cooling powers of the six MLCs are given in Table 7.1. The best-performing MLC that was modelled, PVDF-TrFE with Ag electrodes, showed a cooling power of 2.88 kW kg $^{-1}$, a 128-fold improvement on the commercial MLC which was the worst performing. To set this number in context the authors noted a typical cooling power for an air-conditioning unit of 20 kW.

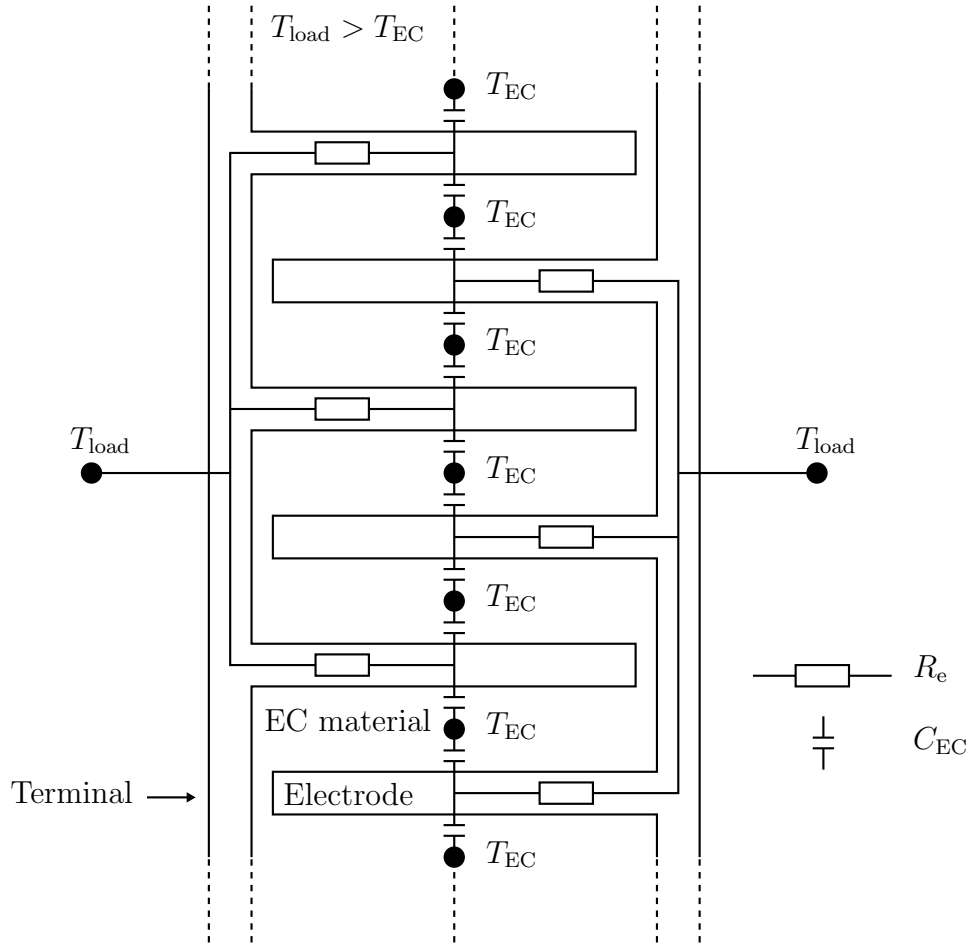


Figure 7.2: Lumped thermal circuit model of an MLC developed by Kar-Narayan and Mathur [19].

Parameter	Unit	Y5V-Ni	Y5V-Ag	PZT-Ni	PZT-Ag	PVDF-TrFE-Ni	PVDF-TrFE-Ag
d_e	μm	2.0	2.0	0.1	0.1	0.3	0.3
d_{EC}	μm	6.5	6.5	0.35	0.35	1.0	1.0
D	mm	3.3	3.3	3.3	3.3	3.3	3.3
w	mm	2.56	2.56	2.56	2.56	2.56	2.56
n		200	200	200	200	200	200
κ_e	$\text{W m}^{-1} \text{K}^{-1}$	94	428	94	428	94	428
ϱ_e	kg m^{-3}	8907	10500	8907	10500	8907	10500
c_e	$\text{J kg}^{-1} \text{K}^{-1}$	429	235	429	235	429	235
κ_{EC}	$\text{W m}^{-1} \text{K}^{-1}$	2.6	2.6	2.03	2.03	0.2	0.2
ϱ_{EC}	kg m^{-3}	5840	5840	7800	7800	1770	1770
c_{EC}	$\text{J kg}^{-1} \text{K}^{-1}$	434	434	330	330	1500	1500
ΔT	K	0.74	0.74	12	12	12	12
P_{M}	kW kg^{-1}	0.022	0.099	0.29	1.25	0.7	2.88

Table 7.1: Parameters of the MLCs modelled with the lumped thermal circuit. Data from Kar-Narayan and Mathur [19], where d is layer thickness, D is overall layer length, w is MLC width, n is number of layers, κ is thermal conductivity, ϱ is density, c is specific heat capacity and the subscripts ‘e’ and ‘EC’ refer to electrodes and electrocaloric layers, respectively. The top line gives the MLC model in the form ‘EC material-electrode material’. Apart from the Y5V-Ni MLC, a standard electronic component available commercially, these MLCs are hypothetical. Predicted cooling power per unit mass P_{M} was evaluated by taking the MLC mass as that of the MLC layers alone, i.e. ignoring the terminals.

7.2 Finite element model

The finite element method (FEM) is a well-established approach for modelling 2- or 3-dimensional systems of arbitrary geometry [188,189]. The physical object or system of objects being modelled is first broken down into a mesh of small volumetric ‘elements’. Elements can take a variety of shapes that are bounded by ‘nodes’. For example, a simple brick-shaped (cuboid) element is defined by eight nodes, one at each corner. Nodes are shared between adjacent elements, thus a corner node located within the bulk of a solid object would be shared between eight adjacent brick-shaped elements. Each element in the model is assigned physical properties, which for thermal FEM are density, heat capacity and thermal conductivity. Each node is assigned a starting temperature.

During the simulation the model is perturbed from equilibrium, for example by admitting heat into certain elements. The finite element ‘solver’ is a computer program which uses physical laws to predict the dynamic evolution of the temperatures of the nodes (with the elements as the transmissive medium) as a result of the perturbation.

The MLC model developed for the present work is illustrated in Figure 7.3a.

Geometrically, the FEM model differed from the lumped thermal circuit model in the following ways:

- In the FEM model the *electrically unaddressed* electrocaloric material at the ends of the MLC layers was included, and given a length L_U .
- In the FEM model the MLC terminals were included, and given a length $L_T = 0.2$ mm, the value from the commercial MLC tested experimentally in [45]. The terminals were assumed to be of the same material as the electrodes.

Figure 7.3b shows how the FEM model was ‘meshed’ into FEM elements. The elements were brick-shaped and of variable sizes, with the largest element densities occurring at the edges of the MLC layers as those were the areas expected to show the largest thermal inhomogeneity. The nodal structure will be discussed in Section 7.2.1.

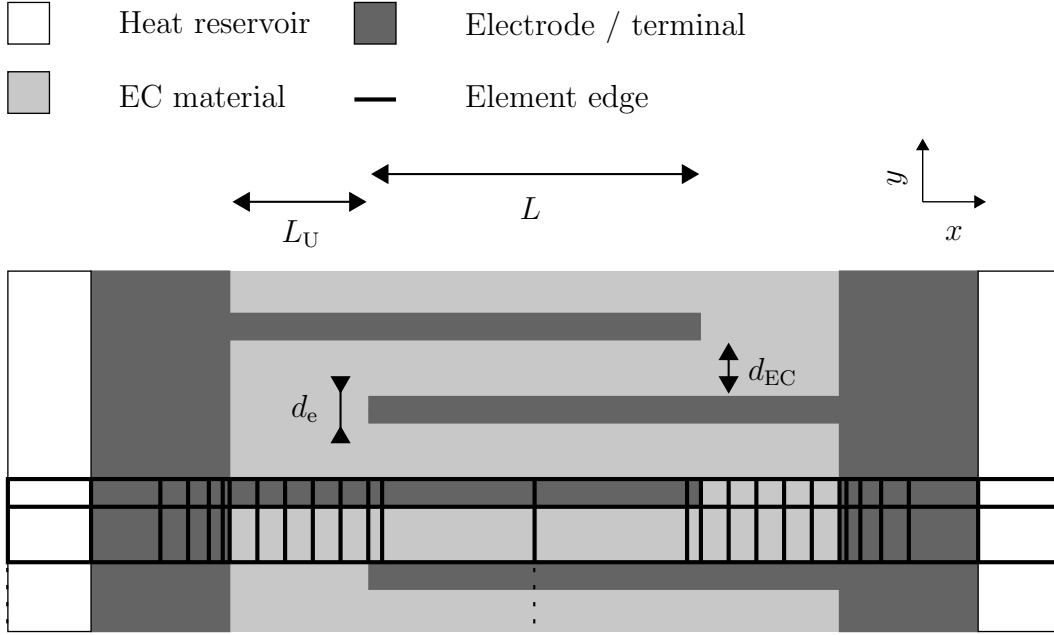
It is emphasised that FEM is simply a way of characterising heat flow in an MLC. It models the *consequences* of electrocaloric processes which happen to be occurring in an MLC environment. It does not model the electrocaloric processes themselves. The FEM has no knowledge or consideration of electric fields, polarisations, electrocaloric strengths, or any other electric or electrocaloric properties, other than the amount of electrocaloric heat that is evolved, a given parameter.

The simulations were conducted on a standard AMD64 desktop server (type Optiplex 755, Dell). The FEM ‘solver’ was Calculix, a freely available program written by Guido Dhondt [189]. Calculix was selected because its source code was in the public domain, improving scientific integrity. The user interface was written for web browsers in the PHP programming language, allowing the simulations to be controlled remotely from any internet station (Figure 7.4). A MySQL database was created to store all the MLC models that were simulated. Once created, models went into an automatic queue as the solver could only simulate one model at a time. Each simulation took around 3 minutes to complete. The simulation consisted of the following stages:

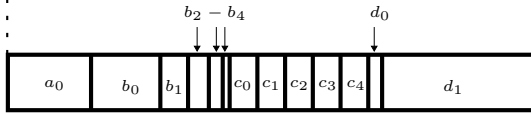
- The bespoke application `make_mlc.cc`, written by the author in C++, created a mesh file from the geometric and material parameters of the MLC model.
- The mesh file was passed to the Calculix solver. The solver produced output in the form of a text file containing the simulated heat flux at the edges of the MLC terminals, as a function of time, after electrocaloric heating and cooling.
- The bespoke application `interpret_mlc_fea.cc`, written by the author in C++, processed the output file from the solver to extract the thermal time constant τ .

Systematic mapping of cooling power P in MLC parameter space was straightforward, because a large number of models could be generated programmatically and placed in the queue for automatic processing over a time period of several days.

(a)



(b)

*x*-axis lengths

$$a_0 = 0.2 \text{ mm}$$

$$b_n = 0.2/2.75 \quad [n = 0]$$

$$= 0.1b_0 \quad [n = 4]$$

$$= b_0 - \frac{n(b_0 - b_4)}{4} \quad [\text{otherwise}]$$

$$c_n = 0.2L_U$$

$$d_n = L/22 \quad [n = 0]$$

$$= 10d_0 \quad [n = 1]$$

y-axis lengths

$$d_e \quad [\text{electrode layer}]$$

$$d_{EC} \quad [\text{EC layer}]$$

z-axis lengths

$$2.5 \text{ mm} \quad [\text{all elements}]$$

Figure 7.3: FEM model of the an MLC. **(a)** Drawing showing the geometry of the model. Only five electrocaloric layers are shown, the actual model used twenty such layers, with electrodes at the extremes of the *y*-axis. The heat reservoir was held at a fixed temperature. **(b)** Distribution of FEM elements along the *x*-axis. The dimensions of all the FEM elements are described as a function of MLC parameters.

MLC FEA modelling system

Pre-processor: developed in-house by SC (C++ for Linux).
Solver: [Calculix CCX](#)(multithread build)

Real-time system status

Current job	System idle
CPU % load	19
Memory % usage	78.8

[Real-time status](#)

Menu

Job queue	Jobs (0D)	Scans (1D)	Scans (2D)
Manage	New job	New scan	New scan
	View jobs in development	View scans in development	View scans in development
	View solved jobs	View solved scans	View solved scans

Viewing job #8523 (processed)

Simulation results (SI units)

Time constant (from exp fit to data)	0.000195497
Mass of 1 layer	2.80168e-06
Heat pumped per layer	0.0010875
Cooling power per unit mass	1.9855e+06
Cooling power per layer	5.56274

Files

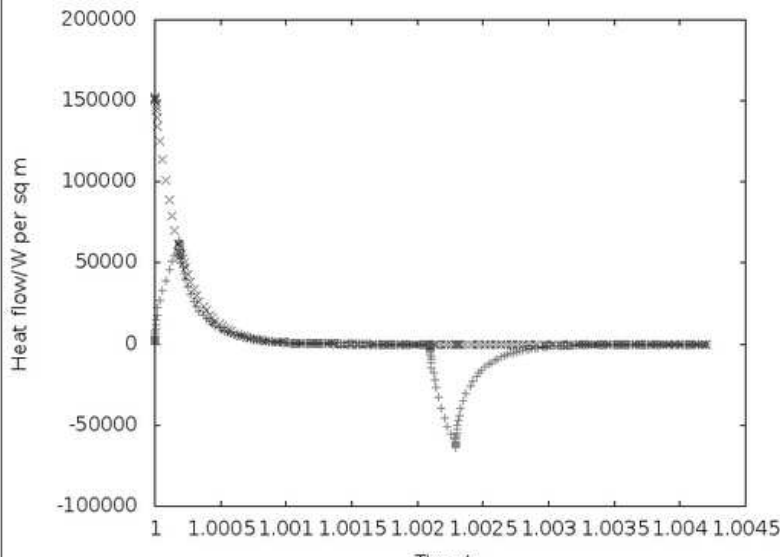
Name	jobs/job8523/job_input_deck_heatfluxes.png
Description	Time-resolved heatflux at RHS of RHS MLC terminal showing exponential fit
Image	

Figure 7.4: Web-based interface to FEM program, showing a model MLC which has been simulated. The results of the simulation are being viewed.

7.2.1 Generation of mesh

The purpose of `make_mlc.cc` was to generate an FEM mesh file using the parameters of the MLC model, i.e. d_e , d_{EC} , L , L_U , κ_e , ϱ_e , c_e , κ_{EC} , ϱ_{EC} , c_{EC} , ΔT and T (Figure 7.3 and Table 7.1).

Brick-shaped FEM elements were used in the mesh. As previously discussed, brick-shaped elements use at least eight nodes, one for each corner. However, Calculix also allows 20-node brick-shaped elements with additional nodes at the centres of the 12 sides (Figure 7.5), which were used for the present work as they provide a more accurate simulation [189].

The C++ code will not be discussed in detail. To illustrate the general approach, some aspects of the object-oriented³ design will be briefly outlined. Special variable types (i.e. C++ `structs`) were conceived to represent FEM nodes and elements. Nodes were specified by three numbers representing their position in 3D space. All the nodes in the model were stored in an array called `all_nodes`. Elements were specified by three numbers representing κ , ϱ and c and a reference number for each of its requisite 20 nodes (from `all_nodes`). All the elements in the model were stored in an array called `all_elements`.

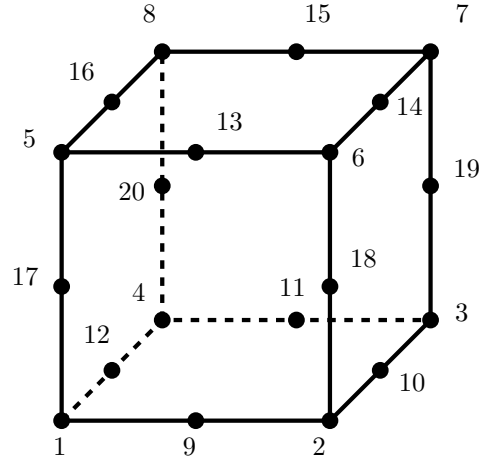


Figure 7.5: Illustration of 20-node brick-shaped FEM element, showing nodes and their labels. After [189].

The following procedure was used to populate the arrays `all_elements` and `all_nodes` and thus generate the FEM mesh:

- The array `all_elements` was populated with all of the FEM elements required by the model, as shown in Figure 7.3. For each element created, the four nodes at

³C++ provides variable types such as `double` (for floating point variables) and `int` (for integers). Additionally, the programmer is able to define their own variable types via the `struct` or `class` commands. This is an example of object-oriented programming which allows the programmer to work in terms of variables ('objects') which are convenient for the problem, rather than being convenient or efficient for the computer.

positions 1, 9, 12 and 17, i.e. the four nodes at or near one of the element corners (Figure 7.5), were simultaneously created in `all_nodes`. The remaining node indices were left unassigned.

- Figure 7.5 shows that the node at positions 1 on an element with spatial index (i,j,k) is the same as the node at position 5 on an element with spatial index $(i,j-1,k)$, etc. So the next stage of the program was to go through all the elements in `all_elements` and assign the node indices 2-8, 10-11, 13-16 and 18-20 by means of looking up the node indices in positions 1, 9, 12 and 17 in adjacent elements. If an adjacent element could not be found (because the edge of the model MLC had been reached), new nodes were created in those positions. By the end of this step, all the elements and nodes in the model would have been created and cross-referenced to each other.
- All of the nodes and elements were written out to a mesh file in the correct format for interpretation by Calculix.

It was necessary to define a total time-frame t_s for the simulation, which needed to be large enough for the MLC to reach a state of equilibrium after the thermal perturbation in the electrocaloric layers. As such it was set at $m\tau_s$, where τ_s was an initial estimate for τ using the lumped thermal circuit model of Kar-Narayan and Mathur, and m was a user-specified multiplier set on a case-by-case basis by trial and error (the default value was 10, which sufficed for the vast majority of simulations). The increment time of the simulation was controlled by internal algorithms of Calculix, but constrained to lie between $0.000002t_s$ (the value at the start of the simulation) and $0.01t_s$.

The remaining task for `make_mlc.cc` was to define a thermal perturbation for the model to represent the electrically driven change in temperature within the electrocaloric layers of the MLC. The perturbation was defined in terms of FEM ‘steps’, as follows:

- All the nodes were set to an initial temperature T .
- The electrically addressed sections of the electrocaloric layers (i.e. those spanned by L but not L_U , Figure 7.3) were steadily supplied over $0.1t_s$ with ‘electrocaloric’ heat totalling $\Delta T_{\text{EC}}\varrho_{\text{EC}}$ per unit volume of electrocaloric layers.
- The model waited a time period of t_s to allow thermal equilibrium to be re-established.

The justification for supplying electrocaloric heat over a finite time of $0.1t_s$ was to avoid discontinuities or very rapid changes in the first time-derivative of T . Such discontinuities were found to compromise the accuracy⁴ of the simulation.

7.2.2 Interpretation of simulated data

The purpose of `interpret_mlc_fea.cc` was to extract the value of the thermal time constant τ of the model from the output datafiles of Calculix. Following Weisstein [190], a fit of form $y = A \exp(x/B)$ to a set of datapoints x_i, y_i is best performed by minimising the function $\sum_i y_i (\log y_i - a - bx_i)^2$ where a and b are approximations to $\log(A)$ and B (the more obvious route of taking natural logarithms of both sides and performing linear regression gives a result that is unduly weighted towards the smaller values of y_i). The fitted values of a and b are then given by:

$$a = \frac{\sum_i [x_i^2 y_i] \sum_i [y_i \log y_i] - \sum_i [x_i y_i] \sum_i [x_i y_i \log y_i]}{\sum_i y_i \sum_i [x_i^2 y_i] - (\sum_i [x_i y_i])^2} \quad (7.2)$$

$$b = \frac{\sum_i y_i \sum_i [x_i y_i \log y_i] - \sum_i [x_i y_i] \sum_i [y_i \log y_i]}{\sum_i y_i \sum_i [x_i^2 y_i] - (\sum_i [x_i y_i])^2} \quad (7.3)$$

Having thus obtained estimates for the value of τ from the simulated data (which closely followed an exponential decay curve), the predicted mass-normalised intrinsic cooling power of the MLC was evaluated as $P_M = Q_{EC}/[20\tau M]$ where Q_{EC} is the total electrocaloric heat, i.e. $\Delta T c_{EC} \rho_{EC}$ multiplied by the total volume of the electrically addressed electrocaloric layers, and M is the total mass of the MLC (including the terminals). Sheet-area normalised intrinsic cooling power was evaluated as $P_A = Q_{EC}/[20\tau A]$, where A is the sheet area (the cross-section in the $y-z$ plane of Figure 7.3) for an MLC terminal. The intrinsic operating frequency of the MLC was evaluated as $f = 1/[20\tau]$, i.e. allowing a time period of 20τ for a complete electrocaloric cycle as justified in Section 7.1. For convenience the simulated heat-flow data $\phi(t)$ were

⁴As assessed via a comparison of the total heat removed from the MLC (from integration of outward heat flux) with the total heat supplied to the MLC (i.e. the electrocaloric heat). Using the specified time period for the supply of electrocaloric heat, these numbers showed agreement within 10%, and usually within 1%.

plotted, along with the fit, for direct viewing via the web interface (an example of this was shown in Figure 7.4).

7.2.3 Testing of mesh

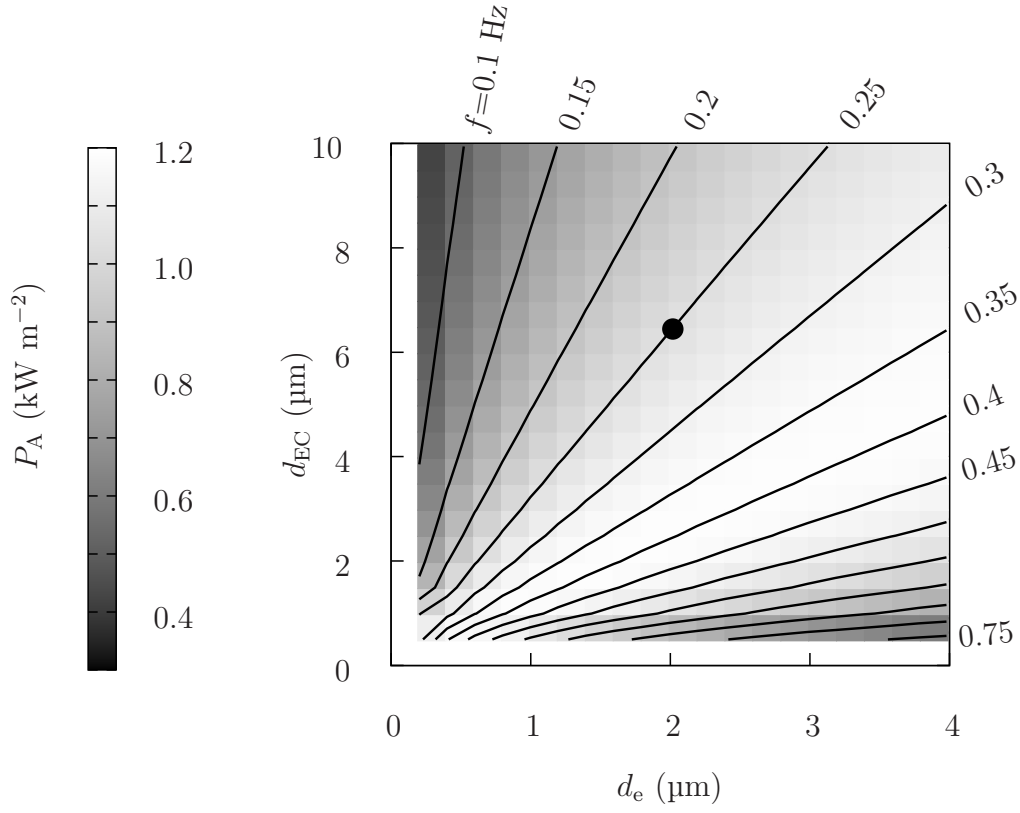
To test the adequacy of the mesh density of the standard FEM model, a model of the Y5V-Ni MLC was created with double the standard mesh density from Figure 7.3 in the x and y dimensions. The time constant of model with the high-density mesh was 0.2016 s, which was very close to the value of 0.2014 s of the model with the standard-density mesh. This agreement justified the use of the more efficient standard mesh density for simulations.

7.3 Geometric optimisation of MLCs for cooling

7.3.1 Optimisation of d_e and d_{EC}

The FEM simulation was iterated over a large number of different MLC geometries to find the most favourable for electrocaloric cooling. The existing Y5V-Ni MLC (Table 7.1, with $L = 2.9$ mm and $L_U = 0.15$ mm) was used as a starting point. Figure 7.6a shows the effect of varying d_e and d_{EC} . The results reveal a ‘magic ratio’ of $d_e/d_{EC} \sim 0.75$ corresponding to the largest values of P_A . The magic ratio is the result of a trade-off between the volumetric fractions of electrocaloric material and electrode material: a large fraction of electrocaloric material leads to larger amounts of electrocaloric heat Q_{EC} , but a large fraction of the more thermally conductive electrode material leads to larger values of operating frequency f . The magic ratio varied very slightly when d_{EC} was increased by an order of magnitude, but remained static when d_{EC} was decreased by up to two orders of magnitude (Figure 7.6b). The simulation suggests that a 1.2-fold increase in cooling power is associated with altering d_e from its starting value of 2.0 μm to an optimal value of ~ 4.9 μm .

(a)



(b)

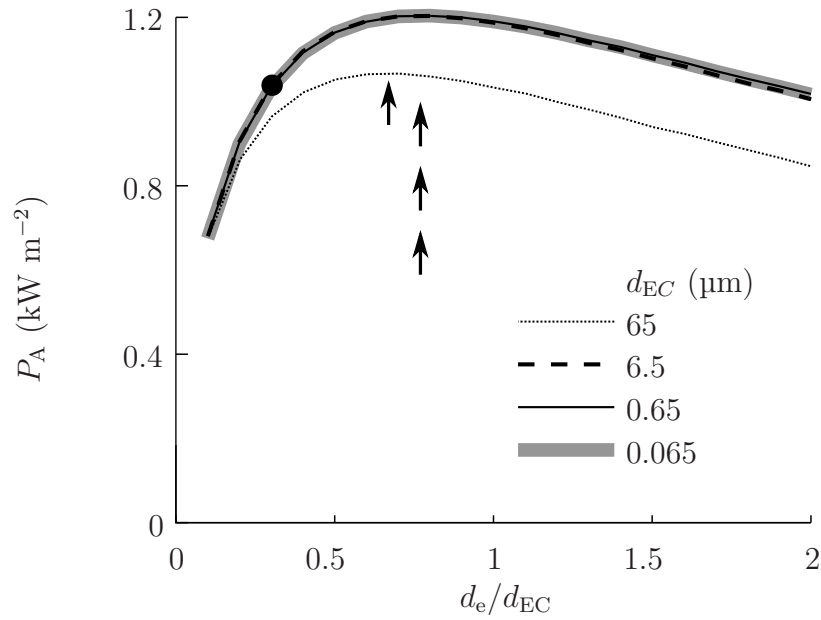


Figure 7.6: **(a)** The effect on f and P_A of varying d_e and d_{EC} for the Y5V-Ni MLC (black dot). **(b)** The effect on P_A of varying d_e and d_{EC} over four orders of magnitude, for the Y5V-Ni MLC (black dot). The locations of the optima are indicated with an arrow.

7.3.2 Effect of electrode material on optimal d_e and d_{EC}

The predicted ‘magic ratio’ was investigated on varying κ_e (Figure 7.7a) [note that although the tested values of κ_e in this Figure corresponded to well-known electrode materials, c_e and ϱ_e remained constant at the values for Ni, as this simulation was testing the effect of κ_e alone]. Reducing κ_e from $94 \text{ W m}^{-1} \text{ K}^{-1}$ (the value for Ni) to $15.6 \text{ W m}^{-1} \text{ K}^{-1}$ (the value for Ti) reduced the magic ratio to ~ 0.5 , but increasing it to $424 \text{ W m}^{-1} \text{ K}^{-1}$ (the value for Ag) had minimal effect. This is best explained by imagining the effect of drastically reducing κ_e to $2.6 \text{ W m}^{-1} \text{ K}^{-1}$, the value for the Y5V electrocaloric layers. For this extreme case the electrodes would not enhance the thermal conductivity of the MLC over that of bulk Y5V, and their presence would simply serve to dilute the electrocaloric heat produced in the Y5V layers. Thus, the magic ratio would be expected to tend to zero as κ_e tends to κ_{EC} from above in a manner consistent with the simulated data. As might have been expected, the corresponding value of f and hence $P_A \propto f$ scale almost linearly with κ_e for $\kappa_e \gg \kappa_{EC}$ (Figure 7.7b).

Replacing the Ni electrodes with Ag (i.e. setting $\kappa_e = \kappa_{Ag} = 428 \text{ W m}^{-1} \text{ K}^{-1}$, $c_e = c_{Ag} = 235 \text{ J K}^{-1} \text{ kg}^{-1}$ and $\varrho_e = \varrho_{Ag} = 10500 \text{ kg m}^{-3}$) resulted in an increase of the magic ratio to ~ 0.9 (Figure 7.7c). Figure 7.7a shows that this is not due to the fact that Ag has a higher value of κ_e than Ni, so the magic ratio must depend on one or both of c_e and ϱ_e .

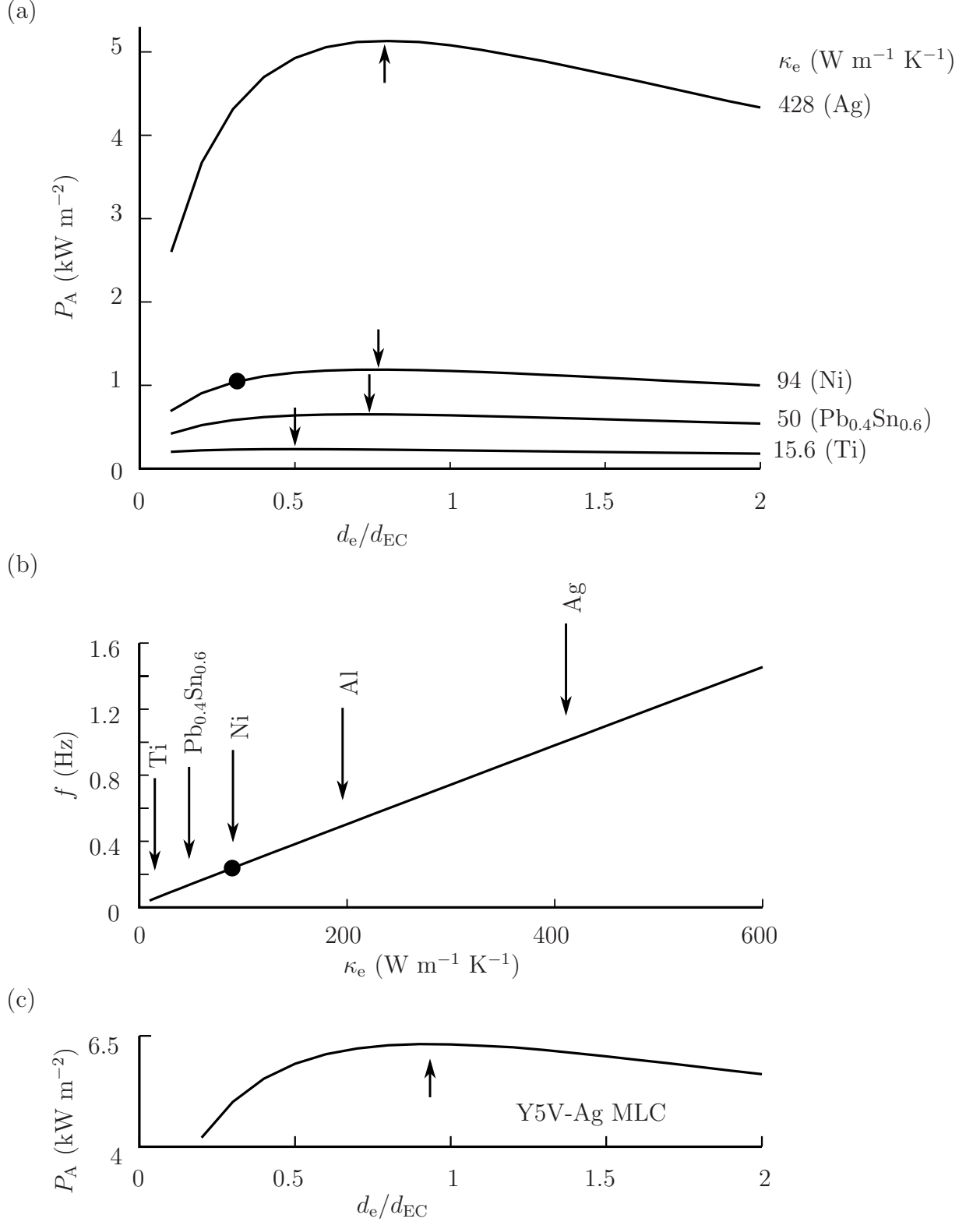


Figure 7.7: (a) ‘Magic ratios’ for various values of κ_e , corresponding to well-known electrode materials, for the Y5V-Ni MLC (black dot). Although the tested values of κ_e in this Figure corresponded to well-known electrode materials, c_e and ρ_e remained constant at the values for Ni, as this simulation was testing the effect of κ_e alone. (b) The effect on f of varying κ_e for the Y5V-Ni MLC (black dot). (c) Magic ratio of the Y5V-Ag MLC.

7.3.3 Optimisation of L

Varying MLC length L for various values of L_U revealed an optimum for L which scaled with L_U for $0.015 < L_U < 1.5$ mm (Figure 7.8a). The simulation suggests that for $L_U = 0.15$ mm (i.e. the existing Y5V-Ni MLC), a two-fold increase in P_A is associated with reducing L from its starting value of 2.9 mm to the optimal value of ~ 0.4 mm. Figure 7.8b shows how f varies as a function of L for the same discrete values of L_U as Figure 7.8a. For $L \gg L_U$, f would be expected to vary as $1/L^2$, because thermal resistance $R \propto L$ and heat capacity $C \propto L$, such that $f \propto \tau^{-1} \propto (RC)^{-1} \propto L^{-2}$. For $L \ll L_U$, f would be expected to be invariant of L , as the fixed thermal impedance of L_U would dominate the thermal time constant. This analysis is consistent with the simulated data for f . As $Q_{EC} \propto L$, $P_A \propto Q_{EC}f$ would be expected to vary as $1/L$ at large values of L and to vary as L at small values of L . The observed optimal values of L for given values of L_U (Figure 7.8a) are thus rationalised.

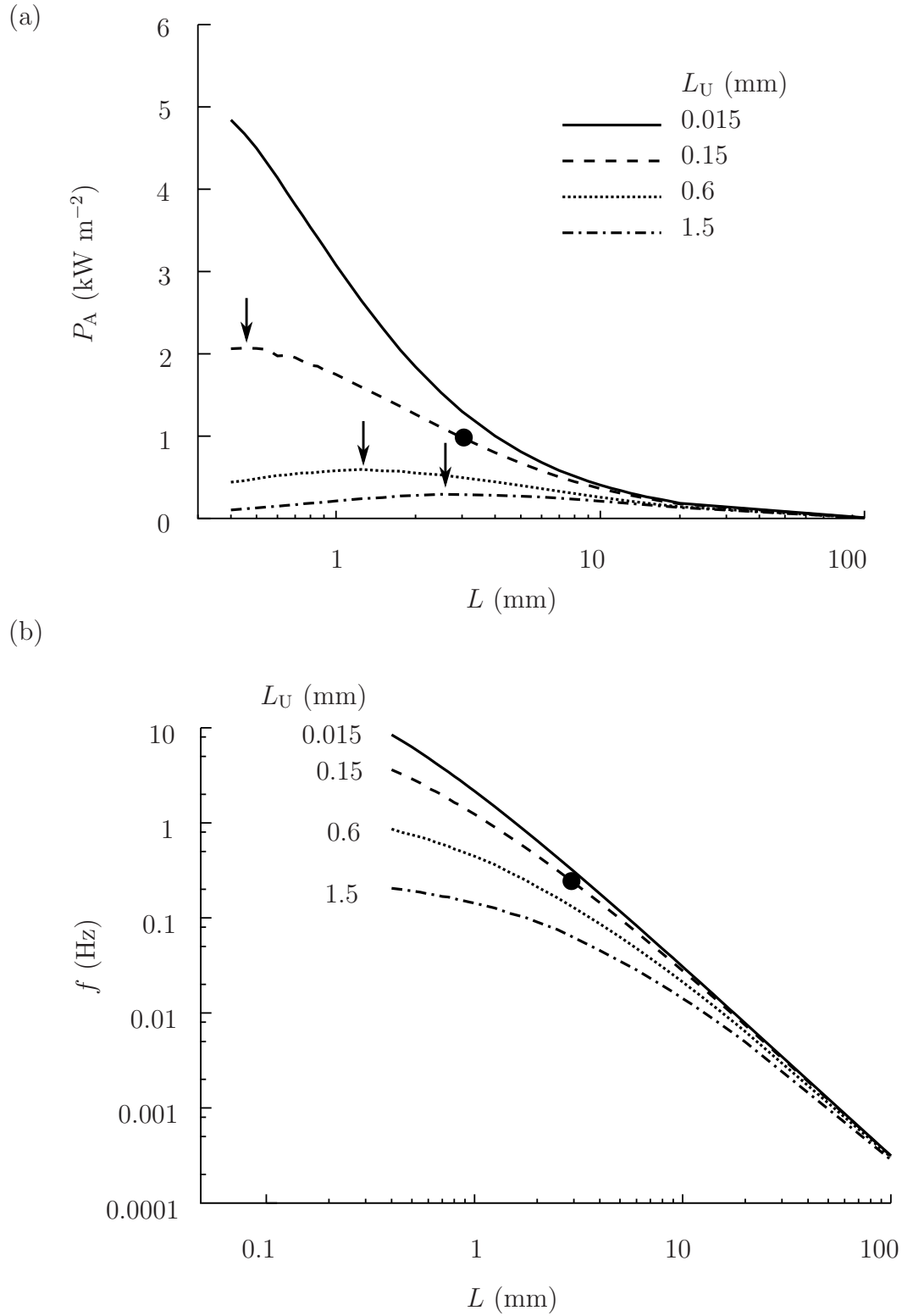


Figure 7.8: **(a)** The effect on P_A of varying L for various values of L_U , for the Y5V-Ni MLC (black dot). **(b)** The effect on f of varying L for various values of L_U , for the Y5V-Ni MLC (black dot).

7.4 Optimisation of realistic coolers

The FEM simulation predicted the intrinsic cooling power P_A and intrinsic operating frequency f of model MLCs, and did not consider the effect of the thermal impedance of the other components that would necessarily be present in a practical electrocaloric cooler, such as the thermal load and the heat reservoir. The reader will note that care has been taken to plot *both* P_A and f on the same axes in Figures 7.6-7.8. Presenting the results in this way will enable the geometric optimisations to be quantitatively modified and applied to *any* practical cooling device with MLCs at its heart.

The non-MLC components of a practical cooler would have their own thermal time constant corresponding to an intrinsic operating frequency f_C . This value of f_C represents an upper bound on the operating frequency. Geometric optimisation of a realistic cooler thus amounts to applying a constraint of form $f < f_C$ to the results in the existing Figures. As an example, the cooler demonstrated by Jia and Ju [51] used the Y5V-Ni MLC described in Table 7.1, and operated at 0.12 Hz which for illustration purposes shall be assumed to be a limitation imposed by the non-MLC components of this cooler, i.e. $f_C = 0.12$ Hz. For this system, the optimal MLC geometry may be derived as follows:

- Considering first only d_e and d_{EC} , it is noted that the intrinsic magic ratio for d_e/d_{EC} for the Y5V-Ni MLC is ~ 0.75 (Figure 7.6b) at ~ 0.35 Hz (Figure 7.6a). However, the Jia and Ju cooler was operated at 0.12 Hz which limits d_e/d_{EC} to 0.1 (Figure 7.6a). This corresponds to a 1.18-fold increase in the volumetric fraction (i.e. $d_{EC}/[d_e + d_{EC}] = 1/[1 + d_e/d_{EC}]$) of electrocaloric material in the MLC layers from the starting Y5V-Ni MLC which had $d_e/d_{EC} = 0.3$ (Table 7.1), and thus a 1.18-fold increase in P_A .
- Considering now L at fixed $L_U = 0.15$ mm, it is noted that the optimal value of L for the Y5V-Ni MLC is ~ 0.4 mm (Figure 7.8a) at 3.6 Hz (Figure 7.8b). As the Jia and Ju cooler was limited to 0.12 Hz, the optimal value for L is instead found by increasing L such that the intrinsic frequency f of the MLC is also 0.12 Hz (Figure 7.8b), giving $L_{opt} \sim 4.5$ mm. This corresponds to a 1.55-fold increase in the amount of electrocaloric material in the MLC layers from the starting amount ($L = 2.9$ mm) and thus a 1.55-fold increase in P_A .

It is also straightforward to compute the effect of replacing the Ni electrodes with Ag.

Ag electrodes provide a ~ 5 -fold increase in f as compared to Ni electrodes, as a result of the ~ 5 -fold larger value of κ_e (Figure 7.7b). Given that the optimised Jia and Ju cooler with Ni electrodes already operates at the maximum frequency of 0.12 Hz, with a volumetric fraction of electrode material of $d_e/[d_e + d_{EC}] = 0.09$, substitution with Ag keeping f constant enables this fraction to be reduced by a factor of 5 to 0.018. But the volumetric fraction of electrocaloric material ($\propto P_A$) is barely changed by this, from 0.91 to 0.98, an increase of just 7 %.

In summary the FEM simulation results may be used to geometrically optimise the MLC used in the cooling system of Jia and Ju geometrically, leading to an overall 2-fold gain in P_A , even though their cooling system was not explicitly modelled. FEM results have also been used to show that, for this cooler, the upgrade from Ni to Ag electrodes provides only a 7 % improvement in P_A and might not be cost effective, given the much higher cost of Ag.

7.5 Predicted cooling powers for MLCs

The FEM programs were used to predict the cooling powers of the six hypothetical MLCs which were considered by the lumped thermal circuit model (Table 7.1). Additionally, the cooling powers of geometrically optimised versions of those MLCs were predicted. Optimisation of d_e/d_{EC} and L was performed separately for each MLC model. As such, an assumption was made that the optima in d_e/d_{EC} and L were not strongly coupled (this assumption was justified mathematically using an improved version of the lumped thermal circuit model, see Section 7.6.5). The thickness of Zr-rich PZT was 300 nm for the FEM simulation, not 350 nm as used by the lumped thermal circuit model.

Table 7.2 shows the properties and FEM results for f , Q_M (electrocaloric heat per unit mass, per cycle), P_M and P_A for the twelve MLCs. Operating frequencies were ~ 0.25 Hz and ~ 4.5 Hz for unoptimised and optimised MLCs with Ni electrodes respectively, and ~ 1.25 Hz and ~ 26 Hz for unoptimised and optimised MLCs with Ag electrodes respectively. In terms of P_M , the optimised PVDF-TrFE-Ag MLC ($P_M = 25.9$ kW kg $^{-1}$) was the best, performing better than the optimised PZT-Ag MLC ($P_M = 19.2$ kW kg $^{-1}$), partly because of the small density of PVDF-TrFE. In terms of P_A , the optimised PZT-Ag MLC ($P_A = 218.2$ kW m $^{-2}$) was the best, performing better than the optimised PVDF-TrFE-Ag MLC ($P_A = 215.1$ kW m $^{-2}$) as density has no role

in the equation for area-normalised cooling power. Furthermore, the optimised MLCs had a 5.1-7.1-fold advantage over unoptimised MLCs in P_M , and a ~ 2.5 -fold advantage in P_A , as a change of L when optimising affects mass M but not sheet area A . The cooling powers obtained are impressive in the context of a typical cooling power for an air-conditioning unit of ~ 20 kW [19].

Parameter	Unit	Y5V—Ni	Y5V—Ni (opt)	Y5V—Ag	Y5V—Ag (opt)	PZT—Ni	PZT—Ni (opt)	PZT—Ag	PZT—Ag (opt)	PVDF—TrFE—Ni	PVDF—TrFE—Ni (opt)	PVDF—TrFE—Ag	PVDF—TrFE—Ag (opt)
d_e	μm	2.0	4.9	2.0	5.9	0.1	0.22	0.1	0.27	0.3	0.75	0.3	0.9
d_{EC}	μm	6.5	6.5	6.5	6.5	0.3	0.3	0.3	0.3	1.0	1.0	1.0	1.0
L	mm	2.9	0.5	2.9	0.5	2.9	0.5	2.9	0.5	2.9	0.5	2.9	0.5
L_U	mm	0.15	0.15	0.15	0.15	0.15	0.15	0.15	0.15	0.15	0.15	0.15	0.15
w	mm	2.56	2.56	2.56	2.56	2.56	2.56	2.56	2.56	2.56	2.56	2.56	2.56
n		20	20	20	20	20	20	20	20	20	20	20	20
κ_e	$\text{W m}^{-1} \text{K}^{-1}$	94	94	428	428	94	94	428	428	94	94	428	428
ρ_e	kg m^{-3}	8907	8907	10500	10500	8907	8907	10500	10500	8907	8907	10500	10500
c_e	$\text{J kg}^{-1} \text{K}^{-1}$	429	429	235	235	429	429	235	235	429	429	235	235
κ_{EC}	$\text{W m}^{-1} \text{K}^{-1}$	2.6	2.6	2.6	2.6	2.03	2.03	2.03	2.03	0.2	0.2	0.2	0.2
ρ_{EC}	kg m^{-3}	5840	5840	5840	5840	7800	7800	7800	7800	1770	1770	1770	1770
c_{EC}	$\text{J kg}^{-1} \text{K}^{-1}$	434	434	434	434	330	330	330	330	1500	1500	1500	1500
ΔT	K	0.74	0.74	0.74	0.74	12	12	12	12	12	12	12	12
f	Hz	0.25	4.7	1.22	25.7	0.25	4.7	1.28	26.8	0.22	4.4	1.15	25.7
Q_M	kJ kg^{-1}	0.17	0.06	0.16	0.05	2.2	0.9	2.1	0.7	4.9	1.3	4.4	1.0
P_M	kW kg^{-1}	0.04	0.27	0.19	1.2	0.57	4.0	2.7	19.2	1.1	5.7	5.1	25.9
P_A	kW m^{-2}	1.0	2.5	5.1	12.6	17.0	41.6	86.0	218.2	15.7	39.7	81.7	215.1

Table 7.2: Parameters of the MLCs modelled with the FEM simulation. Material properties from Kar-Narayan and Mathur [19]. Q_M and P_M (electrocaloric heat per unit mass and cooling power per unit mass) were evaluated by including the MLC terminals in the mass of the MLC. As such, these cooling powers are not directly comparable to those from the lumped thermal circuit model in Table 7.1 (see later discussion).

7.5.1 Accuracy of predictions

The only MLC described in Table 7.2 which had been studied for electrocaloric effects experimentally was the unoptimised Y5V-Ni MLC. The most sensitive measurements in the literature are by Kar-Narayan *et al.*, using scanning thermal microscopy and infra-red imaging to measure temperature changes as a function of time for this system [52]. For an IR camera focussed directly on the side of the MLC, and thus probing the electrocaloric layers themselves, a thermal decay time of 0.13 s was reported [52], slightly shorter than the 0.2 s (Table 7.2, using $\tau = 1/[20f]$) predicted by FEM, but consistent within error.

7.6 New lumped thermal circuit models

7.6.1 Recreation of previous lumped model

The lumped thermal circuit model of Kar-Narayan and Mathur [19] was *recreated* for the present work, in order to assess agreement with the FEM results. For this work, the twelve MLCs in Table 7.2 were used. As described in [19] and Section 7.1, the equation for cooling power from the lumped thermal circuit model was:

$$P_A = \frac{2\kappa_e w d_e n \Delta T}{20DA} \quad (7.4)$$

Unfortunately the lumped thermal circuit and the FEM models were parameterised differently, as the former modelled the MLC with a single lateral length D , whereas the latter differentiated between an electrically addressed section of length L , two electrically unaddressed sections of length L_U and two terminal sections of length $L_T = 0.2$ mm. Two lumped thermal circuit models were initially used for the present comparison, model C (where ‘C’ stands for ‘centre’) and model CE (where ‘CE’ stands for ‘centre and ends’), with model C ignoring the thermal resistance of L_U and L_T , and model CE including it, i.e. $D = L$ for model C, and $D = L + 2L_U + 2L_T$ for model CE. All other geometric parameters were the same as those from Table 7.2.

Table 7.3 shows the values of P_A from the lumped models C and CE, as a fraction of the FEM value. Agreement between the FEM and model C was poor, with model C underestimating P_A for the unoptimised MLCs by a factor of at least 2, and overestimating P_A for the optimised MLCs, also by a factor of around 2. Model CE showed very good agreement with the FEM model for the optimised MLCs, but even worse agreement than model C for the unoptimised MLCs.

MLC model	P_A from FEM (kW m ⁻²)	P_A from lumped model (as fraction of FEM result)	Model C	Model CE
Y5V-Ni	1.0		0.55	0.44
Y5V-Ag	5.1		0.51	0.41
PZT-Ni	17.0		0.57	0.46
PZT-Ag	86.0		0.51	0.41
PVDF-TrFE-Ni	15.7		0.57	0.46
PVDF-TrFE-Ag	81.7		0.50	0.40
Y5V-Ni (opt)	2.5		2.38	0.99
Y5V-Ag (opt)	12.6		2.39	0.99
PZT-Ni (opt)	41.6		2.29	0.96
PZT-Ag (opt)	218.2		2.23	0.93
PVDF-TrFE-Ni (opt)	39.7		2.4	1.02
PVDF-TrFE-Ag (opt)	215.1		2.26	0.94

Table 7.3: Comparison between FEM simulation results and lumped models C and CE, which are described in the main text.

7.6.2 Requiring heat to flow to the nearest terminal

There was a large disparity between the results for optimised and unoptimised MLCs, for both models C and CE. This suggested that the accuracy of these models was a function of L , as optimised MLCs had much smaller values of L than unoptimised MLCs.

It was postulated that the issue lay with the assumption of models C and CE that electrocaloric heat would flow to the nearest electrode, even if the terminal attached to that electrode were at the opposite end of the MLC to the source region of the electrocaloric heat (Figure 7.9a). A new

model was devised which divided the single heat source at the centre of the electrocaloric layers into *two* heat sources, one at the quarter point and the other at the three-quarter point, along the full length of L (Figure 7.10). This model was named Q, where ‘Q’ stands for ‘quarter’. In the language of heat-transfer engineering, the ‘characteristic length’ of the electrocaloric layers in model Q was $0.25L$, smaller than the $0.5L$ of models C and CE. Thus in model Q, electrocaloric heat should flow to the nearest terminal (Figure 7.9b).

The thermal impedance of each quarter-electrode in model Q was evaluated as $R_e = [\frac{L}{4} + L_T + L_U]/[\kappa_e w d_e]$, ignoring the thermal capacitance c_e (as for models C and CE), giving the following expression for P_A :

$$P_A = \frac{\kappa_e w d_e n \Delta T}{20A(\frac{L}{4} + L_T + L_U)} \quad (7.5)$$

Table 7.4 shows the results of the model Q for each of the twelve MLCs. Model Q tended to underestimate the cooling powers of the unoptimised MLCs by a factor of ~ 1.4 and overestimate the cooling powers of the optimised MLCs by a factor of ~ 1.25 . Overall, this was an improvement on the results of models C and CE, but the search continued for a model which would give consistent results across all of the MLCs, and thus be robust against arbitrary changes in MLC geometry.

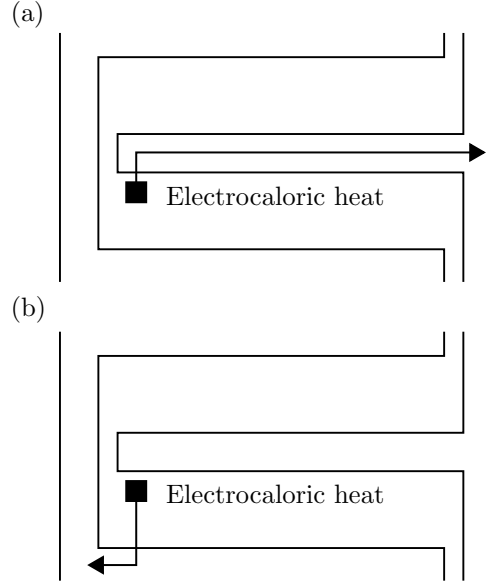


Figure 7.9: Illustration of heat paths in models (a) C and CE and (b) Q.

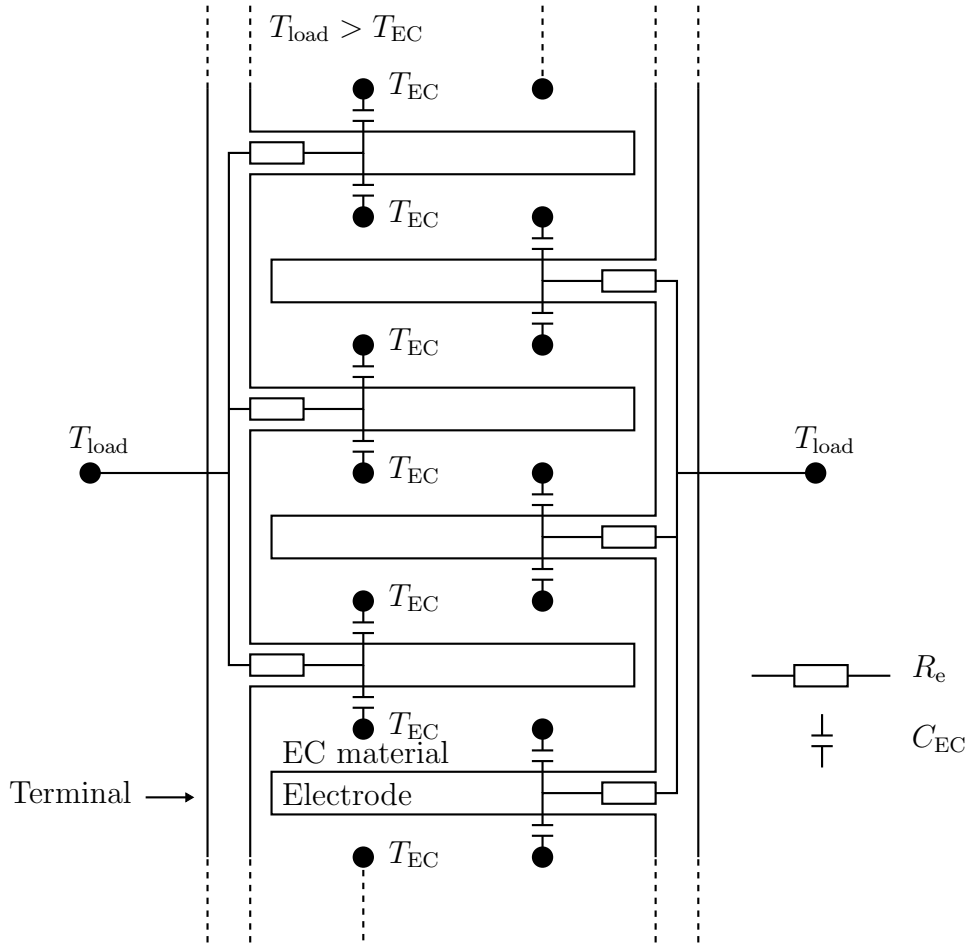


Figure 7.10: Lumped thermal circuit model Q, requiring electrocaloric heat to flow to the nearest MLC terminal.

MLC model	P_A from FEM (kW m^{-2})	P_A from lumped model (as fraction of FEM result)	Model C	Model CE	Model Q
Y5V-Ni	1.0		0.55	0.44	0.74
Y5V-Ag	5.1		0.51	0.41	0.68
PZT-Ni	17.0		0.57	0.46	0.77
PZT-Ag	86.0		0.51	0.41	0.69
PVDF-TrFE-Ni	15.7		0.57	0.46	0.77
PVDF-TrFE-Ag	81.7		0.50	0.40	0.67
Y5V-Ni (opt)	2.5		2.38	0.99	1.25
Y5V-Ag (opt)	12.6		2.39	0.99	1.26
PZT-Ni (opt)	41.6		2.29	0.96	1.21
PZT-Ag (opt)	218.2		2.23	0.93	1.17
PVDF-TrFE-Ni (opt)	39.7		2.4	1.02	1.28
PVDF-TrFE-Ag (opt)	215.1		2.26	0.94	1.19

Table 7.4: Comparison between FEM simulation results and lumped models C, CE and Q, which are described in the main text.

7.6.3 Short thermal homogenisation step

Because the electrocaloric layer thickness d_{EC} of the MLCs was small in comparison to the layer length L , it was postulated that the exponential decay of heat flux $\phi(t)$ from the MLC could be preceded by a short ‘thermal homogenisation’ step of negligible duration, whereupon the temperatures of the electrodes and electrocaloric material equilibrate. After this homogenisation step, the MLC layers could be regarded as a simple bulk solid with a thermal capacitance equal to the volume-weighted average of that of its constituent materials, and a thermal resistance equal to the area-weighted average of that of its constituent materials. Thus, following thermal homogenisation, the heat capacity of each half of the MLC is given by:

$$C_L = v_e c_e \varrho_e + v_{\text{EC}} c_{\text{EC}} \varrho_{\text{EC}} \quad (7.6)$$

where v_e and v_{EC} are the total volumes of electrode and electrocaloric material in half of the MLC layers. The thermal resistance of each end-quarter of the MLC layers is given by:

$$1/R_L = (L/4\kappa_e A_e)^{-1} + (L/4\kappa_{\text{EC}} A_{\text{EC}})^{-1} \quad (7.7)$$

where A_e and A_{EC} are the total cross-sectional areas of electrode and electrocaloric material in the yz plane and the factor of 4 reflects the continued assumption that the characteristic length of the layers is $L/4$. The sections of the MLC spanned by L_U and L_T were modelled as thermal resistances alone connected in series with the MLC layers, again using area-weighted averages of constituent materials to calculate thermal resistances (Figure 7.11). This model was named model H, where ‘H’ stands for ‘homogenisation’. Cooling power was evaluated as $P_A = Q_{\text{EC}}/[20\tau A]$, where $\tau = R_{\text{total}} C_{\text{total}}$, yielding:

$$P_A = \frac{1}{10} L \Delta T (d_e + d_{\text{EC}})^{-1} (L + d_{\text{EC}})^{-1} \left(1 + \frac{c_e \varrho_e d_e}{c_{\text{EC}} \varrho_{\text{EC}} d_{\text{EC}}} \right)^{-1} \left[\frac{0.25L}{\kappa_e d_e + \kappa_{\text{EC}} d_{\text{EC}}} + \frac{2L_U}{\kappa_e d_e + \kappa_{\text{EC}} (2d_{\text{EC}} + d_e)} + \frac{L_T}{\kappa_e (d_e + d_{\text{EC}})} \right]^{-1} \quad (7.8)$$

where the term proportional to $L/(L + d_{\text{EC}})$ adjusts to take into account the heat

capacity of a $0.5d_{\text{EC}}$ -thick slice of the ‘unaddressed’ electrocaloric material into the model, as it would be affected in an identical manner to the MLC layers during the short ‘thermal homogenisation’ step.

Table 7.5 shows the results of model H for each of the twelve MLCs. Model H overestimates the cooling powers of the unoptimised MLCs by a factor of ~ 1.1 and that of the optimised MLCs by a factor of ~ 1.15 . Thus, there remains some L dependence on the accuracy of model H, but it is small, and thus model H achieves the overall aim of being robust against arbitrary changes in MLC geometry.

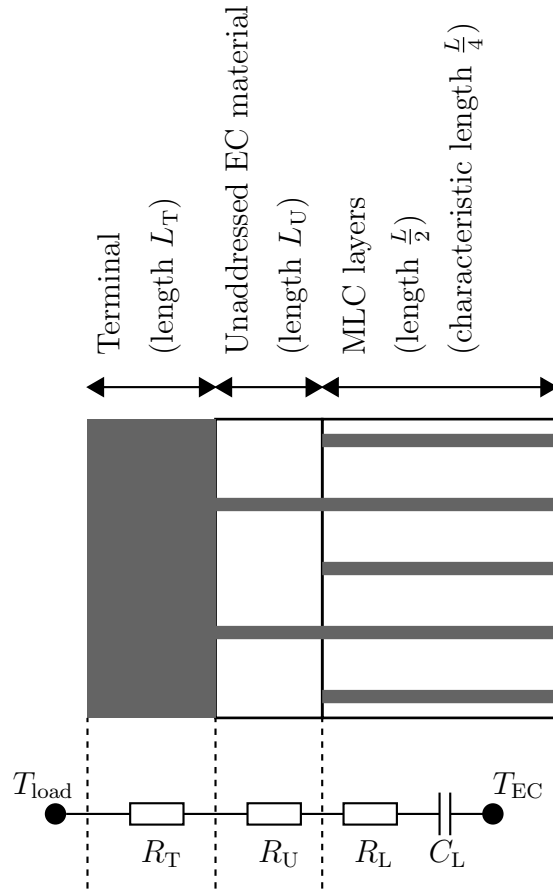


Figure 7.11: Lumped thermal circuit model H, treating all the electrocaloric layers collectively as a single thermal capacitor in series with a thermal resistor. The MLC is treated as two separate halves for the purposes of calculating the thermal time constant - only one half is shown in the Figure.

MLC model	P_A from FEM (kW m^{-2})	P_A from lumped model (as fraction of FEM result)	Model C	Model CE	Model Q	Model H
Y5V-Ni	1.0		0.55	0.44	0.74	1.12
Y5V-Ag	5.1		0.51	0.41	0.68	1.08
PZT-Ni	17.0		0.57	0.46	0.77	1.12
PZT-Ag	86.0		0.51	0.41	0.69	1.07
PVDF-TrFE-Ni	15.7		0.57	0.46	0.77	1.09
PVDF-TrFE-Ag	81.7		0.50	0.40	0.67	1.06
Y5V-Ni (opt)	2.5		2.38	0.99	1.25	1.15
Y5V-Ag (opt)	12.6		2.39	0.99	1.26	1.21
PZT-Ni (opt)	41.6		2.29	0.96	1.21	1.13
PZT-Ag (opt)	218.2		2.23	0.93	1.17	1.16
PVDF-TrFE-Ni (opt)	39.7		2.4	1.02	1.28	1.15
PVDF-TrFE-Ag (opt)	215.1		2.26	0.94	1.19	1.18

Table 7.5: Comparison between FEM simulation results and lumped models C, CE, Q and H, which are described in the main text.

7.6.4 Geometric optimisation via lumped model

The FEM plots of P_A against d_e and d_{EC} (Figure 7.6) and L (Figure 7.8) were previously used to optimise MLC geometry for cooling. Model H was used to plot P_A in the same range of parameter space. Model H reproduced the FEM results for P_A against d_e and d_{EC} reasonably closely, giving a similar value for the magic ratio of $d_e/d_{EC} \sim 0.75$ and generally slightly higher values of P_A (Figure 7.12). For P_A against L and L_U , model H gave incorrect optima for L , but for $L > L_U$ followed the FEM simulation reasonably closely (Figure 7.13). For $L < L_U$ the assumption of a rapid ‘thermal homogenisation’ step was likely invalid, as the thermal impedance of the electrically unaddressed electrocaloric material and the terminals would dominate over that of the MLC layers.

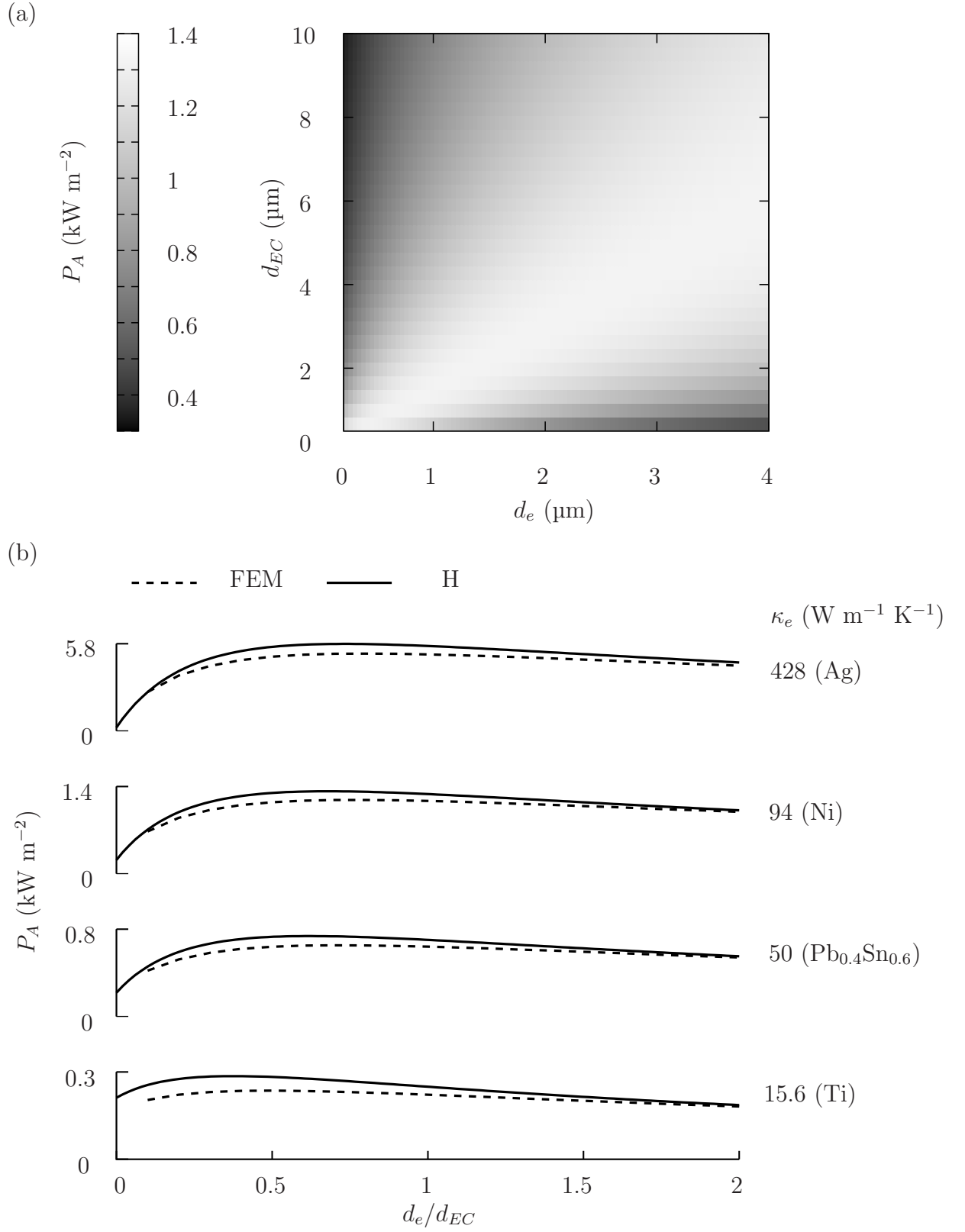


Figure 7.12: **(a)** P_A as a function of d_e and d_{EC} for the Y5V-Ni MLC, using lumped model H. **(b)** The effect on P_A of varying d_e/d_{EC} for the Y5V-Ni MLC for various values of κ_e , using lumped model H. For comparison with Figures 7.6-7.7 (FEM).

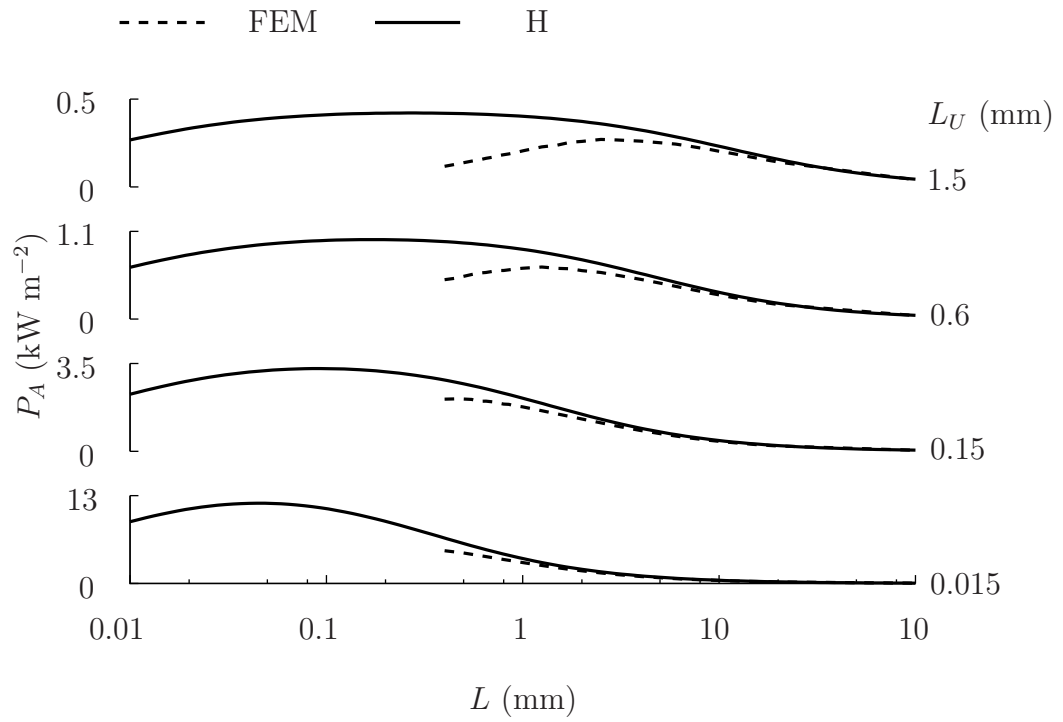


Figure 7.13: P_A as a function of L for various values of L_U for the Y5V-Ni MLC, using lumped model H. For comparison with Figure 7.8 (FEM).

7.6.5 Analytical expression for the ‘magic ratio’

The formulae for τ and P_A for model H were as follows:

$$\tau = \frac{L + d_{\text{EC}}}{2} (c_e \varrho_e d_e + c_{\text{EC}} \varrho_{\text{EC}} d_{\text{EC}}) \left[\frac{fL}{\kappa_e d_e + \kappa_{\text{EC}} d_{\text{EC}}} + \frac{2L_{\text{U}}}{\kappa_e d_e + \kappa_{\text{EC}} (2d_{\text{EC}} + d_e)} + \frac{L_{\text{T}}}{\kappa_e (d_e + d_{\text{EC}})} \right] \quad (7.9)$$

$$P_A = \frac{1}{10} \Delta T (d_e + d_{\text{EC}})^{-1} (L + d_{\text{EC}})^{-1} \left(1 + \frac{c_e \varrho_e d_e}{c_{\text{EC}} \varrho_{\text{EC}} d_{\text{EC}}} \right)^{-1} \left[\frac{fL}{\kappa_e d_e + \kappa_{\text{EC}} d_{\text{EC}}} + \frac{2L_{\text{U}}}{\kappa_e d_e + \kappa_{\text{EC}} (2d_{\text{EC}} + d_e)} + \frac{L_{\text{T}}}{\kappa_e (d_e + d_{\text{EC}})} \right]^{-1} \quad (7.10)$$

Where $fL = 0.25L$ is the assumed characteristic length of the MLC layers. It might be possible to improve model H by varying the characteristic length.

Assuming that $\kappa_e \gg \kappa_{\text{EC}}$, Equation 7.10 simplifies to:

$$P_A \sim \frac{1}{10} \kappa_e \Delta T (d_e + d_{\text{EC}})^{-1} (L + d_{\text{EC}})^{-1} \left(1 + \frac{c_e \varrho_e d_e}{c_{\text{EC}} \varrho_{\text{EC}} d_{\text{EC}}} \right)^{-1} \left[\frac{fL + 2L_{\text{U}}}{d_e} + \frac{L_{\text{T}}}{d_e + d_{\text{EC}}} \right]^{-1} \quad (7.11)$$

Taking $1/P_A$:

$$\frac{1}{P_A} = k (d_e + d_{\text{EC}}) \left(1 + a \frac{d_e}{d_{\text{EC}}} \right) \left(\frac{fL + 2L_{\text{U}}}{d_e} + \frac{L_{\text{T}}}{d_e + d_{\text{EC}}} \right) \quad (7.12)$$

where $k = 10(L + d_{\text{EC}})/[\kappa_e \Delta T]$ and $a = c_e \varrho_e / [c_{\text{EC}} \varrho_{\text{EC}}]$. Letting $r = d_e / d_{\text{EC}}$ and simplifying:

$$\frac{1}{P_A} = k [a(fL + 2L_U + L_T)r + (fL + 2L_U)r^{-1} + (1 + a)fL + 2(1 + a)L_U + L_T] \quad (7.13)$$

Differentiating with respect to r :

$$\frac{\partial}{\partial r} \left(\frac{1}{P_A} \right) = k [a(fL + 2L_U + L_T) - (fL + 2L_U)r^{-2}] \quad (7.14)$$

Equating to zero and solving for r :

$$r = \sqrt{\frac{fL + 2L_U}{a(fL + 2L_U + L_T)}} \quad (7.15)$$

Equation 7.15 gives a magic ratio of 0.75 for the Y5V-Ni MLC and 0.9 for the Y5V-Ag MLC. These values are very similar to those obtained via FEM (Figure 7.7). Equation 7.15 confirms that the magic ratio is a weak function of L provided $L \gg 2L_U + L_T$, justifying the assumption of the FEM simulation that the optimisations found for d_e/d_{EC} and L are independent.

7.7 Conclusions

The finite element method (FEM) has been used to optimise the intrinsic cooling power of MLCs for electrocaloric coolers. Commercial MLCs with Y5V dielectric layers and Ni electrodes have layer thickness ratio $d_e/d_{EC} \sim 0.3$, and layer length $L \sim 2.9$ mm. A ‘magic ratio’ of $d_e/d_{EC} \sim 0.75$ and a layer length $L \sim 0.5$ mm results in a ~ 2.5 -fold enhancement of terminal area-normalised cooling power, and a ~ 6.8 -fold enhancement of mass-normalised cooling power. Use of Ag electrodes increases the ‘magic ratio’ to $d_e/d_{EC} \sim 0.9$, and the length of electrically unaddressed dielectric greatly influences the optimal value of L . Optimal geometries for realistic coolers may be deduced without further modelling, by applying appropriate constraints to operating frequency. For a hypothetical MLC with PVDF-TrFE dielectric layers and Ag electrodes, FEM results suggest an intrinsic cooling power, for optimal geometry, of 25.9 kW per kg of MLC mass, or 215.1 kW per m² of MLC terminal sheet area.

Chapter 8

Conclusions and Outlook

The seven previous Chapters will be summarised consecutively, with selected links and comparisons emphasised. The present work considered a wide variety of issues in electrocalorics, from measurements, to device fabrication, to the design of hypothetical cooling elements. This is a reflection of the present status of the research field of electrocalorics, which has been recently reinvigorated by inspirational papers [20,21], and holds enough promise for commercialisation that engineering research is being actively conducted in parallel with the more fundamental materials research. However, the electrocalorics literature still lacks systematic measurements as seen in more mature fields such as ferroelectrics.

The focus of Chapter 1 was a review of literature and an investigation of candidate materials, by considering families of ferroelectrics briefly and systematically. Electrocaloric effects have not been explored in the majority of ferroelectric materials, despite the fact that several show promising zero-field entropy changes or pyroelectric coefficients, e.g. $\text{Sr}_x\text{Ba}_{1-x}\text{Nb}_2\text{O}_6$ [55], HCl [71] and $\text{NaH}_3(\text{SeO}_3)_2$ [82]. Most of the thin-film materials that have been tested for electrocaloric effects have been perovskite oxides containing lead, and ferroelectric polymers. Thus, it was attractive here to explore inorganic salts with entropic order-disorder transitions.

In Chapter 2, the theory of measurement of electrocaloric effects was discussed. The majority of electrocaloric measurements for thin films have used an ‘indirect’ method, where isothermal $|\Delta S|$ is evaluated by numerically processing $P(E)$ data via the Maxwell relation $(\partial P/\partial T)_E = (\partial S/\partial E)_T$. ‘Standard’ indirect measurements use the upper positive branch of major (i.e. switching) $P(E)$ loops for analysis, but this provides no way of observing hysteresis in field-driven phase transitions, as one assumes

$P(E, T)$ to be single valued. This deficiency can be corrected by performing Maxwell analysis on minor (i.e. non-switching) loops. A side-benefit of minor loops is that they provide information about parasitic leakage currents. A second deficiency of the ‘standard’ indirect method, which was first described in analogous magnetocaloric systems [92], is the appearance of spurious, sharp peaks in isothermal $|\Delta S|$ at hysteretic first-order phase transitions, if the sample is not ‘reset’ at a temperature away from the hysteretic region in between each $P(E)$ measurement. However, this ‘resetting’ procedure has not hitherto been applied to electrocaloric systems.

Values of adiabatic ΔT are usually evaluated via $|\Delta T| \sim c_E T |\Delta S|$, where c_E is specific isofield heat capacity, which is generally only known at zero-field. However, first-order transitions can show peaks in $c_E(T)$ due to latent heat. Mapping of entropy changes $\Delta S(E, T)$ from independent evaluations of isothermal $|\Delta S|$ at various temperatures, and zero-field ΔS , is demonstrated as a means of avoiding the highly dubious assumption that $c_E(E)$ is uniform near a first-order phase transition. Once $\Delta S(E, T)$ is evaluated, adiabats are readily identified.

In Chapter 3, the construction of three bespoke temperature control systems and associated software was described. A cryogenic probe was constructed for work in 77-420 K with ~ 5 mK resolution in vacuum or exchange gas. A high-temperature stage with vacuum enclosure provided access to temperatures up to 700 K with ~ 15 mK resolution. Operation is possible in vacuum, exchange gas or open air. Both of these systems feature high-voltage ceramic-insulated wiring, and low-parasitics coaxial wiring, to enable a broad variety of electrical measurements. Additionally, a table-top low-temperature stage for 120-400 K in N_2 gas was constructed, with electrical access via micropositioner tips. Both direct and indirect electrocaloric measurements are automated by bespoke software. Previously, $P(E)$ loops were typically collected at a rather limited number of temperatures, possibly due to restrictions of industry-standard Radiant software. These restrictions have been overcome in the present work, enabling dense datasets to be compiled systematically with minimal operator intervention.

In Chapter 4, measurements on single crystals of the inorganic salts $(NH_4)_2SO_4$, KNO_3 and $NaNO_2$ were described. These crystals show order-disorder transitions with zero-field entropy changes of $133.2 \text{ J K}^{-1} \text{ kg}^{-1}$, $53.4 \text{ J K}^{-1} \text{ kg}^{-1}$ and $76.8 \text{ J K}^{-1} \text{ kg}^{-1}$, respectively. These values are approximately an order-of-magnitude larger than the values for nominally displacive ferroelectrics such as $BaTiO_3$ (zero-field $|\Delta S| = 2.6 \text{ J K}^{-1} \text{ kg}^{-1}$) [10] or Zr-rich PZT (zero-field $|\Delta S| = 8 \text{ J K}^{-1} \text{ kg}^{-1}$) [20]. A

sample preparation process was developed for $(\text{NH}_4)_2\text{SO}_4$ to yield devices resistant to arcing, with thicknesses in the 10s of micron range, enabling fields of up to 400 kV cm^{-1} to be applied. Isothermal $|\Delta S|$ was $\sim 20 \text{ J K}^{-1} \text{ kg}^{-1}$ or $35.4 \text{ J K}^{-1} \text{ dm}^{-3}$, evaluated via the indirect method near $T_C = 223 \text{ K}$. Without the ‘resetting’ indirect method, $|\Delta S| \sim 45 \text{ J K}^{-1} \text{ kg}^{-1}$ would have been spuriously obtained. Adiabats were mapped in $E - T$ space by combining the dataset for isothermal $|\Delta S|$ with zero-field $|\Delta S|$ from calorimetry, yielding $|\Delta T| \sim 4 \text{ K}$. Preliminary indirect measurements on KNO_3 and NaNO_2 give isothermal $|\Delta S| \sim 75 \text{ J K}^{-1} \text{ kg}^{-1}$ or $\sim 158 \text{ J K}^{-1} \text{ dm}^{-3}$ under $|\Delta E| = 31 \text{ kV cm}^{-1}$ near $T_C = 400 \text{ K}$ and $\sim 16 \text{ J K}^{-1} \text{ kg}^{-1}$ or $\sim 34.7 \text{ J K}^{-1} \text{ dm}^{-3}$ under $|\Delta E| = 15 \text{ kV cm}^{-1}$ near $T_C = 435 \text{ K}$, respectively. For KNO_3 , a spurious result of $|\Delta S| \sim 450 \text{ J K}^{-1} \text{ kg}^{-1}$ was obtained via the ‘standard’ indirect method. Thus, KNO_3 exemplifies the failure of the ‘standard’ indirect method near hysteretic, entropic first-order phase transitions. Further work on $(\text{NH}_4)_2\text{SO}_4$ could attempt to measure unclamped, thinned crystals, which could show field-driven transitions at lower electric fields than the clamped samples measured here. For KNO_3 , the next step could be to thin down single crystals to apply larger fields. Inorganic salts with more modest zero-field entropy changes, such as KH_2PO_4 (zero-field $|\Delta S| = 29.5 \text{ J K}^{-1} \text{ kg}^{-1}$ [39]) may also be worth investigating as they could show field-driven transitions at lower electric fields.

For Chapter 5, ceramic samples of cation-ordered $\text{PbSc}_{0.5}\text{Ta}_{0.5}\text{O}_3$ were obtained, showing a nominally first-order transition at 295 K with a zero-field entropy change of $\sim 3.13 \text{ J K}^{-1} \text{ kg}^{-1}$ or $\sim 28.4 \text{ J K}^{-1} \text{ dm}^{-3}$. For samples with thicknesses in the 100s of micron range, the paraelectric-ferroelectric phase transition was fully driven from $\sim 295 - 307 \text{ K}$. A plot of indirectly-measured isothermal $|\Delta S|$ in $E - T$ space revealed a phase boundary obeying the Clausius-Clapeyron equation $dT/dE = |\Delta P|/|\Delta S|$. This was also visible in adiabats plotted in $E - T$ space (Figure 8.1). The maximum value of isothermal $|\Delta S|$ was $\sim 3.25 \text{ J K}^{-1} \text{ kg}^{-1}$ or $\sim 30 \text{ J K}^{-1} \text{ dm}^{-3}$, and $|\Delta T| \sim 2 \text{ K}$, the latter in good agreement with direct measurements of $|\Delta T| \sim 2 \text{ K}$. Clamped samples show broadening of the field-induced transition.

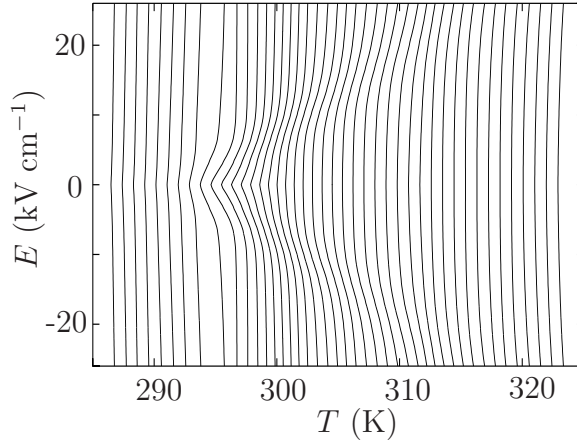


Figure 8.1: Adiabats for $\text{PbSc}_{0.5}\text{Ta}_{0.5}\text{O}_3$ (from Figure 5.8).

The high density in E and T of the measurements reported in Chapters 4-5 provides an enhanced picture of electrocaloric effects, thus helping to understand them in terms of the underpinning phase transitions. This achievement would not have been possible without automation. Measurement times for high-resolution direct electrocaloric measurements in, for example, $\text{PbSc}_{0.5}\text{Ta}_{0.5}\text{O}_3$, were of the order of several days, due to the complex series of temperature and field ramps involved, and the need to wait for thermal stabilisation at the end of each step. Automation will undoubtedly play an important role in systematic measurements of electrocaloric properties, in future studies. This tool should now be employed to systematically investigate a range of bulk materials with varying transition mechanisms to gain detailed empirical insight into electrocaloric mechanisms.

Chapter 6 described the growth by pulsed laser deposition of epitaxial, 63.8 nm-thick SrTiO_3 films on NdGaO_3 (001) substrates with a $\text{La}_{0.67}\text{Sr}_{0.33}\text{MnO}_3$ bottom electrode. The physical properties of materials can be enhanced via epitaxial growth on single-crystal substrates [59, 151, 152]. Strain-induced room-temperature ferroelectricity in the incipient ferroelectric SrTiO_3 was first demonstrated by Haeni *et al.* [59]. Preliminary analysis of the strained SrTiO_3 films via the indirect method gives $|\Delta S| \sim 8 \text{ J K}^{-1} \text{ kg}^{-1}$ or $\sim 41 \text{ J K}^{-1} \text{ dm}^{-3}$ and $|\Delta T| \sim 3.5 \text{ K}$, in $\sim 120 - 200 \text{ K}$ under $|\Delta E| \sim 780 \text{ kV cm}^{-1}$. The Curie temperature was not observed — either it lay below 120 K, or it was suppressed by anisotropy of the substrate lattice. These films, at $\sim 64 \text{ nm}$ -thick, are among the thinnest ever tested for electrocaloric effects, but their electrical properties remained good, perhaps due to the high level of crystalline quality associated with epitaxy. The next step should be to investigate sub-120 K properties of

the SrTiO_3 films to establish the nature of the transition.

Chapter 7 described the development and use of a finite element model (FEM) to optimise geometry for multilayered capacitors (MLCs) for electrocaloric cooling. MLCs were recently suggested for electrocaloric cooling as they show the favourable electrocaloric properties of thin films, a substantial thermal mass for cooling of macroscopic loads, and a high thermal conductivity owing to the metallic interdigitated electrodes [45]. A previous lumped thermal circuit model by Kar-Narayan and Mathur [19] suggested cooling powers of 2.88 kW kg^{-1} could be attained in hypothetical MLCs with PVDF-TrFE dielectric layers and Ni electrodes. The predictions of the FEM improve this value to 5.1 kW kg^{-1} for an MLC of comparable geometry, and, via geometric optimisation, further increase it to 25.9 kW kg^{-1} . An improved thermal circuit for MLCs is described, and it is able to reproduce the FEM results closely in the range of parameter space of interest for cooling applications. The MLC models are not restricted to the idealised case of thermal loads that impose zero thermal impedance on the thermal circuit, as the plots of MLC performance in parameter space are readily applied to more realistic scenarios by imposing load-specific constraints on the operating frequency of the cooler. The models developed may prove valuable for the future fabrication of MLCs optimised for electrocaloric cooling.

Bibliography

- [1] J. D. Jackson, *Electromagnetism*. Wiley, 3rd ed., 1999.
- [2] M. E. Fisher, “Scaling, Universality and Renormalisation Group Theory,” in *Critical Phenomena* (F. J. W. Hayne, ed.), Springer Verlag, 1983.
- [3] M. E. Lines and A. M. Glass, *Principles and applications of ferroelectrics and related materials*. Clarendon Press, 1977.
- [4] B. Naranjo, J. K. Gimzewski, and S. Putterman, “Observation of nuclear fusion driven by a pyroelectric crystal,” *Nature*, vol. 434, pp. 1115–7, Apr. 2005.
- [5] J. Valasek, “Piezo-electric and allied phenomena in Rochelle salt,” *Phys. Rev.*, vol. 17, p. 475, 1921.
- [6] C. J. Adkins, *Equilibrium thermodynamics*. Cambridge University Press, 3rd ed., 1983.
- [7] P. W. Anderson, *Basic notions of condensed matter physics*. Benjamin/Cummings, 1984.
- [8] P. Chandra and P. B. Littlewood, “A Landau Primer for Ferroelectrics,” in *Physics of ferroelectrics* (K. M. Rabe, C. H. Ahn, and J.-M. Triscone, eds.), p. 69, Springer, 2007.
- [9] J. F. Scott, *Ferroelectric memories*. Springer Verlag, 2000.
- [10] X. Moya, E. Stern-Taulats, S. Crossley, D. González-Alonso, S. Kar-Narayan, A. Planes, L. Mañosa, and N. D. Mathur, “Giant Electrocaloric Strength in Single-Crystal BaTiO₃,” *Adv. Mater.*, vol. 25, pp. 1360–1365, Jan. 2013.
- [11] W. Cochran, “Crystal stability and the theory of ferroelectricity,” *Adv. Phys.*, vol. 9, p. 387, 1960.

- [12] E. K. H. Salje, *Phase transitions in ferroelastic and co-elastic crystals*. Cambridge University Press, 1989.
- [13] D. ter Haar, *Collected papers of L. D. Landau*. Pergamon, Oxford, 1965.
- [14] P. B. Littlewood, *Ferroelectrics*. University of Cambridge (Lecture notes), 2002.
- [15] L. E. Cross, “Relaxor ferroelectrics,” *Ferroelectrics*, vol. 76, pp. 241–267, 1987.
- [16] R. A. Cowley, S. N. Gvasaliya, S. G. Lushnikov, B. Roessli, and G. M. Rotaru, “Relaxing with relaxors: a review of relaxor ferroelectrics,” *Adv. Phys.*, vol. 60, pp. 229–327, Apr. 2011.
- [17] A. A. Bokov and Z.-G. Ye, “Recent progress in relaxor ferroelectrics with perovskite structure,” *J. Mater. Sci.*, vol. 41, pp. 31–52, Jan. 2006.
- [18] B. Rožič, M. Kosec, H. Uršič, J. Holc, B. Malič, Q. M. Zhang, R. Blinc, R. Pirc, and Z. Kutnjak, “Influence of the critical point on the electrocaloric response of relaxor ferroelectrics,” *J. Appl. Phys.*, vol. 110, p. 064118, 2011.
- [19] S. Kar-Narayan and N. D. Mathur, “Predicted cooling powers for multilayer capacitors based on various electrocaloric and electrode materials,” *Appl. Phys. Lett.*, vol. 95, p. 242903, 2009.
- [20] A. S. Mischenko, Q. Zhang, J. F. Scott, R. W. Whatmore, and N. D. Mathur, “Giant Electrocaloric Effect in Thin-Film $\text{PbZr}_{0.95}\text{Ti}_{0.05}\text{O}_3$,” *Science*, vol. 311, pp. 1270–1, Mar. 2006.
- [21] B. Neese, B. Chu, S.-G. Lu, Y. Wang, E. Furman, and Q. M. Zhang, “Large Electrocaloric Effect in Ferroelectric Polymers near Room Temperature,” *Science*, vol. 321, pp. 821–3, Aug. 2008.
- [22] P. Kobeko and I. Kurtschatov, “Dielectric properties of ferroelectrics,” *Z. Phys.*, vol. 66, no. 3, pp. 192–205, 1930.
- [23] C. B. Sawyer and C. H. Tower, “Rochelle salt as a dielectric,” *Phys. Rev.*, vol. 35, no. 3, pp. 269–273, 1930.
- [24] G. Busch and P. Scherrer, “A new ferroelectric substance,” *Naturwissenschaften*, vol. 23, no. 43, p. 737, 1935.

- [25] L. J. Sivian, “Energy translation utilizing pyroelectricity (United States Patent 2299260),” 1942.
- [26] B. Wul, “Barium Titanate: a New Ferro-Electric,” *Nature*, vol. 157, p. 808, 1946.
- [27] B. T. Matthias, “New ferroelectric crystals,” *Phys. Rev.*, vol. 75, p. 1771, 1949.
- [28] B. T. Matthias and J. P. Remeika, “Ferroelectricity in the Ilmenite Structure,” *Phys. Rev.*, vol. 76, p. 1886, 1949.
- [29] G. Shirane, S. Hoshino, and K. Suzuki, “X-ray Study of the Phase Transition in Lead Titanate,” *Phys. Rev.*, vol. 80, p. 1105, 1950.
- [30] A. Kikuchi and E. Sawaguchi, “Electrocaloric effect in SrTiO_3 ,” *J. Phys. Soc. Japan*, vol. 19, p. 1497, 1964.
- [31] P. D. Thacher, “Electrocaloric Effects in Some Ferroelectric and Antiferroelectric $\text{Pb}(\text{Zr}, \text{Ti})\text{O}_3$ Compounds,” *J. Appl. Phys.*, vol. 39, no. 4, pp. 1996–2002, 1968.
- [32] H. Kawai, “The piezoelectricity of poly (vinylidene fluoride),” *Japan. J. Appl. Phys.*, vol. 8, p. 975, 1969.
- [33] W. N. Lawless, “Specific heat and electrocaloric properties of KTaO_3 at low temperatures,” *Phys. Rev. B*, vol. 16, no. 1, pp. 433–439, 1977.
- [34] B. A. Tuttle and D. A. Payne, “The effects of microstructure on the electrocaloric properties of $\text{Pb}(\text{Zr}, \text{Sn}, \text{Ti})\text{O}_3$ ceramics,” *Ferroelectrics*, vol. 37, pp. 603–606, 1981.
- [35] L. A. Shebanov, E. H. Birks, and K. J. Borman, “X-ray studies of electrocaloric lead-scandium tantalate ordered solid solutions,” *Ferroelectrics*, vol. 90, p. 165, 1989.
- [36] L. Shebanov and K. Borman, “On lead-scandium tantalate solid solutions with high electrocaloric effect,” *Ferroelectrics*, vol. 127, p. 143, 1992.
- [37] L. Shebanovs, A. Sternberg, W. N. Lawless, and K. Borman, “Isomorphous ion substitutions and order-disorder phenomena in highly electrocaloric lead-scandium tantalate solid solutions,” *Ferroelectrics*, vol. 184, p. 239, 1996.
- [38] L. Shebanovs, K. Borman, W. N. Lawless, and A. Kalvane, “Electrocaloric effect in some perovskite ferroelectric ceramics and multilayer capacitors,” *Ferroelectrics*, vol. 273, p. 137, 2002.

- [39] J. F. Scott, “On the theory of ferroelectric susceptibilities,” *J. Phys. Soc. Japan*, vol. 58, pp. 4487–4490, 1989.
- [40] J. F. Scott and C. A. Paz De Araujo, “Ferroelectric Memories,” *Science*, vol. 246, pp. 1400–1405, 1989.
- [41] Y. V. Sinyavsky and V. M. Brodyansky, “Experimental testing of electrocaloric cooling with transparent ferroelectric ceramic as a working body,” *Ferroelectrics*, vol. 131, pp. 321–325, 1992.
- [42] G. Akcay, S. P. Alpay, G. A. Rossetti, and J. F. Scott, “Influence of mechanical boundary conditions on the electrocaloric properties of ferroelectric thin films,” *J. Appl. Phys.*, vol. 103, p. 024104, 2008.
- [43] H. Chen, T.-L. Ren, X.-M. Wu, Y. Yang, and L.-T. Liu, “Giant electrocaloric effect in lead-free thin film of strontium bismuth tantalite,” *Appl. Phys. Lett.*, vol. 94, p. 182902, 2009.
- [44] T. M. Correia, J. S. Young, R. W. Whatmore, J. F. Scott, N. D. Mathur, and Q. Zhang, “Investigation of the electrocaloric effect in a $\text{PbMg}_{2/3}\text{Nb}_{1/3}\text{O}_3$ - PbTiO_3 relaxor thin film,” *Appl. Phys. Lett.*, vol. 95, p. 182904, 2009.
- [45] S. Kar-Narayan and N. D. Mathur, “Direct and indirect electrocaloric measurements using multilayer capacitors,” *J. Phys. D: Appl. Phys.*, vol. 43, p. 032002, 2010.
- [46] S. G. Lu, B. Rožič, Q. M. Zhang, Z. Kutnjak, X. Li, E. Furman, L. J. Gorny, M. Lin, B. Malič, M. Kosec, R. Blinc, and R. Pirc, “Organic and inorganic relaxor ferroelectrics with giant electrocaloric effect,” *Appl. Phys. Lett.*, vol. 97, p. 162904, 2010.
- [47] S. G. Lu, B. Rožič, Q. M. Zhang, Z. Kutnjak, R. Pirc, M. Lin, X. Li, and L. Gorny, “Comparison of directly and indirectly measured electrocaloric effect in relaxor ferroelectric polymers,” *Appl. Phys. Lett.*, vol. 97, p. 202901, 2010.
- [48] S. G. Lu, B. Rožič, Q. M. Zhang, Z. Kutnjak, and B. Neese, “Enhanced electrocaloric effect in ferroelectric poly(vinylidene-fluoride/trifluoroethylene) 55/45 mol % copolymer at ferroelectric-paraelectric transition,” *Appl. Phys. Lett.*, vol. 98, p. 122906, 2011.

- [49] J. Scott, “Electrocaloric Materials,” *Annu. Rev. Mater. Res.*, vol. 41, pp. 229–240, Aug. 2011.
- [50] T. M. Correia, S. Kar-Narayan, J. S. Young, J. F. Scott, N. D. Mathur, R. W. Whatmore, and Q. Zhang, “PST thin films for electrocaloric coolers,” *J. Phys. D: Appl. Phys.*, vol. 44, p. 165407, Apr. 2011.
- [51] Y. Jia and Y. S. Ju, “A solid-state refrigerator based on the electrocaloric effect,” *Appl. Phys. Lett.*, vol. 100, p. 242901, 2012.
- [52] S. Kar-Narayan, S. Crossley, X. Moya, V. Kovacova, J. Abergel, A. Bontempi, N. Baier, E. Defay, and N. D. Mathur, “Direct electrocaloric measurements of a multilayer capacitor using scanning thermal microscopy and infra-red imaging,” *Appl. Phys. Lett.*, vol. 102, p. 032903, 2013.
- [53] B. Peng, H. Fan, and Q. Zhang, “A Giant Electrocaloric Effect in Nanoscale Antiferroelectric and Ferroelectric Phases Coexisting in a Relaxor $\text{Pb}_{0.8}\text{Ba}_{0.2}\text{ZrO}_3$ Thin Film at Room Temperature,” *Adv. Funct. Mater.*, vol. 23, pp. 2987–2992, Jan. 2013.
- [54] E. Defay, S. Crossley, S. Kar-Narayan, X. Moya, and N. D. Mathur, “The Electrocaloric Efficiency of Ceramic and Polymer Films,” *Adv. Mater.*, vol. 25, pp. 3337–3342, May 2013.
- [55] C. J. Chen, Y. Xu, R. Xu, and J. D. Mackenzie, “Ferroelectric and pyroelectric properties prepared by the sol-gel method of strontium barium niobate films,” *J. Appl. Phys.*, vol. 69, pp. 1763–1765, 1990.
- [56] E. C. Subbarao, “Ferroelectric and antiferroelectric materials,” *Ferroelectrics*, vol. 5, p. 267, 1973.
- [57] A. Kumar, R. S. Katiyar, and J. F. Scott, “Fabrication and characterization of the multiferroic birelaxor lead–iron–tungstate/lead–zirconate–titanate,” *J. Appl. Phys.*, vol. 108, p. 064105, 2010.
- [58] C. C. Wu, W. L. Zhang, Y. R. Li, X. Z. Liu, J. Zhu, and B. W. Tao, “High pyroelectric $\text{Ba}_{0.65}\text{Sr}_{0.35}\text{TiO}_3$ thin films with $\text{Ba}_{0.65}\text{Sr}_{0.35}\text{RuO}_3$ seeding-layer for monolithic ferroelectric bolometer,” *Infrared. Phys. Techn.*, vol. 48, pp. 187–191, Aug. 2006.

- [59] J. H. Haeni, P. Irvin, W. Chang, R. Uecker, P. Reiche, Y. L. Li, S. Choudhury, W. Tian, M. E. Hawley, B. Craigo, A. K. Tagantsev, X. Q. Pan, S. K. Streiffer, L. Q. Chen, S. W. Kirchoefer, J. Levy, and D. G. Schlom, “Room-temperature ferroelectricity in strained SrTiO_3 ,” *Nature*, vol. 430, pp. 758–761, 2004.
- [60] S. H. Kim, S. H. Lee, T. H. Kim, T. Zyung, Y. H. Jeong, and M. S. Jang, “Growth, Ferroelectric Properties, and Phonon Models of YMnO_3 Single Crystal,” *Cryst. Res. Technol.*, vol. 35, pp. 19–27, 2000.
- [61] H. Tamura, E. Sawaguchi, and A. Kikuchi, “Ferroelectric Hysteresis Character of YMnO_3 ,” *Japan. J. Appl. Phys.*, vol. 4, p. 621, 1965.
- [62] M. Fukunaga and Y. Noda, “New Technique for Measuring Ferroelectric and Antiferroelectric Hysteresis Loops,” *J. Phys. Soc. Japan*, vol. 77, p. 064706, May 2008.
- [63] K. Tanaka, O. Nakagawara, M. Nakano, T. Shimuta, H. Tabata, and T. Kawai, “Epitaxial growth of $(\text{Sr}, \text{Ba})\text{Nb}_2\text{O}_6$ thin films by pulsed laser deposition,” *Japan. J. Appl. Phys.*, vol. 37, pp. 6142–6145, 1998.
- [64] S. S. Thony, K. E. Youden, J. S. Harris, and L. Hesselink, “Growth of epitaxial strontium barium niobate thin films by pulsed laser deposition,” *Appl. Phys. Lett.*, vol. 65, pp. 2018–2020, 1994.
- [65] S. L. Swartz, C. A. Randall, and A. S. Bhalla, “Dielectric and pyroelectric properties of cadmium niobate ceramics,” *J. Am. Ceram. Soc.*, vol. 72, pp. 637–641, 1989.
- [66] J. F. Scott, “Phase transitions in BaMnF_4 ,” *Rep. Prog. Phys.*, vol. 12, p. 1055, 1979.
- [67] A. Fouskova, “The specific heat of $\text{Gd}_2(\text{MoO}_4)_3$,” *J. Phys. Soc. Japan*, vol. 27, p. 1699, 1969.
- [68] T. Miyashita and T. Murakami, “The Coexistence of the Spontaneous Electric Polarization and Magnetization in Ni-I Boracite,” *J. Phys. Soc. Japan*, vol. 29, p. 1092, 1970.
- [69] H. H. Wieder, A. R. Clawson, and C. R. Parkerson, “Ferroelectric and Pyroelectric Properties of Mineral and Synthetic Colemanite,” *J. Appl. Phys.*, vol. 33, p. 1720, 1962.

- [70] J. R. Ghulghule and A. G. Katpatal, “Pyroelectric behaviour of pure and lanthanum-doped lead germanate single crystal,” *J. Phys. Chem. Solids*, vol. 60, pp. 425–428, Mar. 1999.
- [71] H. Chihara and A. Inaba, “Thermodynamic properties of solid hydrogen halides and deuterium halides,” *J. Chem. Thermodynamics*, vol. 8, p. 915, 1976.
- [72] S. Hoshino, K. Shimaoka, and N. Niimura, “Ferroelectricity in solid hydrogen halides,” *Phys. Rev. Lett.*, vol. 19, p. 1286, 1967.
- [73] T. Mori, H. Tamura, and E. Sawaguchi, “Specific Heat Measurement of Ferroelectric SbSI,” *J. Phys. Soc. Japan*, vol. 20, p. 281, 1965.
- [74] C. B. van den Berg, J. E. van Delden, and J. Bouman, “ α -Transition in FeS - a Ferroelectric Transition,” *Phys. Stat. Sol.*, vol. 36, p. K89, 1969.
- [75] M. Sakiyama, A. Kimoto, and S. Seki, “Heat Capacities and Volume Thermal Expansion of NaNO_2 Crystal,” *J. Phys. Soc. Japan*, vol. 20, p. 2180, 1965.
- [76] M. Dawber, I. Farnan, and J. F. Scott, “A classroom experiment to demonstrate ferroelectric hysteresis,” *Am. J. Phys.*, vol. 71, p. 819, 2003.
- [77] I. N. Flerov and E. A. Mikhaleva, “Electrocaloric effect and anomalous conductivity of the ferroelectric NH_4HSO_4 ,” *Phys. Solid State*, vol. 50, pp. 478–484, Feb. 2008.
- [78] F. Jona, K. Vedam, T. Mitsui, and R. Pepinsky, “Ferroelectric behaviour of $\text{NH}_4\text{Fe}(\text{SO}_4)_2 \cdot 12\text{H}_2\text{O}$ (Abstract for American Physical Society, Washington Meeting, April 25-27, 1957),” Mar. 1957.
- [79] Sigma Aldrich Corporation, “Chemical data sheets,” 2013.
- [80] M. Szafrński, “Simple guanidinium salts revisited: room-temperature ferroelectricity in hydrogen-bonded supramolecular structures,” *J. Phys. Chem. B*, vol. 115, pp. 8755–62, July 2011.
- [81] G. A. Samara and D. H. Anderson, “Ferroelectric-paraelectric transition in lithium trihydrogen selenite,” *Solid. State. Commun.*, vol. 4, pp. 653–655, 1966.
- [82] Y. Makita and H. Miki, “Anomalous specific heat and configurational entropy change in sodium trihydrogen selenite,” *J. Phys. Soc. Japan*, vol. 28, p. 1221, 1970.

- [83] A. M. Glass, J. S. Patel, J. W. Goodby, D. H. Olson, and J. M. Geary, "Pyroelectric detection with smectic liquid crystals," *J. Appl. Phys.*, vol. 60, p. 2778, 1986.
- [84] G. J. Goldsmith and J. G. White, "Ferroelectric Behavior of Thiourea," *J. Chem. Phys.*, vol. 31, p. 1175, 1959.
- [85] X. K. Chen, G. Li, W. M. Du, and H. Z. Cummins, "The intrinsic $\frac{1}{8}$ lock-in improper ferroelectric phase in thiourea: dielectric susceptibility and hysteresis loop analysis," *Ferroelectrics*, vol. 137, pp. 251–283, 1992.
- [86] J. M. Igartua, A. Lopez-Echarri, T. Brezowski, and I. Ruiz-Larrea, "The phase transition sequence in thiourea ($\text{SC}(\text{NH}_2)_2$). A heat capacity study," *Phase Transit.*, vol. 46, p. 47, 1993.
- [87] R. I. Epstein and K. J. Malloy, "Electrocaloric devices based on thin-film heat switches," *J. Appl. Phys.*, vol. 106, p. 064509, 2009.
- [88] E. Kruglick, "Heterogeneous electrocaloric effect heat transfer device (United States Patent 13/145,948 [Application])," 2011.
- [89] P. F. Liu, J. L. Wang, X. J. Meng, J. Yang, B. Dkhil, and J. H. Chu, "Huge electrocaloric effect in Langmuir–Blodgett ferroelectric polymer thin films," *New J. Phys.*, vol. 12, p. 023035, Feb. 2010.
- [90] *ITS 90 thermocouple database*. <http://srdata.nist.gov/>, 1990.
- [91] Agilent Technologies Corporation, *Agilent Impedance Measurement Handbook*. Agilent Technologies Corporation, 4th ed., 2009.
- [92] L. Caron, Z. Q. Ou, T. T. Nguyen, D. T. Cam Thanh, O. Tegus, and E. Brück, "On the determination of the magnetic entropy change in materials with first-order transitions," *J. Magn. Magn. Mater.*, vol. 321, pp. 3559–3566, Nov. 2009.
- [93] L. Tocado, E. Palacios, and R. Burriel, "Entropy determinations and magnetocaloric parameters in systems with first-order transitions: Study of MnAs," *J. Appl. Phys.*, vol. 105, p. 093918, 2009.
- [94] L. Mañosa, A. Planes, and M. Acet, "Advanced materials for solid-state refrigeration," *J. Mater. Chem. A*, vol. 1, p. 4925, 2013.

- [95] M. J. Druyvesteyn and F. M. Penning, “The mechanism of electrical discharges in gases of low pressure,” *Rev. Mod. Phys.*, vol. 12, p. 87, 1940.
- [96] E. K. H. Salje, S. Crossley, S. Kar-Narayan, M. A. Carpenter, and N. D. Mathur, “Improper ferroelectricity in lawsonite $\text{CaAl}_2\text{Si}_2\text{O}_7(\text{OH})_2 \cdot \text{H}_2\text{O}$: hysteresis and hydrogen ordering,” *J. Phys.: Condens. Matter*, vol. 23, p. 222202, June 2011.
- [97] W. M. Haynes, ed., *Handbook of Chemistry and Physics*. Taylor & Francis, 94th ed., 2013.
- [98] S. Sawada, S. Nomura, S. Fujii, and I. Yoshida, “Ferroelectricity in NaNO_2 ,” *Phys. Rev. Lett.*, vol. 1, p. 320, 1958.
- [99] J. L. Gronshaw and J. Ritter *Z. Physik. Chem. B*, vol. 16, p. 143, 1932.
- [100] I. Nitta and K. Suenaga, “On the Thermal Transition in Solid Deuterio-Ammonium Sulphate, $(\text{ND}_4)_2\text{SO}_4$,” *B. Chem. Soc. Jpn.*, vol. 13, p. 36, 1938.
- [101] C. H. Shomate, “Specific heats at low temperatures of $(\text{NH}_4)_2\text{SO}_4$, $\text{NH}_4\text{Al}(\text{SO}_4)_2$ and $\text{NH}_4\text{Al}(\text{SO}_4)_2 \cdot 12\text{H}_2\text{O}$,” *J. Am. Chem. Soc.*, vol. 67, p. 1096, 1945.
- [102] B. T. Matthias and J. P. Remeika, “Ferroelectricity in ammonium sulfate,” *Phys. Rev.*, vol. 103, p. 262, 1956.
- [103] H. G. Unruh, “The spontaneous polarization of $(\text{NH}_4)_2\text{SO}_4$,” *Solid. State. Commun.*, vol. 8, pp. 1951–1954, 1970.
- [104] A. Sawada, S. Ohya, Y. Ishibashi, and Y. Takagi, “Ferroelectric Phase-Transition in $(\text{NH}_4)_2\text{SO}_4\text{-K}_2\text{SO}_4$ Mixed Crystals,” *J. Phys. Soc. Japan*, vol. 38, p. 1408, 1975.
- [105] H. G. Unruh and U. Rudiger, “The ferroelectric transition of $(\text{NH}_4)_2\text{SO}_4$,” *J. Phys. Colloq.*, vol. 33, pp. C2–77, 1972.
- [106] S. Sawada, T. Yamaguchi, and N. Shibayama, “Ferroelectricity in $(\text{NH}_4)_2\text{SO}_4$, $(\text{NH}_4)_2\text{BeF}_4$ and K_2SeO_4 ,” *J. Phys. Soc. Japan*, vol. 48, p. 1395, 1980.
- [107] Y. Higashigaki and H. Chihara, “Phase transition in ammonium-d4 sulfate as studied by heat capacity measurements between 3 and 300 K,” *B. Chem. Soc. Jpn.*, vol. 54, p. 901, 1981.

- [108] A. Ogg and F. Lloyd Hopwood, "A critical test of the crystallographic law of valency volumes; a note on the crystalline structure of the alkali sulphates," *Philosophical Magazine*, vol. 32, pp. 518–525, 1916.
- [109] E. O. Schlemper and W. C. Hamilton, "Neutron-Diffraction Study of the Structures of Ferroelectric and Paraelectric Ammonium Sulfate," *J. Chem. Phys.*, vol. 44, pp. 4498–4509, 1966.
- [110] D. O'Reilly and T. Tsang, "Deuteron magnetic resonance and proton relaxation times in ferroelectric ammonium sulfate," *J. Chem. Phys.*, vol. 46, p. 1291, 1967.
- [111] J. Kobayashi, Y. Enomoto, and Y. Sato, "A phenomenological theory of dielectric and mechanical properties of improper ferroelectric crystals," *Phys. Stat. Sol. (b)*, vol. 50, pp. 335–343, Mar. 1972.
- [112] A. Sawada, Y. Takagi, and Y. Ishibashi, "The Origin of the Ferroelectric Phase Transition in Ammonium Sulfate," *J. Phys. Soc. Japan*, vol. 34, p. 748, 1973.
- [113] V. Dvorák and Y. Ishibashi, "Two-sublattice model of ferroelectric phase transitions," *J. Phys. Soc. Japan*, vol. 41, p. 548, 1976.
- [114] A. Onodera, H. Fujishita, and Y. Shiozaki, "X-ray diffraction study of sub-lattice order parameters in ferroelectric ammonium sulphate," *Solid. State. Commun.*, vol. 27, pp. 463–465, 1978.
- [115] A. Onodera, O. Cynshi, and Y. Shiozaki, "Landau theory of the ferroelectric phase transition with two order parameters," *J. Phys. C: Solid State Phys.*, vol. 18, p. 2831, 1985.
- [116] Y. S. Jain, P. K. Bajpai, R. Bhattacharjee, and D. Chowdhury, "Phase transition and temperature dependence of the molecular distortion of ions in ammonium sulphate," *J. Phys. C: Solid State Phys.*, vol. 19, p. 3789, 1986.
- [117] P. K. Bajpai and Y. S. Jain, "The phase transition in ammonium sulphate: dynamics of deuterated NH_4^+ ions and the heat of transition," *J. Phys. C: Solid State Phys.*, vol. 20, p. 387, 1987.
- [118] H. G. Unruh and O. Ayere, "Raman and dielectric measurements on ferroelectric ammonium sulphate," *Ferroelectrics*, vol. 12, pp. 181–183, 1976.

- [119] K. Hasebe, “Studies of the crystal structure of ammonium sulfate in connection with its ferroelectric phase transition,” *J. Phys. Soc. Japan*, vol. 50, pp. 1266–1274, 1981.
- [120] K. Hasebe, “Phase transition of ammonium sulfate,” *J. Phys. Soc. Japan*, vol. 50, p. 2660, 1981.
- [121] K. Fujii, H. Mori, and T. Matsubara, “Phase transition of $(\text{NH}_4)_2\text{SO}_4\text{-K}_2\text{SO}_4$ mixed crystal,” *J. Phys. Soc. Japan*, vol. 59, p. 4488, 1990.
- [122] G. V. Kozlov, S. P. Lebedev, A. A. Volkov, J. Petzelt, B. Wynche, and F. Brehat, “Dielectric dispersion of $(\text{NH}_4)_2\text{SO}_4$ in the near-millimetre and far-infrared range: manifestations of disorder,” *J. Phys. C: Solid State Phys.*, vol. 21, p. 4883, 1988.
- [123] D. De Sousa Meneses, “Phenomenological Landau theory of the $[\text{NH}_4]_2\text{SO}_4$ para-ferroelectric phase transition,” *Solid. State. Commun.*, vol. 96, pp. 5–9, 1995.
- [124] S. Hoshino, K. Vedam, Y. Okaya, and R. Pepinsky, “Dielectric and Thermal Study of $(\text{NH}_4)_2\text{SO}_4$ and $(\text{NH}_4)_2\text{BeF}_4$ Transitions,” *Phys. Rev.*, vol. 112, p. 405, 1958.
- [125] V. Y. Stadnyk, M. O. Romanyuk, B. V. Andrievskii, and N. R. Tuzyak, “Refractive indices of $(\text{NH}_4)_2\text{SO}_4$ crystals under uniaxial pressure,” *Crystallogr. Rep.*, vol. 54, pp. 313–319, Mar. 2009.
- [126] F. C. Kracek, “The polymorphism of potassium nitrate,” *J. Phys. Chem.*, vol. 34, p. 225, 1930.
- [127] M. J. Westphal, J. W. Wood, R. D. Redin, and T. Ashworth, “Calorimetric and photoacoustic investigation of KNO_3 phase transitions,” *J. Appl. Phys.*, vol. 73, p. 7302, 1993.
- [128] J. K. Nimmo and B. W. Lucas, “The crystal structures of γ - and β - KNO_3 and the $\alpha \leftarrow \gamma \leftarrow \beta$ phase transformations,” *Acta Cryst.*, vol. B32, pp. 1968–1971, 1976.
- [129] S. Sawada, N. Shoichiro, and Y. Asao, “Dielectric Behaviour of KNO_3 in its Ferroelectric Phase III,” *J. Phys. Soc. Japan*, vol. 16, p. 2486, 1961.
- [130] A. Chen and F. Chernow, “Nature of Ferroelectricity in KNO_3 ,” *Phys. Rev.*, vol. 154, p. 493, 1967.

- [131] J. K. Nimmo and B. W. Lucas, "A neutron diffraction determination of the crystal structure of α -phase potassium nitrate at 25 °C and 100 °C," *J. Phys. C: Solid State Phys.*, vol. 6, p. 201, 1973.
- [132] E. Y. Wang, "Latent Heat Measurement of Phase Transformations in Potassium Nitrate," *J. Electrochem. Soc.*, vol. 123, p. 435, 1976.
- [133] J. F. Scott, M. Zhang, R. B. Godfrey, C. Araujo, and L. McMillan, "Raman spectroscopy of submicron KNO₃ films," *Phys. Rev. B*, vol. 35, no. 8, p. 4044, 1987.
- [134] E. J. Freney, L. A. J. Garvie, T. L. Groy, and P. R. Buseck, "Growth and single-crystal refinement of phase-III potassium nitrate, KNO₃," *Acta Cryst.*, vol. B65, pp. 659–63, Dec. 2009.
- [135] S. Tanisaki, "X-ray Study on the Ferroelectric Phase Transition of NaNO₂," *J. Phys. Soc. Japan*, vol. 18, p. 1181, 1963.
- [136] S. Hoshino, "An Evidence for Existence of a Third Phase in NaNO₂," *J. Phys. Soc. Japan*, vol. 19, p. 140, 1964.
- [137] S. Nomura, "Thermal Properties of NaNO₂," *J. Phys. Soc. Japan*, vol. 16, p. 1352, 1961.
- [138] I. Hatta and A. Ikushima, "Specific heat of NaNO₂ near its transition points," *J. Phys. Chem. solids*, vol. 34, pp. 57–66, 1973.
- [139] L. Kourkova, R. Svoboda, G. Sadovska, V. Podzemna, and A. Kohutova, "Heat capacity of NaNO₂," *Thermochimica Acta*, vol. 491, pp. 80–83, July 2009.
- [140] M. I. Kay, J. A. Gonzalo, and R. Maglic, "The phase transition in sodium nitrite," *Ferroelectrics*, vol. 9, p. 179, 1975.
- [141] Z. Kutnjak, B. Vodopivec, R. Blinc, A. V. Fokin, Y. A. Kumzerov, and S. B. Vakhrushev, "Calorimetric and dielectric studies of ferroelectric sodium nitrite confined in a nanoscale porous glass matrix," *J. Chem. Phys.*, vol. 123, p. 084708, Aug. 2005.
- [142] R. Nevin, "Understanding international crime trends: the legacy of preschool lead exposure," *Environ. Res.*, vol. 104, pp. 315–36, July 2007.

- [143] H. W. Mielke and S. Zahran, “The urban rise and fall of air lead (Pb) and the latent surge and retreat of societal violence,” *Environment International*, vol. 43, pp. 48–55, Aug. 2012.
- [144] C. G. F. Stenger, F. L. Scholten, and A. J. Burggraaf, “Ordering and diffuse phase transitions in $\text{Pb}(\text{Sc}_{0.5}\text{Ta}_{0.5})\text{O}_3$ ceramics,” *Solid. State. Commun.*, vol. 32, pp. 989–992, 1979.
- [145] C. G. F. Stenger and A. J. Burggraaf, “Order-Disorder Reactions in the Ferroelectric Perovskites $\text{Pb}(\text{Sc}_{1/2}\text{Nb}_{1/2})\text{O}_3$ and $\text{Pb}(\text{Sc}_{1/2}\text{Ta}_{1/2})\text{O}_3$ I,” *Phys. Stat. Sol. (a)*, vol. 61, p. 275, 1980.
- [146] C. G. F. Stenger and A. J. Burggraaf, “Order-Disorder Reactions in the Ferroelectric Perovskites $\text{Pb}(\text{Sc}_{1/2}\text{Nb}_{1/2})\text{O}_3$ and $\text{Pb}(\text{Sc}_{1/2}\text{Ta}_{1/2})\text{O}_3$ II,” *Phys. Stat. Sol. (a)*, vol. 61, pp. 653–664, 1980.
- [147] N. Setter and L. E. Cross, “The role of B-site cation disorder in diffuse phase transition behavior of perovskite ferroelectrics,” *J. Appl. Phys.*, vol. 51, no. 8, p. 4356, 1980.
- [148] P. C. Osbond and R. W. Whatmore, “High dielectric constant ceramics in the $\text{PbSc}_{0.5}\text{Ta}_{0.5}\text{O}_3$ - PbZrO_3 system,” *Ferroelectrics*, vol. 133, p. 159, 1992.
- [149] N. Shorrocks, R. Whatmore, and P. Osbond, “Lead scandium tantalate for thermal detector applications,” *Ferroelectrics*, vol. 106, no. June 2013, p. 387, 1990.
- [150] A. B. Posadas, M. Lippmaa, F. Walker, M. Dawber, C. H. Ahn, and J. M. Triscone, “Growth and novel applications of epitaxial oxide thin films,” in *Physics of ferroelectrics* (K. Rabe, C. H. Ahn, and J.-M. Triscone, eds.), p. 219, Springer, 2007.
- [151] K. J. Choi, M. Biegalski, Y. L. Li, A. Sharan, J. Schubert, R. Uecker, P. Reiche, Y. B. Chen, X. Q. Pan, V. Gopalan, L.-Q. Chen, D. G. Schlom, and C. B. Eom, “Enhancement of ferroelectricity in strained BaTiO_3 thin films,” *Science (New York, N.Y.)*, vol. 306, pp. 1005–9, Nov. 2004.
- [152] X. Moya, L. E. Hueso, F. Maccherozzi, A. I. Tovstolytkin, D. I. Podyalovskii, C. Ducati, L. C. Phillips, M. Ghidini, O. Hovorka, A. Berger, M. E. Vickers, E. Defay, S. S. Dhesi, and N. D. Mathur, “Giant and reversible extrinsic

- magnetocaloric effects in $\text{La}_{0.7}\text{Ca}_{0.3}\text{MnO}_3$ films due to strain,” *Nature materials*, vol. 12, pp. 52–8, Jan. 2013.
- [153] Y. A. Abramov, V. G. Tsirelson, V. E. Zavodnik, S. A. Ivanov, and I. D. Brown, “The chemical bond and atomic displacements in SrTiO_3 from X-ray diffraction analysis,” *Acta Cryst.*, vol. B51, pp. 942–951, Dec. 1995.
 - [154] R. P. Liferovich and R. H. Mitchell, “A structural study of ternary lanthanide orthoscandate perovskites,” *J. Solid State Chem.*, vol. 177, pp. 2188–2197, June 2004.
 - [155] J. K. Hulm, “The dielectric properties of some alkaline earth titanates at low temperatures,” *Proc. Phys. Soc. A*, vol. 63, p. 1184, 1950.
 - [156] J. F. Youngblood, “Low temperature dielectric measurements,” *Phys. Rev.*, vol. 98, p. 1201, 1955.
 - [157] P. A. Fleury and J. M. Worlock, “Electric-Field-Induced Raman Scattering in SrTiO_3 and KTaO_3 ,” *Phys. Rev.*, vol. 174, p. 613, 1968.
 - [158] P. A. Fleury, J. F. Scott, and J. M. Worlock, “Soft phonon modes and the 110 °K phase transition in SrTiO_3 ,” *Phys. Rev. Lett.*, vol. 21, p. 16, 1968.
 - [159] R. A. Cowley, W. J. L. Buyers, and G. Dolling, “Relationship of normal modes of vibration of strontium titanate and its antiferroelectric phase transition at 110 °K,” *Solid. State. Commun.*, vol. 7, p. 181, 1969.
 - [160] G. Shirane and Y. Yamada, “Lattice-dynamical study of the 110 °K phase transition in SrTiO_3 ,” *Phys. Rev.*, vol. 177, pp. 858–863, 1969.
 - [161] W. J. Burke and R. J. Pressley, “Stress induced ferroelectricity in SrTiO_3 ,” *Solid. State. Commun.*, vol. 9, pp. 191–195, 1971.
 - [162] H. Uwe and S. Tunetaro, “Stress-induced ferroelectricity and soft phonon modes in SrTiO_3 ,” *Phys. Rev. B*, vol. 13, p. 271, 1976.
 - [163] P. A. Fleury and J. M. Worlock, “Electric-field-induced Raman effect in paraelectric crystals,” *Phys. Rev. Lett.*, vol. 18, p. 665, 1967.
 - [164] J. M. Worlock and P. A. Fleury, “Electric field dependence of optical-phonon frequencies,” *Phys. Rev. Lett.*, vol. 19, p. 1176, 1967.

- [165] T. Sakudo and H. Uwe, “Raman scattering study of the soft phonon modes in the ferroelectric SrTiO_3 ,” *Ferroelectrics*, vol. 8, p. 587, 1974.
- [166] R. Wang, Y. Inaguma, and M. Itoh, “Predominant factors for quantum paraelectric - quantum ferroelectric transition in SrTiO_3 -based oxides,” *Physica B*, vol. 284-288, pp. 1141–1142, 2000.
- [167] H. E. Weaver, “Dielectric properties of single crystals of SrTiO_3 at low temperatures,” *J. Phys. Chem. Solids*, vol. 11, pp. 274–277, Oct. 1959.
- [168] M. A. Saifi and L. E. Cross, “Dielectric properties of strontium titanate at low temperature,” *Phys. Rev. B*, vol. 2, p. 677, 1970.
- [169] N. Pertsev, A. Tagantsev, and N. Setter, “Phase transitions and strain-induced ferroelectricity in SrTiO_3 epitaxial thin films,” *Phys. Rev. B*, vol. 61, no. 2, pp. 825–829, 2000.
- [170] N. Pertsev, A. Tagantsev, and N. Setter, “Erratum: Phase transitions and strain-induced ferroelectricity in SrTiO_3 epitaxial thin films [Phys. Rev. B 61, R825 (2000)],” *Phys. Rev. B*, vol. 65, p. 219901, May 2002.
- [171] M. D. Biegalski, Y. Jia, D. G. Schlom, S. Trolier-McKinstry, S. K. Streiffer, V. Sherman, R. Uecker, and P. Reiche, “Relaxor ferroelectricity in strained epitaxial SrTiO_3 thin films on DyScO_3 substrates,” *Appl. Phys. Lett.*, vol. 88, p. 192907, 2006.
- [172] T. Yamada, J. Petzelt, A. Tagantsev, S. Denisov, D. Noujni, P. Petrov, A. Mackova, K. Fujito, T. Kiguchi, K. Shinozaki, N. Mizutani, V. Sherman, P. Muralt, and N. Setter, “In-Plane and Out-of-Plane Ferroelectric Instabilities in Epitaxial SrTiO_3 Films,” *Phys. Rev. Lett.*, vol. 96, p. 157602, Apr. 2006.
- [173] D. Nuzhnyy, J. Petzelt, S. Kamba, X. Martí, T. Cechal, C. M. Brooks, and D. G. Schlom, “Infrared phonon spectroscopy of a compressively strained (001) SrTiO_3 film grown on a (110) NdGaO_3 substrate,” *J. Phys.: Condens. Matter*, vol. 23, p. 045901, Feb. 2011.
- [174] E. Hegenbarth, “Studies of the electrocaloric effect of ferroelectric ceramics at low temperatures,” *Cryogenics*, vol. 1, pp. 242–243, 1961.
- [175] J. H. Qiu and Q. Jiang, “Effect of misfit strain on the electrocaloric effect in epitaxial SrTiO_3 thin films,” *Eur. Phys. J. B*, vol. 71, pp. 15–19, July 2009.

- [176] J. Zhang, I. B. Misirlioglu, S. P. Alpay, and G. A. Rossetti, “Electrocaloric properties of epitaxial strontium titanate films,” *Appl. Phys. Lett.*, vol. 100, p. 222909, 2012.
- [177] L. Vasylechko, L. Akselrud, W. Morgenroth, U. Bismayer, A. Matkovskii, and D. Savytskii, “The crystal structure of NdGaO₃ at 100 K and 293 K based on synchrotron data,” *J. Alloys Comp.*, vol. 297, pp. 46–52, 2000.
- [178] G. Koster, L. Klein, W. Siemons, G. Rijnders, J. S. Dodge, C.-B. Eom, D. H. A. Blank, and M. R. Beasley, “Structure, physical properties, and applications of SrRuO₃ thin films,” *Rev. Mod. Phys.*, vol. 84, pp. 253–298, Mar. 2012.
- [179] L. C. Phillips, M. Ghidini, X. Moya, F. Maccherozzi, S. S. Dhesi, and N. D. Mathur, “Low-temperature transverse magnetic domains in nominally uniaxial La_{0.67}Sr_{0.33}MnO₃ films on NdGaO₃ (001),” *J. Phys. D: Appl. Phys.*, vol. 46, p. 032002, Jan. 2013.
- [180] R. J. Bouchard and J. L. Gillson, “Electrical properties of CaRuO₃ and SrRuO₃ single crystals,” *Mat. Res. Bull.*, vol. 7, pp. 873–878, 1972.
- [181] A. Urishabara, Y. Moritomo, T. Arima, A. Asatmisu, G. Kido, and Y. Tokura, “Insulator-metal transition and giant magnetoresistance in La_{1-x}Sr_xMnO₃,” *Phys. Rev. B*, vol. 51, p. 14103, 1995.
- [182] H. Béa, S. Fusil, K. Bouzehouane, M. Bibes, M. Sirena, G. Herranz, E. Jacquet, J.-P. Contour, and A. Barthélémy, “Ferroelectricity Down to at Least 2 nm in Multiferroic BiFeO₃ Epitaxial Thin Films,” *Japan. J. Appl. Phys.*, vol. 45, pp. L187–L189, Feb. 2006.
- [183] N. A. Burnham, O. P. Behrend, F. Oulevey, G. Gremaud, P. J. Gallo, D. Gourdon, E. Dupas, A. J. Kilik, H. Pollock, and G. Briggs, “How does a tip tap?,” *Nanotechnology*, vol. 8, p. 67, 1997.
- [184] B. D. Cullity and S. R. Stock, *Elements of X-ray Diffraction*. Prentice Hall, 3rd ed., 2002.
- [185] P. F. Fewster, *X-ray Scattering from Semiconductors*. Imperial College Press, 2000.
- [186] I. Hatta, Y. Shiroishi, K. A. Muller, and W. Berlinger, “Critical behaviour of the heat capacity in SrTiO₃,” *Phys. Rev. B*, vol. 16, p. 1138, 1977.

- [187] S. Kar-Narayan, S. Crossley, and N. D. Mathur, “Electrocaloric multilayer capacitors,” in *Electrocaloric Materials: A new generation of coolers?* (T. M. Correia, ed.), Springer, 2013.
- [188] O. C. Zienkiewicz and R. L. Taylor, *The Finite Element Method*. Butterworth-Heinemann, 5th ed., 2000.
- [189] G. Dhondt, *Calculix 2.4 documentation*. <http://www.calculix.de/>, 2012.
- [190] E. W. Weisstein, *Least Squares Fitting — Exponential*. <http://mathworld.wolfram.com/>, 2013.